Investigation of Structure, Properties and Applications of Bulk and Nanoscale Intermetallic Compounds Derived from AlB_2-Prototype

A Thesis

Submitted for the degree of

Doctor of Philosophy

as a part of

PhD Programme (Chemical Science)

By

Mr. Sumanta Sarkar

New Chemistry Unit

Jawaharlal Nehru Centre for Advanced Scientific Research

(A Deemed University)

Bangalore - 560064 (INDIA)

September-2015

Dedicated to my Family

and Teachers

Declaration

I hereby declare that the matter embodied in the thesis entitled "**Investigation of Structure, Properties and Applications of Bulk and Nanoscale Intermetallic Compounds Derived from AlB_2-Prototype**" is the result of investigations carried out by me at the New Chemistry Unit, Jawaharlal Nehru Centre for Advanced Scientific Research, Bengaluru, India under the supervision of Dr. Sebastian C. Peter and that it has not been submitted elsewhere for the award of any degree or diploma.

In keeping with the general practice in reporting scientific observations, due acknowledgement has been made whenever the work described is based on the findings of other investigators. Any omission that might have occurred by oversight or error of judgment is regretted.

Date: 30.12.2015

Bengaluru, India Sumanta Sarkar

Certificate

I hereby certify that the matter embodied in this thesis entitled "**Investigation of Structure, Properties and Applications of Bulk and Nanoscale Intermetallic Compounds Derived from AlB_2-Prototype**" has been carried out by Mr. Sumanta Sarkar at the New Chemistry Unit, Jawaharlal Nehru Centre for Advanced Scientific Research, Bengaluru, India under my supervision and that it has not been submitted elsewhere for the award of any degree or diploma.

Date: 30.12.2015

Bengaluru, India

Dr. Sebastian C. Peter

Assistant Professor
New Chemistry Unit
JNCASR
(Research Supervisor)

Acknowledgements

First of all, I take this opportunity to express my immense gratitude to my research supervisor Dr. Sebastian C. Peter for his constant support, inspiration and enthusiasm and the kind of freedom he has given me for my work. His suggestions pertaining to my work and his way of tackling problems have altogether helped me immensely. It has been a great pleasure for me to work under his guidance. I also thank Mrs. Ashly Sebastian for her hospitability and homely food.

I have been extremely fortunate to have got encouragement from Prof. C. N. R. Rao, F.R.S. at the beginning of my research career. I owe a deep sense of gratitude to his great personality and immense contribution to science.

I am also thankful to all the faculty members of New Chemistry Unit for selecting me as one of the candidates for Mid Year PhD Program 2011 and giving me the opportunity to carry out my research.

I am thankful to JNCASR and SSL for wonderful research facilities and highly competitive environment.

I must thank CSIR, India for providing me fellowship and contingency grant for pursuing research.

I am grateful to various funding bodies like Department of Science and Technology, Department of Atomic Energy, India, and CERIC, Italy which supported me for performing experiments in PETRA III, Germany, Photon factory, Japan and Elletra, Italy.

I am also thankful to I2CAM and NSF, USA for their travel grant for attending Gordon Research Conference in 2014.

I would like to thank my collaborators Prof. Swapan K Pati, Prof. Umesh V. Waghmare, Prof. Chandrabhas Narayana, Prof. A. Sundaresan, Prof. Aninda J. Bhattacharyaa, Dr. Sudhindra Rayaprol, Dr. Matthias J. Guttman, Dr. Rajeev Rawat, Dr. A. K. Reddy, Prof. S. Sampath, Ms.

Suchitra, Ms. Dhanya R., Ms. Swastka Banerjee, Mr. Balamurugan Tappa, Mr. Santhosha L., Mr. Somnath Ghara.

I specially thank Dr. Ritesh Haldar, Mr. Rana Saha, Mr. Bharat, Mr. Arpan Hazra, Mr. Dheeraj K. Singh for helping me with various measurements.

I would like to thank Dr. Sebastian C Peter, Dr. Tapas K. Maji, Prof. A. Sundaresan, Prof. S. M. Shivaprasad and Prof. Shobhana Narashinham for various courses which were extremely helpful to me.

I am thankful to all my past and present labmates Mr. Abishek K. Iyer, Mr. Pradeep Shanbough, Ms. Deepti Kalsi, Mr. Pramod Halappa, Ms. Prakriti A. N., Ms. Oinam Bijeta, Mr. Aloke K Ghosh, Mr. K.V.V. Satyanaraya, Ms. Swathi, Mr. Ramesh Shiva, Mr. Udumula Subbarao, Mr. Soumyabrata Roy, Mr. Rajkumar Jana, Mr. Duddappa Mumbaraddi, Mr. Saurav Sarma, Dr. Vijay Marakatti, Ms. Swetha Ramani, Ms. Shreya Sarkar, Mr. Vidyanshu Mishra, for their help, encouragement and for maintaining a team spirit in the lab. I would like to thank the summer students Rashmi, Navami, Lahari, Rohan, Hiranmayee, Juhi who worked with me during their summer project.

I would also like to acknowledge all my teachers who enlightened me throughout my life with knowledge and sowed the seed of interest for science inside me.

I also thank all my friends, seniors and juniors for making my stay at JNCASR pleasant and enjoyable.

I would like to express my sincere gratitude to all the staffs of academic, administrative, security, library, complab and health center for making our campus life smooth and easy.

I would like to thank the technical staffs Mrs. Usha, Mrs. Bhavya, Mrs. Selvi, Mr. Anil, Mr. Vasu, Mr. Srinivas, Mr. Mahesh and Mr. Jagadish for their helps in various measurements.

Above all, I would like to thank my family for all their love and constant support through all my ups and downs.

List of Abbreviations

RE = Rare Earth

HF = High Frequency

PXRD = Powder X-ray Diffraction

TEM = Transmission Electron Microscopy

SAED = Selected Area Electron Diffraction

FE SEM = Field Emission Scanning Electron Microscopy

XANES = X-ray Absorption Near Edge Spectroscopy

XPS = X-ray Photoelectron Spectroscopy

Preface

Intermetallic compounds belong to a class of inorganic compounds which are formed by two or more metals or metalloids bound mostly by covalent bonding with an ordered crystallographic structure. This thesis mainly focuses on a particular family of intermetallics which are derived from AlB_2 structure type which crystallizes in hexagonal *P*6/*mmm* space group and envisages a large and versatile groups of derivative superstructures with interesting structural and physical properties. The thesis is divided in seven chapters as briefly described below. Among which five chapters are dedicated to bulk intermetallic compounds and the last chapter discusses about ordered intermetallic nanoparticles which were used as a catalyst for ethanol electro-oxidation.

Chapter 1 gives an introduction about the structure of AlB_2 structure type and derivation of different superstructures by various symmetry reduction methods. The chapter also discusses various synthesis strategies to explore novel compounds using AlB_2 prototype as a structural motif in both bulk and nanoscale. The major emphasis is given to mixed valent rare earth based materials and their impact on the generation of unique properties in condensed matter physics.

Chapter 2 deals with two Ce based compounds - Ce_2PdGe_3 and Ce_2PtGe_3. The former shows three different crystal structures with slight variation in Pd to Ge ratios. Among the polymorphs, γ- Ce_2PdGe_3 crystallizes in a new superstructure of the AlB_2 type. The detailed magnetic measurements suggest magnetic exchange bias in γ- Ce_2PdGe_3, which is the first ever report in an intermetallic compound as in intrinsic state. β- Ce_2PdGe_3 adopts tetragonal structure having spin glass behavior. Ce_2PtGe_3, on the other hand, crystallizes in a new orthorhombic superstructure type with *Cmca* space group and undergoes spin-glass transition at low temperature.

Chapter 3 discusses crystallographic structure of three Eu based compounds- Eu_2CuGe_3, Eu_2AuSi_3 and Eu_2AgGe_3. This last compound showed temperature dependent reentrant structural phase transitions, which was explained based on a lattice displacive mechanism. The compound also underwent multiple magnetic transitions at low temperature.

Chapter 4 discusses structural characterization of Yb_2CuGe_3, Yb_2AuSi_3 and Yb_2AuGe_3. The compounds were synthesized using high frequency induction furnace and indium as an inactive

metal flux. Yb_2AuGe_3 showed temperature dependent structural phase transition which was explained based on a general order-disorder phase transition mechanism and Yb was found out to be in mixed valence state.

Chapter 5 discusses synthesis, crystal structure and physical properties of three new compounds, RE_2AgGe_3 (RE = Ce, Pr, Nd), which crystallize in the α-$ThSi_2$ structure type. The structural relationship between AlB_2 and α-$ThSi_2$ prototypes is discussed in this chapter. The magnetic and transport properties of all the compounds have aslo been studied.

Chapter 6 describes the synthesis, structural characterization and physical properties of $EuTIn_4$ (T = Ir, Pt, Au) and $EuAu_2In_4$ series of compounds. It also discusses about the structural evolution of these two families from AlB_2 prototype. The preliminary magnetic and transport properties have been studied.

Chapter 7 discusses about the synthesis, characterization and study of electrocatalytic activity of Pd_2Ge nanoparticles and its variants substituted with first row transition metals, which crystallize in Fe_2P crystal structure. The catalytic activity of all these compounds has been studied by the electrochemical oxidation of ethanol. The deficiency at the Ge site and alloying played major roles in improving the activity compared to the commercial materials. The catalyst was found to be more active and stable than commercial Pd/C.

Finally the results have been summarized.

Table of Contents

Chapter 1
Introduction

1.1 Background and Motivation

The relation between structure and properties in *RE* based intermetallic compounds has been crucial to design materials for particular applications.[1-2] Several physical phenomena in the field of condensed matter physics such as superconductivity,[3] Kondo behavior,[4] heavy fermion, non-Fermi liquid behavior[4] and topological insulator[5] are well correlated with the structure of these compounds. These anomalous physical properties mostly originate from the interactions between the localized 4*f* (or 5*f*) electrons of the *RE* atoms and the delocalized conduction electrons.[6-9] These interactions can be controlled by various parameters such as doping,[10] substitution of atoms,[11] by applying external pressure and/or temperature,[12] and magnetic field,[13] which may give rise to diverse crystal structures, phase transitions and properties. In this context, AlB_2 structure drew attention of both chemists and condensed matter physicist since last two decades. The compound consists of planar hexagonal network of boron atoms and the aluminium atoms are embedded between adjacent parallel boron networks.[14] A fascinating fact about this structure is that it gives rise to one of the largest derivative superstructure in *RE* based intermetallic compounds with diverse crystal structures and physical properties.[15] Although interesting physical properties of these compounds were studied in detail one of the major persisting challenges is the difficulty in the synthesis of these compounds. Disordered structures are often observed in which *RE* occupies the Al site, but B site is mixed with *T* and *X* atoms. Depending on the size and chemical nature of the metals used, the disordered compounds crystallize in wide solubility range, which raise the questions of the phase purity and limit the property studies. Another major problem is unavailability of high quality of single crystals for anisotropic property measurements.

The work presented in this thesis is motivated by the above challenges and focuses on the synthesis of three *RE* based families derived from AlB_2 structure type: RE_2TX_3, $RETIn_4$ and $REAu_2In_4$. Most of the compounds were synthesized using indium as a metal flux to obtain high quality single crystals. The crystal structure of all the compounds were determined by XRD measurements. The magnetic and transport properties were also studied. Compounds with the general formula RE_2TX_3 are one such family exhibiting diverse structures and physical properties; they crystallize in an ordered superstructure of the AlB_2 type.[16-25] Höffman et al discussed the structural similarities of the different types of these superstructures through group-subgroup relations using the concept of Bärnighausen formalism.[13-15] The ordering of the transition metal atoms and

main group elements at the boron positions in the planar hexagonal ring of the AlB_2 type may result in the loss of the basic hexagonal symmetry and the formation of ordered superstructures.[13, 21-27] The tilting and distortions of the hexagonal rings cause reduction of symmetry leading to the formation of superstructures. Various factors like variable atomic size, valence electron count and bonding nature may give rise to this kind of distortion.

1.2 Intermetallic Compounds

The above background just gives a glimpse of the importance of intermetallic compounds crystallizing in AlB_2 structure in bulk and nanoscale and hence it will be worth discussing about the definition, classifications, properties and applications of intermetallic compounds in the subsequent sections as a whole.

1.2.1 Definition

Although with time the definition of intermetallic compound has become broadened, the widely accepted concept states that intermetallic compounds are a class of inorganic solids having *ordered crystallographic structure* among the constituent *metals and/or metalloids* with well defined composition. Intermetallics are further classified into several subclasses based on their crystallographic and electronic structure.

1.2.2 Classification

1.2.2.1 Polar Intermetallics and ZintI Phases

Polar intermetallic compounds are interconnected, highly condensed cluster growth closed shell compounds consisting of transition metals and *p*-block metals leading to high degree of polarity in the bonding.[28-29] A classic example in this class is Zr_5Sn_3.[29] Zintl phases[30] were originally compounds formed between alkali/alkaline earth metals with *p*-block elements.[31] However with time the concept was extended to make room for a large family of compounds with the following features:

(i) the compound should contain alkali, alkaline/rare earth metals and a *p*-block element(/s)

(ii) these compounds are electronically balanced or closed-shell

(iii) mostly fall in narrow band gap semiconductor however metallic Zintl phase such as $Na_3K_8Tl_{11}$ is also known.[32] Some of the classic compounds in this series are NaTl, Cs_4Ge_9, Cs_4Pb_9, etc.[30]

1.2.2.2 Heusler phases

Heusler phases are a class of intermetallic compounds that are formed by transition metals and *p*-block elements crystallizing in face centered cubic structure.[33] Magnetic compounds of the Cu_2MnAl-type (X_2YZ) which can be imagined as an structure resulting from the interpenetrating NaCl and ZnS structures. The crystal structures of Heusler and half Heusler are compared in **Figure 1.1**. The half Heusler phase can be obtained from the Heusler structure by simply putting a void in alternative X sites.[31]

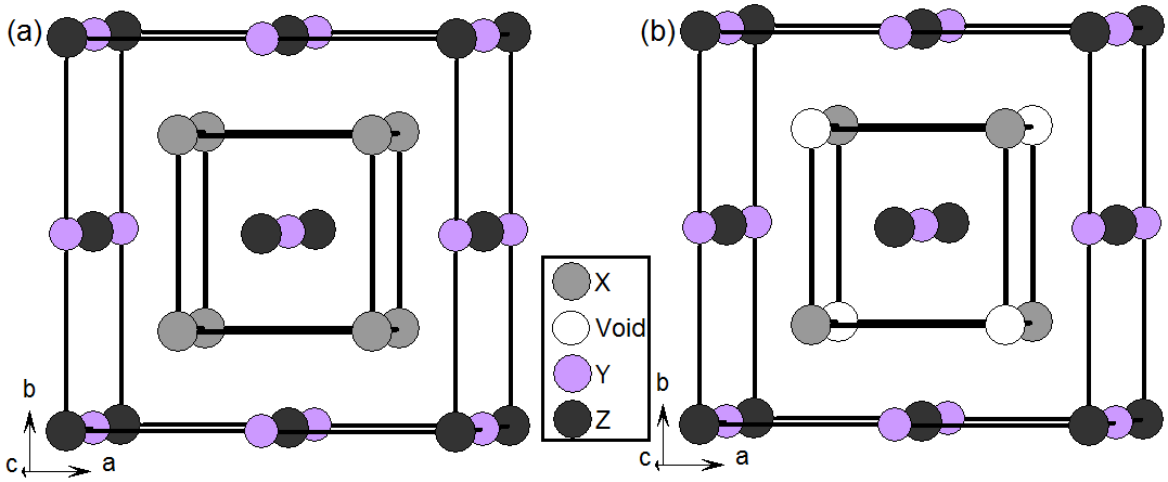

Figure 1.1 Unit cell of Heusler (a) and half Heusler (b) compounds.

1.2.2.3 Samson phases

Samson phases involve giant cells constructed by fused polyhedra mostly truncated tetrahedra unlike the Frank-Kasper cages, which mostly consist of icosahedra.[34] β-Mg_2Al_3 was the first compound in this category. The unit cell of this cubic compound (*Fd*-$\bar{3}$m) contains 1168 atoms distributed over 1832 atomic positions. About 3/4th of atoms form the framework of the structure. The framework is made up of Samson's positions, which are occupied by atoms with unique site occupancies. The remaining 1/4th of the atoms partially occupy 953 positions with the average occupation probability of 30%.[34]

1.2.2.4 Frank-Kasper phases

Frank-Kasper structures can be considered as interpenetrating polyhedra in such a way that every atom situated at the corners becomes center of another polyhedron and each atom will have a high coordination number ranging from 12-16. These coordination numbers can only be achieved considering a maximum of 5-6 tetrahedra sharing a single corner atom. Many Laves phases like Cu_2Mg, $MgZn_2$ fall under this category. Recently reported $SmCu_6In_6$ also contains Frank-Kasper cages as shown in **Figure 1.2**.[31]

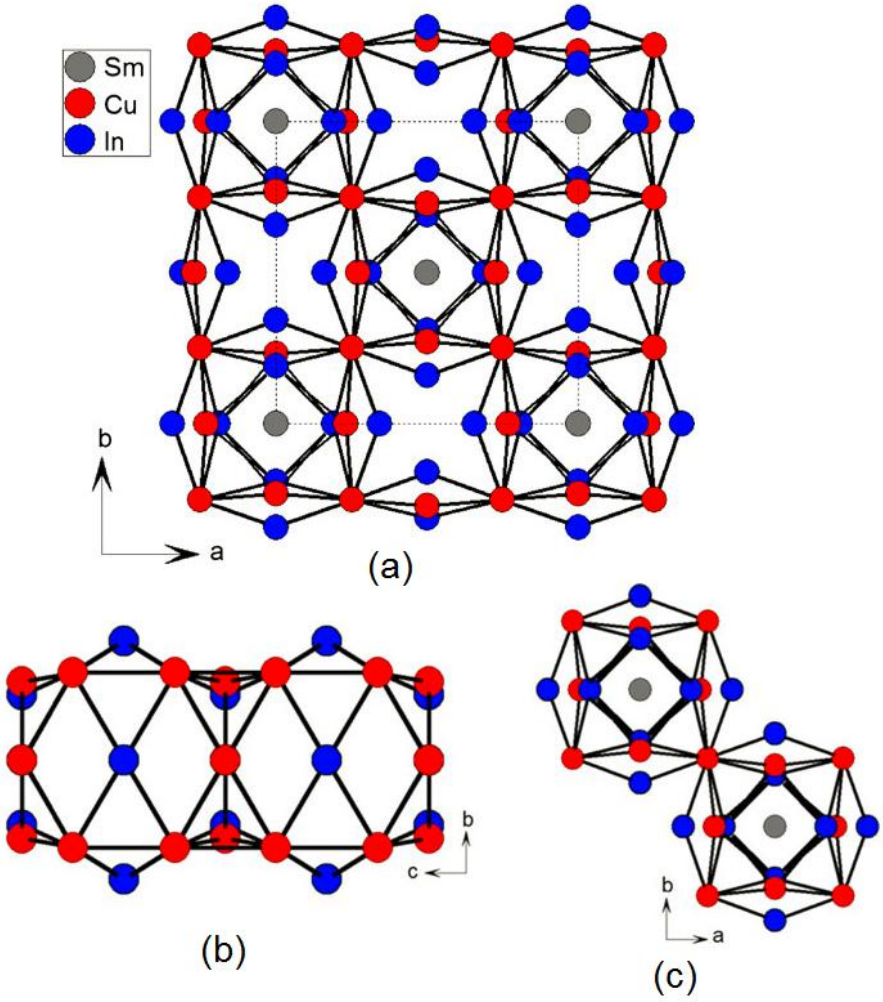

Figure 1.2 (a) Structure of $SmCu_6In_6$ as viewed along the *c*-axis; the unit cell is outlined as dot lines. Pseudo-Frank–Kasper cages in $SmCu_6In_6$ are shared through the (c) edges of the split atoms and (d) corner of Cu atoms along *ab* plane (reproduced with permission from Indian Academy of Science).

1.2.2.5 Hume-Rothery Phases

Hume-Rothery phases refer to those compounds which crystallize in the same structure type if they have the average number of valence electrons per atom included within certain well-defined ranges.[31] A classical example of a Hume-Rothery phase is Cu-Zn binary alloy. Au-Cd system is another example. All these phases abide by all or most of the following rules:

(i) atomic radius of the constituent elements must not differ more than 15%

(ii) electronegativity of the constituents must be similar

(iii) crystal structure of the constituents should be similar

(iv) valency of the constituents should be the same

1.2.2.6 Nowotny-Juza Phases

Nowotny-Juza phases, also known as *chimney-ladder superstructure* phases consist of two different subcells e.g. A and B with number *n* and *m* interpenetrating each other along the supercell growth direction. This may give rise to cross linking units (ladder) of A along the one dimensional channels (chimney) of B. $Mn_{11}Si_{19}$ crystallizing in tetragonal, *P*4*n*2 space group (*a* = 5.518 Å, *c* = 48.136 Å), is a *chimney-ladder superstructure* along the *c*-direction of $TiSi_2$ which crystallizes in orthorhombic *Fddd* space group (*a* = 4.7960 Å, *b* = 8.2580 Å and *c* = 8.5430 Å).[31]

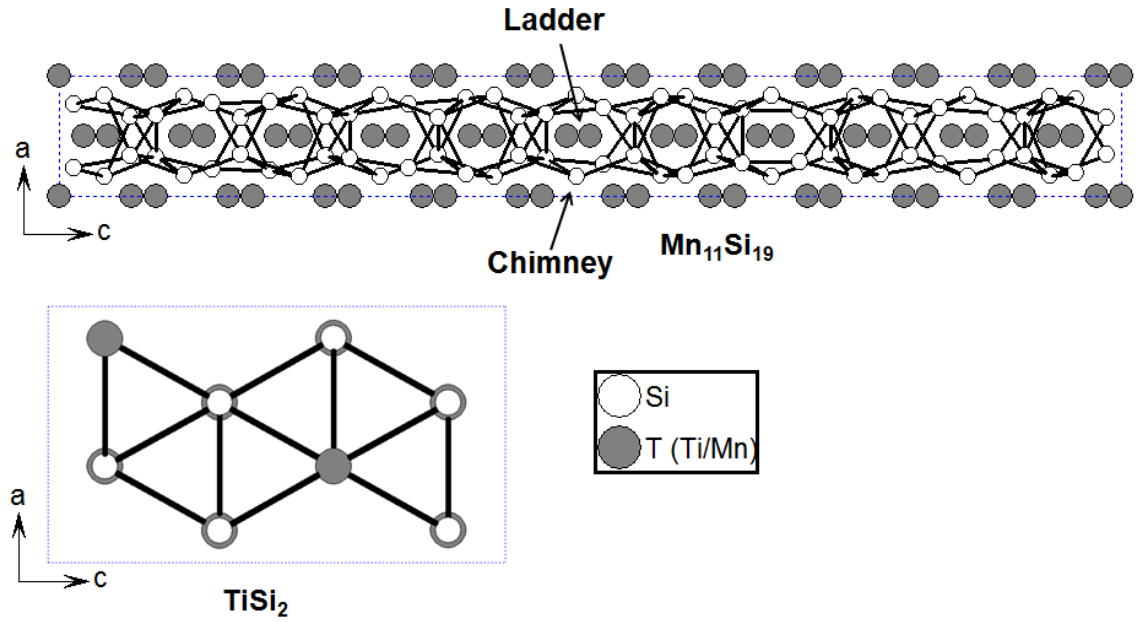

Figure 1.3 $Mn_{11}Si_{19}$- a chimney-ladder superstructure of $TiSi_2$ subcell.

1.2.3 Difference with Alloys, Solid Solutions and Bimetallics

Intermetallic compounds differ from the alloys/solid solutions and bimetallics both structurally and as well as in terms of bonding characteristics. Intermetallics are mostly covalently bonded with ordered crystal structure and composition, whereas in alloys one metal is mixed in another within its *solubility limit* forming a range of phases with a range of compositions. Naturally, they do not possess a unique composition. The binding in these compounds mostly occur by metallic bond. Bimetallic/multimetallic compounds are another class of compounds where the constituent metals do not mix together forming a clear interphase boundary and hence they are essentially heterogeneous in nature. **Figure 1.4** shows the basic difference in the structure of these compounds.

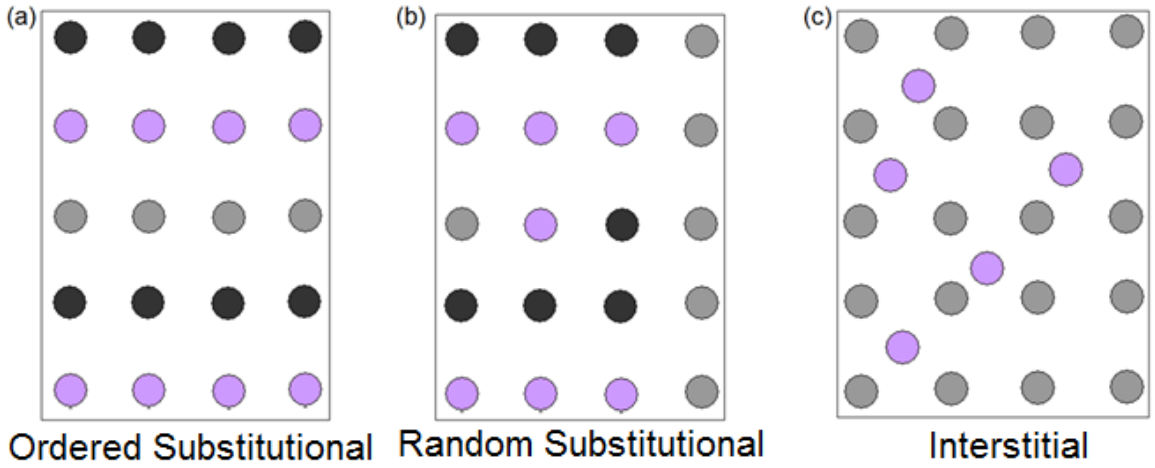

Figure 1.4 Schematic representation of (a) order substitutional, (b) random substitutional and interstitial superstructures.

1.2.4 Factors Affecting the Structure of Intermetallic Compounds

There are a number of factors, which can dictate the phase formation in intermetallic compounds as summarized by Pearson.

1.2.4.1 Chemical bond factor

One of the basic rules that govern the structure of the intermetallic compounds (and in general any other compound) is the *chemical bond factor* which[31] can control the structure of the compound in terms of interatomic distances and unit cell dimensions which are actually determined by a set of chemical bonds. Two different kinds of bonding scenario may be encountered, first, bonds having high non-directional ionic contribution or highly directional covalent feature, which determines the structural arrangement in the phase. A *normal valence compound* (X_mY_n,) is defined by the following equation where the number of valence electrons of cations and anions are e_C and e_A, respectively:

$$me_c = n(8 - e_A) \ldots \textbf{eq. 1.1}$$

1.2.4.2 Energy band factor

The electronic structure of a solid and properties associated with it can be calculated on the basis of the states of the electrons (known as density of states, DOS) in the crystal. Modern calculations can also take account of the lattice vibrations (phonons) which are intrinsic to the lattice arrangements and their interactions with the conduction electrons.[35]

In case of *RE* based compounds, further information can be obtained on the hybridization of localized f states and itinerant conduction electrons.

It should be noted that in many cases valence electron count (VEC) may be much helpful to predict the structure and properties of a compound e.g. in case of Heusler compounds.

1.2.4.3 Geometrical factors

The following factors are to be considered while considering the geometric constraints for intermetallic phase formation:

(i) efficient use of space
(ii) consideration of highest symmetry
(iii) greatest number of connections (coordination number)

1.2.5 Group-Subgroup Relationship

Many structures which apparently may appear different but can be related crystallographically using a series of *symmetry reduction methods* and this procedure is known as group-subgroup relation which was first shown by Bärnighausen (popularly known as *Bärnighausen formalism* or *Bärnighausen tree*) and was further elaborated by Müller, Burns, Glazer and Nesper. There are mainly three kinds of symmetry operations, which can be used to derive a supercell corresponding to a superstructure from the corresponding subcell, which corresponds to a subcell. (i) *klassengleiche* (*k*) operation - in this operation, there is no change in crystal class upon lowering the space group symmetry, both the group and the subgroup belong to the same crystal class, e.g. cubic crystal system will remain cubic system only a decentering of a lattice and/or an enlargement of the asymmetric unit may occur. (ii) *translationengleiche* (*t*) operation - in this case no loss of translational symmetry occurs, only a change in crystal class occurs which basically leads to loss of rotational symmetry in terms of either inversion center or/and a reduction in the multiplicity of the symmetry axis to a partial element. (iii) *isomorphic* (*i*) operation is a special case of the klassengleiche operations which results in an enlargement of the asymmetric unit with the same space group type leading to additional reflections in the reciprocal lattice. There are several factors, which may drive

superstructure formations, e.g. atomic size, electronegativity of the elements, puckering of the rings, valence transition, etc.

At this point, it is worthwhile to introduce the AlB_2 prototype and its large variety of intermetallic compounds derived from the AlB_2 structure. The compound crystallizes in hexagonal crystal structure with *P*6/*mmm* space group. The unit cell of AlB_2, shown in **Figure 1.5**, hosts only three atoms with two crystallographically unique sites, aluminum atoms occupy the 1*a* Wyckoff site while the two boron atoms occupy 2*d* site in a trigonal prismatic coordination environment. The boron atoms form a two-dimensional infinite network, in which each boron atom has three other boron neighbors at a distance of 1.74 Å. These honey-combs like layers are well separated from each other by the lattice parameter *c* of 3.26 Å.

The general formula for the binary and ternary compounds possible from AlB_2 related structures are respectively RET_2, REX_2, $RETX$, RE_2TX_3, and $RE_3T_2X_4$ (*RE* = alkaline earth, rare earth metals; *T* = transition metals; *X* = main group elements). The *RE* atoms occupy the aluminum positions, while the *T* and *X* atoms form the parallel stacking hexagonal networks. It is only the hexagons which undergo distortions in case of the binary compounds, whereas for the substitution variants, a number of possibilities could be realized which range from the variable *T*:*X* ratio of an ordered or a statistical arrangement to planar or puckered hexagonal rings.

In the subsequent sections various types superstructure ordering will be discussed in the light of AlB_2 structure and the compounds derived from it.

1.2.5.1 Degenerate and derivative superstructures

Two important classes of superstructures are *derivative structures* and *degenerate structures.* A *derivative structure* can be obtained from a prototype or parent structure by ordered atomic substitution, subtraction or addition processes or by unit cell distortions. The so called *degenerate structures* correspond to opposite kinds of transformation. A derivative structure has lesser symmetry operations than the parent structure with either a larger cell or a lower symmetry (or both). e.g. UHg_2 is directly derived from the AlB_2 structure with slight enhancement of the unit cell edges (**Table 1.1a**) without changing the *P*6/*mmm* symmetry, whereas $EuGe_2$ and $CaIn_2$ can be derived from the AlB_2 structure by systematic symmetry reduction method (**Figure 1.6**).

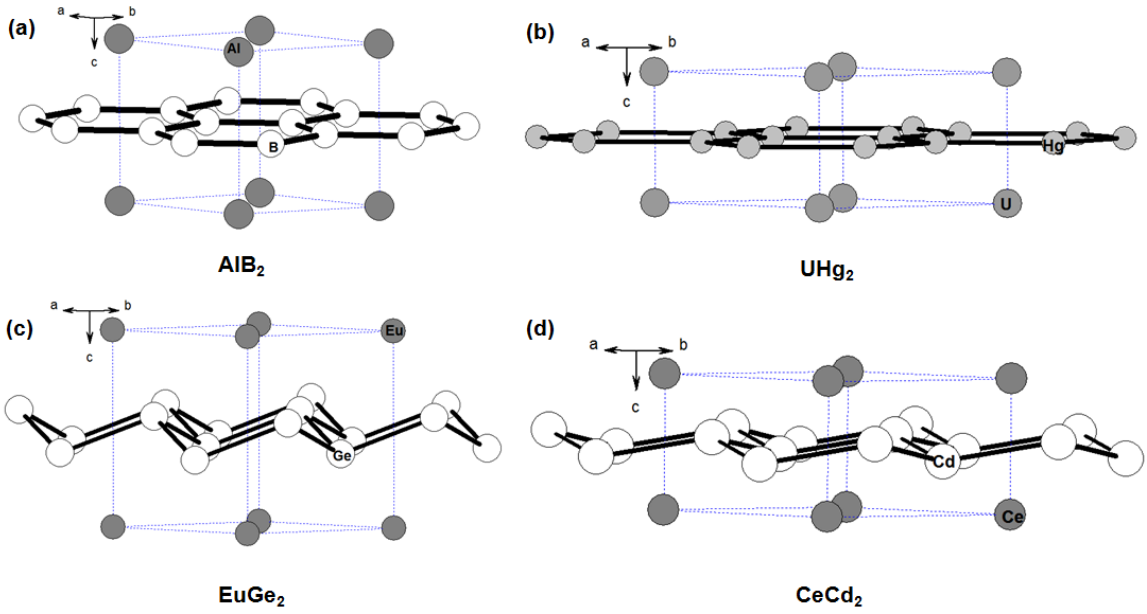

Figure 1.5 Representative unit cells of (a) AlB_2, (b) UHg_2, (c) $EuGe_2$ and (d) $CeCd_2$.

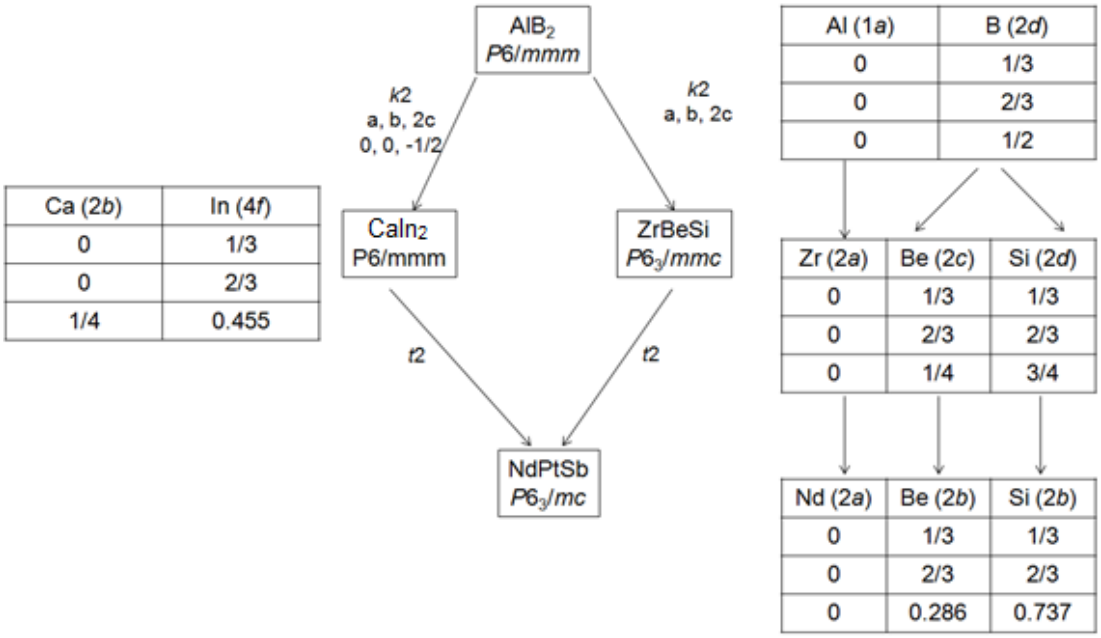

Figure 1.6 Derivation of $CaIn_2$ and ZrBeSi structures from the AlB_2 structure by systematic symmetry reduction method.

The Derived structures can also be formed with the introduction of *ordered vacant sites* (**Figure 1.7a** and **c**), while the *filled-up superstructures* (**Figure 1.7b** and **d**) can be obtained by simply filling up these vacancies, e.g. α and β-K_4P_6 structures are apt

examples of the *ordered vacant variant* superstructures where the vacancies are placed in the $[P_6]^{4-}$ hexagonal network in an ordered manner which are again filled up Ag and Li atoms to give rise to $Ca_4Ag_2Si_6$ and $Ba_4Li_2Si_6$, respectively, where $[(Ag/Li)_2Si_6]$ hexagonal rings exist. The latter two compounds, which crystallize in orthorhombic structure are examples of *filled-up superstructures*.

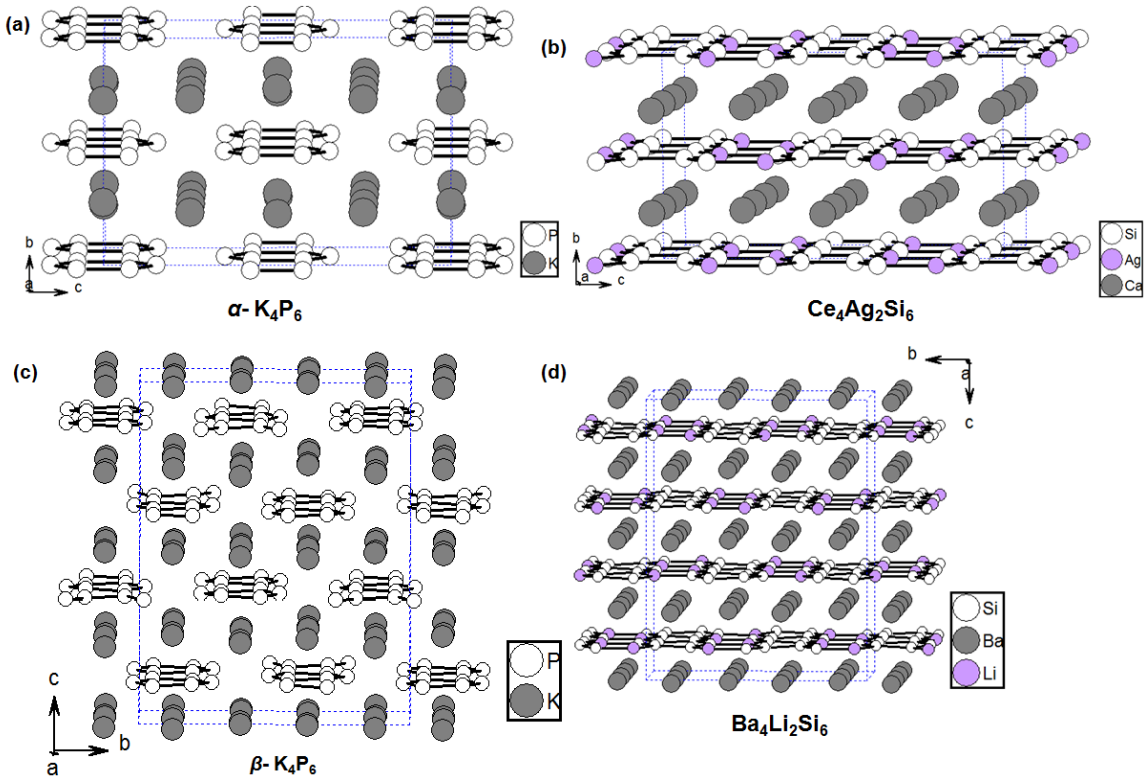

Figure 1.7 Crystallographic representations of the ordered vacancy variant (a) α-K_4P_6, (b) β-K_4P_6, (c) $Ca_4Ag_2Si_6$ and (d) $Ba_4Li_2Si_6$.

The following tables (**Table 1.1a** and **1.1b**) show many important hexagonal/trigonal and orthorhombic/monoclinic superstructures derived from AlB_2 structure type along with their enhanced cell parameters and/or space groups. The corresponding Bärnighausen trees are shown in the subsequent **Figures 1.8** and **1.9** respectively, which utilize a series of symmetry reduction operations discussed in the beginning of this section.

Table 1.1a Crystallographic data on AlB_2 structure and derived superstructures in (a) hexagonal/trigonal.

Compound	*a* (Å)	*c* (Å)	*c*/*a*	Space Group
AlB_2	3.000	3.240	1.080	*P*6/*mmm*
UHg_2	4.976	3.218	0.647	*P*6/*mmm*
$BaSn_5$	5.373	7.097	0.660	*P*6/*mmm*
ZrBeSi	3.710	7.190	0.969	$P6_3/mmc$
Ni_2In	4.171	5.121	1.228	$P6_3/mmc$
$CaIn_2$	4.895	7.750	0.792	$P6_3/mmc$
SrPtSb	4.504	4.507	1.001	$P\bar{6}m2$
$EuGe_2$	4.102	4.995	1.218	$P\bar{3}m1$
$CeCd_2$	5.073	3.450	0.680	$P\bar{3}m1$
YPtAs	4.250	15.165	0.892	$P6_3/mmc$
NdPtSb	4.534	7.866	0.867	$P6_3mc$
LiGaGe	4.175	6.783	0.812	$P6_3mc$
ScAuSi	4.212	6.803	0.808	$P\bar{6}m2$
U_2RuSi_3	8.148	3.855	0.946	*P*6/*mmm*
Th_5Ga_4	7.861	5.452	0.601	$P6_3/mcm$
Hf_5CuSn_3	8.527	5.822	0.591	$P6_3/mcm$
Th_3Pd_5	7.149	3.899	0.945	$P\bar{6}2$m
Fe_2P	5.865	3.456	1.021	$P\bar{6}2$m
$Th_3Rh_2In_3$	7.287	3.067	0.729	$P\bar{6}2$m
YbAgPb	4.873	11.017	0.745	$P\bar{6}m2$
Er_2RhSi_3	8.113	7.756	0.956	$P6_3/mcm$
CaLiSn	4.940	10.900	0.735	$P\bar{3}m1$
YLiSn	9.296	7.346	0.790	$P6_3mc$
Pr_8CoGa_3	10.489	6.910	0.659	$P6_3mc$
α-Ce_2PdGe_3	4.261	4.252	0.998	*P*6/*mmm*
γ-Ce_2PdGe_3	4.313	12.363	2.866	*P*6/*mmm*

Table 1.1b Crystallographic data on AlB_2 structure and derived superstructures in orthorhombic/monoclinic crystal system.

Compound	*a* (Å)	*b* (Å)	*c* (Å)	β (°)	Space Group
Er_3Si_5	3.793	6.538	4.082		*Pmmm*
$YAl_{1.4}Si_{0.6}$	4.072	5.812	8.823		*Immm*
KHg_2	5.160	8.770	8.100		*Imam*
$CeCu_2$	4.430	7.450	7.050		*Imam*
UPt_2	4.120	9.680	5.600		*Cmcm*
YAlGe	4.050	10.440	5.764		*Cmcm*
α-K_4P_6	8.624	14.253	9.347		*Fmmm*
$Ca_4Ag_2Si_6$	8.315	14.391	8.646		*Fmmm*
EuAuGe	4.601	7.881	7.371		*Im*2*m*
Eu_2AuGe_3	8.577	14.855	9.002		*Fmmm*
Yb_2AuGe_3	8.512	14.720	8.499		*Fmmm*
TiNiSi	3.669	7.017	6.148		*Pmcn*
EuZnSn	4.767	8.079	7.894		*Pmcn*
$Tb_3Co_2Ge_4$	10.692	4.164	8.067	107.72	*C*2/*m*
β-K_4P_6	8.305	14.772	18.650		*Fddd*
$Ba_4Li_2Si_6$	8.726	15.174	19.322		*Fddd*
CaPtP	8.311	6.519	4.344		*Pb*2_1*m*
YPdSi	4.308	7.431	13.912		*Pmmm*
α-UFeGe	4.308	6.992	6.986	α = 93.71	*P*2_1/*m*
CaCuGe	4.360	7.494	21.249		*Pmcn*
CaPdAs	16.590	7.137	8.646		*Pbnm*
Ba_2PdP_3	6.425	7.222	12.836	91.97	*P*2_1/*c*
EuAuSn	4.791	8.201	38.336		*Im*2*m*
CaAuSn	4.705	8.136	36.903		*Pmcn*

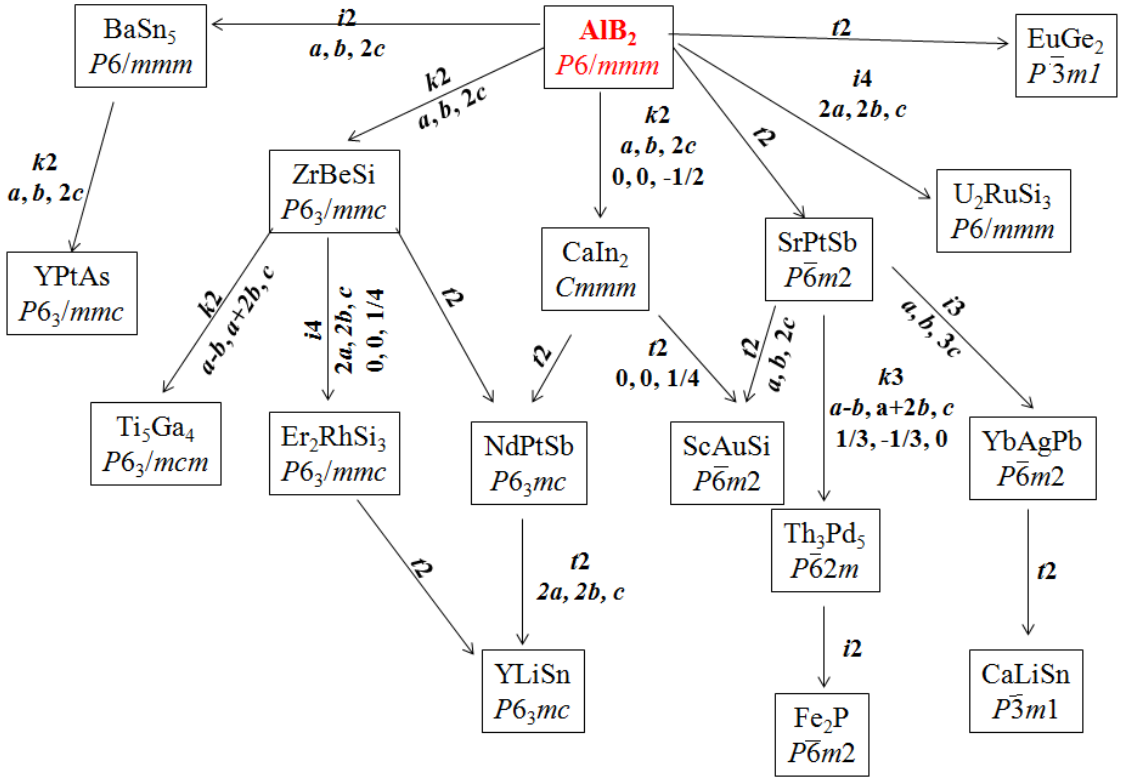

Figure 1.8 Bärnighausen tree for the symmetry reduction of AlB_2 structure to hexagonal /trigonal branch.

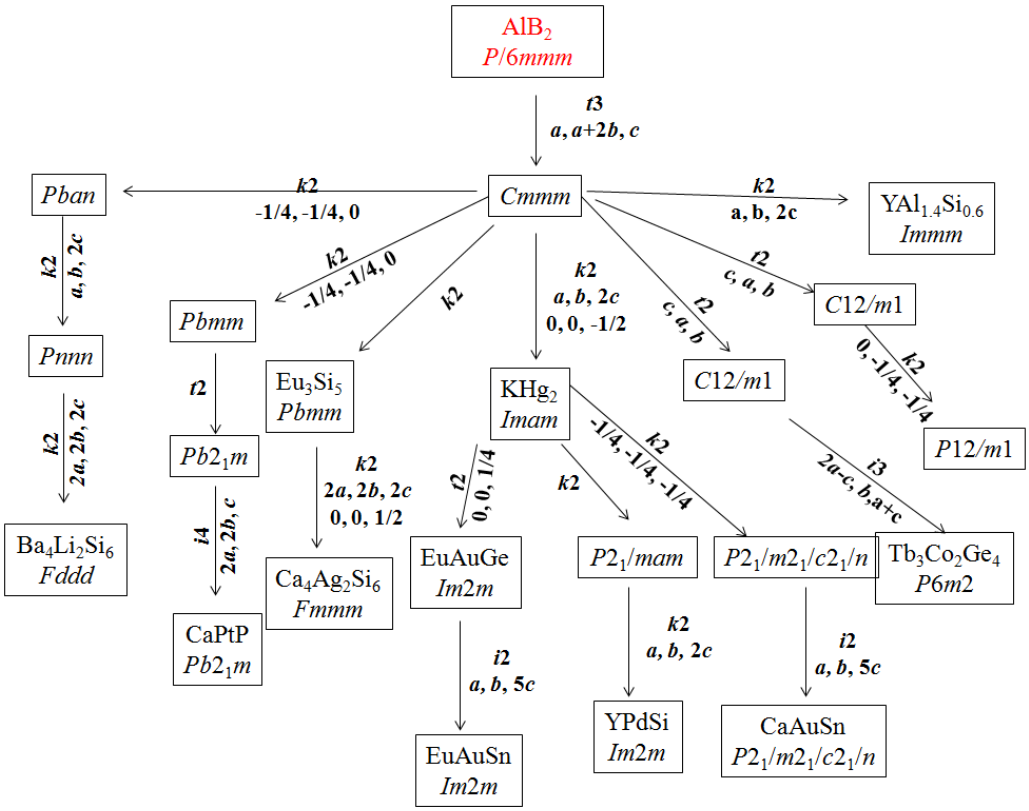

Figure 1.9 Bärnighausen tree for the symmetry reduction of AlB_2 structure to orthorhombic/monoclinic branch.

1.2.5.2 Ordering-disordering transformation

One of the most important classes of transformations in solid state chemistry involves *ordering-disordering transformations* in which a structure undergoes a systematic structural transition from a less symmetric phase to a high symmetric phase or vice-versa. An example in this class was shown by Peter *et al* in the case of Eu_2AuGe_3 where a probable structural transition from orthorhombic to monoclinic phase was detected while lowering the temperature below 130 K.

Two groups of superstructures may emerge from the order-disorder transformation: *substitutional superstructure* and *interstitial superstructure*. The former superstructure can be obtained upon substituting the atoms of the parent structure by other atoms with different size and electronegativity. An example in this category is ZrBeSi[15] can be derived from the AlB_2 prototype by systematic symmetry reduction as shown in **Figure 1.6**. Interstitial superstructures are obtained when very small guest atoms are incorporated in the reference structure leading to chemical effect which involves the charge transfer between hydrogen and the host compound as well as the magnetovolume effect caused by lattice expansion e.g. GdTiGe shows anti and ferromagnetic transitions at T_N = 412 K and T_c = 376 K, while the hydrogenated compound GdTiGeH becomes paramagnetic.[36]

In this context it is important to discuss about *long range* and *short range order*.[31] The essential condition for a solid solution of suitable composition to become ordered is that dissimilar atoms must attract each other more than similar atoms in order to lower the free energy upon ordering.

The above approach is too simple to account for the possibility of the existence of magnetic domains as well other types of fluctuations in the ordered array of atoms that may cause a nominal or significant departure from perfect order.

In order to encompass such scenarios, an alternative method of defining the state of order was devised which considers the number of unlike nearest neighbors around a given atom, instead of considering the probability of finding A or B atoms on designated α or β lattice sites and the revised parameter is called *short-range order parameter*,[31] σ, and is defined as follows:

$$\sigma = (q - q_r)/(q_m - q_r) \ldots \textbf{eq. 1.2}$$

Here, q denotes the fraction of unlike nearest neighbors at a given temperature and q_r and q_m respectively denote the fractions of unlike nearest neighbors at given conditions of maximum randomness and maximum order.

1.2.5.3 Displacive Phase transition

A second kind of structural phase transition is known as *displacive phase transition* or *diffusion less phase transition*.[37] The most important example in this class is martensitic transformation wherein a structural change occurs by a well organized movement of atoms relative to their neighbours (**Figure 1.10**). The transformation may occur via different mechanisms e.g. by *dilation* where the cell expands keeping the angle between adjacent edges same, or by *shear* forces.[37] Another kind of mechanism is known as *shuffles* which involves movement of atoms within the unit cell resulting in changes in symmetry and structure.[37]

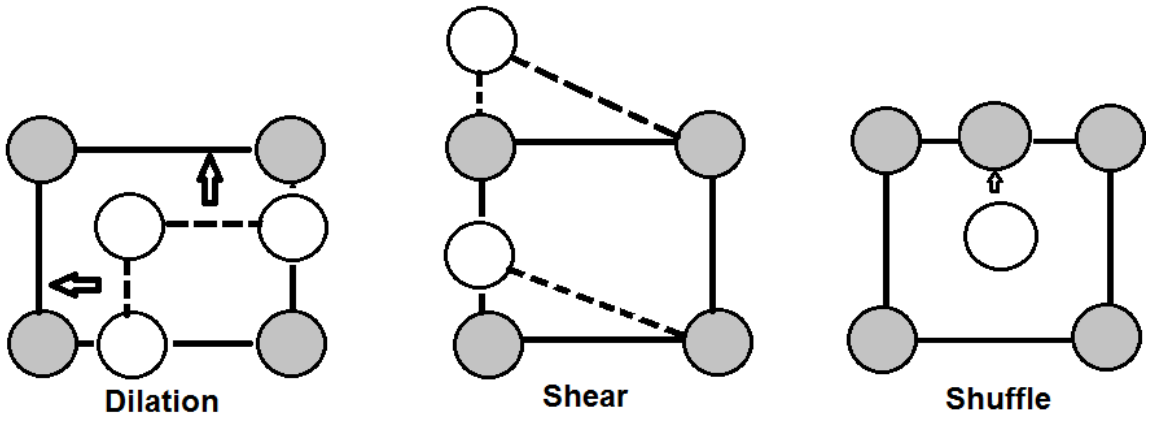

Figure 1.10 Schematic representations of different types of displacive phase transitions.

There are other superstructures such as *antiphase domain superstructures*,[31] which can be obtained after a periodic shift of a subcell by certain degree of the translation vector along a particular direction. Another kind of superstructure is called *homeotect* or *polytypic superstructure*,[31] which can be described as different stacking variants of identical structural units. Within a certain set, all the structures are built up by sandwiching identical unit slabs one above another.

1.2.6 Synthetic Strategies

At this point, having discussed the basic structural relationships in AlB_2 family, it will be convenient to discuss about the synthetic strategies that have been used for the synthesis of intermetallic compounds. This class of compounds can be synthesized by the same techniques which most of the solid state chemists use for the synthesis of other type solid

state compounds like oxides, chalcogenides, carbides, nitrides, etc. The major conventional techniques used in this thesis are direct heating in a tubular furnace, *HF*-induction furnace, arc melter, etc. Another novel technique which has been utilized in this thesis work is *metal flux method* and in the following subsections.

To better understand the advantages of using metal flux method, it is important to know the basic laws that govern diffusion- the Fick's law deduced by Adolf Fick.[38] The First law of diffusion describes that the *molar flux* due to diffusion is proportional to the *concentration gradient.*

Fick's second law reveals that, in diffusive processes, *there is a fundamental relation between the elapsed time and the square of the length over which diffusion takes place.* $\frac{\delta c}{\delta t}$ $\nabla^2 \frac{\delta c}{\delta t}$

1.2.6.1 Metal Flux Technique

1.2.6.1.1 Challenges in the Synthesis of Intermetallics- Rise of Metal Flux Method

There is a wide variety of synthetic strategies available to a solid-state chemist with its unique advantages and shortcomings. Synthesis of intermetallic compounds generally requires very high temperatures as the starting materials employed in these reactions are usually of high melting point and hence high temperatures are compulsory to make sufficient diffusion among the constituents in the reaction mixture. In addition, repeated grinding and remelting are necessary during the synthesis to ensure proper homogenization. There are mainly two limitations in using the conventional high temperatures syntheses, typically, arc-melting and *HF*- furnace; first, the reactions generally yield the most thermodynamically stable products, which are basically binary or ternary compounds leaving virtually no room for kinetically controlled metastable compounds. Once a thermodynamically stable phase is formed, it is difficult to obtain any other compound from that reaction mixture. Secondly, the fast cooling of the reaction mixture is not favorable for crystal growth process. A probable solution to the above mentioned challenges could be use of methods which involve lower temperatures, which may give rise to new compounds. Additionally, high diffusion rates are desirable in order to lower the activation energy barrier of the solid–solid reactions, which could be achieved by increasing the solubility of the starting materials in a solvent. To achieve enhanced diffusion of reactants in solid-state synthesis, molten salts, which are called

fluxes have already been used since long back. Two kinds of fluxes are used, one that only acts as a solvent is called an inactive flux, whereas the other which not only acts as a solvent but also as a reactant is called a reactive flux. In a similar way, molten metals can also be used for the synthesis of intermetallic compounds. **Figure 1.11** shows a schematic representation of the process to obtain high quality single crystals of versatile compounds in metal flux.

1.2.6.1.2 Features of a Good Metal Flux

Several key characteristics must be met for a metal to be a viable flux for reaction chemistry: (i) the metal should form a flux (i.e. a melt) at reasonably low temperatures (30-700 ^{o}C), so that normal heating equipment and containers can be used, (ii) the metal should have a large difference between its melting point and boiling point temperatures, (iii) it should be possible to separate the metal from the products, by chemical dissolution, filtration during its liquid state, or if necessary mechanical removal, (iv) the metal flux should not form highly stable binary compounds with any of the reactants. Only the following set of metals complies all or most of the above conditions as listed in **Table 1.2**.

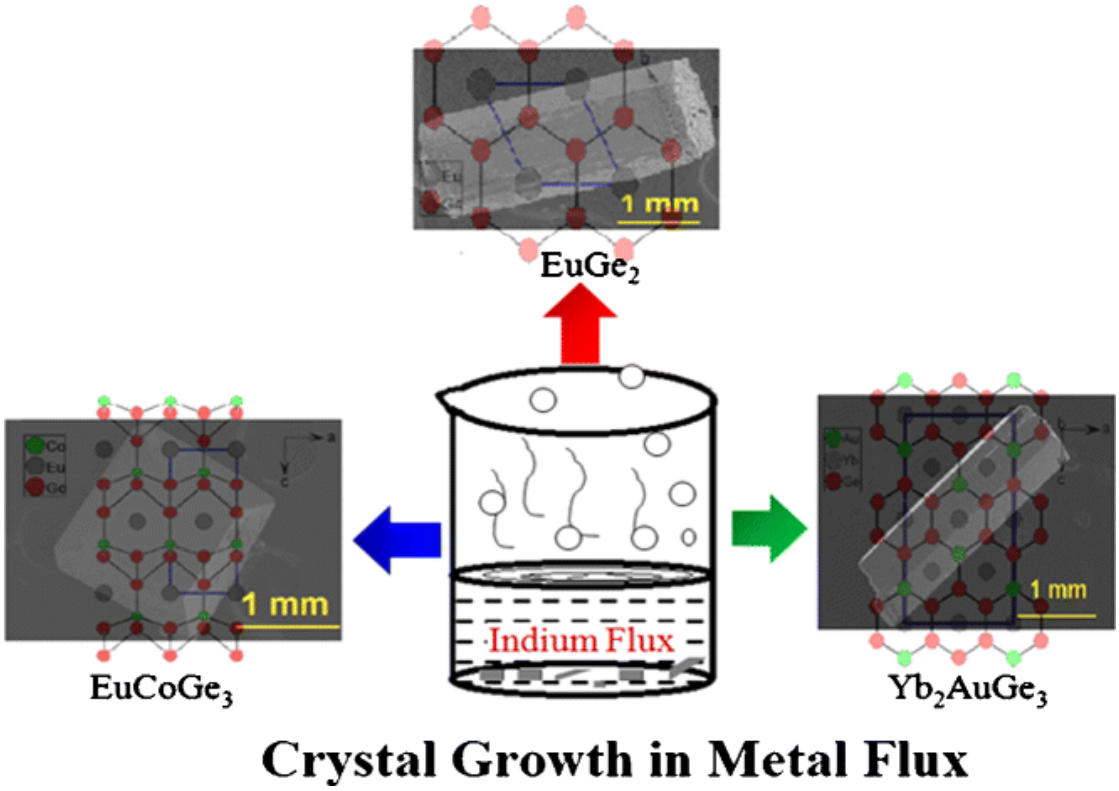

Figure 1.11 Cartoonic representation of crystal growth of intermetallic phases by metal flux method.

Table 1.2 List of metallic elements that are suitable for use as metal flux

Metal	MP(^oC)	BP(^oC)
Al	660	2467
Ga	30	2403
In	157	2000
Sn	232	2270
Pb	327	1740
Li	180	1347

1.2.7 Physical Properties of Intermetallic Compounds

Ordered superstructures derived from the AlB_2 structure type and have been studied extensively for last two decades for their fascinating physical properties, e.g. Anisotropic giant magnetoresistance, magnetocaloric effect were observed in Tb_2PdSi_3,[39] formation of metallic magnetic cluster was also observed in this compound.[40] Large negative magnetoresistance was observed in Gd_2PdSi_3[41] whereas Gd_2CuGe_3[42] shows electrical resistance minimum above Neel temperature. Eu_2CuSi_3 also showed large negative magnetoresistance above the Curie temperature.[43] In the following sections some of the general and interesting physical properties will be discussed.

1.2.7.1 Magnetism

In *diamagnetic materials*, the magnetic susceptibility χ is negative and close to zero and it does not depend on temperature and the momentum vectors of spins completely cancel each other, whereas in *paramagnetic material*, χ is positive and inversely proportional to temperature (Curie's law). The electronic spins are randomly oriented. The magnetic susceptibility is high in case of *ferromagnetic materials*, which is observed below the curie temperature (T_C). The magnetization increases drastically with applied magnetic field. The magnetic susceptibility of antiferromagnetic materials decreases below a critical temperature known as the Néel temperature (T_N), the spins align opposite to each other, however unlike *diamagnets* complete cancelation does not occur. The *ferrimagnets* are a special case of antiferromagnets where the oppositely aligned spins are unequal.

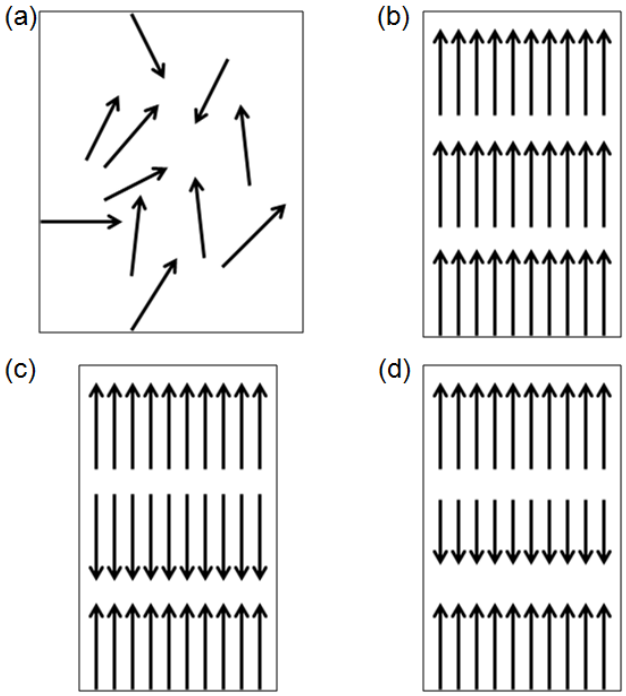

Figure 1.12 Schematic representation of different kinds of magnetic properties, (a) paramagnetism, (b) ferromagnetism, (c) antiferromagnetism and (d) ferrimagnetism.

A *metamagnetic transition* occurs when a large external magnetic field overwhelms the weak antiferromagetic interactions which aligns the net moments in antiparallel orientation and turns the system to a ferro-, ferri-, or *w*eak-*f*erromagnetic state. This phenomenon is generally observed in strong anisotropy.

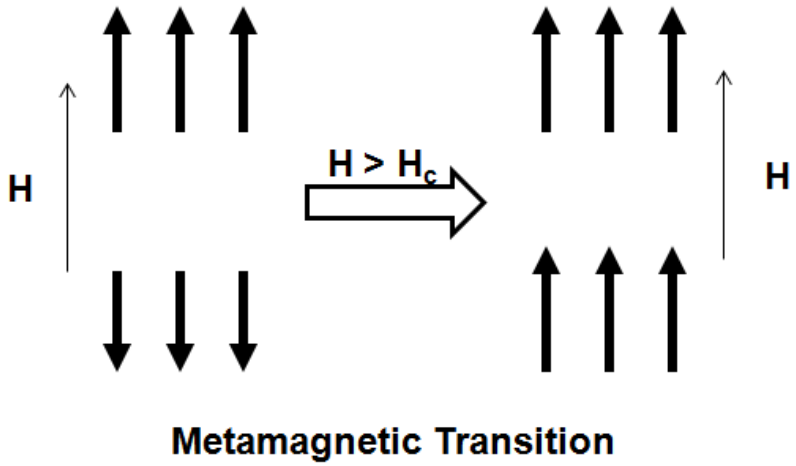

Figure 1.13 Schematic representation of metamagnetic transition under the influence of external applied magnetic field.

1.2.7.2 Spin Glass

One of the most attractive topics in the field of condensed matter physics is slow dynamics such as non exponential relaxation and memory effects. The spin glass state arises in a spin lattice which are topologically frustrated e.g. in **Figure 1.14**, a 2D frustrated system has been shown where on the antiferromagnetic site is disordered. Many Laves phases[44] like $FeAl_2$,[45] $GdAl_2$,[46] etc are known to show spin glass like behaviour at low temperature.

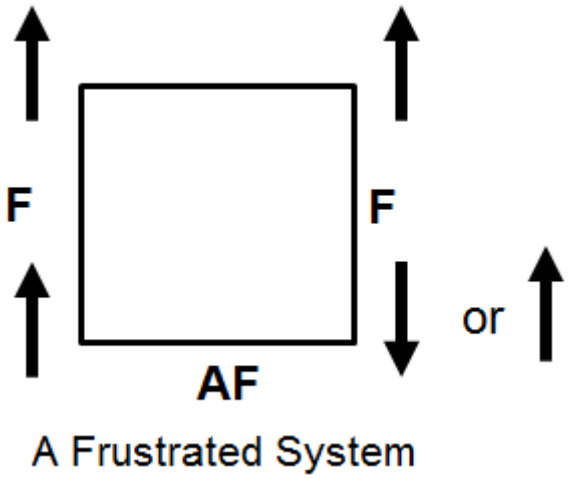

Figure 1.14 A simple frustrated contour in a 2D lattice showing interlayer interactions of the adjacent spins

1.2.7.2.1 Theoretical Models on Spin Glasses

The following sections briefly discuss about the fundamental theories on spin glass systems. It important to note that in the cases of crystals, uniform ferromagnets, etc, the physical and mathematical analysis is simpler as they possess spatial symmetries. As these symmetries are absent in disordered systems like spin glasses, it is highly complicated to build up a theoretical understanding on these systems. It would not be an exaggeration to say that finding a universal law and order parameter for disordered systems is a like a treasure hunt for the theoretical physicists.

1.2.7.2.1a Edwards and Anderson Model

Edwards and Anderson (EA) model assumed that the spins are arranged on the sites of a regular lattice, and the interactions between the spins are randomly chosen from a Gaussian distribution. The spins are taken to be Ising spins and the exchange couplings are short range, occurring between nearest neighbor sites only. The EA model correctly predicts some of the observed experimental features of real spin glasses, however it also predicts zero residual entropy. Zero residual entropy is applicable if there is only one

possible ground state, or many ground states with a zero probability of a transition between them, but not to a real spin glass with a multi-degenerate ground state.

1.2.7.2.1b Sherrington and Kirkpatrick Model

An infinite-ranged version of the EA model was developed by Sherrington and Kirkpatrick (SK model), using a mean field theory approach. In the SK model of a spin glass the coupling interactions take place equally between all spins in the system. The spins are Ising spins and the coupling interactions are described by a Gaussian distribution. The SK model also correctly predicts some behaviour of spin glasses, but incorrectly predicts a negative value for the residual entropy, $S_0 = k_B \times -0.15915\ N = -1.322$ J/Kmol. This unphysical value of the residual entropy was improved upon by Parisi, using a *replica symmetry breaking scheme*, to $S0 = k_B \times -0.01\ N = -0.0831$ J/Kmol.

1.2.7.2.2 Experimental Verification of Spin Glass Transition

There are a number of ways by which a spin glass transition can be verified. The preliminary experimental verification comes from the bifurcation of zero field cooled (ZFC) and field cooled (FC) magnetic susceptibility curves, however, similar phenomenon is also observed in case of superparamagnets, therefore more confirmative test from isothermal relaxation measurements and ac susceptibility are necessary. Spin glass compounds possess a slow spin dynamics and hence can be probed by studying relaxation of the magnetization upon applying a short-timed magnetic field with time at a temperature below the glass transition temperature (T_g).[47] Similarly, an alternating frequency can be used as a probe in place of magnetic field. As the interparticle or inter domain interactions are quite strong in case of spin glasses, the glass transition temperature is affected by increasing the electrical frequency.[47]

1.2.7.3 Magnetic Exchange Bias

When materials with ferromagnetic and antiferromagnetic interfaces are cooled through the Néel temperature (T_N) of the antiferromagnet an anisotropy is induced in the ferromagnet. This phenomenon is known as exchange bias and was discovered by Meiklejohn and Bean in 1956 while studying Co particles embedded in antiferromagnetic cobalt oxide.[48] The effect is generally regarded as the *unidirectional* pinning of a ferromagnetic layer by an adjacent antiferromagnet stacked upon each other. Many parallelly stacked thin layer heterostructures of binary alloys/metals have been studied for

the exchange bias phenomenon, one classic example in this context is Co/FeMn bilayer thin films.[49] Recently Nayak et al observed giant tunable exchange bias in a compensated ferromagnetic Mn-Pt-Ga Heusler phase.[50] Similar phenomenon was also observed in a single phase intermetallic compound $YMn_{(12-x)}Mn_x$ with homogenous inter sublattice exchange coupling.[51]

Many of today's key magnetic memory storage devices and MP3 players utilize this effect to pin the magnetization of a ferromagnetic layer in a fixed direction. Once the direction of magnetization of the reference layer is fixed, the magnetization direction of a second ferromagnetic layer, known as the *sensor layer* can be aligned at an arbitrary angle with respect to that of the reference layer. There are two situations possible at this point, *first*, if the direction of magnetization in the sensor layer is rotated by a magnetic field, the device can act as a sensor for the direction and strength of the magnetic field and is utilized in magnetic recording heads; *second*, if two different directions of the magnetization in the sensor layer are used as two distinct states to the reference layer, a memory cell can be obtained consisting of "1" and "0" bits.

The pinning effect can be understood by the following figure wherein the external magnetic field has been applied at temperature $T_c>T>T_N$, the ferromagnet spins line up with the field, while the antiferromagnet spins remain random (**Figure 1.15a**). In the next step, while cooling below T_N, in the presence of the field, the antiferromagnet spins next to the ferromagnet align ferromagnetically due to the interaction at the interface. The other spin planes in the antiferromagnet layer follow the antiferromagnetic order so as to produce zero net magnetization (**Figure 1.15b**). When the field is reversed, the ferromagnet spins also start to rotate. However, the antiferromagnet spins manage to remain unchanged due to sufficiently large antiferromagnet anisotropy (**Figure 1.15c**). The antiferromagnet spins at the interface exert a microscopic torque on the FM spins, to keep them in their original position (ferromagnetically aligned at the interface) (**Figure 1.15iii**). Therefore, the ferromagnet spins have only one stable configuration and hence the anisotropy is unidirectional. Therefore, the field needed to completely reverse ferromagnetic spins will be larger if it is in contact with an AFM, as an extra field is needed to overcome the microscopic torque (**Figure 1.16**) and hence the hysteresis loop corresponding to the ferromagnet is shifted in the field axis.

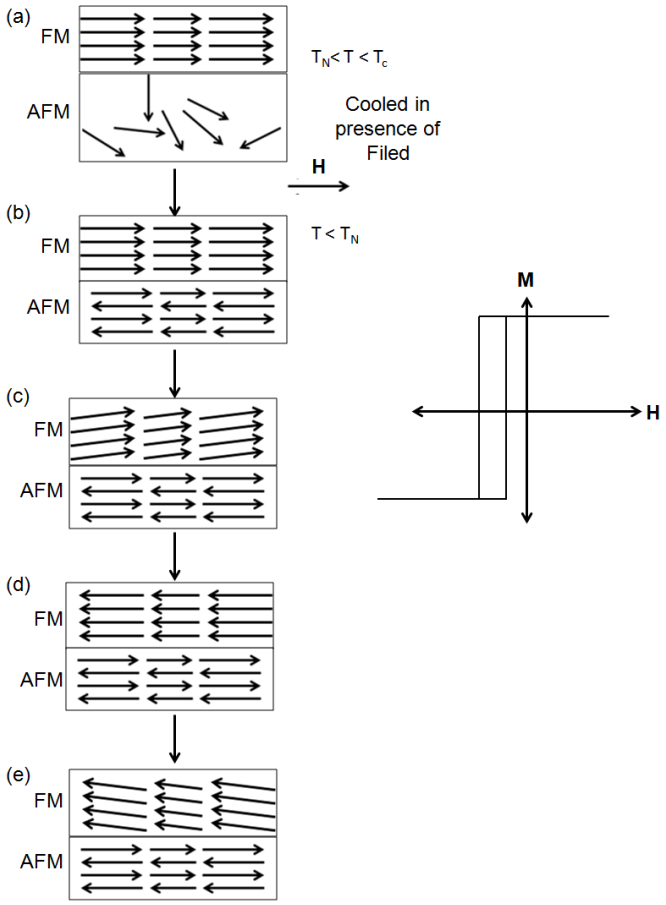

Figure 1.15 Schematic diagram of the spin configuration of an FM and AFM bilayer at different stages.

1.2.7.3.1 Theoretical Model on Magnetic Exchange Bias

In order to understand the origin of exchange bias, Many Body Interactions have been applied by the theoretical physicists and the energy per unit area of an exchanged bias system assuming coherent rotation is given by the following equation:

$$E = - H M_{FM} t_{FM} \cos(\theta - \beta) + K_{FM} t_{FM} \sin^2\beta + K_{AFM} t_{AFM} \sin^2\alpha - J_{INT} \cos(\beta - \alpha) \ldots \textbf{eq 1.3}$$

where, H is the applied field, M_{FM} is the saturation magnetization, t_{FM} is the thickness of the ferromagnetic layer, t_{AFM} is the thickness of the antiferromagnetic layer, K_{FM} is the anisotropy of the ferromagnetic layer, K_{AFM} is the anisotropy of the antiferromagnetic layer and J_{INT} is the interface coupling constant; β, α and θ are the angles between the magnetization and the ferromagnetic anisotropy axis, the antiferromagnet sublattice magnetization (M_{AFM}) and the antiferromagnet anisotropy axis, and the applied field and the ferromagnet anisotropy axis. Minimizing the energy with respect to α and β, the loop shift is found to be as following:

$$H_B = \frac{J_{INT}}{M_{FM}\, t_{FM}} \ldots \textbf{eq 1.4}$$

1.2.7.3.2 Experimental Verification of Magnetic Exchange Bias

There are experimental techniques by which a magnetic exchange bias can be verified. The most commonly used ones are listed below[48]:

(i) *Magnetization measurement* under field cooled conditions. The sample is cooled in the presence of a magnetic field below the antiferromagnetic ordering temperature to calculate both the bias field (H_B) and coercive field (H_c).

(ii) *AC susceptibility measurements*, in this measurement the change in magnetic flux created by the sample due to the presence of an alternating field is measured as a function of the applied AC and DC fields, temperature or frequency. This measurements show that the ferromagnetic moment is inhomogeneous throughout its layer thickness

(iii) *Magnetoresistance measurements* can give the information about the formation of any transition layer by the ferromagnetic layer at the interfacial region.

(iv) *Neutron diffraction measurements* for exchange biased systems are generally carried out in two modes, grazing incidence mode in which, the homogeneity of the interface is determined by probing the magnetization with depth and by high angle neutron diffraction the spin configuration of the different magnetic layers can be studied and also some indirect information on domain formation can be extracted from the scans.

1.2.7.4 Kondo effect

Scattering of the conduction electrons by the vibrating crystal lattice accounts for the dominant contribution to the electrical resistivity in metals. The electrical resistivity increases monotonically with temperature in most of the metals because of rapid increase of this scattering as more and more lattice vibrations take place. The residual temperature independent resistivity arises due to the scattering of the electrons with defects, impurities and vacancies in the very low temperature range where the lattice vibrations are almost absent.

The interaction between the localized electrons with delocalized electrons is one of the central questions in solid state physics.[52-54] One of the scenarios in this case is the Kondo effect, which is encountered when an impurity atom with an unpaired electron is placed in a metal.[53] At low temperatures a spin singlet state is formed between the unpaired localized electron and delocalized electrons at the Fermi energy[55], whereas at higher temperature formation of degenerate doublet is also possible. In 1964 Kondo made a startling discovery when considering the scattering from a magnetic ion that interacts with the spins of the conducting electrons. He found that the second term in the

calculation could be much larger than the first. The upshot of this result is that the resistance of a metal increases logarithmically when the temperature is lowered.

$$\rho(T) = \rho_0 + aT^2 + c_m \ln \frac{\mu}{T} + bT^5 \text{ ... } \textbf{eq. 1.5}$$

In the above resistivity expression as a function of temperature, ρ_0 is the residual resistivity, the second term arises from *Fermi liquid* properties, the third logarithmic term accounts for what is known as Kondo scattering. $CeAl_2$ is a well known system that shows the Kondo effect and is closely related with the presence of a 4*f* level close to the Fermi level which produces a large resonant-scattering effect.

1.2.7.5 Heavy Fermions

Heavy fermions are systems wherein the local magnetic moments dominate the dynamics of the itinerant conduction electrons. These strong electron correlations result in an increase in the effective mass of the conduction electrons to 100 - 1000 times to that of free electron masses at low temperatures. Classic examples for intermetallic heavy Fermion compounds are, $CeCu_2Si_2$[56], $YbRh_2Si_2$,[57] $EuNi_2P_2$,[58] UPt_3[56] and UPd_2Al_3.[59]

Heavy fermion systems may possess different kind of ground state: conducting, superconducting, magnetically ordered with or without superconductivity. At temperatures much below the Debye temperature and Fermi temperature, the heat capacity of metals can be written as the following:

$$C = \gamma T + \beta T^3 \text{ ... } \textbf{eq. 1.6}$$

The first and second term respectively accounts for electron and phonon contributions. γ is proportional to the effective electron mass m^* and is material specific.[60]

The heavy fermion compounds are prototype systems for the study of quantum phase transitions. Microscopically, electrons in partially filled *f* shells behave as localized magnetic moments. They interact with conduction electrons through a Kondo exchange interaction, which favours a non-magnetic ground state that entangles the local moments and the spins of the conduction electrons. They also interact among themselves through an Ruderman-Kittel-Kasuya-Yosida (RKKY) exchange interaction, which typically induces antiferromagnetic order. The best characterized Quantum Critical Point (QCP) in heavy fermion compounds with anisotropic structures. Examples include the monoclinic $CeCu_{(6-x)}Au_x$,[61] and tetragonal $CePd_2Si_2$,[62] $YbRh_2Si_2$[63] and Ce*M*In_5 (*M* = Co,Rh).[64]

1.2.8 Application of Intermetallic Compounds in Fuel Cells

As discussed in the beginning as well as in the properties section of this chapter, intermetallic compound may find a huge application in a variety technological frontiers. Another important aspect in this context is catalysis, especially electrocatalysis. A vast number of intermetallic nanoparticles have been studied in this field and hence the last chapter of this thesis is dedicated to one of this kind of systems.

1.2.8.1 What Is a Fuel Cell?

A fuel cell is a device that converts chemical energy stored in a fuel into electrical energy through a chemical reaction with oxygen or other oxidizing agents (**Figure 1.16**).

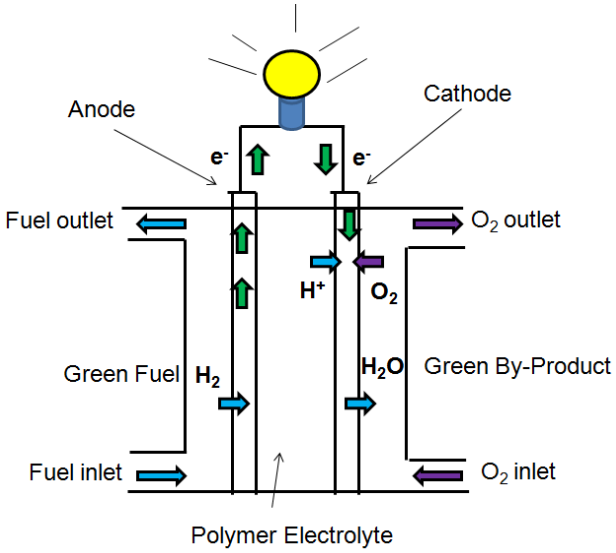

Figure 1.16 A schematic diagram of a H_2-O_2 Fuel cell converting chemical energy to electrical energy.

The fuel gas (mainly hydrogen rich) is passed towards the anode where the following oxidation occurs.[65]

$$1/2H_2 \longrightarrow H^+ + e^- \quad \ldots \textbf{eq. 1.7}$$

The liberated electrons pass through external circuit and go to cathode and positive hydrogen ion (H^+) migrates through electrolyte towards cathode. At the cathode H^+ ions react with oxygen (from air) to form water and heat and electricity generated.

$$H_2 + 1/2O_2 \longrightarrow H_2O + \text{Electricity} + \Delta \quad \ldots \textbf{eq. 1.8}$$

In the area of energy storage and conversion devices, electrochemical systems play an important role. The electrochemical energy conversion means the conversion of chemical energy to electrical energy of vice versa. Electrochemical energy systems possess several advantages, (1) chemical energy is directly converted to electrical energy without Carnot limitation and hence they are very efficient; (2) low emission of pollutants and (3) they are easily transportable.[66-68]

1.2.8.2 Fundamental Aspects of Fuel Cell

The goal of research on electrocatalysis is to obtain maximum efficiency of conversion with minimum overpotential. Fuel cells should be able to provide substantial electrical energy when reasonably large currents are drawn. However, when there is a current load, the cell voltage (V) decreases due to various irreversible processes, called 'polarization losses'. Three different polarization limitations are identified (i) ohmic polarization (η_{ohm}), (ii) concentration polarization (η_{conc}) and (iii) activation polarization (η_{act}).

Ohmic polarization is due to the movement of ions within electrolyte and resistance to electron flow. η_{ohm} can be expressed by

$$\eta_{ohm} = I.\ R \ldots \textbf{eq. 1.9}$$

where I is the cell current and R is the overall cell resistance including electronic, ionic and contact resistances.[69-70]

Concentration polarization arises at high reaction rates, where a high concentration gradient develops between concentration of reactant at the electrode surface (C_s) and bulk (C_{bulk}) of the solution. Fuel cell polarization losses are mainly influenced by η_{conc}, especially at high current densities due to diffusion limited mass transport. The mass transport can be described by applying Fick's law of diffusion.[71]

$$i = [nFD\ (C_{bulk}-C_s)]/\delta \ldots \textbf{eq. 1.10}$$

where D is diffusion co-efficient, F is Faraday constant and δ is thickness of diffusion layer. At the limiting current condition when $C_s=0$,

$$i_L = (nFDC_{bulk})/\delta \ldots \textbf{eq. 1.11}$$

η_{conc} can be defined as the difference between the equilibrium potential for which $C_s = C_{bulk}$ and the equilibrium potential in case of $C_s<C_{bulk}$. The following expression can be obtained, when Nernst equation is combined with Fick's law of diffusion.

$$\eta_{conc} = (RT/nF) \ln(C_s/C_{bulk}) = (RT/nF) \ln (1-i/i_L) \ldots \textbf{eq. 1.12}$$

Activation polarization, η_{act} comes into play in case of sluggish reaction kinetics. It is greatly influenced by adsorption/desorption of reactant and/or product species. Also, the transfer of electrons across double layer and nature of electrode surface (smooth or rough) dictates activation polarization. η_{act} is generally described by Tafel equation,

$$\eta_{act} = (RT/\alpha nF) \ln (i/i_o) \ldots \textbf{eq. 1.13}$$

where α is transfer coefficient and i_o is exchange current density.

The Butler−Volmer equation generally governs the kinetics and thermodynamics of electrochemical reactions. The Tafel analysis is used in extreme cases when the reaction is taken away from equilibrium, where either the anodic or the cathodic current is dominating the total current measured. The logarithm of the current density log |i| (i = current density) is then plotted as a function of over potential η (= $E_{(i)}$-E°) and the plot is used to calculate the kinetics of the reaction.

1.2.8.3 Proton Exchange Membrane Fuel Cells

Proton exchange membrane fuel cells (PEMFC) consist of a proton conducting polymer electrolyte. The generally used electrolyte is a perfluorosulfonic acid membrane (Nafion, DuPont, USA) consisting of hydrophilic and hydrophobic part.[72] The -CF_2 groups in the polymer (**Figure 1.17**) are equivalent to Teflon giving high stability in oxidizing and reducing environments.[73-77] A very thin membrane (50-100 µm) is used to achieve high efficiency as it reduces ohmic resistance loss considerably. Corrosion related issues are minimal in case of PEMFCs as it uses solid electrolyte and the reaction product is only water. PEMFCs can produce high power densities and offer advantages of low weight and small volume.

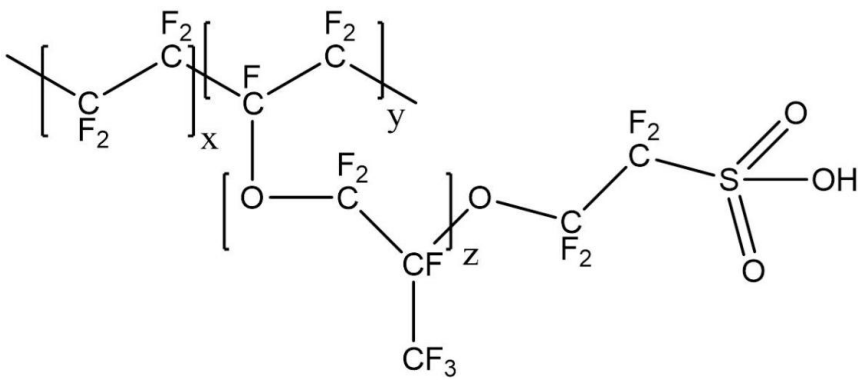

Figure 1.17 Structure of Nafion polymer.

1.2.8.4 Direct Alcohol Fuel Cell

The problems associated with H_2-O_2 fuel cells have led to a class of liquid feed fuel cells i.e. direct fuel cells where liquid fuel solutions are fed to the anode compartment.[78-80] Some of the fed fuels include methanol, ethanol, hydrazine, glycerol and ascorbic acid.[78, 81-83] In direct alcohol fuel cells, alcoholic solutions are used along with either gaseous oxygen or liquid hydrogen peroxide as fuel and oxidant respectively. The most used alcohols in direct alcohol fuel cells (DAFC) are methanol and ethanol, which can be produced from natural gas or renewable biomass resources.[78, 81, 84-87] Since the fuels are fed as liquids, storage and transport problems associated with H_2-O_2 fuel cells are minimized.[78, 81, 83] The DAFCs are generally projected for low power applications such as consumer electronics.

1.2.8.5 Ethanol Electroxidation on Metal Nanoparticles

It is evident from general discussion that a fuel cell consists of three important architectural components namely, (1) fuel, the energy source, (2) membrane, which allows internal communication between anode and cathode and (3) electrocatalysts over which the fuel undergoes oxidation or reduction reactions. Several small organic molecules (SOMs) like methanol, ethanol, formic acid etc in liquid state have been projected as alternate fuels to hydrogen in order to overcome the issues related to safety and storage.[78, 80] These molecules have drawn the attention of fuel cell community because of the low temperature application due to their appreciable energy density and attractive theoretical voltage.[88-89] Ethanol is a potential renewable fuel[90-91] having theoretical energy density (8 KWh/Kg as against 6.1 KWh/Kg for methanol).[92-93] However, complete oxidation of ethanol to CO_2 demands high activation energies to overcome as it involves 12 electrons and also the breaking of C-C bond.[92, 94-97] Many of the intermediates (mainly CO and –CHO) produced during the oxidation reaction poison the anode electrocatalyst and reduce the catalytic efficiency.[94] Ethanol oxidation has been reported to be very facile on Pt and its alloys such as PtSn, PtRu, PtNi and PtIr. Ethanol oxidation on Pt also follows a parallel pathway mechanism as in the case of methanol (**Figure 1.18**).[98-101] In the first pathway, ethanol oxidizes to acetaldehyde and acetic acid via four electron transfer without breaking C-C bond. The other pathway involves the cleavage of C-C bond, which results in the accumulation of CO on Pt sites. An efficient electrocatalyst should favour the second pathway of cleavage of C-C bond, which

corresponds to a 12 electron transfer. Kowal et al have reported a ternary catalyst comprising Pt, Rh and SnO_2 for the complete oxidation of ethanol to CO_2.[99]

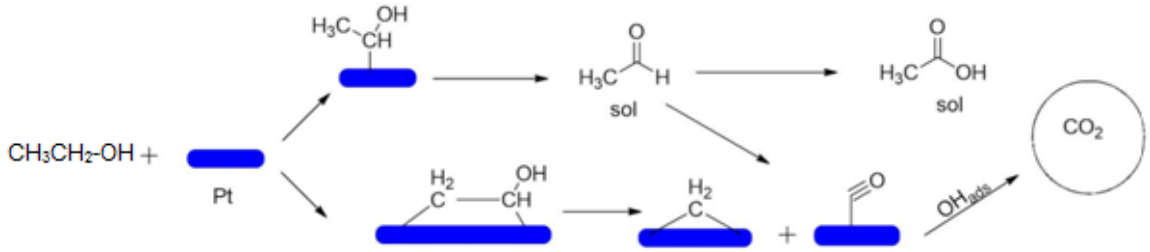

Figure 1.18 Schematic illustration of the oxidation of ethanol on Pt surface oxidation via different pathways.

From the above mechanistic details of SOMs oxidation, it is evident that CO is one of the most common intermediates in all types of fuel. CO is known to be surface poison that drastically reduces the performance of the electrocatalysts. Alleviation of CO poisoning is necessary to improve the performance. Several ways have been proposed to mitigate poisoning of CO. One of the main issues related to the use of the best known Pt catalyst for SOMs oxidation is CO poisoning. Even in H_2-O_2 fuel cells, CO poisoning is of serious concern because CO is produced as a by-product of hydrocarbon reforming to hydrogen.[73] About 10-50 ppm concentration of CO is sufficient to poison the catalyst which causes severe degradation of performance over time.[67, 73, 77, 102-104] After dehydrogenative adsorption and reorientation of ethanol, the formed CO gets adsorbed on Pt. There is synergetic interaction between CO and Pt. According to molecular orbital diagram of metal-CO (M-CO) bonding, there is electron donation from the highest occupied molecular orbital (HOMO) of the CO molecule (sp-hybrid orbital based on carbon) to the metal. Then back donation of electron from to metal to lowest unoccupied molecular orbital (LUMO) occurs. The LUMO is the empty antibonding π* orbital. Thus CO bond weakens due to the population of electron in the antibonding π* with the increase in back donation, the bond order (bond strength) of M-C bond increases whereas bond order of C-O bond decreases. High activation energies are to be overcome to free the Pt surface from CO, which in turn reduces the efficiency of the fuel cell dramatically.

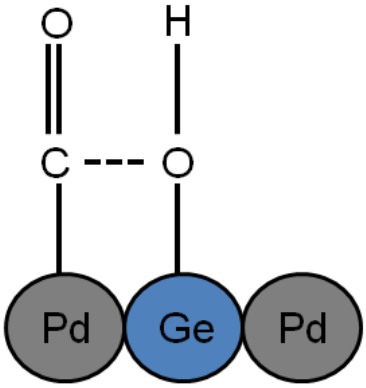

Figure 1.19 Schematic presentation of bi-functional mechanism in PtRu catalyst.

In this thesis two strategies have been applied in order to overcome the above problems: first Pt is replaced by Pd which is much less susceptible to CO poisoning compared to Pt owing to comparatively low adsorption energy of Co on Pd surface, second, Ge has been used as a promoter in the catalyst which reduces the extent of back donation from Pt to adsorbed CO thereby weakening the Pd-C bonding strength. This would further free the Pd sites for ongoing reactions. In order to remove CO from the metal surface, adsorption of hydroxyl species on its surface should happen[89, 105-110] and then CO will be removed as shown in **Figure 1.19**. Both the reactions happen at low over potentials and hence adsorbed CO on Pd can be removed by the mechanism called 'bifunctional mechanism' as shown in **Figure 1.19**.

1.2.9 Conclusion

In the subsequent chapters, synthesis, structural characterization, properties and applications of compounds related to AlB_2 structure type will be discussed in detail with special focus on Ce, Eu and Yb as they can exhibit valence fluctuations or mixed valence states- $Ce^{3+/4+}$, $Eu^{2+/3+}$ and $Yb^{2+/3+}$,[111] which may give rise to many interesting properties like heavy fermion behaviour,[112-113] Kondo effect,[114-116] valence fluctuation as well as structural transition.[35, 112-113, 117-122]

1.7 References

1. Kraft, R.; Höffmann, R. D.; Sebastian, C. P.; Pöttgen, R.; Prots, Y.; Schnelle, W.; Schmidt, M.; Grin, Y., *Chem. Mater.* **2008,** *20* (5), 1948-1955.

2. Sebastian, C. P.; Rayaprol, S.; Hoffmann, R. D.; Rodewald, U. C.; Pape, T.; Pöttgen, R., *Z. Naturforsch B* **2007,** *62* (5), 647-657.

3. Samsel-Czekała, M.; Winiarski, M. J., *Intermetallics* **2012,** *20* (1), 63-67.

4. Lu, J. J.; Mo, T. S.; Gan, K. J.; Lin, T. C.; Lee, M. K., *J. Supercond. Novel Magn.* **2010,** *23* (8), 1473-1477.

5. Liu, Z. K.; Zhou, B.; Zhang, Y.; Wang, Z. J.; Weng, H. M.; Prabhakaran, D.; Mo, S.-K.; Shen, Z. X.; Fang, Z.; Dai, X.; Hussain, Z.; Chen, Y. L., *Science* **2014,** *343* (6173), 864-867.

6. Aynajian, P.; Neto, E. H. D.; Gyenis, A.; Baumbach, R. E.; Thompson, J. D.; Fisk, Z.; Bauer, E. D.; Yazdani, A., *Nature* **2012,** *486* (7402), 201-206.

7. Custers, J.; Lorenzer, K. A.; Muller, M.; Prokofiev, A.; Sidorenko, A.; Winkler, H.; Strydom, A. M.; Shimura, Y.; Sakakibara, T.; Yu, R.; Si, Q.; Paschen, S., *Nat. Mater.* **2012,** *11* (3), 189-194.

8. Tran, V. H.; Kaczorowski, D.; Khan, R. T.; Bauer, E., *Phys. Rev. B* **2011,** *83* (6).

9. Shim, J. H.; Haule, K.; Kotliar, G., *Science* **2007,** *318* (5856), 1615-1617.

10. Phelan, W. A.; Menard, M. C.; Kangas, M. J.; McCandless, G. T.; Drake, B. L.; Chan, J. L. Y., *Chem. Mater.* **2012,** *24* (3), 409-420.

11. Winkelmann, H.; Abd-Elmeguid, M. M.; Micklitz, H.; Sanchez, J. P.; Geibel, C.; Steglich, F., *Phys. Rev. Lett.* **1998,** *81* (22), 4947-4950.

12. Bianchi, A.; Movshovich, R.; Vekhter, I.; Pagliuso, P. G.; Sarrao, J. L., *Phys. Rev. Lett.* **2003,** *91* (25).

13. Höffmann, R. D.; Pöttgen, R., *Z. Kristallogr.* **2001,** *216* (3), 127-145.

14. Höfmann, W.; Jäniche, W., *Naturwissenschaften* **1935,** *23*, 851.

15. Müller, U. *Symmetry Relationships Between Crystal Structures: Applications of Crystallographic Group Theory in Crystal Chemistry*, Oxford University Press, Oxford: 2013, Vol. 18.

16. Hwang, J. S.; Lin, K. J.; Tien, C., *Solid State Commun.* **1996,** *100* (3), 169-172.

17. Kalsi, D.; Rayaprol, S.; Siruguri, V.; Peter, S. C., *J. Solid State Chem.* **2014,** *217* (0), 113-119.

18. Majumdar, S.; Sampathkumaran, E. V.; Brando, M.; Hemberger, J.; Loidl, A., *J. Magn. Magn. Mater.* **2001,** *236* (1-2), 99-106.

19. Nakamoto, G.; Shibai, Y.; Kurisu, M.; Andoh, Y., *Physica B* **2000,** *281*, 76-78.

20. Patil, S.; Medicherla, V. R. R.; Singh, R. S.; Pandey, S. K.; Sampathkumaran, E. V.; Maiti, K., *Phys. Rev. B* **2010,** *82* (10).

21. Peter, S. C.; Sarkar, S.; Kanatzidis, M. G., *Inorg. Chem.* **2012,** *51* (20), 10793-10799.

22. Sarkar, S.; Gutmann, M. J.; Peter, S. C., *CrystEngComm.* **2013,** *15*, 8006–8013.

23. Sarkar, S.; Peter, S. C., *J. Chem. Sci.* **2012,** *124* (6), 1385-1390.

24. Sarkar, S.; Peter, S. C., *Inorg. Chem.* **2013,** *52* (17), 9741–9748.

25. Sebastian, C. P.; Malliakas, C. D.; Chondroudi, M.; Schellenberg, I.; Rayaprol, S.; Hoffmann, R. D.; Pöttgen, R.; Kanatzidis, M. G., *Inorg. Chem.* **2010,** *49* (20), 9574-9580.

26. Bärnighausen, H., *Commun. Math. Chem.* **1980,** *9*, 139-175.

27. Bärnighausen, H.; Müller, U., Universität Karlsruhe and Universität-Gh Kassel: Germany, 1996.

28. Schäfer, H., *Annual Rev. Mater. Sci.* **1985,** *15* (1), 1-42.

29. Kwon, Y. U.; Corbett, J. D., *Chem. Mater.* **1992,** *4* (6), 1348-1355.

30. Fässler, T., *Zintl Phases: Principles and Recent Developments*. Springer: 2011.

31. Cahn, R. W.; Haasen, P., *Phys. Metall.* 1996; Vol. 1.

32. Dong, Z.-C.; Corbet, J. D., *J. Am. Chem. Soc.* **1995,** *117*, 6447-6455.

33. Knowlton, A. A.; Clifford, O. C., *Trans. Faraday Soc.* **1912,** *8* (October), 195-206.

34. Samson, S., *Acta Crystallogr.* **1965,** *19*, 401–413.

35. Duke, C. B.; Laramore, G. E., *Phys. Rev. B* **1970,** *2* (12), 4765-4782.

36. Gaudin, E.; Matar, S. F.; Pöttgen, R.; Eul, M.; Chevalier, B., *Inorg. Chem.* **2011,** *50* (21), 11046-11054.

37. Cohen, M.; Olson, G. B.; Clapp, P. C. Proceedings of ICOMAT, Cambrige, Massachusetts, MIT Press: Cambrige, Massachusetts, 1979.

38. Fick, A., *Phil. Mag.* **1855,** *10*, 30.

39. Majumdar, S.; Sampathkumaran, E. V.; Paulose, P. L.; Bitterlich, H.; Löser, W.; Behr, G., *Phys. Rev. B* **2000,** *62* (21), 14207-14211.

40. Kovaleva, N. N.; Kugel, K. I.; Bazhenov, A. V.; Fursova, T. N.; Löser, W.; Xu, Y.; Behr, G.; Kusmartsev, F. V., *Sci. Rep.* **2012,** *2*, 890.

41. Saha, S. R.; Sugawara, H.; Matsuda, T. D.; Sato, H.; Mallik, R.; Sampathkumaran, E. V., *Phys. Rev. B* **1999,** *60* (17), 12162-12165.

42. Majumdar, S.; Sampathkumaran, E. V., *Phys. Rev. B* **2000,** *61* (1), 43-45.

43. Majumdar, S.; Mallik, R.; Sampathkumaran, E. V.; Rupprecht, K.; Wortmann, G., *Phys. Rev. B* **1999,** *60* (9), 6770-6774.

44. Houard, J.; Bisch, P. M.; Gomes, A. A., *J. Phys. F* **1983,** *13* (12), 2629.

45. Lue, C. S.; Öner, Y.; Naugle, D. G.; Ross, J. H., *Phys. Rev. B* **2001,** *63* (18), 184405.

46. Zhou, G. F.; Bakker, H., *Phys. Rev. Lett.* **1994,** *73* (2), 344-347.

47. Bibekananda, M.; Suresh, K. G.; Nigam, A. K., *J. Phys. Cond. Mat.* **2011,** *23* (50), 506002.

48. Nogués, J.; Schuller, I. K., *J. Magn. Mag. Mater.* **1999,** *192*, 203-232.

49. Dzhun, I. O.; Dushenko, S. A.; Chechenin, N. G.; Konstantinova, E. A., *J. Phys.: Confer. Ser.* **2011,** *303*, 012103.

50. Nayak, A. K.; Nicklas, M.; Chadov, S.; Khuntia, P.; Shekhar, C.; Kalache, A.; Baenitz, M.; Skourski, Y.; Guduru, V. K.; Puri, A.; Zeitler, U.; Coey, J. M. D.; Felser, C., *Nat. Mater.* **2015,** *14* (7), 679-684.

51. Y. Xia; R. Wu; S. Liu; H. Du; J. Han; C. Wang; X. Chen; L. Xie; Y. C. Yang; Yang, J., *arXiv:1508.07833* **2015**.

52. Lawrence, J. M.; Mills, D. L., *Comments Cond. Mat. Phys.* **1991,** *15*, 163-174.

53. Gru¨ner, G.; Zawadowski, A., *Rep. Prog. Phys.* **1974,** *37*, 1497–1583.

54. Varma, C. M., *Rev. Mod. Phys.* **1976,** *48*, 219–238.

55. Goldhaber-Gordon, D.; Shtrikman, H.; Mahalu, D.; Abusch-Magder, D.; Meirav, U.; Kastner, M. A., *Nature* **1998,** *391*, 156-159.

56. Stewart, G. R., *Rev. Mod. Phys.* **1984,** *56*, 755-787.

57. Vyalikh, D. V.; Danzenbächer, S.; Yaresko, A. N.; Holder, M.; Kucherenko, Y.; Laubschat, C.; Krellner, C.; Hossain, Z.; Geibel, C.; Shi, M.; Patthey, L.; Molodtsov, S. L., *Phys. Rev. Lett.* **2008,** *100* (5), 056402.

58. Danzenbächer, S.; Vyalikh, D. V.; Kucherenko, Y.; Kade, A.; Laubschat, C.; Caroca-Canales, N.; Krellner, C.; Geibel, C.; Fedorov, A. V.; Dessau, D. S.; Follath, R.; Eberhardt, W.; Molodtsov, S. L., *Phys. Rev. Lett.* **2009,** *102* (2), 026403.

59. Jourdan, M.; Huth, M.; Adrian, H., *Nature* **1999,** *398*, 47-49.

60. Fulde, P., *J. Phys. F: Met. Phys.* **1988,** *18*, 601.

61. Löhneysen, H. v.; Pietrus, T.; Portisch, G.; Schlager, H. G.; Schröder, A.; Sieck, M.; Trappmann, T., *Phys. Rev. Lett.* **1994,** *72*, 3262-3265.

62. Mathur, N. D.; Grosche, F. M.; Julian, S. R.; Walker, I. R.; Freye, D. M.; Haselwimmer, R. K. W.; Lonzarich, G. G., *Nature* **1998,** *394*, 39-43.

63. Gegenwart, P.; Westerkamp, T.; Krellner, C.; Tokiwa, Y.; Paschen, S.; Geibel, C.; Steglich, F.; Abrahams, E.; Si, Q., *Science* **2007,** *315*, 969-971.

64. Park, T.; Ronning, F.; Yuan, H. Q.; Salamon, M. B.; Movshovich, R.; Sarrao, J. L.; Thompson, J. D., *Nature* **2006,** *440*, 65-68.

65. Phelan, W. A.; Menard, M. C.; Kangas, M. J.; McCandless, G. T.; Drake, B. L.; Chan, J. Y., *Chem. Mater.* **2012,** *24*, 409−420.

66. Ostwald, F. W., *J. Electrochem.* **1894,** *1*, 122.

67. Kordesch, K. V.; Simader, G. R., *Chem. Rev.* **1995,** *95* (1), 191-207.

68. Winter, M.; Brodd, R. J., *Chem. Rev.* **2004,** *104* (10), 4245-4270.

69. Bockris, J. O. M. R., A. K. N. , *Modern electrochemistry-Electrodics in Chemistry, Engineering, Biology and environmental science*. **2000**.

70. Kinoshita, K.; McLarnon, F.; Cairns, E. *Fuel cell handbook*; Lawrence Berkeley Lab., CA (USA): 1988.

71. Hamann, C. H.; Hamnett, A.; Vielstich, W., *Electrochemistry*. Wiley-VCH: 1998.

72. Sheng, W., *Dissertation* **2010.**

73. Srinivasan, S.; Mosdale, R.; Stevens, P.; Yang, C., *Annu. Rev. Energy Environ.* **1999,** *24*, 281-328.

74. James, P. J. M., T. J.; Newton, J. M.; Miles, N.J., *Polymer* **2000,** *41*, 4223.

75. Wakizoe, M.; Velev, O. A.; Srinivasan, S., *Electrochim. Acta* **1995,** *40* (3), 335-344.

76. Kim Y. S.; Wang, F. H. M. M. S. H., Y. T.; Harrison, W.; Zawodzinski, T. A. Mcgrath, J. E. , *J. Poly. Sci. Part B: Poly. Phys.* **2003,** *41*, 2816.

77. Devanathan, R., *Energy Environ. Sci.* **2008,** *1* (1), 101-119.

78. Bianchini, C.; Shen, P. K., *Chem. Rev.* **2009,** *109* (9), 4183-4206.

79. Qi, Z. G.; Kaufman, A., *J. Power Sources* **2002,** *110* (1), 177-185.

80. Santasalo, A.; Kallio, T.; Kontturi, K., *Platinum Metals Rev.* **2009,** *53* (2), 58-66.

81. Lee, C.-G.; Umeda, M.; Uchida, I., *J. Power Sources* **2006,** *160* (1), 78-89.

82. Zeng, Y. Z.; Fujiwara, N.; Yamazaki, S.; Tanimoto, K.; Wu, P., *J. Power Sources* **2008,** *185* (1), 95-103.

83. Asazawa, K.; Yamada, K.; Tanaka, H.; Oka, A.; Taniguchi, M.; Kobayashi, T., *Angew. Chem. Int. Ed.* **2007,** *46*, 8024.

84. Lamy, C.; Lima, A.; LeRhun, V.; Delime, F.; Coutanceau, C.; Leger, J. M., *J. Power Sources* **2002,** *105* (2), 283-296.

85. Richter, B. S., L. D., *Science* **2004,** *305*, 340.

86. Uda, T.; Boysen, D. A.; Chisholm, C. R. I.; Haile, S. M., *J. Electrochem. Soc.* **2006,** *9* (4), A261.

87. Kumar, J. A. K., P.; Saravanan, R., *Int. J. Electrochem. Sci.* **2008,** *3*, 961.

88. Uhm, S.; Lee, H. J.; Lee, J., *Phys. Chem. Chem. Phys.* **2009,** *11* (41), 9326-9336.

89. Wasmus, S.; Küver, A., *J. Electroanal. Chem.* **1999,** *461* (1), 14-31.

90. Cosmi, C.; Macchiato, M.; Mangiamele, L.; Marmo, G.; Pietrapertosa, F.; Salvia, M., *Energy Policy* **2003,** *31* (5), 443-457.

91. Wachsmann, U.; Tolmasquim, M. T., *Ren. Energy* **2003,** *28* (7), 1029-1038.

92. Vigier, F.; Coutanceau, C.; Hahn, F.; Belgsir, E. M.; Lamy, C., *J. Electroanal. Chem.* **2004,** *563* (1), 81-89.

93. Caillard, A.; Coutanceau, C.; Brault, P.; Mathias, J.; Léger, J.-M., *J. Power Sources* **2006,** *162* (1), 66-73.

94. Song, S. Q. Z., W. J.; Liang, Z. X.; Cai, R.; Sun, G. Q.; Xin, Q.; Stergiopoulos, V.; Tsiakaras, P., *Appl. Catal., B* **2005,** *55*, 65.

95. Cao, L. S., G. Q.; Li, H. Q.; Xin, Q., *Electrochem. Commun.* **2007,** *9*, 2541.

96. Park, K.-W.; Choi, J.-H.; Kwon, B.-K.; Lee, S.-A.; Sung, Y.-E.; Ha, H.-Y.; Hong, S.-A.; Kim, H.; Wieckowski, A., *J. Phys. Chem. B* **2002,** *106* (8), 1869-1877.

97. Russell, A. E.; Rose, A., *Chem. Rev.* **2004,** *104* (10), 4613-4636.

98. dos Anjos, D. M.; Hahn, F.; Leger, J. M.; Kokoh, K. B.; Tremiliosi, G., *J. Braz. Chem. Soc.* **2008,** *19* (4), 795-802.

99. Kowal, A.; Li, M.; Shao, M.; Sasaki, K.; Vukmirovic, M.; Zhang, J.; Marinkovic, N.; Liu, P.; Frenkel, A.; Adzic, R., *Nat. Mater.* **2009,** *8* (4), 325-330.

100. Neto, A. O.; Linardi, M.; dos Anjos, D. M.; Tremiliosi, G.; Spinace, E. V., *J. Appl. Electrochem.* **2009,** *39* (7), 1153-1156.

101. Shin, J.; Tornquist, W. J.; Korzeniewski, C.; Hoaglund, C. S., *Surf. Sci.* **1996,** *364* (2), 122-130.

102. Divisek, J.; Oetjen, H.-F.; Peinecke, V.; Schmidt, V.; Stimming, U., *Electrochim. Acta* **1998,** *43* (24), 3811-3815.

103. Bellows, R. J.; Marucchi-Soos, E. P.; Buckley, D. T., *Indust. Eng. Chem. Res.* **1996,** *35* (4), 1235-1242.

104. Watkins, D. S., *Research, development and demonstration of solid polymer fuel cell systems*. 1993.

105. Schultz, T.; Zhou, S.; Sundmacher, K., *Chem. Eng. Technol.* **2001,** *24* (12), 1223-1233.

106. Gasteiger, H. A.; Markovic, N.; Ross Jr, P. N.; Cairns, E. J., *J. Phys. Chem.* **1993,** *97* (46), 12020-12029.

107. Kauranen, P.; Skou, E.; Munk, J., *J. Electroanal. Chem.* **1996,** *404* (1), 1-13.

108. Krewer, U.; Christov, M.; Vidakovic, T.; Sundmacher, K., *J. Electroanal. Chem.* **2006,** *589* (1), 148-159.

109. Shivhare, M.; Jackson, C.; Scott, K.; Martin, E., *J. Power Sources* **2007,** *173* (1), 240-248.

110. Luo, J.; Njoki, P. N.; Lin, Y.; Mott, D.; Wang, L.; Zhong, C.-J., *Langmuir* **2006,** *22* (6), 2892-2898.

111. Shigetoh, K.; Hirata, D.; Avila, M. A.; Takabatake, T., *J. Alloys Compd.* **2005,** *403*, 15-18.

112. Danzenbacher, S.; Kucherenko, Y.; Vyalikh, D. V.; Holder, M.; Laubschat, C.; Yaresko, A. N.; Krellner, C.; Hossain, Z.; Geibel, C.; Zhou, X. J.; Yang, W. L.; Mannella, N.; Hussain, Z.; Shen, Z. X.; Shi, M. P., L.; Molodtsov, S. L., *Phys. Rev. B* **2007,** *75*, 045109.

113. Nishioka, T.; Tabata, Y.; Taniguchi, T.; Miyako, Y., *J. Phys. Soc. Jpn.* **2000,** *69*, 1012-1015.

114. Patil, S.; Iyer, K. K.; Maiti, K.; Sampathkumaran, E. V., *Phys. Rev. B* **2008,** *77*, 094443.

115. Patil, S.; Medicherla, V. R. R.; Singh, R. S.; Pandey, S. K.; Sampathkumaran, E. V.; Maiti, K., *Phys. Rev. B* **2010,** *82*, 104428.

116. Patil, S.; Pandey, S. K.; Medicherla, V. R. R.; Singh, R. S.; Bindu, R.; Sampathkumaran, E. V.; Maiti, K., *J. Phys-Condens. Mat.* **2010,** *22*, 255602.

117. Chondroudi, M.; Peter, S. C.; Malliakas, C. D.; Balasubramanian, M.; Li, Q. A.; Kanatzidis, M. G., *Inorg. Chem.* **2011,** *50*, 1184-1193.

118. Gordon, R. A.; Warren, C. J.; Alexander, M. G.; DiSalvo, F. J.; Pöttgen, R., *J. Alloys Compd.* **1997,** *248*, 24-32.

119. Ivanshin, V. A.; Sukhanov, A. A.; Sokolov, D. A.; Aronson, M. C.; Jia, S.; Bud'ko, S. L.; Canfield, P. C., *J. Alloys Compd.* **2009,** *480*, 126-127.

120. Kaczorowski, D.; Leithe-Jasper, A.; Rogl, P.; Flandorfer, H.; Cichorek, T.; Petri, R.; Andraka, B., *Phys. Rev. B* **1999,** *60*, 422-433.

121. Murani, A. P., *Nato Sci. Ser. Ii. Math.* **2003,** *110*, 297-305.

122. Peter, S. C.; Sarkar, S.; Kanatzidis, M. G., *Inorg. Chem.* **2012,** *51*, 10793-10799.

Chapter 2

Structure and Properties of Ce_2PdGe_3 and Ce_2PdGe_3 Derived from AlB_2 Prototype

2.1 Introduction

Among the *RE* based compounds, the cerium based systems evinced keen interest for both experimentalists and theoreticians, as they provide an ideal ground for exploring and testing new theories for understanding various phenomena such as spin glass behavior,[1-2] Kondo effect,[3] heavy fermion,[4] superconductors,[5] intermediate valence state[6] and complex magnetism[7-9] shown by the strongly correlated electron systems. Cerium plays an interesting role in influencing different physical properties where electrons or holes have significant role in fluctuation between magnetic [$Ce^{3+}(4f^1)$] and non-magnetic [$Ce^{4+}(4f^0)$] states. The mixed valence nature of Ce can be in favor of tilting and distorting the hexagons for diverse structure and physical properties. The 4*f* orbitals may undergo hybridization due to little difference in energy between 4*f* conduction bands to the Fermi energy level,[10-11] which can give rise to the above interesting properties. Ce_2CoSi_3,[12-13] Ce_2RhSi_3,[14-15] Ce_2NiGe_3[16] and Ce_2PdSi_3[17] are a few notable examples of Ce based compounds reported for interesting properties in the AlB_2 family.

Motivated by our recent discoveries of the ordered compounds in the RE_2TX_3 family, and ability of Ce to show wide range of physical properties, Ce_2PdGe_3 and Ce_2PtGe_3 were selected for detailed properties studies. Ce_2PdGe_3 was previously reported in two different disordered compositions $CePd_{0.5}Ge_{1.5}$ and $CePd_{0.75}Ge_{1.25}$ in the AlB_2 structure type with the substitution of aluminum position by cerium and the boron position shared by palladium and germanium atoms.[18-19] Earlier, many compounds $CeAu_xGe_{2-x}$,[20], $CeAl_xGe_{2-x}$,[21] $CeCu_xGe_{2-x}$[22] and $CePd_xGe_{2-x}$[23] were reported as the mixture of AlB_2 and α-$ThSi_2$ structure types. Initial attempts also led to the formation of mixed phases, however, the synthesis of ordered and disordered structures in single phase could be achieved by varying the Pd to Ge ratio. Interestingly, a new ordered superstructure in the AlB_2 family was obtained while varying the atomic ratio. In addition, a tetragonal phase was successfully obtained as well. A tetragonal phase has recently been reported by Baumbach et al that crystallizes in tetragonal $P4_2/mmc$ space group.[24] The crystal structures of the compounds were studied using XRD on selected single crystals. Our study shows that ordering and disordering are also in favor of varying the physical properties. The compound Ce_2PtGe_3 synthesized by arc melting technique, crystallizes in an ordered superstructure of the AlB_2 family, *Cmca* space group: a = 8.5157(17) Å b = 14.7496(3) Å and c = 4.2511(9) Å. Ce_2PtGe_3 shows diverse properties like spin glass behavior, valence fluctuation and a pseudogap at low temperatures.

2.2 Experimental section

2.2.1 Synthesis

The following reagents were used as purchased from Alfa-Aesar without further purification: Ce (chunk, 99.99%), Pd (wire, 99.9%), Pt (wire, 99.9%) and Ge (pieces, 99.999%). Elements were taken in different stoichiometric ratios and arc-melted over a time period under argon atmosphere to produce globular ingots. The globules were remelted several times to ensure homogeneity of the product. $Ce_2Pd_{0.6}Ge_{3.4}$ leads to pure tetragonal phase (henceforth to be represented as β-Ce_2PdGe_3), whereas the composition $Ce_2Pd_{1.4}Ge_{1.6}$ leads to a new hexagonal phase (henceforth to be represented as γ-Ce_2PdGe_3). On the other hand, stoichiometric Ce_2PdGe_3 composition leads into the formation of the mixture of α-Ce_2PdGe_3 (AlB_2 subcell) and β-Ce_2PdGe_3. Ce_2PtGe_3 was synthesized from the stoichiometric 2:1:3 ratio. Other compositions did not yield desired products. The arc melted samples were sealed in the quartz tubes and annealed at 1273 K over the period of two weeks to check the stability.

2.2.2 Powder XRD

Phase identity and purity of all synthesized samples were determined by powder XRD experiments that were carried out on a Bruker D8 Discover diffractometer using Cu$K\alpha$ radiation (λ = 1.5406 Å) and calibrated against corundum standard, over the angular range $10° \leq 2\theta \leq 80°$, with a step size of 0.02° at 300 K. The experimental powder patterns of all phases and the XRD pattern simulated from the single-crystal X-ray structure refinement were found to be in good agreement as shown **Figure 2.1**.

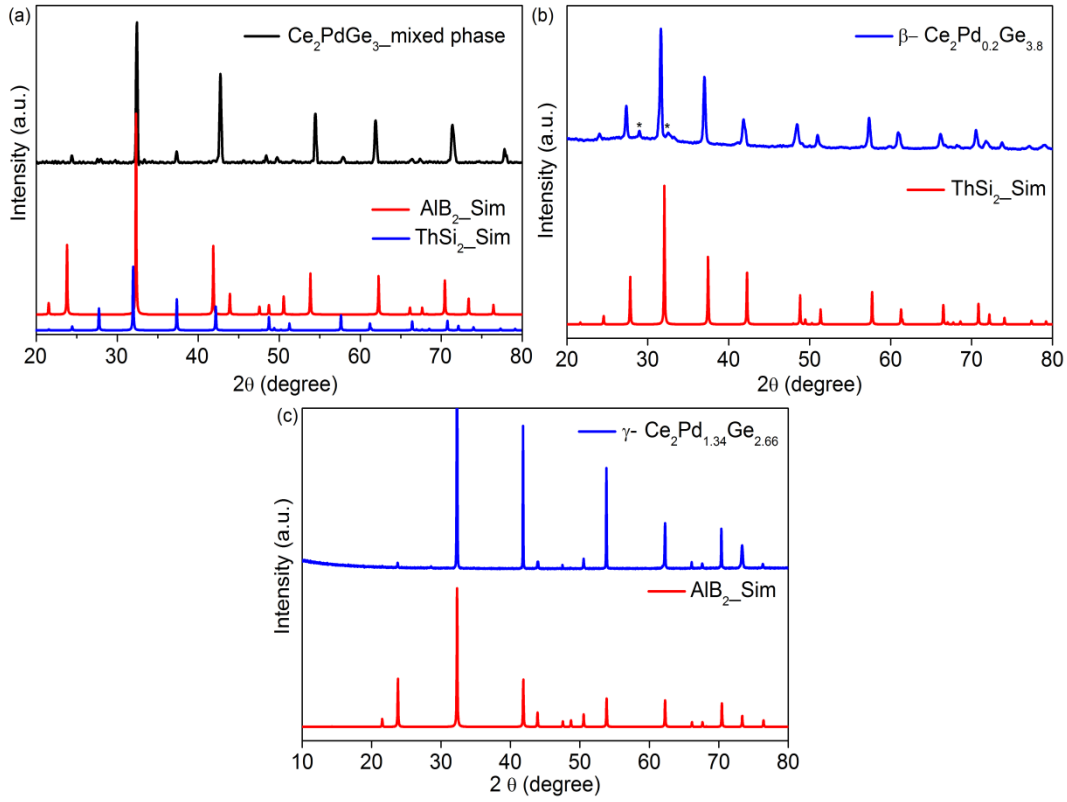

Figure 2.1 Comparison of experimental PXRD patterns of α, β and γ-Ce_2PdGe_3 with simulated structures crystallize in the AlB_2 and α-$ThSi_2$ structure types obtained from the single crystal structure refinement.

2.2.3 Single crystal XRD

X-ray single crystal structural data of all three phases were collected at room temperature (293 K) on irregular shaped single crystals using a Bruker Smart Apex II CCD diffractometer equipped with a normal focus, 2.4 kW sealed tube X-ray source with graphite monochromatic MoKα radiation (λ= 0.71073 Å) operating at 50 kV and 30 mA, with ω scan mode. Crystals of suitable size were cut from irregular shape crystals and mounted on thin glass (~ 0.1 mm) fiber with commercially available super glue. The programme SAINT[55] was used for integration of diffraction profiles and absorption correction were made with SADABS programme.[56]

2.2.4 Powder Neutron Diffraction

Neutron diffraction (ND) experiments were carried out in Time-of-flight mode on GEM at ISIS-RAL, on the polycrystalline samples of the γ-Ce_2PdGe_3 at selected temperatures between 1.8 K and 275 K. Data were recorded in 6-data banks, and all the data were

refined simultaneously assuming the hexagonal structure determined from the single crystal x-ray diffraction refinement.

2.2.5 Structure Refinement

The structures of three compounds were solved by SHELXS 97[58] and refined by a full matrix least-squares method using SHELXL[59] with anisotropic atomic displacement parameters for all atoms. Packing diagrams were generated with Diamond.[60] As a check for the correct composition, the occupancy parameters were refined in a separate series of least-squares cycles. All bond lengths are within the acceptable range compared to the sum of covalent bond distances. For α-Ce_2PdGe_3 the atomic parameters of the reported compound were taken as starting values and the structure was successfully refined in the hexagonal *P*6/*mmm* space group, while for β-Ce_2PdGe_3, the atomic parameters of α-$ThSi_2$ was taken as starting values and the structure was successfully refined in the tetragonal $I4_1/amd$ space group. The unsatisfactory residuals were solved by mixing Pd and Ge atoms at the Si site. The Ce atom occupies 4*a* Wyckoff site while palladium and germanium shared the 8*e* Wyckoff position. Relatively large R_1 parameters for β-Ce_2PdGe_3 obtained from the refinement probably due to insufficient quality of the crystal used for the data collection. Our attempts for a better crystal did not succeed due to the lack of proper single crystals using the arc melting method.

In γ-Ce_2PdGe_3 the systematic absences hinted towardscentro-symmetric space group *P*6/*mmm* with a tripling of *c* axis and lead into the refinement of the structure in a new ordered superstructure of the AlB_2 type. There are four crystallographic positions in the γ- Ce_2PdGe_3 crystal structure. Two different Ce atom occupies the 1*a* Wyckoff site of point symmetry 6/*mmm* and other two different Pd/Ge positions share 2*d* Wyckoff sites (designated as *M*) of point symmetry 6/*mmm*. Initially the positions were assigned for Pd and Ge each resulted in large residual values. By mixing the Pd atoms at the Ge site (2*d*) the residual R_1 dropped from 13% to 3.5% with reasonably well behaved thermal displacement parameters. The X-ray diffraction data on a single crystal of Ce_2PtGe_3 was collected in a similar fashion. The preliminary data suggested a C-centered lattice with Laue symmetry *Cmmm*. Hints on probable structural modulations were also noticed based on extra reflections in the reciprocal image, however the modulated structure could not be solved owing to poor quality of crystals obtained from arc-melting method. Further structure refinement with inclusion of anisotropy in the orthorhombic data set yielded reasonable refinement of the structure. The data collection and structure refinement for all

three phases are listed in **Table 2.1**. The standard atomic positions and the isotopic atomic displacement parameters of this compound are shown in **Table 2.2**. The anisotropic displacement parameters and important bond lengths are listed in **Tables 2.3** and **2.4**, respectively.

2.2.6 Magnetic measurements

Magnetic measurements on both polymorphs of β-Ce_2PdGe_3 and γ-Ce_2PdGe_3 were carried out on a Quantum Design PPMS-VSM magnetometer. Polycrystalline samples were ground and screened by powder XRD for phase identification and purity, were used for magnetization measurements. Magnetic susceptibility for both samples, in zero-field cooled (ZFC) and field cooled (FC) states of the sample, was measured as a function of temperature under different applied magnetic fields. Magnetization measurements were also carried out as a function of field at selected temperatures.

2.2.7 Electrical Resistivity

Resistivity measurements performed on polycrystalline samples of β-Ce_2PdGe_3 and γ-Ce_2PdGe_3 were measured over the temperature range of 2−300 K using a four-probe dc technique with contacts made with silver paste. Measurements were conducted using a Quantum Design PPMS magnetometer.

2.2.8 Specific Heat

Heat capacity (C_p) measurements were performed on polycrystalline samples of β-Ce_2PdGe_3 and γ-Ce_2PdGe_3 by relaxation method using a commercial Quantum Design Physical Property Measurement System (QD-PPMS). Sample was glued to calibrated HC-puck using Apiezon N grease and was measured in the 2−50 K range without applied fields (H).

2.2.9 Computational Details

The first-principles calculations in this work are based on spin-dependent density functional theory calculations using a standard plane-wave code Quantum ESPRESSO[25] with a Generalised Gradient approximation[26] (GGA) to account for the interaction energy of electrons. The GGA−PBE+*U* and GGA-PBE equilibrium volumes deviate by +1.4% and −2.5%, respectively, from experimental results. DFT+*U* study predicts an ferromagnetic and metallic ground state with a pseudogap, which is in agreement with the experimental observations. The description on localized behavior[27-28] of the Ce^{3+} (4*f*)

states in Ce_2O_3, has already been shown to predict correct ground state properties which is incorrectly described by DFT-LDA/GGA. DFT with hybrid functional *U* yields Ce ions in the 3+ state. Projector augmented plane-wave[29] pseudo-potentials were used for Pd and norm-conserved[30] pseudo-potentials were used for Ce and Ge to represent the interactions among the ions. An energy cutoff of 50 Ry (400 Ry) on the plane-wave basis representation of Kohn–Sham wave-functions (density) has been used. All calculations were done considering supercells with 18 atoms. This supercell allows for reconstruction, particularly in the presence of occupancy in different Wyckoff positions. Structural optimization was carried out with BFGS algorithm to minimize energy using Hellman–Feynman forces. The Brillouin zone integrations were sampled on a 5×4×3 mesh of *k*-points by carrying out structural relaxation through energy minimization, and the density of states was calculated by using a 10×10×5 uniform mesh of *k*- points. Self-consistent calculation with SOC has been carried out to account for the interaction of orbital degree of freedom with magnetic spin. In addition, an accurate description of crystal field and exchange splitting, electron correlations associated with a partially filled Ce- 4*f* and Pd-4*d* orbital are included through use of spherically averaged on-site correlations [31] with the Hubbard *U* correction (*U* = 4.5 and 5.0 eV).[27-28] All the results described here are after consideration of the Hubbard term only to the Ce 4*f* states with *U* = 5.0 eV.

Table 2.1a Crystal data and structure refinement for the compound Ce_2PdGe_3 in different phases at 293(2) K.

Empirical formula	α-Ce_2PdGe_3	β-Ce_2PdGe_3	γ-Ce_2PdGe_3
Formula weight	296.12	319.11	153.98
Wavelength	0.71073 Å	0.71073 Å	0.71073 Å
Crystal system	Hexagonal	Tetragonal	Hexagonal
Space group, *Z*	*P*6/*mmm*, 1	$I4_1/amd$, 2	*P*6/*mmm*, 2
Unit cell dimensions	*a* = 4.2613(2) Å, *c* = 4.2517(3) Å,	*a* = 4.2745(11) Å, *c* = 14.499(5) Å,	*a* = 4.3131(6) Å, *c* = 12.364(3) Å,
Volume	66.862(6) $Å^3$	264.93(17) $Å^3$	199.19(6) $Å^3$
Density (calculated)	7.354 g/cm^3	4.000 g/cm^3	2.567 g/cm^3
Absorption coefficient	37.231 mm^{-1}	17.243 mm^{-1}	11.967 mm^{-1}
F(000)	126	272	131
Crystal size (mm^3)	0.03 x 0.01 x 0.01	0.3 x 0.8 x 0.3	0.2 x 0.1 x 0.04
θ range for data collection	4.79 to 31.09°	4.972 to 33.706°	5.46 to 27.49°
Index ranges	-6<=*h*<=3, -3<=*k*<=5, -6<=*l*<=5	-6<=*h*<=3, -6<=*k*<=6, -22<=*l*<=22	-4<=*h*<=5, -5<=*k*<=5, -11<=*l*<=16
Reflections collected	480	763	824
Independent reflections	59 [R_{int} = 0.1070]	167 [R_{int} = 0.0438]	124 [R_{int} = 0.0731]
Completeness to θ = 27.49°	99.7%	100%	90.5%
Refinement method	Full-matrix least-squares on F^2		
Data / restraints / parameters	59 / 0 / 7	167 / 0 / 9	124 / 0 / 14
Goodness-of-fit	0.639	1.134	0.726
Final *R* indices [>2σ(I)]	R_{obs} = 0.0436, wR_{obs} = 0.0916	R_{obs} = 0.0671, wR_{obs} = 0.1750	R_{obs} = 0.0350, wR_{obs} = 0.1023
R indices [all data]	R_{all} = 0.0476, wR_{all} = 0.0954	R_{all} = 0.0698, wR_{all} = 0.1767	R_{all} = 0.0688, wR_{all} = 0.1194
Extinction coefficient	0.0012(13)	0.00000(14)	0.0010(16)
Largest diff. peak and hole (e·$Å^{-3}$)	2.048 and -1.422	3.782 and -3.679	1.434 and -1.678

Table 2.1b Crystal data and structure refinement for Ce_2PtGe_3 at 293(2) K.

Empirical formula	Ce_2PtGe_3
Formula weight	693.10
Crystal system,	Orthorhombic
Space group, *Z*	*Cmca*, 4
Unit cell dimensions	*a* = 8.5157(17) Å, *b* = 14.750(3) Å, *c* = 4.2511(9) Å
Volume	533.95(19) $Å^3$
Density (calculated)	8.622 g/cm^3
Absorption coefficient	59.286 mm^{-1}, 1160
Crystal size	0.10 x 0.06 x 0.04 mm^3
θ range for data collection	5.53 to 45.51°
Index ranges	-17<=*h*<=15, -18<=*k*<=29, -8<=*l*<=7
Reflections collected	6544
Independent reflections	1133 [R_{int} = 0.0498]
Completeness to θ = 45.51°	96.5%
Refinement method	Full-matrix least-squares on F^2
Data / restraints / parameters	1133 / 0 / 28
Goodness-of-fit	0.827
Final *R* indices [>2σ(I)]	R_{obs} = 0.0311, wR_{obs} = 0.0738
R indices [all data]	R_{all} = 0.0986, wR_{all} = 0.1086
Extinction coefficient	0.00034(6)
Largest diff. peak and hole	2.715, -3.835 e·$Å^{-3}$

Table 2.2 Atomic coordinates ($x10^4$) and equivalent isotropic displacement parameters ($Å^2x10^3$) at 293(2) K with estimated standard deviations in parentheses.

Compound	Label	x	y	z	Occupancy	U_{eq}*
α-Ce_2PdGe_3	Ce	0	0	0	1	14(1)
	M	3333	6667	5000	0.15(1)Pd+0.85(1)Ge	17(2)
β-Ce_2PdGe_3	Ce	0	7500	1250	1	14(1)
	M	0	2500	2915(1)	0.90(1)Pd+0.10(1)Ge	25(1)
γ-Ce_2PdGe_3	Ce1	0	0	0	1	10(2)
	Ce2	0	0	3335(4)	1	8(2)
	*M*1	3333	-3333	5000	0.40(1)Pd+0.60(1)Ge	13(3)
	*M*2	3333	-3333	1667(4)	0.31(1)Pd+0.69(1)Ge	10(2)
Ce_2PtGe_3	Ce	0	6250(1)	7506(2)	1	6(1)
	Ge1	2500	4080(1)	2500	0.75	19(2)
	Pt1	2500	4160(1)	2500	0.25	5(1)
	Ge2	2500	2077(3)	2500	0.75	18(2)
	Pt2	2500	2081(2)	2500	0.25	6(2)

Table 2.3 Anisotropic displacement parameters ($Å^2x10^3$) at 293(2) K with estimated standard deviations in parentheses.

Compound	Label	U_{11}	U_{22}	U_{33}	U_{12}	U_{13}	U_{23}
α-Ce_2PdGe_3	Ce1	14(2)	14(2)	14(2)	7(1)	0	0
	Ge1	14(2)	14(2)	24(2)	7(1)	0	0
β-Ce_2PdGe_3	Ce	13(1)	13(1)	14(1)	0	0	0
	M	29(1)	22(1)	23(1)	0	0	0
γ -Ce_2PdGe_3	Ce1	12(2)	12(2)	6(4)	6(2)	0	0
	Ce2	10(2)	10(2)	4(2)	5(1)	0	0
	*M*1	12(3)	12(3)	14(4)	6(2)	0	0
	*M*2	9(2)	9(2)	11(3)	5(1)	0	0
Ce_2PtGe_3	Ce	4(1)	8(1)	7(1)	0	0	1(1)
	Ge1	36(2)	13(2)	9(3)	0	-2(2)	0
	Pt1	6(2)	4(2)	3(2)	0	3(2)	0
	Ge2	18(3)	19(2)	16(2)	0	-3(3)	0
	Pt2	17(3)	1(2)	1(2)	0	2(2)	0

Table 2.4 Selected Bond lengths [Å] at 293(2) K with estimated standard deviations in parentheses.

Compound	Label	Distances		
α-Ce_2PdGe_3	Ce1-*M*	3.25148(13)	*M*-*M*	2.46026(11)
β-Ce_2PdGe_3	Ce-*M*	3.2240(8)	*M*1-*M*1	2.4223(12)
γ-Ce_2PdGe_3	Ce1-*M*1	3.232(3)	*M*2-*M*2	2.4902(3)
	Ce2-*M*2	3.231(3)		
Ce_2PtGe_3	Ce-Ge1#1	3.242(4)	Ge1-Pt2	2.466(7)
	Ce-Ge2#3	3.2448(18)	Ge2-Pt2#2	2.4621(10)
	Ce-Pt2#3	3.2468(14)	Ge2-Ge2#2	2.465(4)
	Ce-Pt1#3	3.2482(17)	Pt1-Ge2	2.450(6)
	Ge1-Ge1#8	2.443(5)	Pt1-Pt1#7	2.454(4)
	Ge1-Pt1#7	2.4488(9)	Pt1-Pt2	2.455(4)
	Ge1-Ge2	2.461(6)	Pt2-Pt2#2	2.459(3)

2.3 Results and Discussion

2.3.1 Reaction Chemistry

Ce_2PdGe_3 was reported in the hexagonal system with the AlB_2 structure type having space group *P*6/*mmm* and lattice parameters $a = b = 4.289$ Å and $c = 4.183$ Å.[23] Initially the stochiometric ratio was taken as 2:1:3 for Ce:Pd:Ge and synthesized by arc melting. The same phase (α-Ce_2PdGe_3) was observed as reported, which was confirmed by powder and single crystal XRD ($a = b = 4.2613(2)$ Å and $c = 4.2517(3)$ Å). Though the disordered phase was formed, the compound was not single phase, but mixed with another phase crystallize in the α-$ThSi_2$ (**Figure 2.1a**). It is interesting to note that the tetragonal phase of this composition was never reported until recently by Baumbach et al.[24] However, the formation of mixture of AlB_2 and α-$ThSi_2$ is not new as it was observed in the case of $CeAu_xGe_{2-x}$,[20] $CeAl_xGe_{2-x}$,[21] $CeCu_xGe_{2-x}$[22] and $CePd_xGe_{2-x}$[23-24] Since our attempt was to synthesize this compound in ordered superstructure of AlB_2 type, the synthesis was tried using the same flux method similar to the work done for a few Eu and Yb based compounds. However our attempts were not successful as it resulted in the formation of more thermodynamically stable $CeGe_2$ phase. In the next step, the elements were taken in several stoichiometric ratios ranging from 0.5:3.4 to 2:2 for Pd to Ge and arc-melted over a time period under argon atmosphere to produce globular ingots. Interestingly, a small variation in the ratio could result in the formation of both compounds in single phase

(**Figure 2.1b and c**). The solid solubility limit for the hexagonal phase and tetragonal phases are $Ce_2Pd_{1.4}Ge_{1.6}$ and $Ce_2Pd_{0.6}Ge_{3.4}$, respectively. Similar compositional variation was attempted in the case of Ce_2PtGe_3 was not successful. Hence, the compound was synthesized in ideal 2:1:3 stoichiometric ratio.

2.3.2. Crystal Chemistry

2.3.2.1. Ce_2PdGe_3. The crystal structures of three phases are shown in Figure 2.2. α-Ce_2PdGe_3 crystallizes in the hexagonal AlB_2 structure type, space group *P*6/*mmm*. The crystal structure of α-Ce_2PdGe_3 (**Figure 2.2a**) consists of two dimensional hexagonal units made up of Pd and Ge atoms and the cerium atoms are sandwiched between them. On the other hands, β-Ce_2PdGe_3 crystallizes in the tetragonal α-$ThSi_2$ structure type, $I4_1/amd$ space group[32] and lattice parameters are, $a = b = 4.2745(11)$ and $c = 14.499(5)$ Å. The crystal structure of β-Ce_2PdGe_3 consists of three-dimensional polyanion sub-network formed by Pd and Ge atoms filled with Ce atoms (**Figure 2.2b**).

The structural relationship between the AlB_2 and α-$ThSi_2$ type structures have been well explained by Kalsi et al.[33] A detailed single crystal XRD for the compound γ-Ce_2PdGe_3 (**Figure 2.2c**) revealed that the hexagonal structure with a tripling of the *c*-axis. This is in fact a new ordered superstructure of the AlB_2 type holding the same space group (*P*6/*mmm*) of the disordered substructure. So far, there are many hexagonal superstructures reported for the compounds with general formula RE_2TX_3 (*RE* = rare earths, *T* = transition metals, *X* = *p*-block elements). The examples are Ce_2NiGe_3 crystallizes in the Er_2RhSi_3 type structure with doubling of all lattice parameters, but in the $P\bar{6}2c$ space group,[16] and U_2RuSi_3 is another hexagonal ordered superstructure of AlB_2 with doubling of only *a* and *b* lattice parameters but same space group.[34]

The geometric evolution of these compounds within the hexagonal AlB_2 (*P*6/*mmm*) prototype is shown in **Figure 2.3**. The compound γ-Ce_2PdGe_3 undergoes a tripling along the *c*-axis with respect to its substructure, which, to the best of our knowledge, was never reported previously.

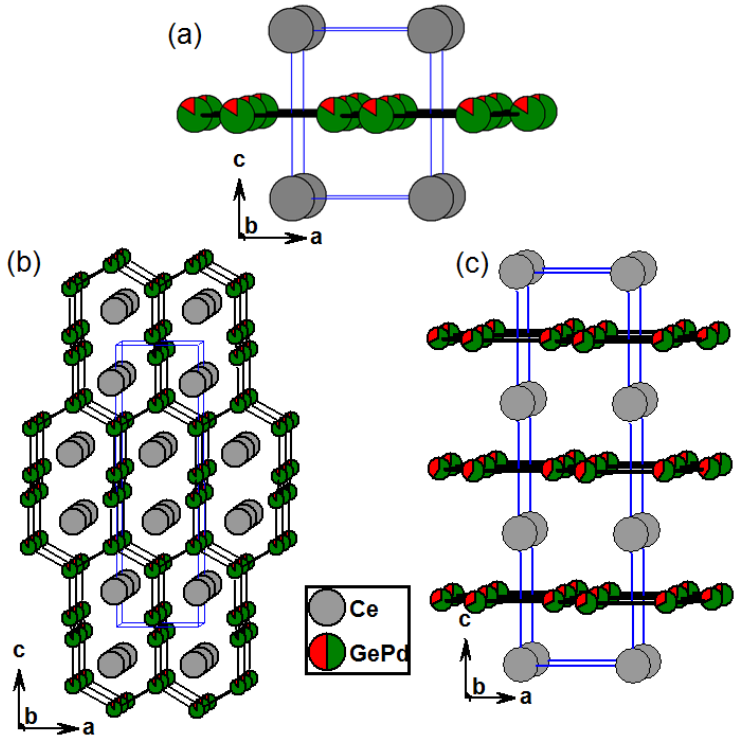

Figure 2.2. Crystal structure of (a) α-Ce_2PdGe_3, (b) β-Ce_2PdGe_3 and (c) γ-Ce_2PdGe_3 approximately along [0 1 0] direction. The unit cell are marked with solid blue line.

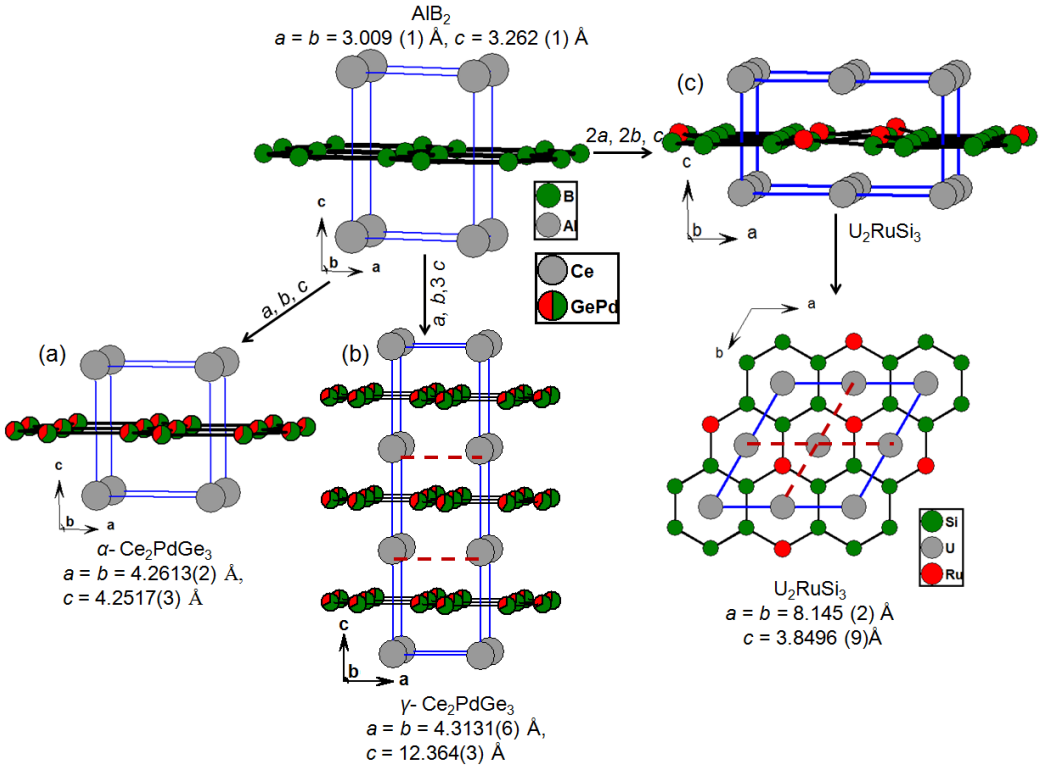

Figure 2.3 Geometric evolution of (a) α-Ce_2PdGe_3, (b) γ-Ce_2PdGe_3 and (c) U_2RuSi_3 from the AlB_2 prototype.

The crystallographic relationship between disordered (α-Ce_2PdGe_3) and ordered (β-Ce_2PdGe_3) structures, and U_2RuSi_3 (another variant of *P*6/*mmm* space group) is shown in **Figure 2.4**. The ordered structures have been derived using several symmetry reduction operations adapted from the Bärnighausen formalism.[35-36] In all the three cases the *RE* atoms occupy the Al position whereas the B position is occupied by Pd and Ge for mixed sited for α-Ce_2PdGe_3. In case of U_2RuSi_3, the boron position is split into two positions (1/3, 2/3, 1/2) and (1/6, 1/3, 0.44) due shift of origin by (1/2, 0, 0). In γ-Ce_2PdGe_3, the boron position is split into two positions (1/3, 2/3, 1/2) and (1/3, 2/3, 1/6) due to shift of origin by (0, 0, 1/3). Interestingly, Pd and Ge share these two positions due to their close covalent radii.

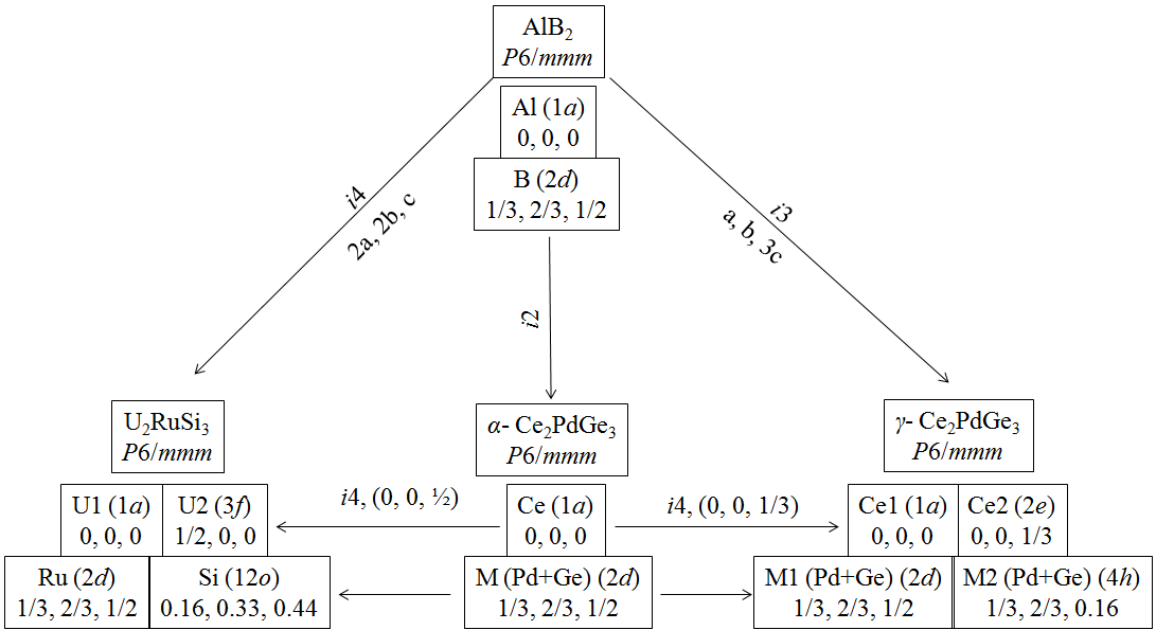

Figure 2.4 Crystallographic evolution of α-Ce_2PdGe_3 (*a*, *b*, *c*), γ-Ce_2PdGe_3 (*a*, *b*, 3*c*), and U_2RuSi_3 (2*a*, 2*b*, *c*) from AlB_2 prototype using the concept of Bärnighausen formalism.

The coordination environments of the *RE* atoms in all the representative hexagonal compounds are shown in **Figure 2.5**. In α-Ce_2PdGe_3, the cerium atoms form distorted pseudo Frank-Kasper cages, while in γ-Ce_2PdGe_3; the Ce atom is sandwiched between the hexagonal biprismatic layers formed by palladium and germanium atoms. In both cases Ce atoms are coordinated by 12*M* (*M* = Pd+Ge) atoms. The Ce-Ce bond distances in α-Ce_2PdGe_3 and γ-Ce_2PdGe_3 are in the range of 4.2079(11) –4.2745(11) Å and 4.1172(71)–4.3131(6) Å, respectively. It is to be noted that these distances are considerably larger than the covalent bond distance of Ce–Ce (3.66 Å),[37] but are comparable to the Ce-Ce distance reposted in $CePd_{0.78}Ge_{1.22}$.[23] It can be concluded that

there is no direct Ce-Ce bonding interaction in this compound, rather it interacts through the itinerant conduction electrons of delocalized 4*d* orbitals of Pd.[38-40] This value indicates a weak interaction between the cerium atoms. The *M-M* bond distance in *α*-Ce_2PdGe_3 and *γ*-Ce_2PdGe_3 are in the following ranges, 2.4222(10)-2.4523(6) and 2.4899(3)-2.4903(2) Å, respectively which are comparatively smaller than the calculated atomic radii of Ge-Pd (2.53 Å) and Pd-Pd (2.62 Å)[41] but very close to the Ge-Ge bond distances of 2.44 Å indicating major contribution of germanium in the covalent bonding.

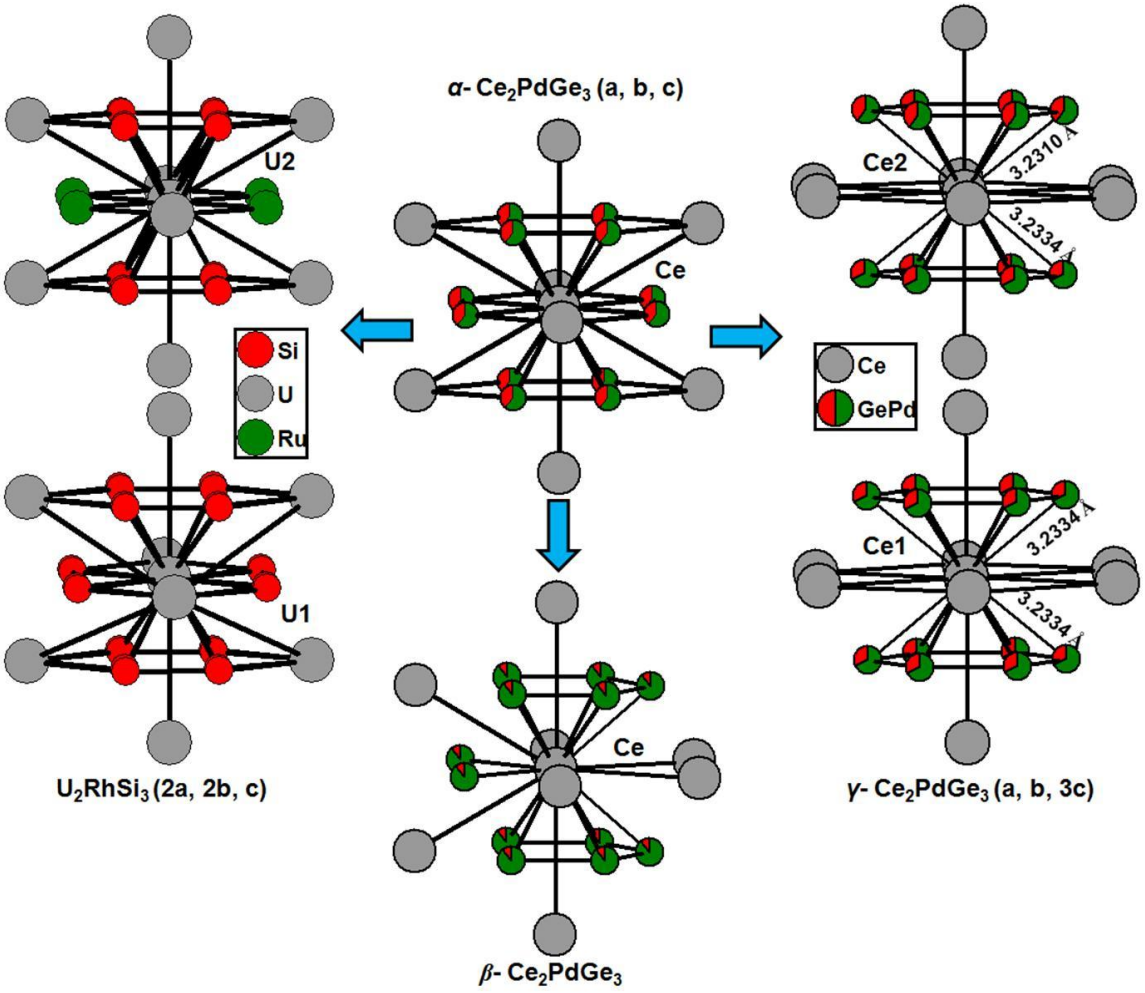

Figure 2.5. Comparison of coordination environments of the *RE* atoms in *α*-Ce_2PdGe_3 (*a*, *b*, *c*), *β*- Ce_2PdGe_3 *γ*- Ce_2PdGe_3 (*a*, *b*, 3*c*) and U_2RuSi_3 (2*a*, 2*b*, *c*).

The neutron diffraction patterns were refined using the structural model as obtained from the single crystal diffraction by Rietveld method in Fullprof. In **Figure 2.6** the Rietveld refinement profiles of the ND patterns recorded at 275 K and 1.8 K. The patterns fit convincingly into the hexagonal structure with no additional peaks. There is no structural change between 275 and 1.8K and no additional peak attributable to

magnetic Bragg peak was observed. The ND data were measured up to higher d-values (about 3 time of *c*-axis in d-spacings), but still no additional magnetic Bragg peaks were observed, thus ruling out any antiferromagnetic ordering. Similarly, intensities of all the peaks were also matched with the structural model itself, ruling out any ferromagnetic order. This conclusively shows that in the given experimental conditions, no long range magnetic ordering has been observed.

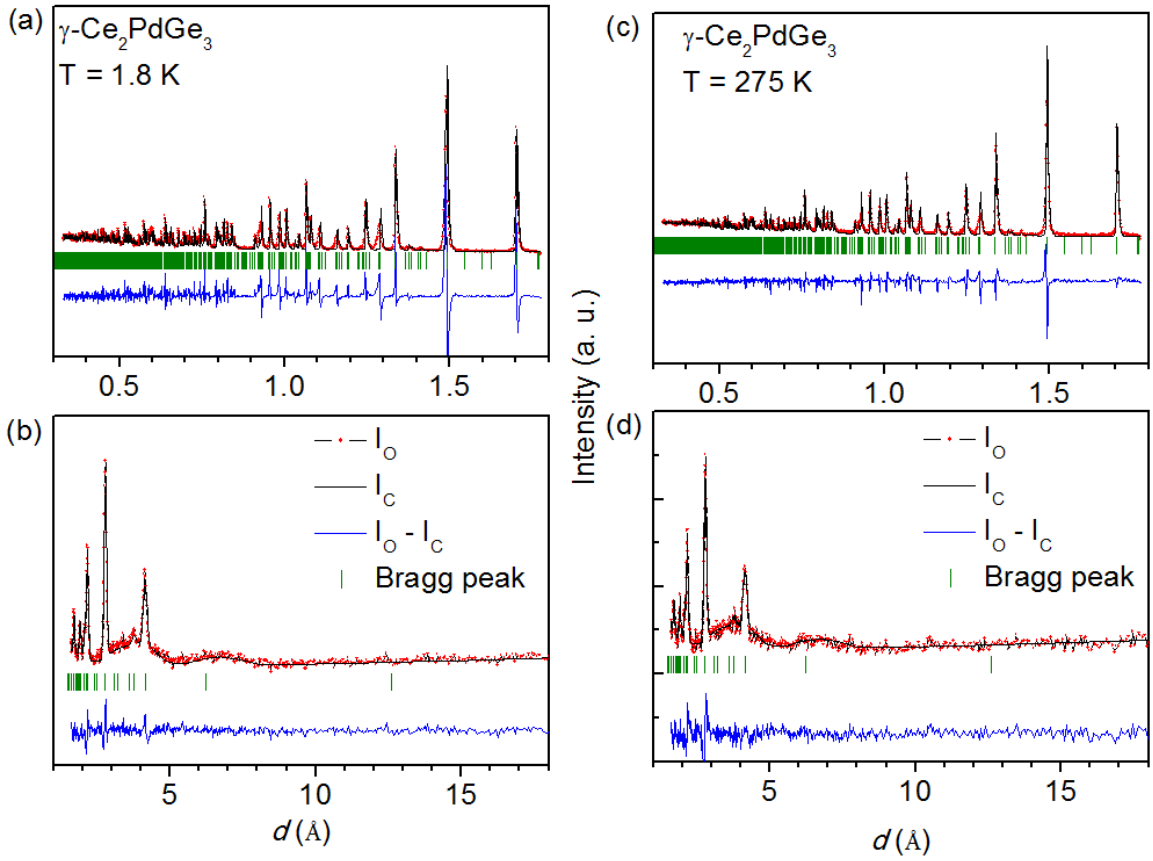

Figure 2.6 Rietveld refined neutron diffraction patterns of γ-Ce_2PdGe_3 samples measured at (a, b) T = 1.8 K and (c, d) 275 K. Data of only two data banks are shown here, which covers the *d*- spacing range from about 0.1 Å to 20 Å.

2.3.2.2 Ce_2PtGe_3

Ce_2PtGe_3 crystallizes in orthorhombic crystal structure with *Cmca* space group which is a new orthorhombic superstructure in the AlB_2 type family of compounds with the lattice parameters are a = 8.5157(17) Å, b = 14.7496(29) Å and c = 4.2511(9) Å. The unit cell along *c* direction is shown in **Figure 2.7a**. The structure of this compound resembles with that of UPt_2 (a = 4.120 Å, b = 9.680 Å, c = 5.600 Å) which is also a superstructure derivative of AlB_2 prototype crystallizing in *Cmcm* space group. In this structure, the

hexagonal network is constructed by both uranium and platinum atoms (Pt1), whereas the Al positions are occupied by second platinum (Pt2). In case of Ce_2PtGe_3, all the Al positions are occupied by Ce atoms; whereas boron positions are occupied by both [GePt] and Pt positions. The coordination environments of Ce, Pt and the mixed site have been shown in **Figure 2.7b-d**. A positional disorder in the Pt and Ge was also observed, which hinted towards a possible modulated structure as shown in **Figure 2.8**. The modulation vector was found approximately to be $\vec{q} = 0.25(\vec{a} + \vec{b} + \vec{c})$. The modulated structure, however, could not be solved due to lack of high quality crystals.

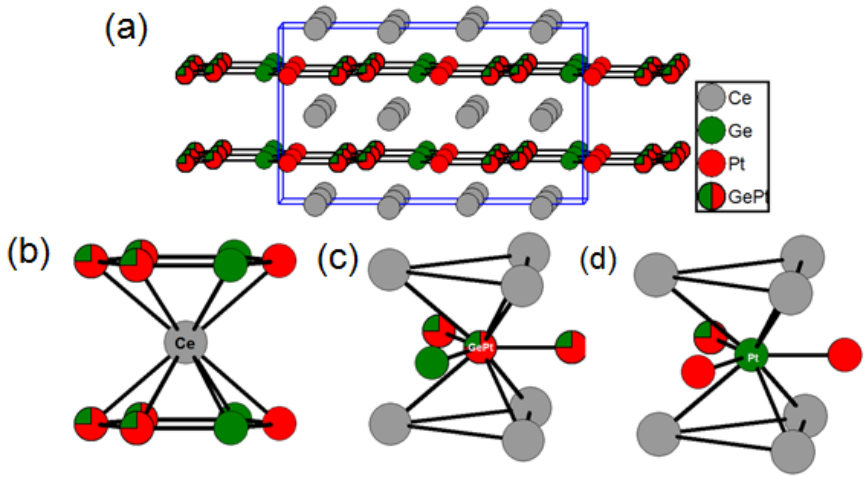

Figure 2.7 (a) Crystal structure of Ce_2PtGe_3 approximately along *c*-direction. The coordination environment of (b) Ce, (c) Pt2 and (d) GePt are also shown.

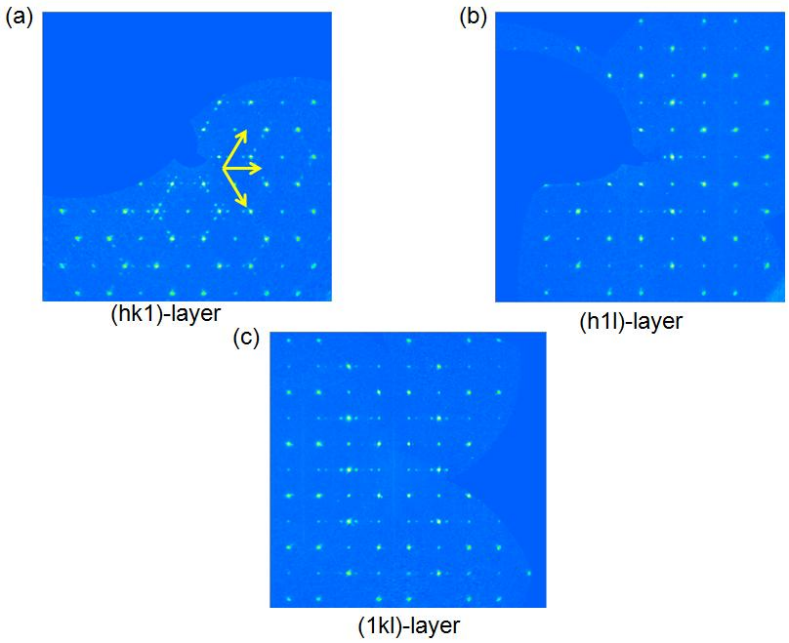

Figure 2.8 Reciprocal images showing spots originated from modulated structure along (a) (hk1), (b) (h1l) and (c) (1kl) layers.

2.3.3 Magnetic Properties

2.3.3.1 Ce_2PdGe_3

The magnetic properties of both tetragonal (β) and hexagonal (γ) polymorphs of Ce_2PdGe_3 were measured on polycrystalline samples within the temperature range 2-300 K. Since the compound α-Ce_2PdGe_3 was not obtained in pure form, the magnetic measurements were not performed. The magnetic susceptibility data of the β-Ce_2PdGe_3 is plotted in **Figure 2.9a**. Magnetic susceptibility increases suddenly at low temperature which is reminiscent of a ferromagnetic ordering. A Curie-Weiss fit at above 50 K resulted paramagnetic Curie temperature (θ_p) and effective magnetic moment (μ_{eff}) values 6 K and 2.56 μ_B/Ce ion, respectively. The positive sign of θ_p indicates the predominant ferromagnetic interactions in this compound. The experimentally obtained value of μ_{eff} (= 2.56 μ_B) is very close to the theoretically expected free ion moment of 2.54 μ_B per Ce^{3+} ion.

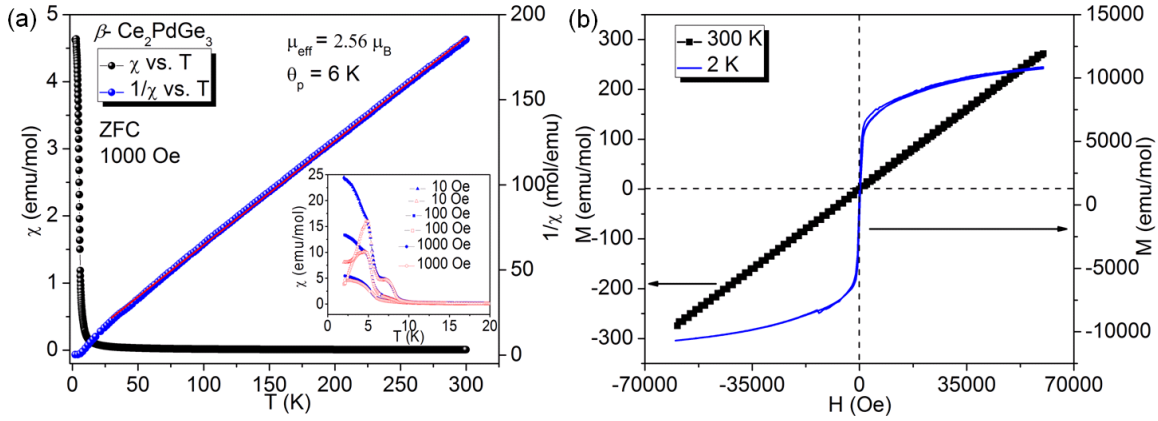

Figure 2.9 a) Temperature dependent magnetic susceptibility and b) field dependent magnetization on β-Ce_2PdGe_3.

In order to explore the magnetism of these compounds in detail, χ(T) measurements were carried out on both polymorphs at lower fields, 10 Oe and 100 Oe. The plot of the magnetic susceptibility of β-Ce_2PdGe_3 measured under 10, 100 and 1000 Oe are plotted as a function of temperature (inset of **Figure 2.9a**). With the increase in the magnetic field (up to 1 kOe) the ordering temperature is suppressed. There is a clear bifurcation between the ZFC and FC curves in all the applied fields, although the difference vanishes as the field increases. The ZFC curve sharply falls down following a sharp maximum with decreasing temperature whereas the FC curve slowly increases. The temperature at which ZFC and FC curves bifurcates is known as the freezing temperature

(T_f) below which the system enters into a disordered spin glass state. The small cusp like feature near 8.8 K appearing in the low magnetic fields (10 and 100 Oe) could be due to ferromagnetic cluster glass which was also previously observed in Eu_2AuGe_3, an orthorhombic superstructure of the AlB_2 prototype.[42] Occurrence of both spin glass as well as ferromagnetic clustering was also observed in $PrRhSn_3$.[43] Magnetization as a function of ramping field was measured at temperatures 2 and 300 K for β-Ce_2PdGe_3 samples in the range of ±60 kOe (shown in **Figure 2.9b**). In case of β-Ce_2PdGe_3, the moment increases sharply with magnetically in a linear fashion and the slope changes above a field of 12 kOe (**Figure 2.9b**). Beyond this field, a magnetic loop opens up signalling some spin reorientation process occurring at higher applied field. The magnetic moment almost saturates at the highest applied field and the saturation moment was calculated to be approximately 1.1 μ_B/Ce ions, which is about 55% of the free Ce^{3+} ion. ($M_{sat} = gJ = 2\ \mu_B$/Ce ion). This could arise due to some crystalline electric field effects.[44] At 10 K, there is a non-linear and non-hysteretic variation of M as a function of H. The curve at 300 K is linear in nature indicating the paramagnetic state of the sample.

In order to confirm the existence of a low temperature spin glass, AC susceptibility measurements were performed on β-Ce_2PdGe_3 in the temperature range of 2.5 and 15 K in the frequency range of 47 Hz to 9997 Hz as shown in **Figure 2.10a**. A sharp peak at about 4.9 K can be observed in the χ' vs. T curve (**Figure 2.10a**) and it is clear from the figure that the peak shifts towards higher temperature with increasing frequency.[45] This peak corresponds to the spin glass transition temperature which is commonly known as freezing temperature (T_f = 5 K). This peak shifts to higher temperature region, up to 5.4 K at higher applied frequency (9997 Hz). The peak at about 8.8 K was found to be frequency independent. These observations clearly indicate the existence of magnetic frustration associated with the spin glass state. Therefore, the relative shift of the spin freezing temperature, calculated from the equation 0.02. This value of δT_f is much lower than superparamagnets and indicates that the material can be classified as a Heisenberg spin glass system or simply canonical spin glass system like CuMn[46] and AuMn alloys.[47]

$$\delta T_f = \frac{\Delta T_f}{T_f \Delta \log_{10} \nu} \quad \textbf{... eq. 2.1}$$

This could arise because of low sensitivity towards the frequency. This also hints that the interaction (antiferromagnetic interaction in this case) among the particles or the magnetic

clusters is very strong and hence fairly large frequencies are required to bring in significant change in T_f value. **Figure 2.10b** represents the plot of relaxation time (τ) with spin freezing temperature (T_f) and spin glass temperature (T_g). The curve was fitted with the equation

$$\tau/\tau_o = (T_f/T_g - 1) \text{ ... } \textbf{eq. 2.2}$$

where, τ is the dynamical fluctuation timescale, τ_o is the microscopic relaxation time, T_f and T_g are spin freezing temperatures respectively and zυ is a dynamical constant. The fitting yields the following values: $\tau_o = 10^{-9}$ s and zυ = 121. The relaxation time is comparable to the values obtained for canonical spin glass systems which lie between 10^{-10} and 10^{-13} s. However, the value of zυ is much higher compared to normal spin glass systems generally between 4 to 13.[48]

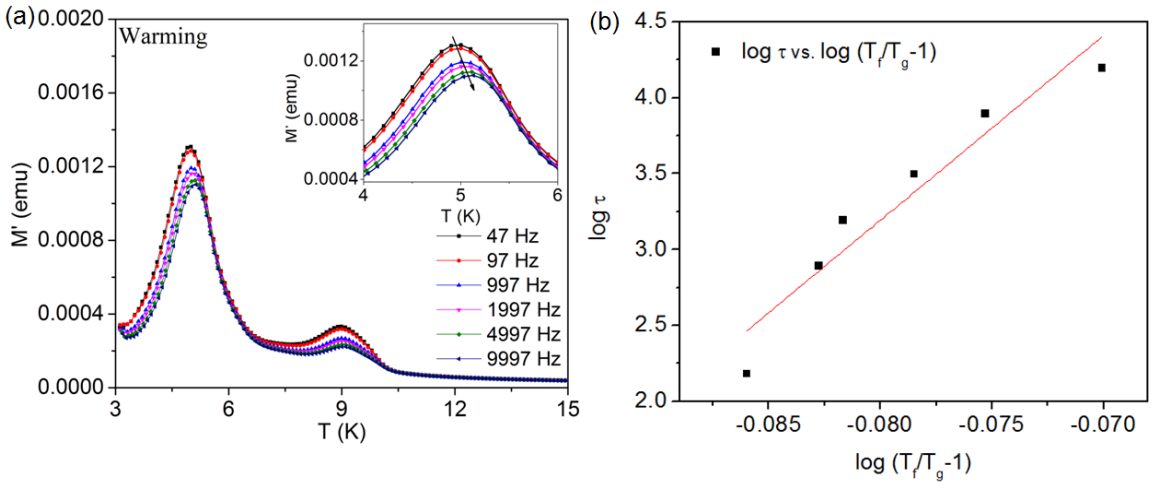

Figure 2.10 (a) Real part of the AC susceptibility plot with varying frequencies. (b) log τ vs. log ($T_f/T_g - 1$) for β-Ce_2PdGe_3.

In **Figure 2.11a**, the plot of magnetic susceptibility, χ of γ-Ce_2PdGe_3 is plotted along with inverse magnetic susceptibility (χ^{-1}) as a function of temperature. The measurement was carried out in a field of 1 kOe after cooling the sample in zero field as well as in presence of field. The magnetic susceptibility suddenly increases below 10 K and maintains a steep slope in the low temperature range below this temperature. This hinted towards a ferromagnetic ordering in the system. However, susceptibility varies linearly at high temperature and follows Curie-Weiss law. Fitting in the temperature range 30 K to 300 K gives the effective magnetic moment 2.54 μ_B/Ce^{3+}, which is very close to theoretical value of the trivalent free Ce ion (2.56 μ_B/Ce^{3+}). The positive θ_P (14

K) is an indication of the ferromagnetic interactions. It is interesting to note that the ZFC and FC curves do not bifurcate down the lowest measured temperature. This rule out any possibility of spin glass like behavior in the system, which is quite common in this class of compounds.[49-52] Hence it can be concluded that all the adjacent Ce moieties strongly interact ferromagnetically with each other. Temperature dependence of magnetic susceptibility was also performed for γ-Ce_2PdGe_3 under various applied magnetic fields (10, 100 and 1000 Oe) as shown as the inset in **Figure 2.11a**. The magnetic susceptibility of this compound measured in ZFC and FC modes were same, which indicates that the system does not go into any frustrated state even at the lowest applied field. However, magnetic moment is drastically suppressed at higher applied field due to magnetic saturation.

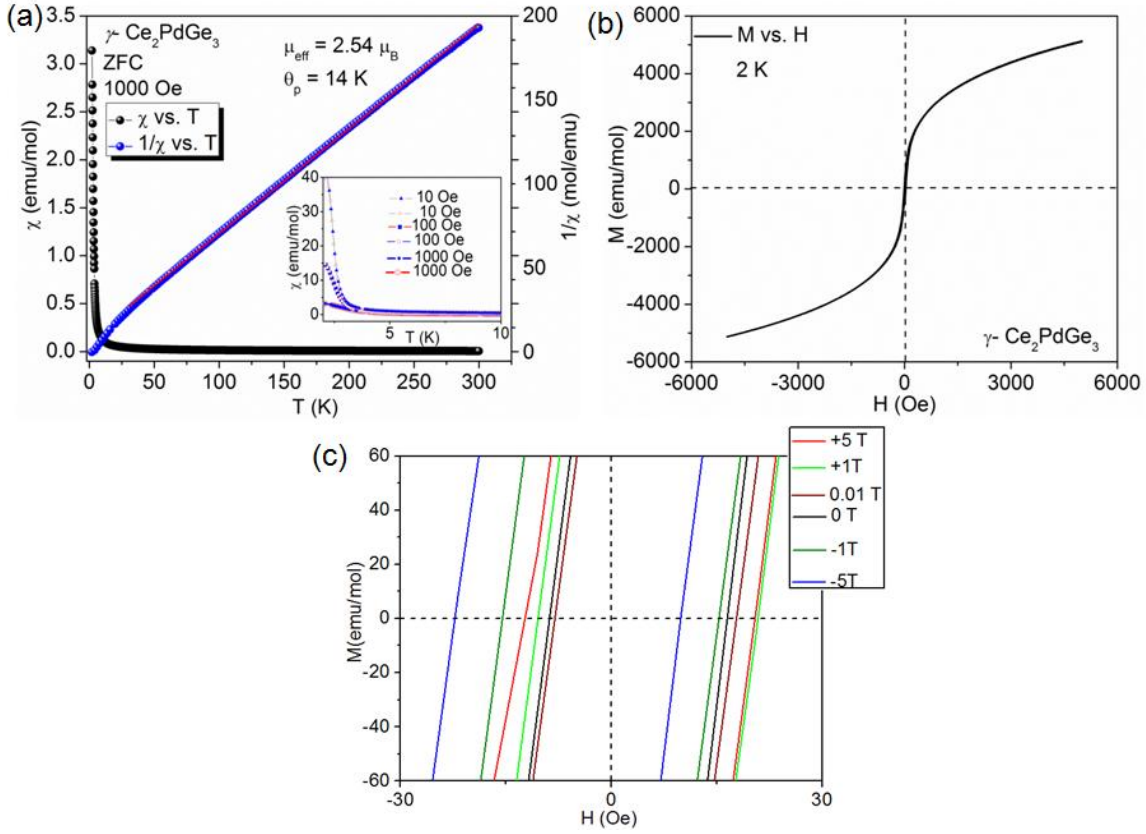

Figure 2.11 (a) Temperature dependence of molar susceptibility and inverse molar susceptibility of γ-Ce_2PdGe_3 at 1000 Oe applied magnetic field, the inset shows magnetic susceptibility in ZFC and FC modes at 10, 100 and 1000 Oe applied fields, (b) Magnetization measured as a function of magnetic field at T = 2 K and 300 K for γ-Ce_2PdGe_3 samples, (c) M vs. H curves cooled under different applied magnetic fields.

The M vs. H plot for γ-Ce_2PdGe_3 has been shown **Figure 2.11b**. At low temperature (2 K) the magnetic moment shows huge hysteresis with a high coercivity (H_c) of around 3.5 kOe indicating the presence of a strong ferromagnetic coupling between the adjacent spins. The room temperature data where magnetic moment varies linearly with magnetic field is conducive to a paramagnet like behavior. In order to confirm the exchange bias phenomenon, magnetization versus field was studied for the sample cooled to 2 K under different applied magnetic field. It was found out that the curve shifts towards both positive and negative direction depending on bias of the applied magnetic field (**Figure 2.11c**). In case of positive bias, it shifts towards the right side of the field axis under the cooling field of +1 T, however it rebounds towards the origin upon application of +5 T during cooling. This suggests that the compound shows positive exchange bias.

2.3.3.2 Ce_2PtGe_3

The temperature dependent magnetic susceptibility measurements were performed in order to probe the magnetic properties of this compound and the plot is shown in **Figure 2.12a**. The curve at 1000 Oe did not change with temperature down to 20 K after which showed a steep increase hinting towards a ferromagnetic coupling, however no long range magnetic ordering was observed down to the lowest measured temperature, 2K. The inverse magnetic susceptibility curve was not linear down to lower temperatures and hence Curie-Weiss law could not be used, instead, a modified Curie-Weiss law was applied which yielded residual magnetic susceptibility (χ_0) = 0.0029 emu/mol, effective magnetic moment, μ_{eff} = 2.49 μ_B and Curie paramagnetic temperature, θ_p = 3.3 K. The positive value of θ_p further supports the ferromagnetic coupling among the adjacent spins, although, the interaction is very weak in nature. The dc curves under an applied magnetic field of 10 Oe at field cooled (FC) and zero field cooled (ZFC) modes were bifurcated at 3.7 K suggesting a possible spin glass behavior. The bifurcation was suppressed at higher applied magnetic field. A mere bifurcation between the χ_{FC} and χ_{ZFC} does not conclusively indicate a spin-glass state. The case of U_2RhSi_3 is an apt example in this context wherein the bifurcation was observed below 10.4 K but no spin-glass-type transition was observed in the AC susceptibility measurement, which was attributed to ferromagnet domain-wall pinning effect.[53] To investigate the effect of magnetic field on the magnetic moment as well as to confirm the absence of any long range magnetic ordering, M vs. H measurements were performed at different temperatures (**Figure 2.12b**). At lower temperatures (1.8-4 K), magnetization varies non-linearly with magnetic

field up to the highest measured magnetic field (± 60 kOe). No magnetic hysteresis was observed at any of these temperatures, which further supports the fact that there is no ferromagnetic ordering at low temperatures. At relatively higher temperature, the curve varies almost linearly with field, which is in line of the fact that the compound is in paramagnetic state at this temperature.

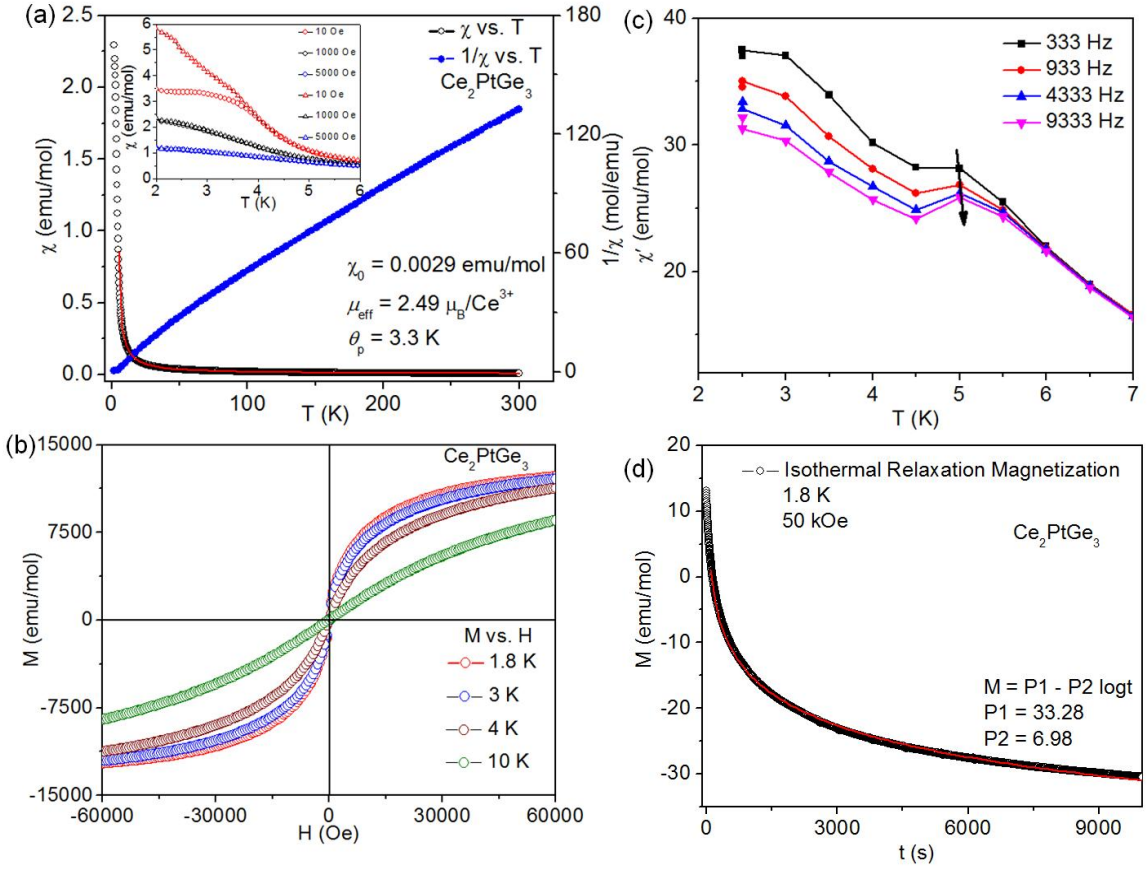

Figure 2.12 (a) Temperature dependence of molar and inverse molar magnetic susceptibility of Ce_2PtGe_3 at 1 kOe. The inset shows the same at ZFC and FC modes under various applied fields, (b) Field dependent magnetization at different temperatures, (c) Real part of the AC susceptibility vs. temperature at different frequencies, (d) Time dependent Isothermal relaxation moment at 2 K.

In order to confirm the frustrated spin glass state, AC susceptibility measurements were performed at four different frequencies, 333, 933, 4333 and 9333 Hz (**Figure 2.12c**). The real part (χ') of the AC susceptibility shows a broad peak at 5.0 K which is designated as the freezing temperature (T_f). The shift in T_f for the frequency change ($\Delta\nu$) of 9000 Hz is ΔT_f = 0.04 K, which yields the relative shift in freezing temperature per decade of frequency as 0.002 given by the following **equation 2.2**.

This value is close to that of 0.005 for CuMn alloy which is considered as one of the classical examples of canonical spin glass.[54] Furthermore, spin glass compounds responds differently to externally applied magnetic field in contrast to superparamagnets due to stronger interparticle/inter domain interactions compared to the latter.[55] This phenomenon can be exploited as effective and supportive evidence towards spin glass state. The isothermal remnant magnetization (M_{IRM}) was studied at 2 K in the zero field cooled mode (**Figure 2.12d**). The curve decayed exponentially with time and was fitted with following equation[56]:

$$M_{IRM} = P1 - P2\log t \ldots \textbf{eq. 2.3}$$

Here, P1 and P2 are fitting parameters which depend on many factors such as temperature, waiting time and relaxation rate directly affecting the dynamics spin relaxation.[56] All these factors hint towards the fact that Ce_2PtGe_3 is a NMAD (non magnetic atom disorder) spin glass compound which is a similar scenario for a number AlB_2 derived compounds like Nd_2AgIn_3,[57] Pr_2AgIn_3[58] and Ce_2CuX_3 (X = Si and Ge),[59 60-61] wherein site disorder among the nonmagnetic transition meta (T) and the p-block elements (X) lead to disorder in the spins of the embedded *RE* atoms.

2.3.4 Resistivity

2.3.4.1 Ce_2PdGe_3

The temperature dependent resistivity data on β-Ce_2PdGe_3 and γ-Ce_2PdGe_3 are shown in **Figure 2.13**.

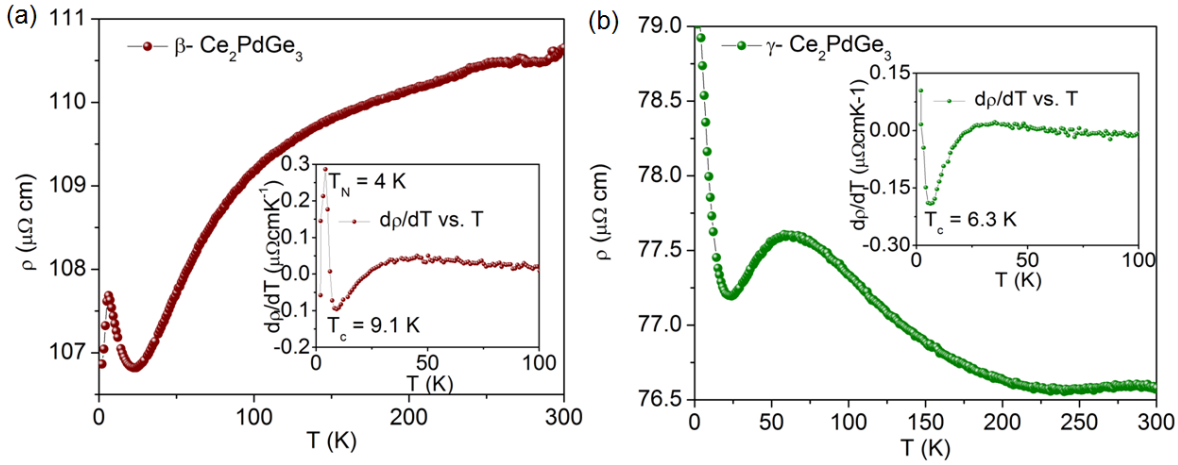

Figure 2.13 Temperature dependence of resistivity for (a) β-Ce_2PdGe_3 and (b) γ-Ce_2PdGe_3 samples. The insets show first ordered derivative of resistivity.

The compound β-Ce_2PdGe_3 shows metallic behavior at relatively high temperature region 50-300 K (**Figure 2.13a**). The broad hump like feature can again be attributed to CEF effects which is prevalent in these class of compounds.[62] The sudden dip near 25 K can arise either due to electron-magnon scattering at the critical point of antiferromagnetic ordering or a pseudo gap opens up due to hybridization between the localized 4*f* orbital and 4*d* orbital from cerium and palladium, respectively.[63-64] The inset of **Figure 2.13a** shows the peak corresponding to the antiferromagnetic ordering at around 4 K. In case of γ-Ce_2PdGe_3 (**Figure 2.13b**), resistivity remains invariable with temperature followed by slow increase parabolically which is reminiscent of semiconductor like behavior. The broad hump in the temperature range 25-150 K followed by a dip could arise either due to crystal electric field excitation or Kondo scattering i.e. scattering of itinerant conduction electrons by magnetic impurities.[62] The exact temperature at which the resistivity suddenly drops down has been pin pointed in the inset of **Figure 2.13b**.

2.3.4.2 Ce_2PtGe_3

The temperature dependent resistivity has been shown in **Figure 2.14**.

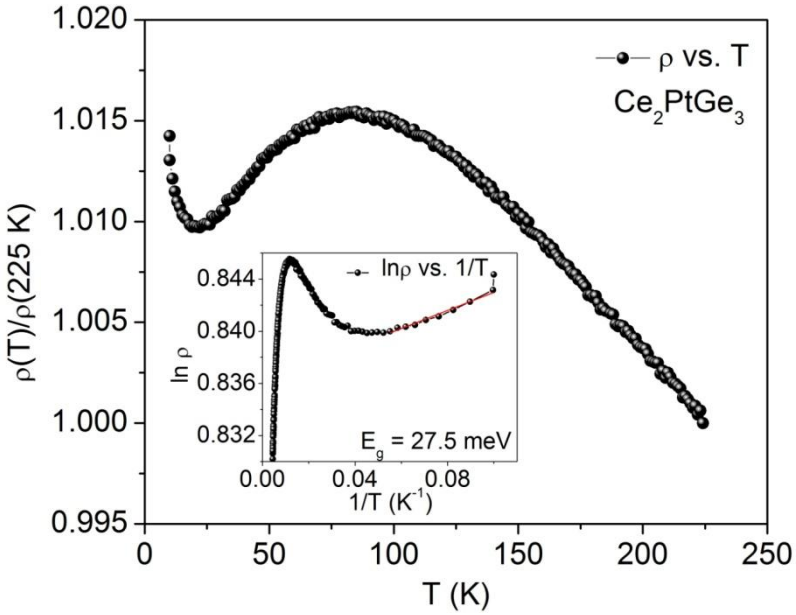

Figure 2.14 Temperature dependent electrical resistivity plot for the compound Ce_2PtGe_3. The inset shows band gap calculation using Arrhenius equation.

The resistivity initially increases exponentially with decreasing temperature to give rise to a broad hump in the range 75-225 K, which is followed by a dip in the temperature range 25-75 K and finally it increases sharply. The overall trend is typical of a Kondo semiconductor which follows the logarithmic law[65]:

$$\rho = - C \log T \text{ ... } \textbf{eq. 2.4}$$

was previously observed in several Ce based intermetallic systems,[66-67] especially in CeRhSb and its hydride analogue, $CeRhSbH_{0.2}$.[68] It was suggested by Chevalier et al that the logarithmic regions in the high temperature and low temperature arise due to excited state doublet and crystal field ground state respectively.[68]

2.3.5 Heat Capacity

2.3.5.1 Ce_2PdGe_3

The overall specific heat capacity is a sum of electronic and phonon contributions

$$C_p = C_e + C_k = \gamma T + \beta T^3 \text{ ... } \textbf{eq. 2.5}$$

Here, C_p is specific heat capacity, C_e and C_k are the electronic and phonon contributions respectively. γ is commonly known as Somerfield coefficient and β is the corresponding phonon coefficient which is directly related to the Debye temperature (θ_D).Temperature dependence of heat capacity of the compound γ-Ce_2PdGe_3 up to 50 K is shown **Figure 2.15a**. The low temperature ferromagnetic transition in γ-Ce_2PdGe_3 was already apparent from the magnetic susceptibility measurements.

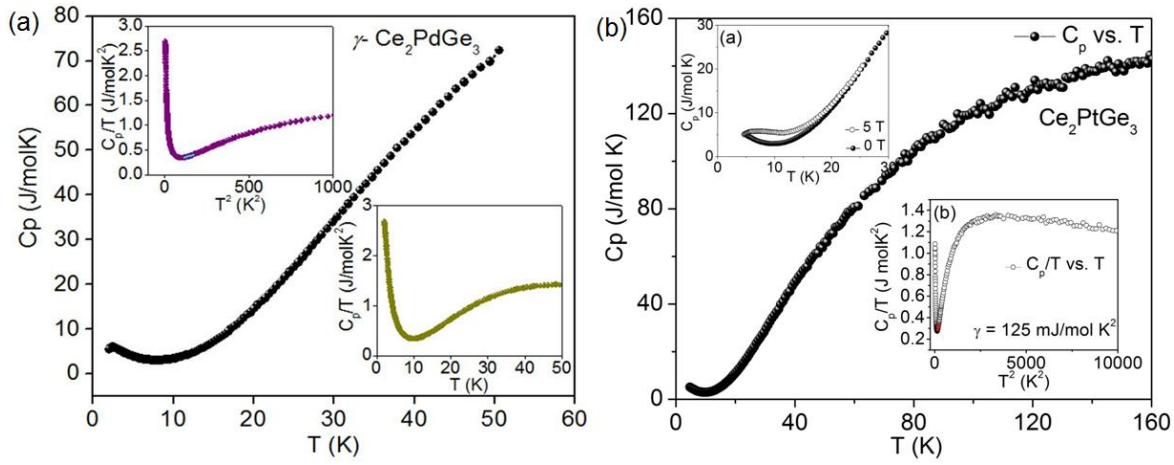

Figure 2.15 Temperature dependence of specific heat of (a) γ-Ce_2PdGe_3 and (b) Ce_2PtGe_3 in the range 3 and 50 K and 160 K, respectively. The insets in the first curve show the plot of C/T vs. T and T^2 respectively. While the insets in the second curve show field dependence and C/T vs. T^2 respectively.

The upturn in the low temperature data of specific heat further shows that there is an onset of magnetic ordering in the system. C_p decreases as the temperature is lowered. C_p has been plotted in different forms as insets in **Figure 2.15a**. The observed specific heat

at low temperatures can be described by the **equation 2.5**, which shows that the total specific heat of the sample as a combination of the contributions from the electronic part (coefficient of electronic specific heat, γ) and the lattice part (β). Thus, according to this equation, at low temperatures C_p should vary as a function of T^3; the plot of Cp/T vs T^2 should be a straight line, but it can be seen that at very low temperature specific heat increase with decreasing temperature which could be attributed to the ferromagnetic ordering in that temperature range.[69] Fitting the plot of C_p/T vs T^2 in the range of 11−13 K resulted in a value of γ = 224 mJ/mol K^2, suggesting a moderate heavy fermion material according to the arbitrary classification of these compounds into "light", "moderate", and classical heavy fermions with γ values lying in the range of 50−60, 100−400, and >400 mJ/mol K^2, respectively.[70] This value of electronic specific heat compares well with the ones found in other mixed-valent or intermediate compounds such as $CeRu_2Si_2$, $CeRh_2Si_2$ and $CePt_3Si$.[71-72]

2.3.5.2 Ce_2PtGe_3

Apart from typical signatures in magnetic measurements, spin glasses can also be characterized by specific heat measurements, wherein the coefficient in the electronic part (γ) in the following equation is higher than conventional paramagnets due to high scattering of electrons from the magnetically disordered spins. The heat capacity plots are shown in **Figure 2.15b** and the relevant parameters (γ and β) were calculated from the linear fitting of the C_p/T vs T^2 which yields γ = 125 mJ/mol K^2 and β = 0.97 mJ/mol K^4 (inset a of **Figure 2.15b**).[73] The moderate value of γ is reminiscent of medium heavy fermion behavior.[61] The high value of γ may however signify crystal field effects or magnetic ordering at low temperatures also.[61] A rise in C_p can easily be noticed below 4.5 K (the lowest temperature measured) in the absence of any external magnetic field (0 T). At 5 T the rise is significantly suppressed (inset b of **Figure 2.15b**) which again hints towards a possible spin glass state.

2.3.6 Theoretical Calculations on γ -Ce_2PdGe_3

The resistivity vs. temperature plot (**Figure 13b**) showed a broad maximum at 70 K followed by a rapid rise below 25 K. This sharp rise at lower temperature (< 25 K) indicates a pseudo-gap formation in the electronic density of states, enhancing the scattering of the charge carriers. The estimates of lattice parameters of γ-Ce_2PdGe_3 obtained from DFT calculations agree reasonably well with experimental findings (**Table**

2.5). After maintaining the preferential occupancy of various crystallographic sites, a hexagonal periodic super-cell containing 18 atoms (three formula units) of γ-Ce_2PdGe_3 (**Figure 2.16 a**) was obtained. As the narest neighbours of Ce atoms are quite closer, with Ce-Ge (Ce-Pd) bond lengths as 3.16-3.25 (3.25-3.30) Å, it is expected that Ce-Pd bonds will exhibit stronger interaction which results in further exchange and correlations. It was found out that minute local distortions of the structure at the Ce sites had occured, resulting in the lowering of the hexagonal symmetry.

Table 2.5 Theoretical results on structural parameters of γ-Ce_2PdGe_3 and comparison with the results from experiments.

Procedure	Lattice Parameters					
	a [Å]	*b* [Å]	*c* [Å]	α [°]	β [°]	γ [°]
Theory	4.25	4.25	12.92	90.00	90.00	120.00
Experiment	4.31	4.31	12.36	90.00	90.00	120.00

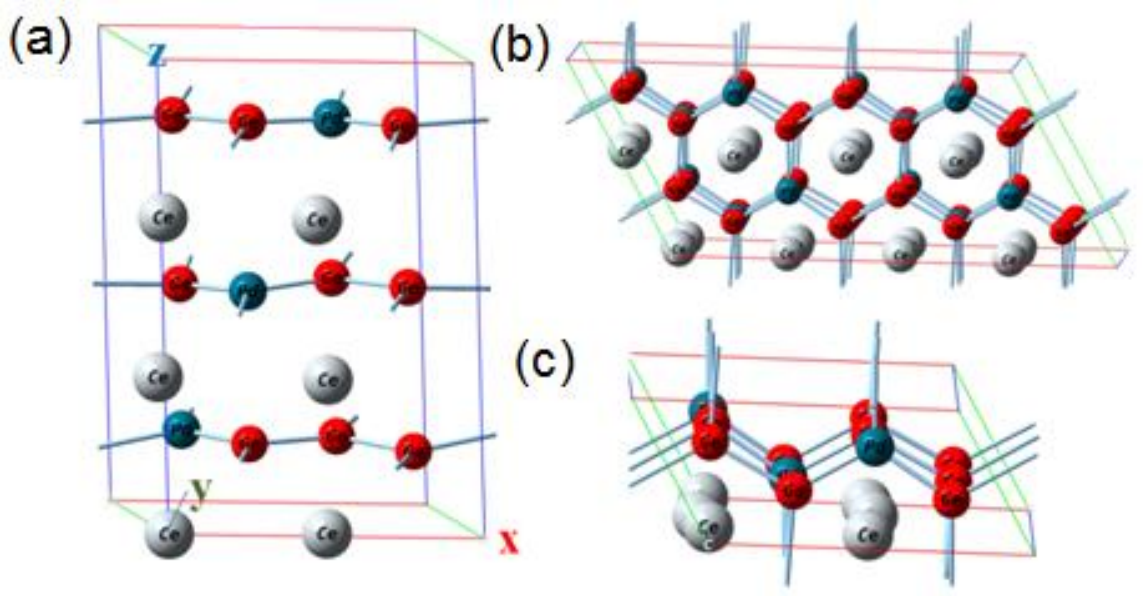

Figure 2.16 Unit cell of γ-Ce_2PdGe_3 crystal structure: (a) side view of the supercell of our consideration. (b) Coordination environment surrounding central Ce atom. (c) Top view of the super-cell with the directions of the translational lattice vectors.

After deducing the most energetically favourable structural configuration, the stability of ground state magnetic configuration was assessed for the bulk γ-Ce_2PdGe_3. Ferromagnetic (FM) and antiferromagnetic (AFM) ordering have been simulated by

initializing spins on the Pd ions to parallel and anti-parallel configurations respectively. The same strategy was also applied for Ce ions. The ferromagnetic state was found to be lower in energy by 1.5 eV per cell compared to antiferromagnetic as well as nonmagnetic states. The density of states in the FM configuration exhibits a dip or a pseudo-gap at the Fermi level (**Figure 2.17a**), which is consistent with its greater stability. It should be noted that this gap is a result of a combination of crystal-field as well as a strong-exchange splitting (U = 5.0 eV). This separates the *f* bands of Ce between conduction and valence bands (**Figure 2.17c** and **d**). The electronic structure calculations showed that the energy gap is attributed to the frontier orbitals of Ce and Ge (**Figure 2.17b**) predominantly. The projected density of states in **Figure 2.17b** revealed that the highest energy valence band is primarily contributed by Ce *s*, *p*, *d* states and Pd *d* states, with a sizeable component of Ge 4*p* orbitals, indicating a strong hybridization between *d* orbitals of Pd and *p* orbitals of Ge. On the other hand, near Fermi level, Pd 4*d* contribution is comparatively lesser. This in-turn proves that, Pd *d* electrons are comparatively localized, whereas, the metallic electron-sea is mostly contributed by Ce and Ge atoms resulting in a ferromagnetic (FM) metallic ground state. Thus, γ-Ce_2PdGe_3 develops the electronic density of states with significant magnetic interactions. Such an electronic structure with two unpaired-spin electrons in the 4*d* orbitals of Pd^{2+} and one in the 4*f* orbital of Ce^{3+} is expected to have the local magnetic moment due to 12 unpaired electrons per cell for ferromagnetic configuration. The origin of such interaction can be understood from interpretation of the density of states (**Figure 2.17**) with exchange interactions. The *f* states in Ce atom get significantly modulated due to different spin configurations. Interestingly, Ce 4*f* electrons in FM states remain uncorrelated with each other and away from the valence (conduction) band-edges. Ce *f* states are also relatively extended (**Figure 2.17c** and **d**) and their energies split up due to spin dependent interaction. For AFM spin state which lies higher in energy than FM state, *f* electrons become more contributory and are closer to the conduction band edge. At ~25 K, the localized electrons are scattered by the delocalized conduction electrons and gave rise to the formation of a singlet (AFM state), with energy scale in the range of above-mentioned temperature. Due to this scattering, the resistivity increases as the temperature is lowered further.

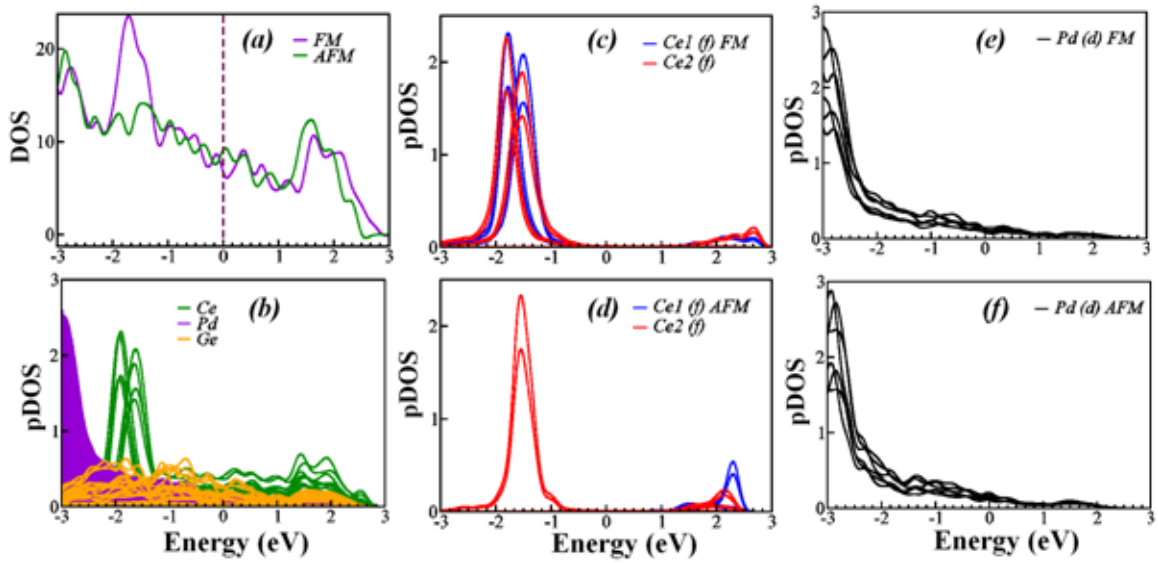

Figure 2.17 Density of States (DOS) and Projected density-of-states (PDOS) for γ-Ce_2PdGe_3.

Top two panels show the projected density of electronic states of FM states for Ce *f* and Pd *d* orbital. In the bottom half, it is shown that the same *f* state is more localized, with larger energy gap between valence and conduction *f* electrons and significantly different from *f* states involved in the FM state. The latter is more stable than the former due to Hund's coupling thus, favouring parallel alignment of spins of electrons in different *f* states.

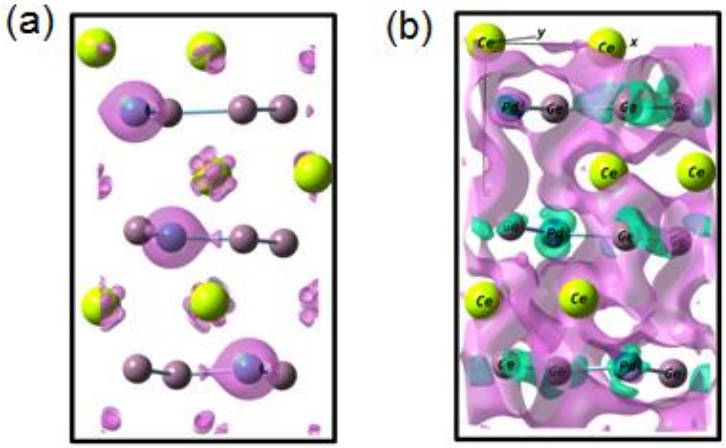

Figure 2.18 (a) Spin averaged charge density with iso-surface and density 0.02 and 0.07e/Å^3 respectively, shows Ce and Pd as the participant atoms for net magnetic moment of γ-Ce_2PdGe_3. (b) Iso-surface of average magnetization density of bulk γ-Ce_2PdGe_3 along z-direction shown for FM state (pink and green iso-surfaces indicate positive and negative magnetization respectively). Iso-value and density are 0.02 and 0.001 e/Å^3, respectively.

Self-consistent calculations also revealed that the ferromagnetic ordering of ground state arises from the spins at Ce and Pd sites (**Figure 2.18a and b**) of the hexagonal cell, which is in agreement with the stable magnetic state found experimentally. Examination of electronic states near the Fermi level reveals correlation between *d* states of Pd ions and *f* states of Ce ions. Magnetic interactions are mediated by these hybridized states, resulting in the ferromagnetic order. The magnetic moment for bulk γ-Ce_2PdGe_3 was estimated to be exactly the same as due to six Ce^{3+} and three Pd^{2+} ions per supercell structure.

2.4 Concluding Remarks

Our findings suggest that although AlB_2 type families are widely studied for their interesting structure and properties, there is still plenty of opportunity to explore new superstructure derivatives and perhaps these compounds may show fascinating properties as well. Polymorphism is a common phenomenon observed for AlB_2 type compounds and they are known to show versatile properties. Ce_2PdGe_3 also shows two different polymorphs and their magnetic and transport properties are entirely different. In most of the syntheses products contains a mixture of polymorphs and it is a challenging task to separate them by any physical or chemical means. A novel strategy was adapted to synthesize a singular product by simply varying the ratio of palladium and germanium. Theoretical studies on γ-Ce_2PdGe_3 suggested two types of magnetic orderings: the magnetic moments of the two transition metal (Pd) and *RE* (Ce) atoms are aligned ferromagnetically and antiferromagnetically. The difference in the two energies yielded the *J* coupling, indicating better stability of the FM states over AFM. Participation of Ce *f* orbitals in both occupied and unoccupied states got significantly modulated by different spin configurations. Ce 4*f* electrons in FM states were uncorrelated with each other and away from the valence and conduction band-edges with relatively extended nature. For AFM spin state, *f* electrons were found to be more contributory and were closer to the conduction band edge which caused 4*f* ions to scatter the conduction electrons independently giving rise to Kondo like behaviour. Ce_2PtGe_3 showed similar Kondo semiconductor behavior and hope that this work will direct further studies in this field in near future.

2.5 References

1. Marcano, N.; Senas, A.; Espeso, J. I.; Barquin, L. F.; Fernandez, J. R.; Sal, J. C. G., *J. Non-Cryst Solids* **2001,** *287* (1-3), 318-323.

2. Mallik, R.; Sampathkumaran, E. V.; Strecker, M.; Wortmann, G.; Paulose, P. L.; Ueda, Y., *J. Magn. Magn. Mater.* **1998,** *185*, L135-L143.

3. Borchi, E.; Gennaro, S. D., *Phys. Rev. B* **1975,** *14* (5), 1989-1994.

4. Hirose, Y.; Nishimura, N.; Honda, F.; Sugiyama, K.; Hagiwara, M.; Kindo, K.; Takeuchi, T.; Yamamoto, E.; Haga, Y.; Matsuura, M.; Hirota, K.; Yasui, A.; Yamagami, H.; Settai, R.; Onuki, Y., *J. Phys. Soc. Jpn.* **2011,** *80* (2), 024711-024712.

5. Stockert, O.; Arndt, J.; Faulhaber, E.; Geibel, C.; Jeevan, H. S.; Kirchner, S.; Loewenhaupt, M.; Schmalzl, K.; Schmidt, W.; Si, Q.; Steglich, F., *Nat. Phys.* **2011,** *7* (2), 119-124.

6. Gschneidner, K. A.; Pecharsky, V. K., *Physica B* **1996,** *223-24* (1-4), 131-134.

7. Thompson, J. D.; Park, T.; Curro, N. J.; Ronning, F.; Movshovich, R.; Bauer, E. D.; Sarrao, J. L., *J. Magn. Magn. Mater.* **2007,** *310* (2), 532-535.

8. Kumar, N.; Das, P. K.; Kulkarni, R.; Thamizhavel, A.; Dhar, S. K.; Bonville, P., *J. Phys.-Condens. Matter.* **2012,** *24* (3), 036005.

9. Majumdar, S.; Sampathkumaran, E. V., *Solid State Commun.* **2001,** *117*, 645-648.

10. Gajewski, D. A.; Dilley, N. R.; Bauer, E. D.; Freeman, E. J.; Chau, R.; Maple, M. B.; Mandrus, D.; Sales, B. C.; Lacerda, A. H., *J. Phys.: Condens. Matter* **1998,** *10* (31), 6973-6985.

11. Szytula, A.; Jezierski, A.; Penc, B., *Physica B* **2003,** *327* (2-4), 171-176.

12. Gordon, R. A.; Warren, C. J.; Alexander, M. G.; DiSalvo, F. J.; Pottgen, R., *J. Alloy Compd.* **1997,** *248* (1-2), 24-32.

13. Patil, S.; Pandey, S. K.; Medicherla, V. R. R.; Singh, R. S.; Bindu, R.; Sampathkumaran, E. V.; Maiti, K., *J. Phys.: Condens. Matter* **2010,** *22* (25).

14. Szytula, A.; Leciejewicz, J.; Maletka, K., *J. Magn. Magn. Mater.* **1993,** *118* (3), 302-306.

15. Patil, S.; Medicherla, V. R. R.; Singh, R. S.; Pandey, S. K.; Sampathkumaran, E. V.; Maiti, K., *Phys. Rev. B* **2010,** *82* (10).

16. Kalsi, D.; Rayaprol, S.; Siruguri, V.; Peter, S. C., *J. Solid State Chem.* **2014,** *217* (0), 113-119.

17. Mallik, R.; Sampathkumaran, E. V., *J. Magn. Magn. Mater.* **1996,** *164* (1-2), L13-L17.

18. Salamakha, P. S.; Ste¸ń-Damm, J.; Bodak, O., *J Alloy Compd* **1996,** *242* (1-2), L1-L2.

19. Gladyshevskii, E. I.; Bodak, O. I., *Dopov. Akad. Nauk. Ukr. RSR* **1965**, 601-604.

20. Sebastian, C. P.; Kanatzidis, M. G., *J. Solid State Chem.* **2010,** *183* (4), 878-882.

21. Dhar, S. K.; Pattalwar, S. M., *J. Magn. Magn. Mater.* **1996,** *152* (1-2), 22-26.

22. Nakamoto, G.; Hagiuda, T.; Kurisu, M., *Physica B* **2002,** *312*, 277-279.

23. Jones, C. D. W.; Gordon, R. A.; DiSalvo, F. J.; Pöttgen, R.; Kremer, R. K., *J. Alloy Compd.* **1997,** *260* (1-2), 50-55.

24. Baumbach, R. E.; Gallagher, A.; Besara, T.; Sun, J.; Siegrist, T.; Singh, D. J.; Thompson, J. D.; Ronning, F.; Bauer, E. D., *Phys. Rev. B* **2015**, *91* (3), 035102.

25. Giannozzi, P.; Baroni, S.; Bonini, N.; Calandra, M.; Car, R.; Cavazzoni, C.; Ceresoli, D.; Chiarotti, G. L.; Cococcioni, M.; Dabo, I., *J. Phys.: Condens. Mat.* **2009,** *21* (39), 395502.

26. Becke, A. D., *Phys. Rev. A* **1988,** *38* (6), 3098.

27. Andersson, D. A.; Simak, S. I.; Johansson, B.; Abrikosov, I. A.; Skorodumova, N. V., *Phys. Rev. B* **2007,** *75* (3), 035109.

28. Loschen, C.; Carrasco, J.; Neyman, K. M.; Illas, F., *Phys. Rev. B* **2007,** *75* (3), 035115.

29. Blächl, P. E., *Phys. Rev. B* **1994,** *50* (24), 17953.

30. Bachelet, G. B.; Schläter, M., *Phys. Rev. B* **1982,** *25* (4), 2103.

31. Dudarev, S. L.; Botton, G. A.; Savrasov, S. Y.; Humphreys, C. J.; Sutton, A. P., *Phys. Rev. B* **1998,** *57* (3), 1505.

32. Brauer, G.; Mitius, A., *Z. Anorg. Allg. Chem.* **1942,** *249*, 325-339.

33. Kalsi, D.; Subbarao, U.; Rayaprol, S.; Peter, S. C., *J. Solid State Chem.* **2014,** *212* (0), 73-80.

34. Pöttgen, R.; Gravereau, P.; Darriet, B.; Chevalier, B.; Hickey, E.; Etourneau, J. R., *J. Mater. Chem.* **1994,** *4* 463-467.

35. Bärnighausen, H., *Commun. Math. Chem.* **1980,** *9* 139–175.

36. Bärnighausen, H.; Müller, U., Universität Karlsruhe and Universität-Gh Kassel: Germany, 1996.

37. Pauling, L., *The Nature of the Chemical Bond*. third edition ed.; Cornel University Press: Ithaca, NY 1960.

38. Yosida, K., *Phys. Rev. B* **1957,** *106*, 893.

39. Kasuya, T., *Prog. Theor. Phys.* **1956,** *16*, 45.

40. Ruderman, M. A.; Kittel, C., *Phys. Rev.* **1954,** *96*, 99.

41. Donohue, J., *The Structures of the Elements.* Wiley: New York, 1974.

42. Peter, S. C.; Malliakas, C. D.; Chondroudi, M.; Schellenberg, I.; Rayaprol, S.; Hoffmann, R. D.; Pöttgen, R.; Kanatzidis, M. G., *Inorg. Chem.* **2010,** *49*, 9574-9580.

43. Anand, V. K.; Adroja, D. T.; Hillier, A. D., *Phys. Rev. B* **2012,** *85* (1), 014418.

44. Abliz, M.; Kindo, K.; Kadowaki, K.; Takeya, H., *J. Phys. Soc. Jpn.* **2003,** *72* (10), 2599-2603.

45. Mulder, C. A. M.; van Duyneveldt, A. J.; van der Linden, H. W. M.; Verbeek, B. H.; van Dongen, J. C. M.; Nieuwenhuys, G. J.; Mydosh, J. A., *Phys. Lett. A* **1981,** *83* (2), 74-76.

46. Mulder, C. A. M.; van Duyneveldt, A. J.; Mydosh, J. A., *Phys. Rev. B* **1981,** *23* (3), 1384-1396.

47. Mulder, C. A. M.; van Duyneveldt, A. J.; Mydosh, J. A., *Phys. Rev. B* **1982,** *25* (1), 515-518.

48. Malinowski, A.; Bezusyy, V. L.; Minikayev, R.; Dziawa, P.; Syryanyy, Y.; Sawicki, M., *Phys. Rev. B* **2011,** *84* (2), 024409.

49. Li, D. X.; Yamamura, T.; Yubuta, K.; Nimori, S.; Haga, Y.; Shikama, T., *J. Phys. Conf. Ser.* **2011,** *320*, 012041.

50. Szlawska, M.; Majewicz, M.; Kaczorowski, D., *J. Phys. Cond. Mat.* **2014,** *26* (12), 126002.

51. Li, D. X.; Zhao, X.; Nimori, S., *J. Phys.: Condens. Matter* **2009,** *21* 026006.

52. Zhou, X. Y.; Wang, G. Y.; Chi, H.; Su, X. L.; Salvador, J. R.; Liu, W.; Tang, X. F.; Uher, C., *J. Electr. Mater.* **2012,** *41* (6), 1589-1594.

53. Chevalier, B.; Pöttgen, R.; Darriet, B.; Gravereau, P.; Etourneau, J., *J. Alloys Comp.* **1996,** *233* (1–2), 150-160.

54. Martin, D. L., *Phys. Rev. B* **1979,** *20* (1), 368-375.

55. Bibekananda, M.; Suresh, K. G.; Nigam, A. K., *J. Phys.: Condens. Matter* **2011,** *23* (50), 506002.

56. Kalsi, D.; Subbarao, U.; Rayaprol, S.; Peter, S. C., *J. Solid State Chem.* **2014,** *212*, 73-80.

57. Li, D. X.; Nimori, S.; Shiokawa, Y.; Tobo, A.; Onodera, H.; Haga, Y.; Yamamoto, E.; Ōnuki, Y., *Appl. Phys. Lett.* **2001,** *79* (25), 4183-4185.

58. Li, D. X.; Yamamura, T.; Yubuta, K.; Nimori, S.; Haga, Y.; Shikama, T., *J. Phys. Conf. Ser.* **2011,** *320* (1), 012041.

59. Li, D. X.; Shiokawa, Y.; Nimori, S.; Haga, Y.; Yamamoto, E.; Matsuda, T. D.; Onuki, Y., *Physica B: Condens. Mat.* **2003,** *329–333*, 506-507.

60. Li, D. X.; Nimori, S.; Ohta, S.; Yamamura, Y.; Shikama, Y., *J. Phys.: Confer. Ser.* **2012,** *400* (3), 032044.

61. Tien, C.; Feng, C. H.; Wur, C. S.; Lu, J. J., *Phys. Rev. B* **2000,** *61* (18), 12151-12158.

62. Lorenzer, K. A.; Inamdar, M.; L Shafeek, L.; Prokofiev, A.; Paschen, S., *J. Phys.: Conf. Ser.* **2012,** *391*, 012036.

63. Okamura, H.; Kawahara, J.; Nanba, T.; Kimura, S.; Soda, K.; Mizutani, U.; Nishino, Y.; Kato, M.; Shimoyama, I.; Miura, H.; Fukui, K.; Nakagawa, K.; Nakagawa, H.; Kinoshita, T., *Phys. Rev. Lett.* **2000,** *84* (16), 3674-3677.

64. Kumigashira, H.; Takahashi, T.; Yoshii, S.; Kasaya, M., *Phys. Rev. Lett.* **2001,** *87*, 067206.

65. Kondo, J., *Prog. Theo. Phys.* **1964,** *32* (1), 37-49.

66. Malik, S. K.; Adroja, D. T., *Phys. Rev. B* **1991,** *43*, 6277.

67. Hiraoka, T.; Kinoshita, E.; Tanaka, H.; Takabatake, T.; Fujii, H., *J. Magn. Magn. Mater.* **1996,** *153*, 124.

68. Chevalier, B.; Decourt, R.; Heying, B.; Schappacher, F. M.; Rodewald, U. C.; Hoffmann, R. D.; Pöttgen, R.; Eger, R.; Simon, A., *Chem. Mater.* **2007,** *19* (1), 28-35.

69. Gopal, E. S. R., *Specific heat at low temperatures*. Plenum: New York, 1966.

70. Goltsev, A. V.; Golubkov, A. V.; Smirnov, I. A.; Misiorek, H.; Sulkovski, C., *Phys. Solid State* **2006, ,** *48*, 622-624.

71. Maldonado, A.; Suderow, H.; Vieira, S.; Aoki, D.; Flouquet, J., *J. Phys.: Condens. Matter* **2012,** *24*, 475602.

72. Ishikawa, M.; Takeda, N., *Solid State Commun.* **2005,** *133* (4), 249-251.

73. Peter, S. C.; Sarkar, S.; Kanatzidis, M. G., *Inorg. Chem.* **2012,** *51* (20), 10793-10799.

Chapter 3

Structure and Properties of New Europium Based 2-1-3 Series of Compounds Derived from AlB_2 Prototype

3.1 Introduction

Cerium based intermetallic compounds are most studied in the literature owing to their relatively easier synthetic feasibility and occurrence of two energetically comparable states which give rise to a wide array of properties as discussed in the previous chapter. Eu and Yb possess the same advantage of multiple valence states, but high air sensitivity limits their synthesis by traditional arc-melting method. High frequency induction heating and metal flux technique can overcome these limitations and are suitable for the synthesis of these compounds. Eu based compounds show variety of physical properties, e.g. structural transition was hinted in Eu_2AuGe_3,[1] strong magnetocrystalline effect was observed in $EuCu_2X_2$ (X = Si and Ge),[2] valence fluctuation, and heavy-fermion behavior was observed in $EuCu_2(Ge_{1-x}Si_x)_2$,[3] $Eu_8Ga_{16}Ge_{30}$ shows highly correlated semimetallic behavior,[4] ferromagnetic ordering at relatively high temperature (T_c = 29 K) along with a dense Kondo effect was observed in $EuFe_2P_2$,[5] Kondo effect was also observed in the corresponding Ni analogue which was later confirmed to have hybridization gap as well, [6] Recently, many compounds were studied for thermoelectric applications, e.g. $Eu_5Sn_2As_6$, $Eu(Zn_{1-x}Cd_x)_2Sb_2$ were studied in detail.[7-8] This chapter is dedicated to discussions on the structural diversity and properties of Eu_2TX_3 class of compounds which are basically derived superstructures of AlB_2 prototype.

Preliminary diffraction data on single crystals of Eu_2CuGe_3 hinted towards a hexagonal structure whereas Eu_2AuSi_3 and Eu_2AgGe_3 were confirmed to adopt orthorhombic structure. Eu_2AuSi_3 adopts the Ca_2AgSi_3 structure type[1] with *Fmmm* space group. Eu_2AgGe_3, on the other hand, crystallizes in the orthorhombic Ba_2LiSi_3 structure type, with *Fddd* space group. Interestingly, Eu_2AgGe_3 underwent reversible phase transitions at high temperature. All three compounds showed magnetic ordering at low temperature.

3.2 Experimental Section

3.2.1 Chemicals

Europium (ingots, 99.99%, ESPI metals), copper (powder, 99.99%, Alfa Aesar), gold (ingots, 99.99%, Alfa Aesar), silicon (shots, 99.999%, Alfa Aesar), indium (tear drops, 99.99%, Alfa Aesar), silver (ingots, 99.99%, Alfa-Aesar) and germanium (metal pieces, 99.999%, Alfa Aesar) were used as purchased without any further purification.

3.2.2 Synthesis

3.2.2.1 Metal flux method

Eu_2CuGe_3 and Eu_2AuSi_3 were synthesized by taking 3 mmol of europium, 2 mmol of gold/copper, 6 mmol of silicon and 30 mmol of indium in an alumina crucible under an inert (argon) atmosphere inside a glove box. The excess indium acts as an inactive metal flux. The crucible was placed in a quartz tube (diameter, 13 mm) and was flame-sealed under vacuum of 10^{-6} torr to prevent oxidation during the progress of the reaction. The evacuated tube was placed in a vertical tube furnace and was heated to 1273 K in 10 h, kept at that temperature for 6 h. The temperature was then lowered down to 1123 K in 2 h and annealed at this temperature for 72 h. Finally, the system was allowed to cool slowly to room temperature in 48 h.

The reaction products were isolated from the excess indium flux by heating at 623 K and subsequent centrifugation through a coarse frit. The remaining flux was removed by immersion and sonication in glacial acetic acid for 24 h. The final crystalline product was rinsed with water and dried with acetone in a vacuum oven at 350 K overnight. Eu_2CuGe_3 grew as shiny black hexagonal shaped crystals which were brittle in nature (**Figure 3.1a**). Eu_2AuSi_3 crystals, on the other hand, were shiny multifaceted (**Figure 3.1b**) with an average dimension of 2-3 mm. The single crystals of Eu_2AuSi_3 were stable in air and moisture with no decomposition observed even after several months. Synthesis of Eu_2AgGe_3 was attempted in a similar fashion using various metal fluxes like indium, gallium, aluminium, etc. but all were failed. Hence both the compounds were synthesized by the following method.

3.2.2.2 High frequency heating method

Europium, corresponding transition metals (Ag and Au) and silicon/germanium metals were taken in the ideal 2:1:3 atomic ratios and sealed in tantalum ampoules in an arc-melting apparatus (Edmund Bìühler Gmbh, compact arc melter MAM-1) under argon atmosphere. The sealed tantalum ampoules were then placed in a water-cooled sample chamber of an induction furnace (EasyHeat induction heating system, Model 7590), first rapidly heated to ca. 1250 K and kept at that temperature for 10 min. Then the sample was cooled down to ca. 1000 K and the sample was annealed at that temperature for another 30 min, followed by quenching by switching off the power supply. The compounds were stable in air for several months.

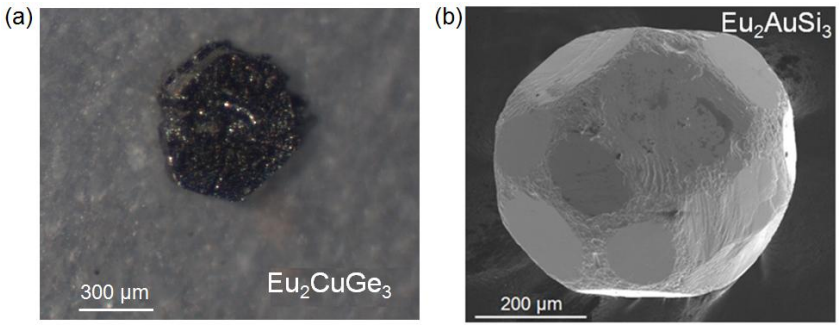

Figure 3.1 (a) A typical hexagonal crystal of Eu_2CuGe_3 taken with a normal laboratory microscope, (b) FE SEM image of a typical Eu_2AuSi_3 single crystal, the edges of the Eu_2AuSi_3 crystal are rounded due to the chemical etching with acetic acid.

3.2.3 PXRD

PXRD patterns of Eu_2AuSi_3[9] and Eu_2AgGe_3[10] were collected at room temperature on a Bruker D8 Discover X-ray diffractometer with Cu-K_α X-ray source (λ = 1.5406 Å) to determine the phase identity and purity. The instrument is equipped with a position sensitive detector. Data were collected in the angular range $20^o \leq 2\theta \leq 80^o$ (for Eu_2AuSi_3) and $30^o \leq 2\theta \leq 65^o$ (for Eu_2AgGe_3) respectively with the step size 0.02^o and scan rate of 0.5 s/step calibrated against corundum standards. The experimental patterns were compared to the pattern calculated from the single crystal structure refinement and are shown in **Figure 3.2a** and **3.2b**, respectively.

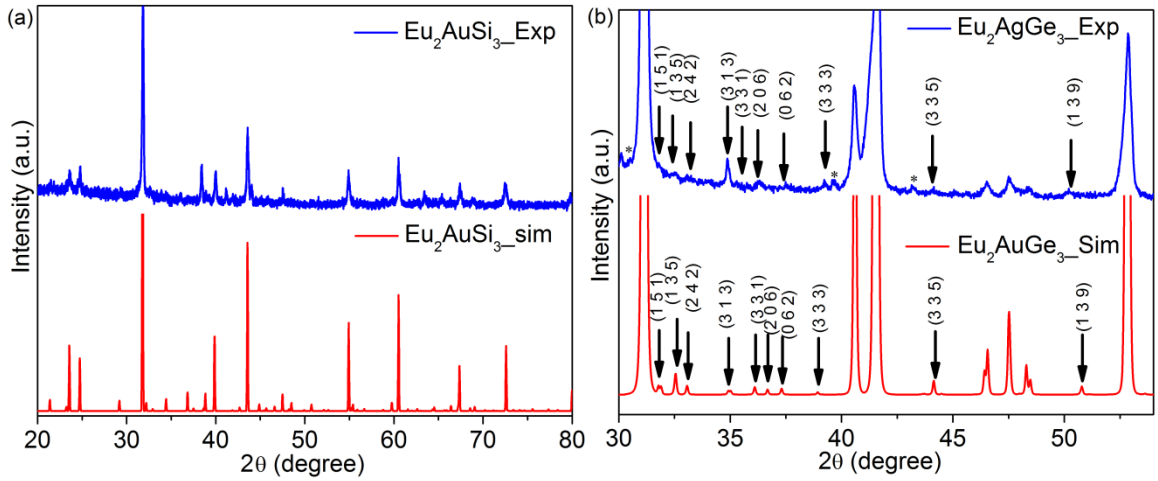

Figure 3.2 Comparison of PXRD pattern of polycrystalline sample of (a Eu_2AuSi_3 and (b) Eu_2AgGe_3 with that of simulated pattern obtained from the SC XRD data. The intensities in the second plot have been enhanced to show the superstructure peaks. Peaks corresponding to *Fddd* superstructure are marked by black arrows with the respective planes and those corresponding to minute quantity of Eu_2O_3 as impurity ($Ia\bar{3}$) are marked with asterisks.

3.2.4 Differential Thermal Analysis

The differential thermal analysis (DTA) was performed using a differential scanning calorimeter **(**METTLER-TOLEDO DSC1) at Indian Institute of Science, Bangalore facility. The sample was kept in an aluminium crucible and heated up to 823 K from room temperature (303 K) at the rate of 5 K/min in an inert N_2 atmosphere followed by cooling at the same rate to room temperature.

3.2.5 Single Crystal XRD

Carefully selected single crystals of Eu_2AuSi_3 and Eu_2AgGe_3 were mounted on a Mitegen pin using a minimum amount of Paratone oil. X-ray single crystal data were collected at room-temperature on Oxford Diffraction Supernova diffractometer equipped with an ATLAS CCD detector. Mo-Kα radiation with a wavelength of λ = 0.71073 Å operating at 50 kV and 0.8 mA. A full sphere of ω scans was recorded using 287 frames with a step of 1 degree and 22.27 s per frame up to 2θ of 58.67° for Eu_2AuSi_3. In case of Eu_2AgGe_3 data was collected up to 2θ of 58.28° with and exposure of 20 s/frame. Data was processed using Crysalis Pro and an analytic absorption correction was applied using a face-indexation of the crystal. Both crystal structures were solved by SHELXS 97 and refined by full matrix least-squares method using SHELXL.

3.2.6 Structure Refinement

3.2.6.1 Eu_2AuSi_3

The single crystal data of Eu_2AuSi_3 showed an orthorhombic cell and the systematic extinctions were compatible with the F lattice. The atomic parameters of Ca_2AgSi_3 were used as the starting parameters and the structure was refined using SHELXL-97 (full-matrix least-squares on F^2) with anisotropic atomic displacement parameters for all atoms. As a check for the correct composition, the occupancy parameters were refined in a separate series of least-squares cycles. Initially, there were five crystallographically different positions in the Eu_2AuSi_3 structure - two for the Eu and Si atoms and one for the Au atom. During the isotropic refinement, it was observed that the atomic displacement parameters of the gold and silicon atoms were anomalously large. Furthermore, the refinement was largely unsatisfactory owing to high residuals (R_1 > 20%), and large electron density residuals (45-23 $eÅ^{-3}$) around the gold and silicon atoms. Anisotropic refinement did not improve the refinement and also resulted in abnormal cigar-shaped gold and silicon atomic displacement ellipsoids (U_{11} = 0.50 $Å^2$). The anomalous atomic

displacement parameter could not be resolved by subsequent refinement of the occupancy parameters. All these features indicated a crystallographic disorder associated with the Si and Au atoms. Consequently, gold and silicon atoms were refined by mixing silicon and gold sites, respectively. The resulting atomic displacement parameters of mixed positions became well-behaved and the final difference maps showed residuals that were reasonably acceptable. The final refinement gives an atomic ratio of Eu_2AuSi_3.

3.2.6.2 Eu_2AgGe_3

The single crystal data of Eu_2AgGe_3 showed an orthorhombic cell. The lattice was established as face centered orthorhombic based on absences of odd h+k, h+l, and k+l reflections and compatible with the space groups *Fmmm*, *Fmm*2 and *F*222. In the first refinement step, all weak superstructure reflections have been neglected and only the subcell intensities have been integrated with lattice parameters a = 8.7069(17) Å, b = 15.011(3) Å and c = 8.8803(18) Å. Since the PXRD of Eu_2AgGe_3 is similar to the pattern of Eu_2AuGe_3[37] and Yb_2AuGe_3[36] compounds (Ca_2AgSi_3 type,[9] space group *Fmmm*), the atomic coordinates of Eu_2AuGe_3 were taken as starting values and the structure was refined with anisotropic displacement parameters for all atoms with SHELXL-97 (full-matrix least-squares on F_o^2).[40] As a check for the correct composition, the occupancy parameters were refined in a separate series of least-squares cycles. Initially, there were five crystallographically different positions in the Eu_2AgGe_3 compound - two for each Eu and Ge atoms and one for the Ag atom. During the isotropic refinement it was observed that the anisotropic displacement parameters of the silver and germanium atoms were anomalously large. Furthermore, the refinement was largely unsatisfactory giving relatively high residuals (R_1 > 10%), and large electron density residuals (15-20 e $Å^{-3}$) around the silver and germanium atoms. Anisotropic refinement did not improve these parameters and also resulted in abnormal cigar-shaped silver and germanium thermal ellipsoids (U_{22} = 0.80 $Å^2$). Similar problems were also faced while refining the crystal structure of the Yb_2AuGe_3 compound as well.[36] The anomalous thermal parameter could not be resolved by subsequent refinement of the occupancy parameters. All these observations indicated a crystallographic disorder associated with the Ge and Ag atoms similar to the Yb_2AuGe_3 compound.[11] Consequently, the refinement was performed by allowing mixed Ag/Ge occupancy of both the "Ge" and "Ag" positions, subject to the constraint that the summed occupancies of both sites were full. This makes the compound slightly off different stoichiometry. At this point, it must be mentioned that the

mixing of silver and germanium was also reported in the equiatomic compound EuAgGe.[42-43] Though the residual R_1 reduced substantially to 5.6% and electron density residuals are behaving properly (2.9 and -1.8 e $Å^{-3}$), the thermal ellipsoid U_{22} for *M*3 (Ge3+Ag3) atoms were significantly larger (0.64 $Å^2$). Nevertheless, an attempt was made to remove the mirror plane along the *c*-axis and refine the crystal structure in *Fmm*2 space group, which resulted in larger residuals and thermal displacement parameters. *F*222 is another space group used, but all the refinement parameters were similar to the refinement in the *Fmmm* space group.

The weak superstructure reflections observed in the PXRD (shown in **Figure 3.2b**) were considered in the second step. The additional reflections suggested doubling of *c*-axis and resulted the lattice parameters *a* = 8.7069 (17) Å, *b* = 15.011 (3) Å and *c* = 17.761 (4) Å. The superstructure reflections were already evident from the PXRD data and indicate that the structure is compatible with the Ba_2LiSi_3 type structure. The atomic parameters of Ba_2LiSi_3 were taken as starting parameters and the structure was refined using SHELXL-97 (full-matrix least-squares on F^2)[40] with anisotropic atomic displacement parameters for all atoms. The refinement within the Ba_2LiSi_3 type structure was also resulted with 5 atomic positions: two europium atoms and three mixed position of silver and germanium. The resulting anisotropic displacement parameters of mixed position became well-behaved and the final difference maps showed residuals that were reasonably acceptable. Owing to many weak reflections and doubling of unit cell, the quality of the refinement did not satisfy criteria of a high-quality structure refinement. Relatively large displacement parameters of *M*2 and *M*3 positions (i.e. along the *c*-axis) indicated a further symmetry reduction at low temperature similar to the previous report on Eu_2AuGe_3.[37] The final refinement gives an atomic ratio of $Eu_2Ag_{1.21(2)}Ge_{2.79(2)}$. The data collection and refinement parameters for both Eu_2AuSi_3 and Eu_2AuGe_3 are summarized in **Table 3.1**. The atomic coordinates, equivalent displacement parameters, anisotropic displacement parameters and important bond lengths are listed in **Tables 3.2**, **3.3** and **3.4**, respectively.

3.2.7 Magnetic Measurements

Magnetic measurements on randomly oriented single crystals of Eu_2CuGe_3 and Eu_2AuSi_3 and powder samples of Eu_2AgGe_3 were carried out with a Quantum Design Magnetic Property Measurement System- Superconducting Quantum Interference Device (MPMS-SQUID) dc magnetometer. Temperature dependent magnetization data were collected in

the field cooled mode (FC) in the temperature range 2 to 300 K at an applied magnetic field of 1000 Oe. Magnetization data were also collected for Eu_2AgGe_3 at three different temperatures *viz*. 5, 18 and 300 K with field sweeping from −55 kOe to 55 kOe

Table 3.1 Crystal data and structure refinement for Eu_2AuSi_3 and Eu_2AgGe_3 at 293(2) K.

Empirical formula	Eu_2AuSi_3	Eu_2AgGe_3
Formula weight	584.52	636.22
Wavelength	0.71073 Å	
Crystal system	Orthorhombic	
Space group	*Fmmm*	*Fddd*
Unit cell dimensions	*a* = 8.306(2) Å, *b* = 9.0369(18) Å, *c* = 14.377(3) Å,	*a* = 8.7069 (17) Å, *b* = 15.011 (3) Å, *c* = 17.761 (4) Å,
Volume	1079.2(4) $Å^3$	2321.33 (8)$Å^3$
Z	8	16
Density (calculated)	7.195 g/cm^3	7.296 g/cm^3
Absorption coefficient	50.479 mm^{-1}	39.319 mm^{-1}
F(000)	1974	4362
Crystal size	0.15 x 0.10 x 0.10 mm^3	0.12 x 0.10 x 0.08 mm^3
θ range for data collection	3.62 to 45.58°	2.9 to 29.14°
Index ranges	-16<=*h*<=14, -18<=*k*<=16, -28<=*l*<=28	-11<=*h*<=11, -20<=*k*<=20, -24<=*l*<=23
Reflections collected	9130	4583
Independent reflections	1279 [R_{int} = 0.1074]	769 [R_{int} = 0.0921]
Completeness to θ = 45.52°	99.8%	98.1%
Refinement method	Full-matrix least-squares on F^2	
Data / restraints / parameters	1279 / 0 / 25	769 / 0 / 34
Goodness-of-fit	1.008	1.424
Final *R* indices [>2σ(I)]	R_{obs} = 0.0320, wR_{obs} = 0.0709	R_{obs} = 0.0769, wR_{obs} = 0.1720
R indices [all data]	R_{all} = 0.0346, wR_{all} = 0.0740	R_{all} = 0.0909, wR_{all} = 0.179
Extinction coefficient	0.00045(3)	0.000125 (2)
Largest diff. peak and hole	8.195 and -7.414 e·$Å^{-3}$	2.442 and -1.655 e·$Å^{-3}$

3.2.8 XANES

XANES experiments were performed at PETRA III, P06 beamline of DESY, Germany. Measurements at the Eu L_{III} edge and at ambient pressure were done in transmission mode using gas ionization chambers to monitor the incident and transmitted X-ray intensities. Monochromatic X-rays were obtained using a Si (111) double crystal monochromator which was calibrated by defining the inflection point (first derivative

maxima) of Cu foil as 8980.5 eV. The beam was focused employing a Kirkpatrick-Baez (K-B) mirror optic. A rhodium coated X-ray mirror was utilized to suppress higher order harmonics. A CCD detector was used to record the transmitted signals. The sample was prepared by mixing an appropriate amount of finely ground powder crushed from the single crystals of Eu_2CuGe_3 and polycrystalline Eu_2AgGe_3 compounds with cellulose and cold pressing them to a pellet.

Table 3.2 Atomic coordinates and equivalent isotropic displacement parameters ($Å^2$x 10^3) for Eu_2AuSi_3 and Eu_2AgGe_3 at 293(2) K with estimated standard deviations in parentheses.

Label	Wy. site	*x*	*y*	*z*	Occupancy	U_{eq}*
Eu_2AuSi_3						
Eu1	8*h*	0.0000	0.2518(1)	0.0000	1	8(1)
Eu2	8*f*	0.2500	0.2500	0.2500	1	9(1)
Si1	8*i*	0.0000	0.0000	0.6642(2)	1	10(1)
*M*1	8*i*	0.0000	0.0000	0.1665(1)	0.80(1)Au + 0.20(1)Si	8(1)
*M*2	16*n*	0.2519(2)	0.0000	0.0826(1)	0.90(1)Au + 0.10(1)Si	9(1)
Eu_2AgGe_3						
Eu1	16*g*	0.1250	0.1250	0.0002(1)	1	9(1)
Eu2	16*g*	0.1250	0.1250	0.5006(1)	1	9(1)
*M*1	16*f*	0.1250	0.4582(1)	0.1250	0.90(1)Ag + 0.10(1)Ge	9(1)
*M*2	32*h*	0.3698	0.0431(1)	0.1215(1)	0.11(1)Ag + 0.89(1)Ge	18(1)
*M*3	16*f*	0.1250	0.2886(1)	0.1250	0.10(1)Ag + 0.90(1)Ge	22(1)

*U_{eq} is defined as one third of the trace of the orthogonalized U_{ij} tensor. *M* = [Au + Si/Ge]

3.2.9 ^{151}Eu Mössbauer Spectroscopic Measurement

The ^{151}Eu Mössbauer measurements on Eu_2AgGe_3 were carried out in the transmission geometry using standard PC based spectrometer in the temperature range of 30-300 K using $^{151}SmF_3$ was used as the source in the experiment and Eu_2O_3 was used as the reference sample.

3.2.10 Electrical Resistivity

The resistivity measurements were performed on a Eu_2CuGe_3 single crystal and a Eu_2AgGe_3 pellet over the temperature range of 2–300 K using a four-probe dc technique. Four very thin copper wires were glued to the pellet of Eu_2AgGe_3 using a strongly

conducting silver epoxy paste. The measurements were conducted using a Quantum Design Physical Property Measurement System (QD-PPMS).

Table 3.3 Anisotropic displacement parameters ($Å^2x10^3$) for Eu_2AuSi_3 and Eu_2AgGe_3 at 293(2) K with estimated standard deviations in parentheses.

Label	U_{11}	U_{22}	U_{33}	U_{12}	U_{13}	U_{23}
Eu_2AuSi_3						
Eu1	8	8	9	0	0	0
Eu2	8	9	9	0	0	0
Si1	5	16	8	0	0	0
*M*1	8	11	7	0	0	0
*M*2	5	14	7	0	0	0
Eu_2AgGe_3						
Eu1	9(1)	9(1)	9(1)	0	0	0
Eu2	10(1)	8(1)	8(1)	0	0	0
*M*1	7(1)	5(1)	16(1)	0	0	0
*M*2	7(1)	6(1)	43(2)	0	0	0
*M*3	8(2)	8(2)	49(2)	0	10(1)	0

The anisotropic displacement factor exponent takes the form: $-2\pi^2[h^2a^{*2}U_{11} + ... + 2hka^*b^*U_{12}]$. *M* = [Au + Si/Ge]

Table 3.4 Bond lengths [Å] for Eu_2AuSi_3 and Eu_2AgGe_3 at 293(2) K with estimated standard deviations in parentheses. *M* = [Au + Si]

Label	Distances	Label	Distances
Eu_2AuSi_3			
Eu1-Si1	3.2565(16)	Si1-*M*2	2.3714(15)
Eu1-*M*2	3.2692(8)	Si1-*M*1	2.434(2)
Eu1-*M*1	3.3026(6)	Si3-*M*2	2.3761(14)
Eu2-*M*1	3.2952(4)	*M*1-*M*2	2.4144(10)
Eu2-*M*2	3.3007(7)		
Eu_2AgGe_3			
*M*1-*M*2	2.5618(16)	*M*3-Eu1	3.3081(19)
*M*1-*M*3	2.547(3)	*M*1-Eu2	3.3393(14)
*M*2-*M*3	2.4596(18)	*M*2-Eu2	3.3275(18)
*M*1-Eu1	3.3527(9)	*M*2-Eu2	3.3622(16)
*M*2- Eu1	3.2716(18)	*M*3-Eu2	3.3759(11)

3.3 Results and Discussions

3.3.1 Crystal Structure

3.3.1.1 Eu_2AuSi_3

Eu_2AuSi_3 crystallizes in the Ca_2AgSi_3 structure type which is an ordered orthorhombic superstructure derivative of the AlB_2 structure type. The overall crystal structure of Eu_2AuSi_3 shown in **Figure 3.3** contains five different kinds of atomic sites - two Eu, two [Au+Si] mixed sites (represented as *M*1 and *M*2) and one Si site. The structure is comprised of infinite hexagonal network of [$M1_2M2_4$] and [Si_2M2_4] and [$Si_2M1_2M2_2$] rings as shown in **Figure 3.3b**. The interlayer Eu-Eu distance in this compound ranges from 4.4850(9) to 4.5519(9) Å. This Eu-Eu bond distance matches the same distance in other Eu based compounds such as Eu_2AuGe_3,[12] $EuCu_2Si_2$,[13,14] $EuGe_2$[15] etc with divalent europium. The distance between two adjacent hexagonal layers is precisely 4.5186(9) Å, means that the hexagonal rings are completely flat and planar. In comparison to the Eu_2AuGe_3[12] and Yb_2AuGe_3 compounds,[16] Au and Si atoms in the Eu_2AuSi_3 structure have well behaved anisotropic thermal parameters and it is anticipated that no probable phase transitions can be expected in higher and lower temperature. The shortest distance between the sites comprising the hexagonal network is 2.3714(4) Å for M_2-Si suggest a strong interaction between them.

Due to the difference in ordering among Au and Si sites in the hexagonal array, the coordination environment around Eu1 and Eu2 slightly varies (**Figure 3.4**). There are two crystallographically different Eu sites in Eu_2AuSi_3. Both of them reside in a hexagonal bipyramidal environment built up of Au and Si sites. Eu1 is sandwiched between [$M1_2M2_4$] and [Si_2M2_4] hexagon rings. The Eu1-Si and Eu1-*M* distances are 3.2565[9] Å and 3.2692(4)-3.3119(4) Å respectively. Eu2, on the other hand, is sandwiched between two [$Si_2M1_2M2_2$] hexagon rings. The Eu2-*M* distance is in the narrow range of 3.2952(4)-3.3007[9] Å and the distance between Eu2 and Si is precisely 3.3070(4) Å.

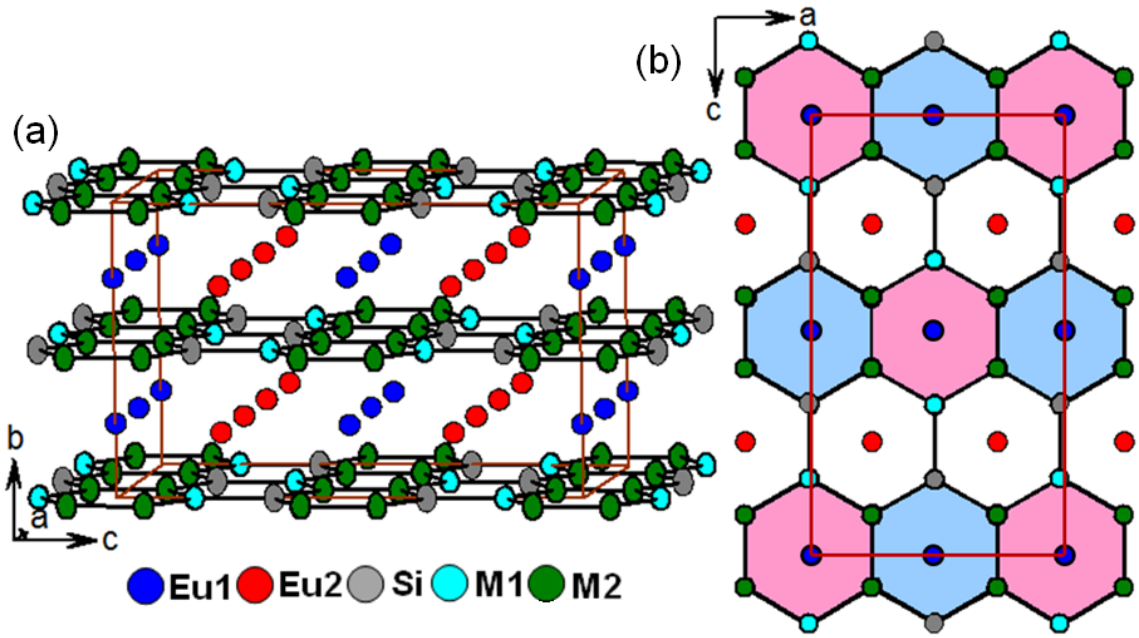

Figure 3.3 Crystal structure of Eu_2AuSi_3 viewed along *a*- and *b*-axis.

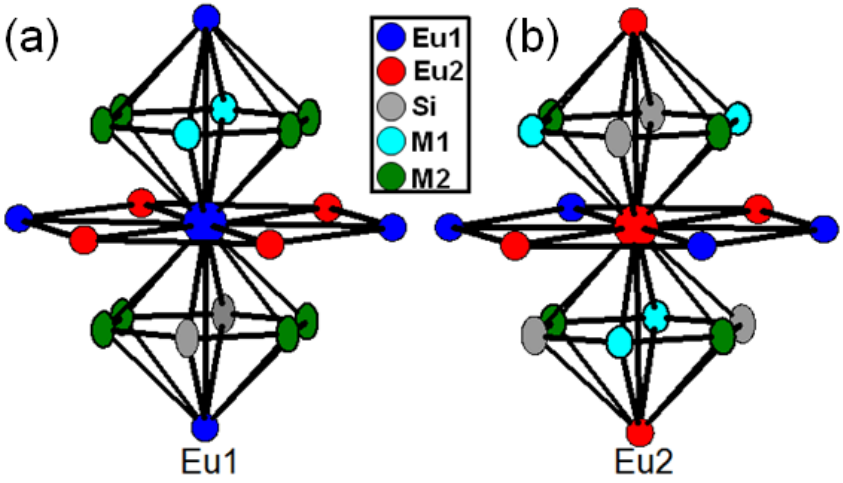

Figure 3.4 Coordination environments of (a) Eu1 and (b) Eu2 in the compound Eu_2AuSi_3.

3.3.1.2 Eu_2AgGe_3

The crystal structure of Eu_2AgGe_3 along *b*-and *c*-axis are shown in **Figure 3.5**. Eu_2AgGe_3 crystallizes in the Ba_2LiSi_3 structure type, an ordered superstructure of the hexagonal AlB_2 type with *Fddd* space group and lattice parameters are a = 8.7069(17) Å, b = 15.011(3) Å and c = 17.761(4) Å.

In analogy to Ba_2LiSi_3 and other related compounds, the crystal structure of Eu_2AgGe_3 can also be described as a "filled variation" of orthorhombic β-K_4P_6 structure[17]

which is another symmetry-reduced variant of the AlB_2 prototype. The crystal structure of Eu_2AgGe_3 consists of infinitely extended hexagonal network of three non-equivalent crystallographic sites namely *M*1, *M*2 and *M*3, all of them are the mixed positions of Ag and Ge atoms with varied occupancy levels (**Table 3.1**).[18-19] These layers are stacked parallel along the [001] direction (considering the *c*-axis as pseudo-hexagonal axis) with two crystallographically different Eu atoms sandwiched between these layers. At this point, it is worthwhile to compare the crystallographic features of Eu_2AgGe_3 (Ba_2LiSi_3 structure type) and Eu_2AuGe_3 (Ca_2AgSi_3 structure type). The hexagonal rings are slightly more puckered owing to the higher degree of ordering between Ag and Ge in comparison to Au and Ge in Eu_2AuGe_3 (*Fmmm*) which has basically planar [Ge_6] and [Au_2Ge_4] hexagons. The layers consisting of Eu atoms are also distorted and they align in a zig-zag fashion which is assumed to be an effect of puckering in the hexagonal ring.[20] The hexagonal layers in Eu_2AgGe_3 are stacked in the sequence: ABCD, ABCD along the [001] axis whereas for Eu_2AuGe_3 the stacking sequence of the hexagonal layers is AB, AB along the same axis. Another noticeable difference lies in the ordering of the transition metal and Ge atoms in the hexagonal network itself. In Eu_2AuGe_3, the [Ge_6] and [Au_2Ge_4] hexagons are linked by Au atoms with no mixed sites between Au and Ge positions, on the contrary, all the positions in the hexagonal network in Eu_2AgGe_3 consist of Ag and Ge mixed sites.

The distance between two parallel hexagonal layers is in the range 4.3699-4.5396 Å. The intralayer distance between two adjacent Eu atoms ranges from 4.3086 to 4.3129 Å, are slightly shorter than the interlayer distances 4.4135-4.4689 Å. These values suggest the possible presence of divalent Eu atoms in Eu_2AgGe_3 as they are close to the values in other already reported intermetallic compounds consisting of purely divalent Eu, such as, Eu_2AuGe_3,[1] $EuCu_2Si_2$, $EuGe_2$[21-23] etc. whereas the Eu-Eu distance in $EuPd_3$ with purely trivalent Eu is 4.10 Å[24] which is comparatively smaller than the values observed in divalent Eu containing intermetallics. Later, these observations were confirmed by magnetic, XANES and Mössbauer spectroscopic studies. The smallest bond distances between different mixed positions within the hexagonal network are 2.5618(16) Å, 2.547(3) Å, and 2.4596 (18) Å for *M*1-*M*2, *M*1-*M*3 and *M*2-*M*3, respectively. The first two bond distances are very close to the sum of the covalent radii of Au and Ge (2.56 Å)[25] whereas the last one is similar to the Ge-Ge bond distance (2.45 Å) in elemental Ge[26] indicating almost negligible bonding contribution from Ag atom for *M*3. A further

band structure calculation study will help to understand the role of bonding (both σ and π electrons) features in the hexagonal network toward the superstructure formation in this compound.

The coordination environments of Eu1, Eu2 and the [Ag+Ge] mixed sites have been shown in **Figure 3.6**. Both the Eu sites are in a slightly distorted hexagonal prismatic coordination environment built up by twelve [AgGe] mixed sites. Each Eu atom has eight nearest Eu neighbors: a hexagonal arrangement of six Eu atoms along with two other Eu atoms perpendicular to this plane. The [AgGe] mixed sites have tricapped trigonal prismatic coordination. The trigonal prism consists of six Eu atoms with the three faces capped with three [AgGe] mixed sites (M_3Eu_6). Though both Eu1 and Eu2 reside in similar coordination environment, the distance between Eu1-*M*1/*M*2/*M*3 (3.3527 (9), 3.2716 (18), 3.3081 (19) Å, respectively) are slightly different from Eu2-*M*1/*M*2/*M*3 (3.3393 (14), 3.3275 (18), 3.3759 (11) Å, respectively). This kind of versatility in bond distances can directly affect the hybridization between the *RE f*-orbital and the *d*-orbital of the transition metal and in turn may give rise to anomalies in magnetic and electronic properties of the intermetallic compound.[27-28]

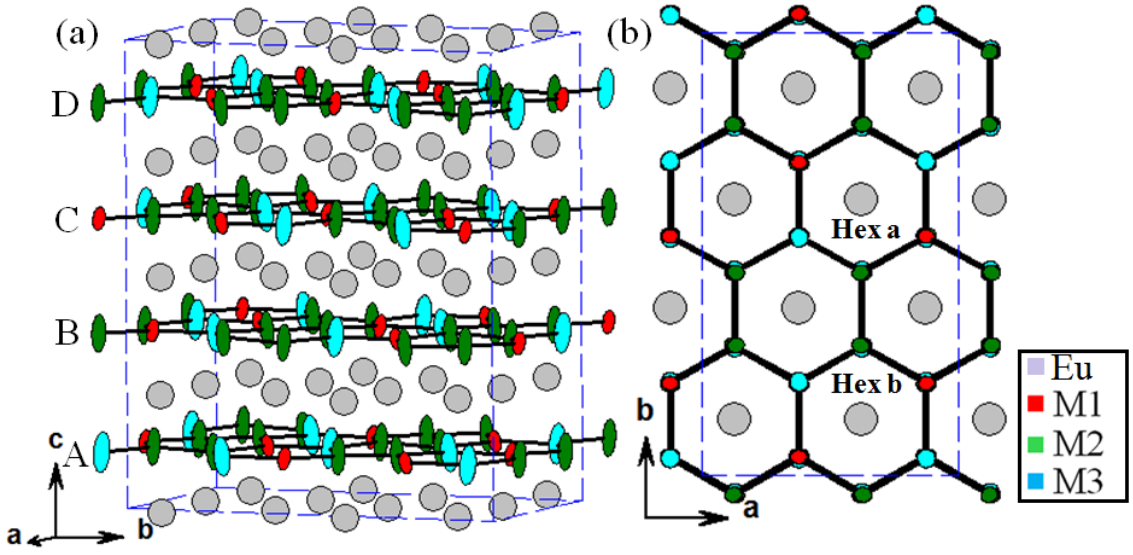

Figure 3.5 Crystal structure of Eu_2AgGe_3 in *Fddd* space group viewed approximately along (a) [100] and (b) [001] directions are shown here in ellipsoid model (Eu sites are kept in spherical model for the sake of simplicity). The three different [AgGe] mixed sites (*M*1, *M*2 and *M*3) are shown in three different color codes. T

Finally, Eu_2AgGe_3 was compared with the equiatomic compound EuAgGe (*P*6/*mmm*).[29] Though both the compounds contain [Ag+Ge] mixed sites, the former is comprised of puckered hexagonal rings whereas the latter contains completely flat rings. This hints toward the fact that d^{10}–d^{10} interactions (which are considered to be important for puckering of hexagonal rings)[1] between the interlayer Ag atoms are dissimilar in these two compounds. Hence with increase in Ge content from EuAgGe to Eu_2AgGe_3, the d^{10}–d^{10} (if any) is somewhat modulated.

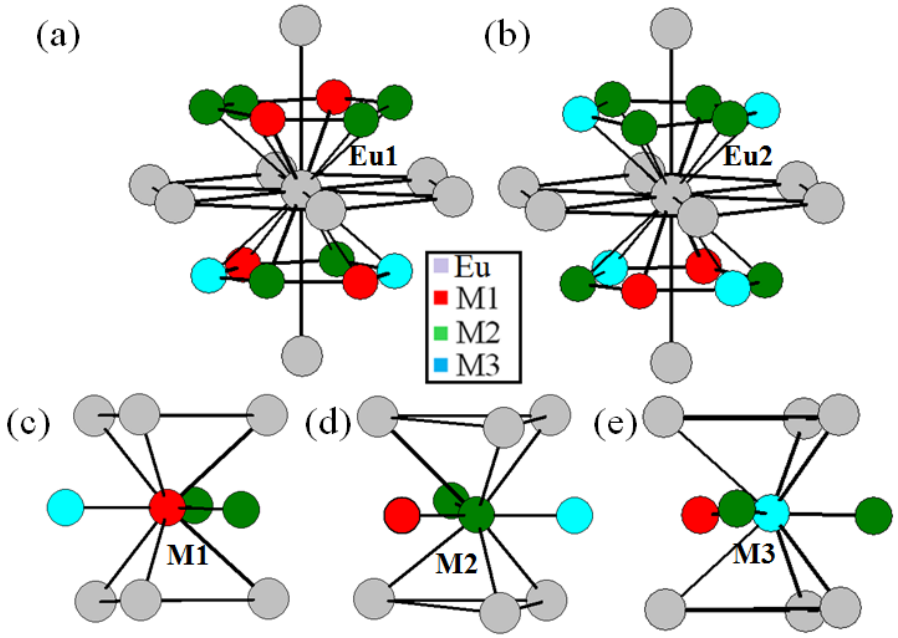

Figure 3.6 Coordination environment of different atoms: (a) Pseudo Frank-Kasper type coordination for Eu1 and (b) Pseudo Frank-Kasper type coordination for Eu2; (c) tricapped trigonal prism type coordination for the mixed positions of Ag and Ge atoms.

3.3.2 Reversible Phase Transition in Eu_2AgGe_3. One can anticipate that the puckered hexagonal rings and valence instability of Eu atoms can influence the structural phase transition in these compounds. In order to find this, temperature dependent PXRD was performed. The comparison of PXRD patterns at temperatures 303 K, 523 K, 723 K and 773 K is shown in **Figure 3.7**. The initial (303 K) pattern corresponds to orthorhombic superstructure of Eu_2AgGe_3 (*Fddd* space group) followed by a phase transition to higher symmetrical hexagonal above 473 K, which was stable up to 723 K. The initial orthorhombic phase reappears at 773 K, which is unusual as with an enhancement in temperature the symmetry of the system is supposed to be increased.

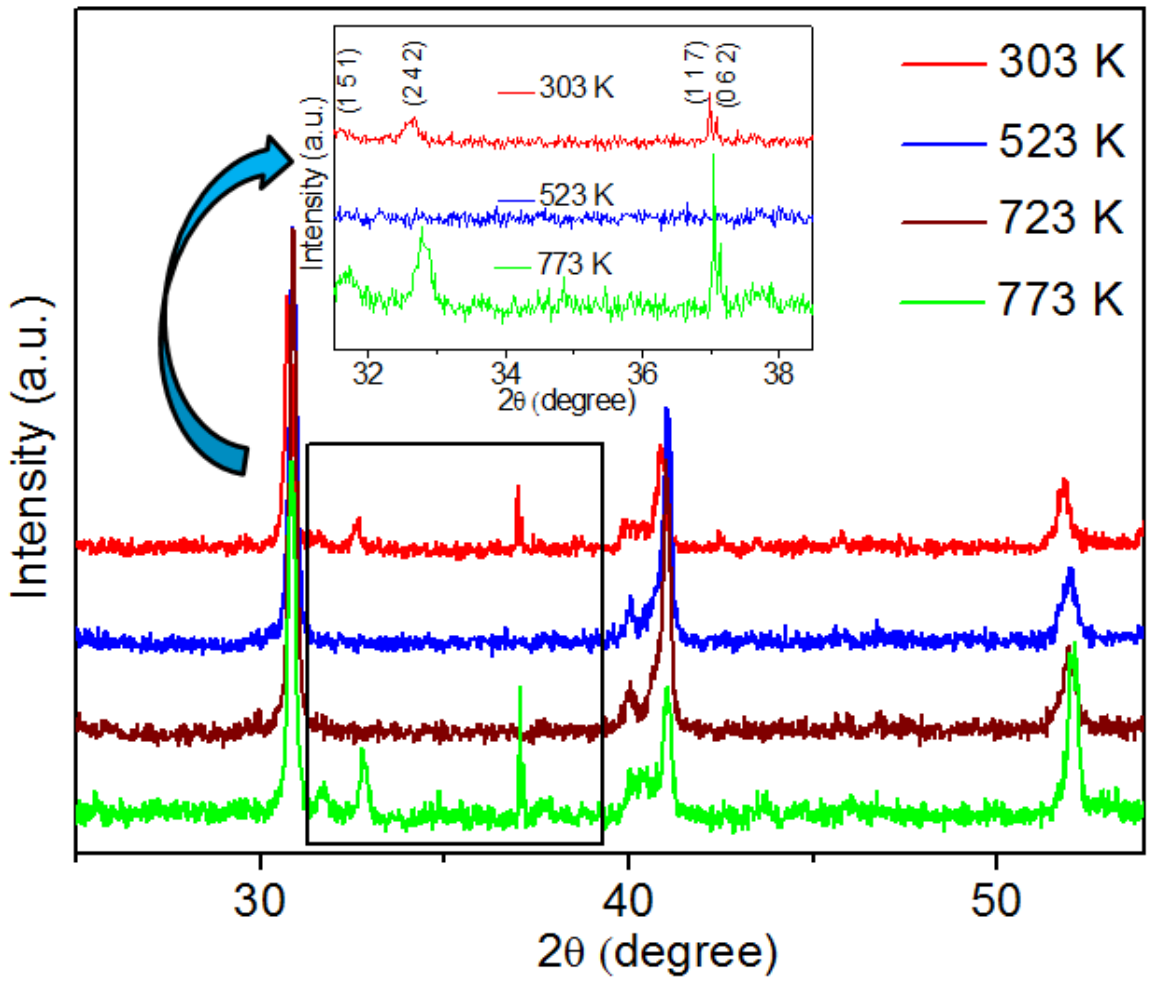

Figure 3.7 Temperature dependent PXRD pattern measured at 303 K, 523 K, 723 K and 773 K. The inset figure shows the expanded ranges of the superstructure peaks observed in the orthorhombic crystal structure and the hkl of four superstructure peaks are marked in the inset figure.

Later, differential thermal analysis (DTA) was performed on the powdered sample of Eu_2AgGe_3 to ascertain the occurrence and exact transition temperature of the phase transitions as observed in the temperature dependent PXRD data. The change in heat flow (in W/g unit) against temperature during both heating and cooling process is shown in **Figure 3.8**. The heating curve shows two consecutive phase transitions at 477 K and 718 K, the first one corresponds to orthorhombic to hexagonal phase and the second one is from hexagonal to orthorhombic phase as observed from the temperature dependent PXRD data (shown as an inset of **Figure 3.8**) whereas there are no hint of other phase transitions during the cooling process indicates that the second phase (orthorhombic) at higher temperature was stable and irreversible in nature.

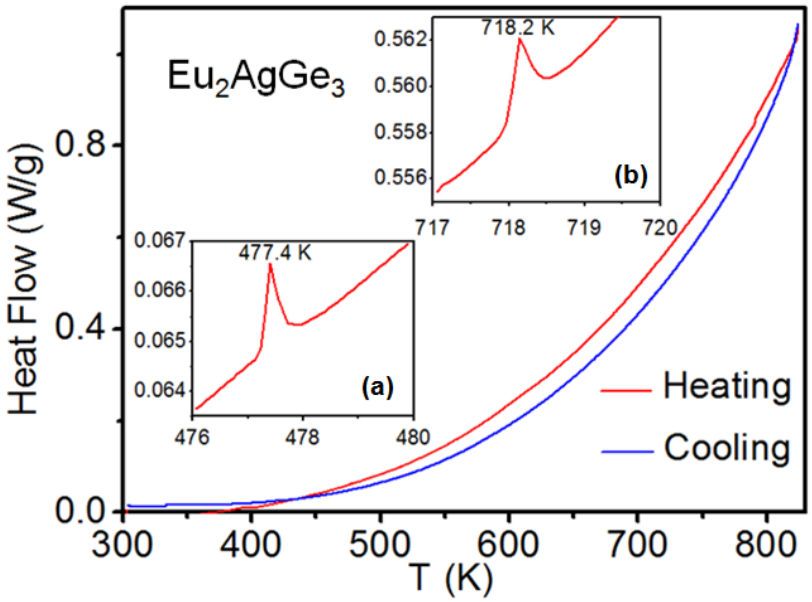

Figure 3.8 Differential scanning calorimetric analysis data plotted as heat change vs. temperature in both heating and cooling mode. Inset (a) shows the first transition at 477 K and inset (b) shows the second broad transition at 718 K.

A displacive phase transition mechanism (**Figure 3.9**) was proposed for this unusual reversible phase transition observed in temperature dependent XRD and DTA studies. At 303 K the hexagonal rings, which are made up of Ag and Ge atoms are puckered as boat shaped and resulted in the orthorhombic crystal system. The extent of puckering is much more at the *M*2 site (32*h* Wyckoff site) compared to other atoms and remained above and below the plane. The two adjacent boat-shaped hexagonal rings (Hex-a and Hex-b) are joined by *M*2-*M*2 bonds. At higher temperature (above 473 K), the *M*2 atoms move alternatively up and down along the *c*-axis and the hexagonal rings become flattened giving rise to planar hexagonal rings. Though the thermal ellipsoids along the *c*-axis (U_{33}) for *M*2 and *M*3 are reasonably large and similar in the *Fddd* refinement (0.43(2) and 0.49(2) $Å^2$, respectively), the higher U_{33} value of *M*2 in *Fmmm* (0.65(2) $Å^2$) compared to *M*3 (0.33(2) $Å^2$) suggests that *M*2 sites are unstable compared to *M*3. It was also noticed that *M*2-*M*2 bonds (2.46 Å) are comparatively more strained than *M*2-*M*3 bonds (2.56 Å). This gives additional indication that the displacive mechanism majorly involves the movement of *M*2 sites along the *c*-axis keeping *M*1 and *M*3 sites intact at their positions. This resulted in addition of symmetries and transformed into more symmetrical hexagonal system (AlB_2 structure type and *P*6/*mmm* space group). As the temperature increased further, the alternate *M*2 positions move further opposite to each other along the *c*-direction or go back to the original position as shown in **Figure 3.9**

resulting in another puckered arrangement of the hexagonal rings which gives rise to second phase transition around 723 K corresponding to the initial orthorhombic phase. This kind of reversible displacive phase transition was never reported in the family of intermetallics, nevertheless it was reported in Ti-Ni based binary[30-31] as well as ternary alloy such as $Ti_{50}Ni_{40}Cu$[32] and the references therein.

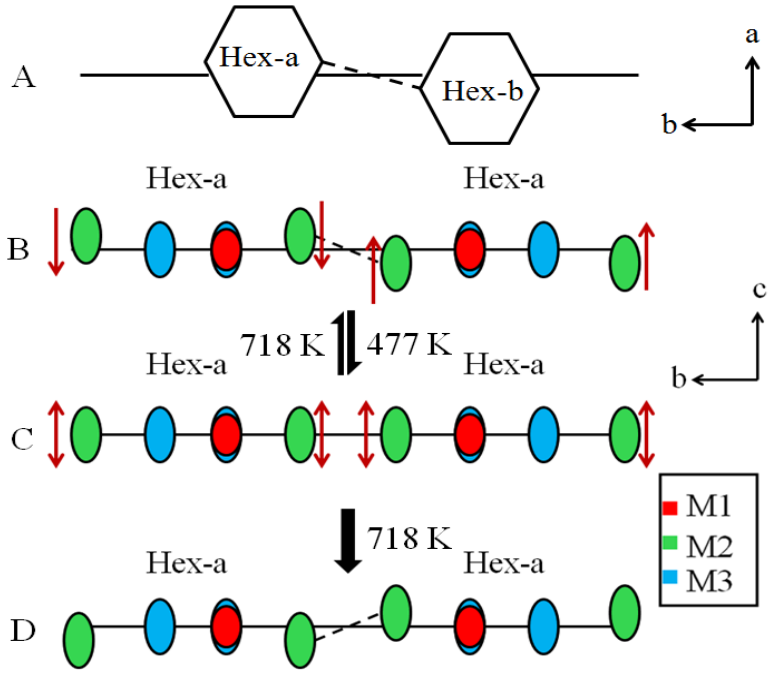

Figure 3.9 Schematic representation of the temperature dependent displacive mechanism for the reversible phase transition in Eu_2AgGe_3.

3.3.3 Magnetic Properties

3.3.3.1 Eu_2CuGe_3

Temperature dependent magnetic susceptibility and inverse susceptibility for the compound Eu_2CuGe_3 is shown in **Figure 3.10a**. Two consecutive magnetic ordering was observed at low temperature: the first transition corresponds to a ferromagnetic ordering around 76 K followed by an antiferromagnetic transition at 17.4 K. Two different kind of magnetic ordering at low temperature was also observed in previously reported Eu_2AuGe_3.[1] The susceptibility curves at FC and ZFC modes were found to diverge from each other around 68 K which is suppressed at higher applied magnetic fields (inset of **Figure 3.10a)**. This may be an indication magnetic frustration in the system and needs further experimental verification. The inverse susceptibility curve was fitted with modified Curie-Weiss law and the effective magnetic moment/Eu (μ_{eff}) was obtained as 7.3 μ_B/Eu atom and Curie paramagnetic temperature (θ_p), 22 K. The magnetic moment

value is slightly lower than the spin only magnetic moment of Eu^{2+} (7.94 μ_B/Eu atom) hinting toward probable presence of mixed valence state of Eu. A sharp peak corresponding to divalent Eu appeared at 6973 eV[10] in the XANES studies (**Figure 3.11a**) on the single crystals of Eu_2CuGe_3 however clearly ruled out any possibility of mixed valence in the system as Eu^{3+} is expected to give a peak at 6987 eV.[10] The highly positive value of θ_p is indicative of strong ferromagnetic coupling between the adjacent Eu spins.

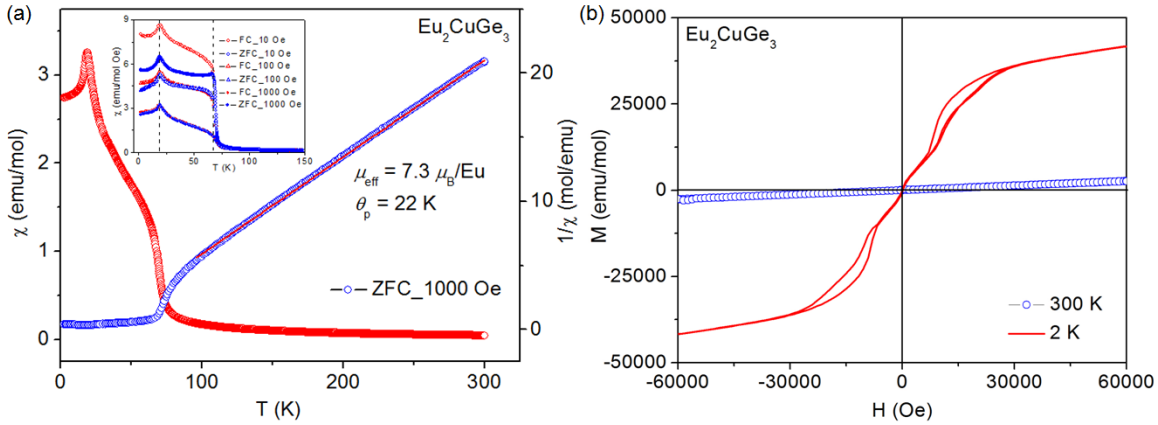

Figure 3.10 (a) Temperature dependent molar magnetic and inverse susceptibilities and (b) field dependence magnetic moment of Eu_2CuGe_3.

The field dependent magnetic susceptibility data at 300 and 2 K are shown in **Figure 3.10b**. At high temperature (300 K) the compound behave as a regular paramagnet whereas at low temperature (2 K) the magnetic moment increases almost monotonously followed by a sudden change in the fields higher than 12 kOe.

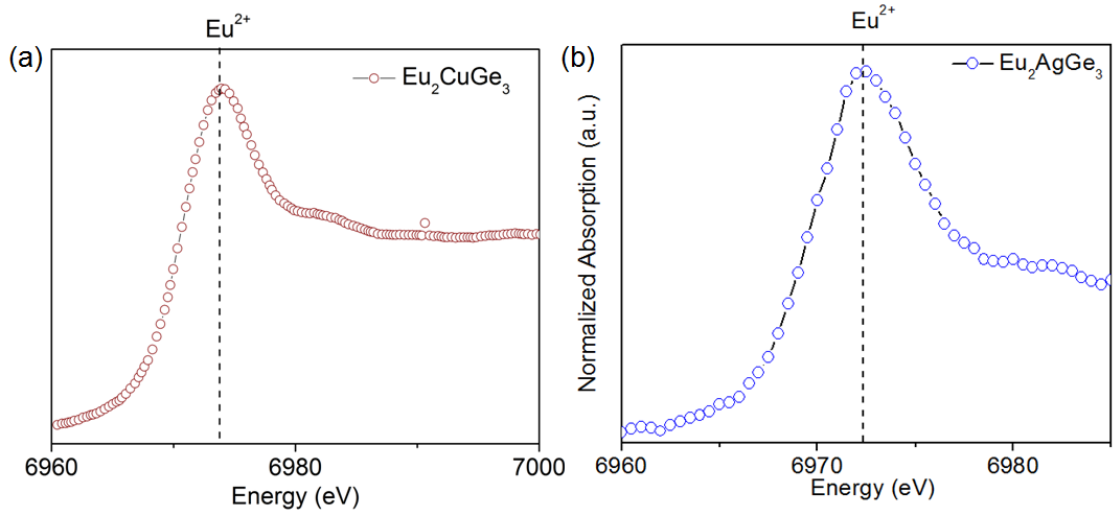

Figure 3.11 Eu L_{III} absorption edge spectra of Eu in (a) Eu_2CuGe_3 and (b) Eu_2AgGe_3 at 300 K.

The weak hysteresis in higher field is indicative of the sudden spin flop transition from the anti ferromagnetic to metamagnetic state.[33]

3.3.3.2 Eu_2AuSi_3

Temperature dependent magnetic susceptibility and inverse susceptibility of Eu_2AuSi_3 at an applied field 1 kOe in both ZFC and FC modes are plotted in **Figure 3.12a**. The magnetic susceptibility sharply increases with decreasing temperature, reaching a maximum at 26 K followed by sharp decrease indicates antiferromagnetic ordering. The two curves in ZFC and FC modes curves do not bifurcate at any point hinting towards absence of any kind of spin-disorder (spin glass behavior).[34] The temperature dependence of inverse magnetic susceptibility curve (**Figure 3.12a**) follows Curie-Weiss law above 30 K. A fit to the curve within the range 30-300 K gave an effective magnetic moment (μ_{eff}) of 8.13 μ_B/Eu, which is close to the spin only magnetic moment of divalent europium (7.94 μ_B/Eu) and paramagnetic Curie temperature (θ_p) 14.6 K. The positive and low value of θ_p indicates an overall weak ferromagnetic interaction present at low temperature. At this point, it is worthwhile to mention that the prototype compound Eu_2AuGe_3 orders antiferromagnetically at 18 K and there is a ferromagnetic clustering at 25 K.[12] Similar coexistence of anti and ferromagnetic interactions is reported in EuSnP which has layered Sn sheets.[35, 36]

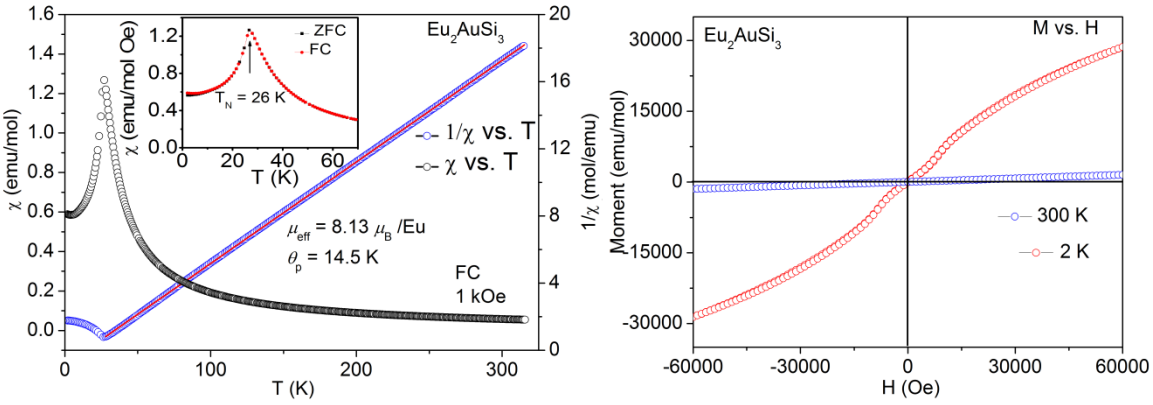

Figure 3.12 (a) Temperature dependent molar magnetic and inverse susceptibilities and (b) field dependence magnetic moment of Eu_2AuSi_3.

The field dependence of magnetization for this compound is shown in **Figure 3.12b**. The low temperature (2 K) curve is sigmoid shaped carrying an overall signature of an antiferromagnetically ordered state. It is to be noted that at the low field (-10 to 10 kOe), the curve is wavy in nature hinting a probable weak metamagnetic transition which

was also observed in case of previously reported Eu_2AuGe_3.[12] The curve shows no sign of saturation up to maximum applied magnetic field 60 kOe.

3.3.3.3 Eu_2AgGe_3

The temperature dependent molar magnetic susceptibility of polycrystalline sample of Eu_2AgGe_3 at an applied field of 1 kOe is shown in **Figure 3.13**. The inverse susceptibility (χ^{-1}) is plotted as a function of temperature, shown in **Figure 3.13a**. The inverse susceptibility curve obeys modified Curie-Weiss law, $\chi = C/(T-\theta_p)$, above 80 K and deviates from linearity below this temperature. A linear fit with the Curie-Weiss law in the temperature range of 80-325 K, gives the value of paramagnetic Curie temperature (θ_p) of 1.8 K and an effective magnetic moment (μ_{eff}) of 7.94 μ_B/Eu ion. The positive sign of θ_p indicates an overall ferromagnetic interaction between the adjacent Eu centers, but the extent of this interaction is very low as evident from the low value of θ_p. The calculated effective magnetic moment/Eu is exactly the same as the spin-only value for a divalent Eu (7.94 μ_B) in the higher temperature range (80-325 K). This is also supported by the adjacent Eu-Eu distance (4.3086 Å to 4.5396 Å) as already discussed in the crystal structure section.

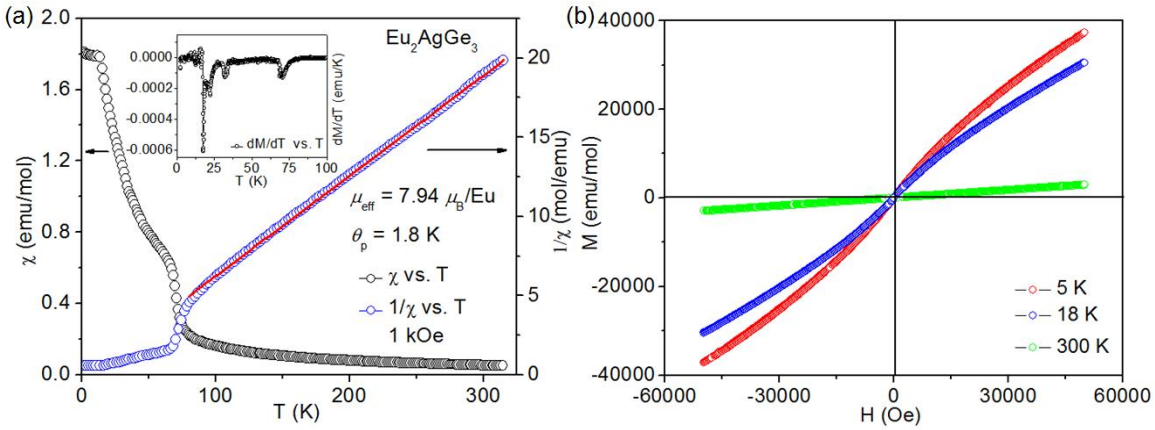

Figure 3.13 (a) The temperature dependence of molar magnetic susceptibility of Eu_2AgGe_3 at 1000 Oe applied magnetic field has been plotted against the temperature on the left hand side; the inset shows plot of derivative of magnetization with temperature.. (b) Variation of magnetization with applied magnetic field for the Eu_2AgGe_3 sample at 5, 18 and 300 K, respectively.

The M vs. H curves at 5, 18 and 300 K temperature are plotted in **Figure 3.13b**. The magnetization does not saturate even at the maximum attainable magnetic field, 55 kOe. This can be attributed to the absence of long range magnetic ordering. The magnetic

moment value decreases with increasing temperature and at room temperature it is around 8.1 μ_B/Eu, which is almost equal to the spin only moment of divalent Eu. Absence of hysteresis in the M vs. H plot proves there is no ferromagnetic interaction in the sample.

XANES is a strong experimental tool in order to firmly establish valence state of an element in a compound. A sharp signal at 6973 eV was observed in the Eu-L_{III} X-ray absorption spectrum of Eu_2AgGe_3 (**Figure 3.11b**). This value is characteristic of the $4f^7$ (Eu^{2+}) configuration and arises due to $2p_{3/2}$ to $5d$ transition.[37-38] The main signal observed for the reference Eu_2O_3 (electronic configuration $4f^6$, Eu^{3+}) is approximately located around 6984 eV.[39-40] Absence of any broad shoulder around this value eliminates the possibility of mixed or intermediate valency for Eu and thus Eu_2AgGe_3 solely contains Eu^{2+} as an active valence state.

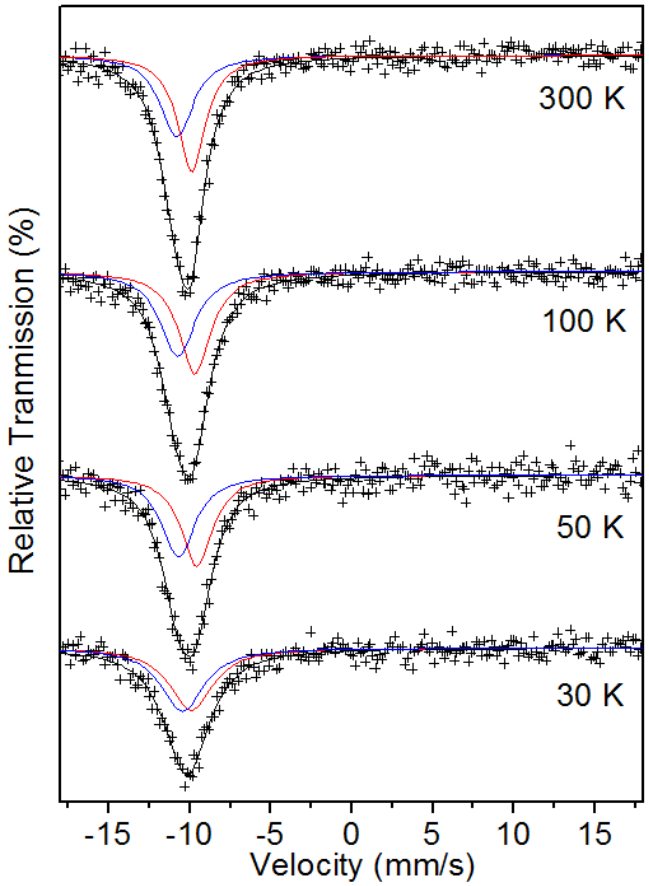

Figure 3.14 Experimental and simulated ^{151}Eu Mössbauer spectra of Eu_2AgGe_3 at temperature range 30-300 K.

To further support the magnetic susceptibility and XANES data and to get an idea about the local environment of the Eu atoms in this compound, ^{151}Eu Mössbauer spectroscopy was performed on Eu_2AgGe_3 samples at 30, 50, 100 and 300 K (**Figure 3.14**).

The data was fitted using Lorentzian model (Area Equal method)[41] and the fitting parameters are shown in the **Table 3.5**. The average isomer shift at 303 K in Eu_2AgGe_3 (-10.34 mm s^{-1}) is slightly higher than Eu_2AuGe_3 (-10.93 mm s^{-1}) and EuAgGe (-10.63 mm s^{-1})[41] indicating slightly lower ionicity (i.e. higher *s* electron density). In all measured temperature the spectra observed as single signal around -10 mm s^{-1}indicates the presence of pure divalent Eu further confirms the magnetic measurements data. A fit to this signal shows the presence of two equivalent Eu^{2+} atoms in 1:1 ratio clearly corroborating the crystallographic studies.

Table 3.5 Fitting parameters of ^{151}Eu Mossbauer spectroscopic measurements of Eu_2AgGe_3

Temp (K)	Isomer shift (mm s^{-1})	FWHM (mm s^{-1})	Area (%)	χ^2
300	-10.8 ±0.06	2.47 ±0.17	50	0.80
	-9.87 ±0.05	2.06 ±0.08	50	
100	-10.74 ±0.05	2.63 ±0.14	50	1.09
	-9.68 ±0.05	2.39 ±0.10	50	
50	-10.44 ±0.30	3.20 ±0.54	50	0.89
	-9.56 ±0.07	2.39 ±0.16	50	
30	-10.8 ±0.06	2.47 ±0.17	50	0.90
	-9.90 ±0.31	3.22 ±0.45	50	

3.4.3 Resistivity

Eu_2CuGe_3. The temperature dependent resistivity plot for Eu_2CuGe_3 has been shown in **Figure 3.15**. In the high temperature regime the resistivity increases almost linearly with increasing temperature indicating metallic behaviour. Deviation from this trend is observed below 75 K below which resistivity starts increasing with decreasing temperature following a broad dip. This could arise due to scattering of conduction electrons by magnetic spins.[42] This phenomenon makes this compound an interesting candidate for magnetoresistance study, which will be performed in near future. A sharp peak exact at 17.4 K clearly indicates antiferromagnetic transitions. The first order derivative curve shown in the inset pinpoints the transition temperatures to 33.3 and 17.4 K corresponding to ferromagnetic cluster glass transition and antiferromagnetic transitions respectively, corroborate very well to the magnetic susceptibility data on this compound.

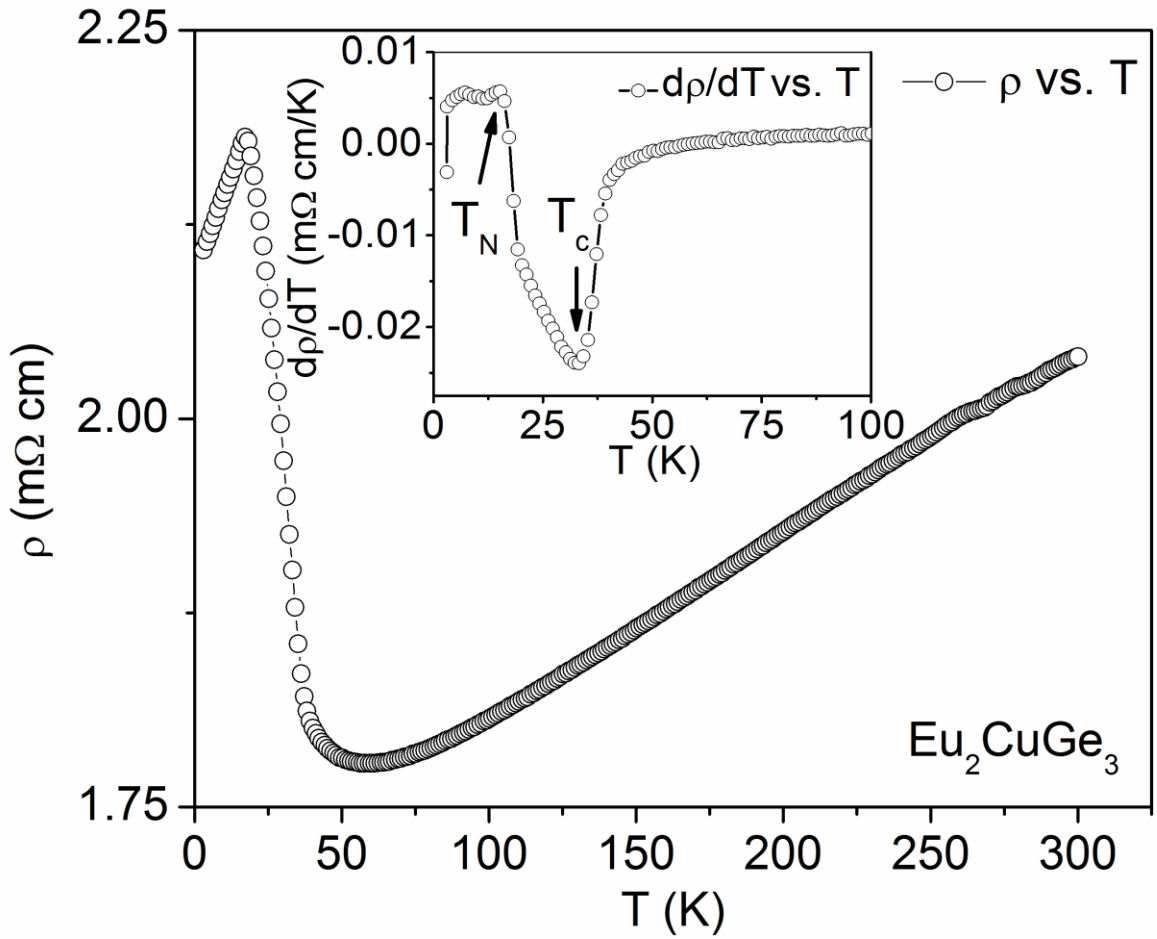

Figure 3.15 Temperature dependence of electrical resistivity for the Eu_2CuGe_3 sample; inset shows the derivative, dρ/dT vs. temperature plot.

Eu_2AgGe_3. The temperature dependent electrical resistivity of the Eu_2AgGe_3 sample in the temperature range 2-300 K is shown in **Figure 3.16a**. In the low temperature range, the resistivity increases sharply with temperature then slowly decreases with a maximum at 12.2 K. In order to see this anomaly, the first order derivative of electrical resistivity with temperature is shown in **Figure 3.16b**. The sharp peak observed at 12.2 K can be designate as the positive Temperature Coefficient of Electrical resistivity (TCE) was attributed to the magnetic transition and metal like behavior at low temperature.[43-44] Another slope change observed above 266 K in which the TCE was found to be negative (**Figure 3.16c**) can be either due to the possible single ion Kondo effect[45] or the onset of a pseudogap.[46]

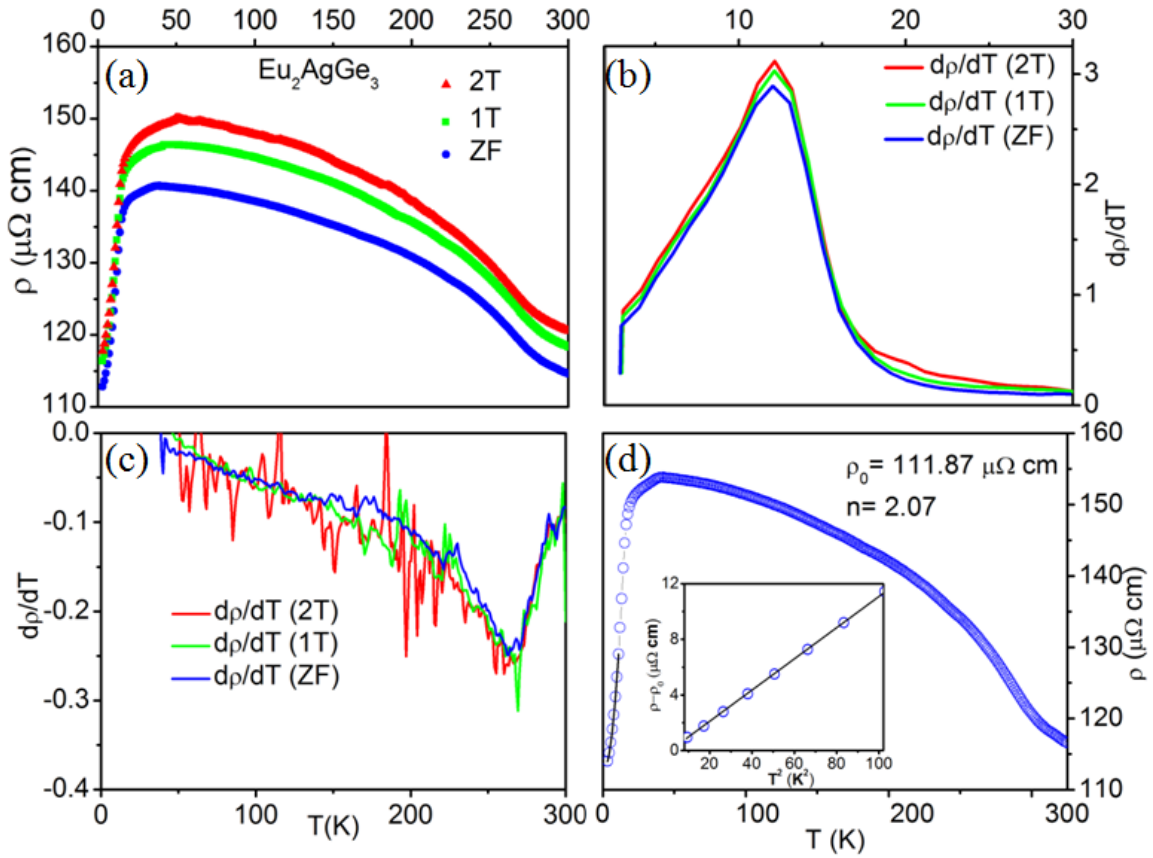

Figure 3.16 (a) The temperature dependence of electrical resistivity for the Eu_2AgGe_3 sample at zero field, 1T and 2T; The derivative spectrum dρ/dT Vs temperature shows (b) a maxima around 12.2 K and (c) minima at 266 K. (d) The ρ vs. T at zero filed is fitted to the Power law and the inset figure shows (ρ-ρ_0) vs. T^2 plot.

At low temperatures in the range of 2.5−9.5 K, the ρ(T) data can be fitted to the power law function, $\rho = \rho_0 + AT^n$, where ρ_0 is the residual resistivity expressed in units of Ω cm and A and n are the fitting parameters.[47] The values obtained from the fit are shown in **Figure 3.16d**. According to Fermi-liquid theory, at low temperatures, the resistivity varies as $\rho = \rho_0 + AT^2$.[48] Experimentally, it has been observed that when electron−electron scattering dominates over electron−phonon scattering, ρ α T^2.[49] The value of n (2.07) obtained from the fit power is close to 2, which is the case for systems exhibiting a Fermi liquid state.[50-51] To further prove the Fermi liquid state (ρ-ρ_0)europi vs. T^2 (shown in inset of **Figure 3.16d**) was plotted and the curve was found to be linear in the temperature range 2.5 to 9.5 K. This strongly established the fact that the ground state is of Fermi liquid nature at low temperature.

3.4 Concluding Remarks

Three new europium containing compounds, Eu_2CuGe_3, Eu_2AuSi_3 and Eu_2AgGe_3 were discovered in the family of AlB_2 type. This work exemplifies both the advantages and limitations of exploratory synthesis by metal flux method where the first two compounds formed easily in melted indium with high degree of reproducibility, whereas the other one did not form in any kind of metal flux attempted. It further stresses on the importance of puckering of the hexagonal rings by the transition and *p*-block metals leading to diverse crystal structure in the two title compounds. A reversible structural transition was observed in case of Eu_2AgGe_3. This compound is in fact the first intermetallic compound which shows the reversible phase transitions. A plausible mechanism was proposed in terms of the displacive transition mechanism of Ag and Ge atoms in the hexagon layers. These observations open up the possibility to study the phase transition in all compounds crystallizing in the AlB_2 family. It would be reasonable to speculate that both size and electronegativity difference play crucial roles in the different ordering of Cu/Ag/Au.

3.5 References

1. Peter, S. C.; Malliakas, C. D.; Chondroudi, M.; Schellenberg, I.; Rayaprol, S.; Hoffmann, R. D.; Pöttgen, R.; Kanatzidis, M. G., *Inorg. Chem.* **2010,** *49*, 9574-9580.

2. Rhyee, J.-S.; Cho, B. K.; Ri, H. C., *J. Appl. Phys.* **2003,** *93* (10), 8346-8348.

3. Hossain, Z.; Geibel, C.; Senthilkumaran, N.; Deppe, M.; Baenitz, M.; Schiller, F.; Molodtsov, S. L., *Phys. Rev. B* **2004,** *69* (1).

4. Paschen, S.; Baenitz, M.; Tran, V. H.; Rabis, A.; Steglich, F.; Carrillo-Cabrera, W.; Grin, Y.; Strydom, A. M.; du Plessis, P. d. V., *J. Phys. Chem. Solids* **2002,** *63* (6–8), 1183-1188.

5. Feng, C. M.; Ren, Z.; Xu, S. G.; Jiang, S. A.; Xu, Z. A.; Cao, G. H.; Nowik, I.; Felner, I.; Matsubayashi, K.; Uwatoko, Y., *Phys. Rev. B* **2010,** *82* (9).

6. Danzenbacher, S.; Vyalikh, D. V.; Kucherenko, Y.; Kade, A.; Laubschat, C.; Caroca-Canales, N.; Krellner, C.; Geibel, C.; Fedorov, A. V.; Dessau, D. S.; Follath, R.; Eberhardt, W.; Molodtsov, S. L., *Phys. Rev. Lett.* **2009,** *102* (2).

7. Wang, J.; Xia, S.-Q.; Tao, X.-T., *Inorg. Chem.* **2012,** *51* (10), 5771-5778.

8. Zhang, H.; Baitinger, M.; Tang, M.-B.; Man, Z.-Y.; Chen, H.-H.; Yang, X.-X.; Liu, Y.; Chen, L.; Grin, Y.; Zhao, J.-T., *Dalton Trans.* **2010,** *39* (4), 1101-1104.

9. Sarkar, S.; Gutmann, M. J.; Peter, S. C., *CrystEngComm.*, **2013**, *15*, 8006-8013.

10. Sarkar, S.; Peter, S. C., *Inorg. Chem.* **2013,** *52* (17), 9741-9748..

11. Peter, S. C.; Sarkar, S.; Kanatzidis, M. G., *Inorg. Chem.* **2012,** *51*, 10793-10799.

12. Peter, S. C.; Malliakas, C. D.; Chondroudi, M.; Schellenberg, I.; Rayaprol, S.; Hoffmann, R. D.; Pottgen, R.; Kanatzidis, M. G., *Inorg. Chem* .**2010,** *49* (20), 9574-9580.

13. Pagliuso, P. G.; Sarrao, J. L.; Thompson, J. D.; Hundley, M. F.; Sercheli, M. S.; Urbano, R. R.; Rettori, C.; Fisk, Z.; Oseroff, S. B., *Phys. Rev. B* **2001,** *63* (9).

14. Takigawa, Y.; Noguchi, S.; Okuda, K., X, *J. Magn. Magn. Mater.* **1988,** *76-7*, 345-346.

15. Bobev, S.; Bauer, E. D.; Thompson, J. D.; Sarrao, J. L.; Miller, G. J.; Eck, B.; Dronskowski, R., *J. Solid State Chem.* **2004,** *177* (10), 3545-3552.

16. Peter, S. C.; Sarkar, S.; Kanatzidis, M. G., *Inorg. Chem.* **2012,** *51* (20), 10793-10799.

17. Abicht, H.-P.; Hönle, W.; von Schnering, H. G., *Z. Anorg. Allg. Chem.* **1984,** *519*, 7–23.

18. Merlo, F.; Pani, M.; Canepa, F.; Fornasini, M. L., *J. Alloys Compd.* **1996,** *232*, 289-295.

19. Pöttgen, R. Z., *Naturforsch. B* **1995,** *50*, 1071-1074.

20. Schnering, H. G. V.; Bolle, U.; Curda, J.; Peters, K.; Carrillo-Cabrera, W.; Somer, M.; Schultheiss, M.; Wedig, U., *Angew. Chem. Int. Ed.* **1996,** *35*, 984-986.

21. Bobev, S.; Bauer, E. D.; Thompson, J. D.; Sarrao, J. L.; Miller, G. J.; Eck, B.; Dronskowski, R., *J. Solid State Chem.* **2004,** *177*, 3545–3552.

22. Pagliuso, P. G.; Sarrao, J. L.; Thompson, J. D.; Hundley, M. F., *Phys. Rev. B* **2001,** *63*, 092406.

23. Takigawa, Y.; Noguchi, S.; Okuda, K., *J. Magn. Magn. Mater.* **1988,** *76–77*, 345–346.

24. Pandey, A.; Mazumdar, C.; Ranganathan, R., *J. Phys.: Condens. Matter.* **2009,** *21*, 216002.

25. Emsley, J., *The Elements*. Clarendon Press: Oxford, 1989.

26. Donohue, J., *The Structures of the Elements*. Wiley: New York, 1974.

27. Chevalier, B.; Pöttgen, R.; Darriet, B.; Gravereau, P.; Etourneau, J. R., *J. Alloys Compd.* **1996,** *233*, 150-160.

28. Endstra, T.; Nieuwenhuys, G. J.; Mydosh, J. A., *Phys. Rev. B* **1993,** *48*, 9595-9605.

29. Belan, B. D.; Soroka, I. N.; Kryvulya, L. V.; Bodak, O. I.; Protsyk, O. S., *Visn. L'viv. Derzh. Univ. (Ser. Khim.)* **1999,** *38*, 54-57.

30. Morawiec, H.; Stróż, D.; Goryczka, T.; Chrobak, D., *Script. Mat.* **1996,** *35*, 485-490.

31. Ren, X.; Miura, N.; Zhang, J.; Otsuka, K.; Tanaka, K.; Koiwa, K.; Suzuki, T.; Chumlyakov, Y. I.; Asai, M., *Mater. Sci. Eng. A* **2001,** *312*, 196-206.

32. Ren, X.; Miura, N.; Otsuka, K.; Suzuki, T.; Tanaka, K.; Chumlyakov, Y. I.; Asai, M., *Mater. Sci. Eng. A* **1999,** *273–275*, 190-194.

33. Sarkar, S.; Subbarao, U.; Joseph, B.; Peter, S. C., *J. Solid State Chem.* **2015,** *225*, 181-186.

34. Majumdar, S.; Sampathkumaran, E. V., *Solid State Commun.* **2001,** *117* (11), 645-648.

35. A. C. Payne; A. E. Sprauve; A. P. Holm; M. M. Olmstead; S. M. Kauzlarich; Klavins, P., *J. Solid State Chem.* **2002,** *338*, 229-234.

36. T. Fujiwara; Y. Saiga; T. J. Sato; M. Hedo; Uwatoko, Y., *Physica B: Condens. Matter* **2006,** *378-380*, 1122-1123.

37. Inoue, T.; Kubozono, Y.; Kashino, S.; Takabayashi, Y.; Fujitaka, K.; Hida, M.; Inoue, M.; Kanbara, T.; Emura, S.; Uruga, T., *Chem. Phys. Lett.* **2000,** *316*, 381–386.

38. Kim, K.-B.; Koo, K.-W.; Cho, T.-Y.; Chun, H.-G., *Mat. Chem. Phys.* **2003,** *80*, 682–689.

39. Kim, K.-B.; Kim, Y. I.; Chun, H.-G.; Cho, T.-Y.; Jung, J.-S.; Kang, J. G., *Chem. Mater.* **2002,** *14*, 5045-5052.

40. Oshio, S.; Matsuoka, T.; Tanaka, S.; Kobayashi, H., *J. Electrochem. Soc.* **1998,** *145*, 3903-3907.

41. Müllmann, R.; Mosel, B. D.; Eckert, H.; Pöttgen, R.; Kremer, R. K., *Hyperfine Interact.* **1997,** *108*, 389-400.

42. Yamada, H.; Takada, S., *Prog. Theo. Phys.* **1973,** *49*, 1401-1419.

43. Kayamiwa, N., *Phys. Rev. B* **1991,** *44*.

44. Matsuoka, T.; Shimizu, K., *Nature* **2009,** *458*, 186-189.

45. Sengupta, K.; Sampathkumaran, E. V.; Nakano, T.; Hedo, M.; Abliz, M.; Fujiwara, N.; Uwatoko, Y.; Rayaprol, S.; Shigetoh, T.; Takabatake, K.; Doert, T.; Jemetio, J. P. F., *Phys. Rev. B* **2004,** *70*, 064406.

46. Sampathkumaran, E. V.; Ekino, T.; Ribeiro, R. A.; Sengupta, K.; Nakano, T.; Hedo, M.; Fujiwara, N.; Abliz, M.; Uwatoko, Y.; Rayaprol, S.; Doert, T.; Jemetio, J. P. F., *Physica B* **2005,** *359– 361*, 108–110.

47. Kambe, S.; Suderow, H.; Fukuhara, T.; Flouquet, J.; Takimoto, T., *J. Low Temp. Phys.* **1999,** *117*, 101-112.

48. Coleman, P., *Introduction to Many Body Physics*. Rutgers University Press: Rutgers, 2004.

49. Li, S. Y.; Taillefer, L.; Hawthorn, D. G.; Tanatar, M. A.; Paglione, J.; Sutherland, M.; Hill, R. W.; Wang, C. H.; Chen, X. H., *Phys. Rev. Lett.* **2004,** *93*, 056401.

50. Varma, C. M., *Rev. Mod. Phys.* **1976,** *48*, 219.

51. Peter, S. C.; Malliakas, C. D.; Nakkotte, H.; Kothapilli, K.; Rayaprol, S.; Schultz, A. J.; Kanatzidis, M. G., *J. Solid State Chem.* **2012,** *187*, 200-207.

Chapter 4

Yb_2TX_3 - Ordered Yb Based Superstructure Derivatives of AlB_2 Prototype and Their Physical Properties

4.1 Introduction

Yb forms a wide variety of binary, ternary as well as quaternary intermetallic compounds. Yb containing compounds have particular scientific interest because they can exhibit two energetically similar electronic configurations: the magnetic Yb^{3+} ($4f^{13}$) and the nonmagnetic Yb^{2+} ($4f^{14}$) one.[1] In this case, the roles of the 4*f* electron and 4*f* hole can be interchanged, and may give rise to interesting phenomena, e.g. $YbFe_4Sb_{12}$ shows intermediate valence state.[2] Some of the compounds are potential candidates for thermoelectric applications due to high Seebeck coefficient and low thermal conductivity, e.g. $YbMn_2Sb_2$ and $YbZn_2Sb_2$ and their substituted variants have large values of figure of merit *ZT* at high temperatures.[3] Kondo effect or heavy-fermion behavior and even structural transformation are also observed.[4-9] $YbRh_2Si_2$ is a classical example of Yb-based intermetallic with mixed valent Yb.[5, 10] This chapter deals with the investigation of three new Yb based RE_2TX_3 compounds. These intermetallics are also derived from the prototype AlB_2 structure by Bärnighausen formalism applying three different types of symmetry operations.[11-12]

Synthesis of single crystalline Yb_2CuGe_3, Yb_2AuSi_3 and Yb_2AuGe_3 were targeted using indium as the metal flux,[13-17] in the context of our previous work on Yb intermetallics.[4, 18-30] Although attempts to synthesize the first compound were unsuccessful leading to other phases like $YbCu_2Ge_2$, $Yb_3Cu_4Ge_4$ and Yb_2CuGe_6 which are already well studied, large single crystals of Yb_2AuSi_3 and Yb_2AuGe_3 were successfully obtained. Yb_2AuSi_3 crystallizes in orthorhombic *Fddd* space group and is a diamagnet without any ordering down to 2 K. Yb_2AuGe_3 shows a phase transition at higher temperature as observed in temperature dependent powder XRD studies. It is worthwhile to mention in this context that reports in this series containing gold as a transition metal are also rare apart from our recent report on Eu_2AuGe_3.[20] Our magnetic measurements suggest that Yb_2AuGe_3 has Yb atoms in a mixed valent state and the material is metallic while temperature dependent electrical resistivity measurements at low temperature indicate possible Fermi-liquid behavior. Finally, heat capacity data suggest moderate heavy fermion behavior for Yb_2AuGe_3.

4.2 Experimental Section

4.2.1 Synthesis

4.2.1.1 Chemicals

The following reagents were used as purchased without further purification: Yb, (in the form of metal pieces cut from metal chunk, 99.9%, Alfa Aesar), copper (beads, 99.99%, Alfa Aesar), gold (pieces, 99.99%, Alfa Aesar), silicon (shots, 99.999%, Alfa Aesar), Ge (ground from metal pieces, 99.999%, Alfa Aesar), and In (tear drops, 99.99%, Alfa Aesar).

4.2.1.2 Metal Flux Method

Single crystals of Yb_2AuSi_3 and Yb_2AuGe_3 were obtained by combining 3 mmol of the ytterbium metal, 2 mmol of gold, 6 mmol of silicon/germanium, and 45 mmol of indium in an alumina (Al_2O_3) crucible under an inert (argon) atmosphere inside a glove box. The crucible was placed in a 13 mm quartz tube and was flame-sealed under vacuum of 10^{-3} torr, to prevent oxidation during heating. The tube was then placed in a vertically aligned tube furnace and heated to 1273 K over the period of 10 h, maintained at that temperature for 5 h to allow proper homogenization, followed by cooling to 1123 K in 2 h, and held at that temperature for 48 h. Finally, the system was allowed to cool slowly to room temperature in 48 h. The reaction product was isolated from the excess In flux by heating at 623 K and subsequent centrifugation through a coarse frit. Any remaining flux was removed by immersion and sonication in glacial acetic acid for 24 h. The final crystalline product was rinsed with water and dried with acetone in a vacuum oven at 350 K overnight. This method produced the target compounds with high yield of ~95% on the basis of the initial amount of Yb metal used in the reaction.

There were no other binary or ternary side products found and the only impurities detectable in the powder XRD pattern were minute amount of (<2% of the overall product obtained) unreacted Ge and In used in excess for the flux method which was quite unavoidable). Yb_2AuSi_3 single crystals were highly air-sensitive and brittle in nature and hence were stored in argon filled glove box. Yb_2AuGe_3 crystals were stable in air and moisture with no decomposition observed even after several months. Several crystals, which grew as metallic silver rods with average size of 5-6 mm, were carefully selected for elemental analysis, structure characterization, and the physical measurements reported

in this article. This method was well reproducible under the same experimental conditions. Similar synthetic trial with Yb_2CuGe_3 did not yield the desired phase.

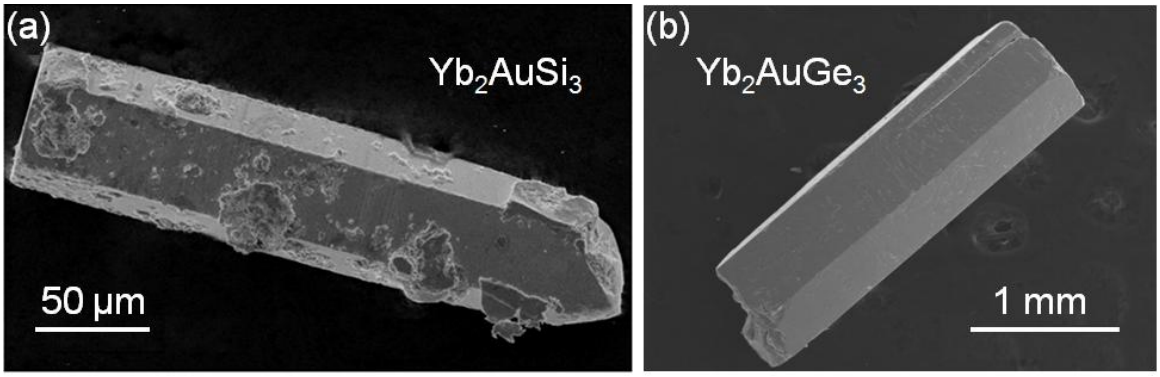

Figure 4.1 SEM image of a single crystal of (a) Yb_2AuSi_3 and (b) Yb_2AuGe_3 grown from In metal flux.

4.2.1.2 High frequency induction heating method

Ytterbium, copper/gold and silicon/germanium were mixed in the ideal 2:1:3 stoichiometric ratios and sealed in tantalum ampoules under an argon atmosphere in an arc-melting apparatus. The tantalum ampoules were subsequently placed in a water-cooled sample chamber of an induction furnace (EasyHeat induction heating system, Model 7590), first rapidly heated to ca. 1250 K and kept at that temperature for 10 min. Finally, the temperature was lowered to 1000 K and the sample was annealed at that temperature for another 30 min, followed by quenching by switching off the power supply. The brittle product could easily be separated from the tantalum tube. No reaction with the container was observed. The obtained compound was pure up to the level of powder XRD.

4.2.3 PXRD

To determine the phase identity and purity of all the three compounds, PXRD data were collected at room temperature on a Bruker D8 Discover X-ray diffractometer with Cu K_α X-ray source (λ = 1.5406 Å), equipped with a position sensitive detector, and were compared to the pattern calculated from the single crystal structure refinement. The comparison of the powder patterns with the corresponding the simulated patterns have been shown in **Figure 4.2a, b** and **c** respectively for Yb_2CuGe_3, Yb_2AuSi_3 and Yb_2AuGe_3. Temperature dependent powder XRD data were collected in the same instrument under

vacuum condition (10^{-6} torr pressure) on a tantalum plate in the temperature range 303-1073 K (both heating and cooling).

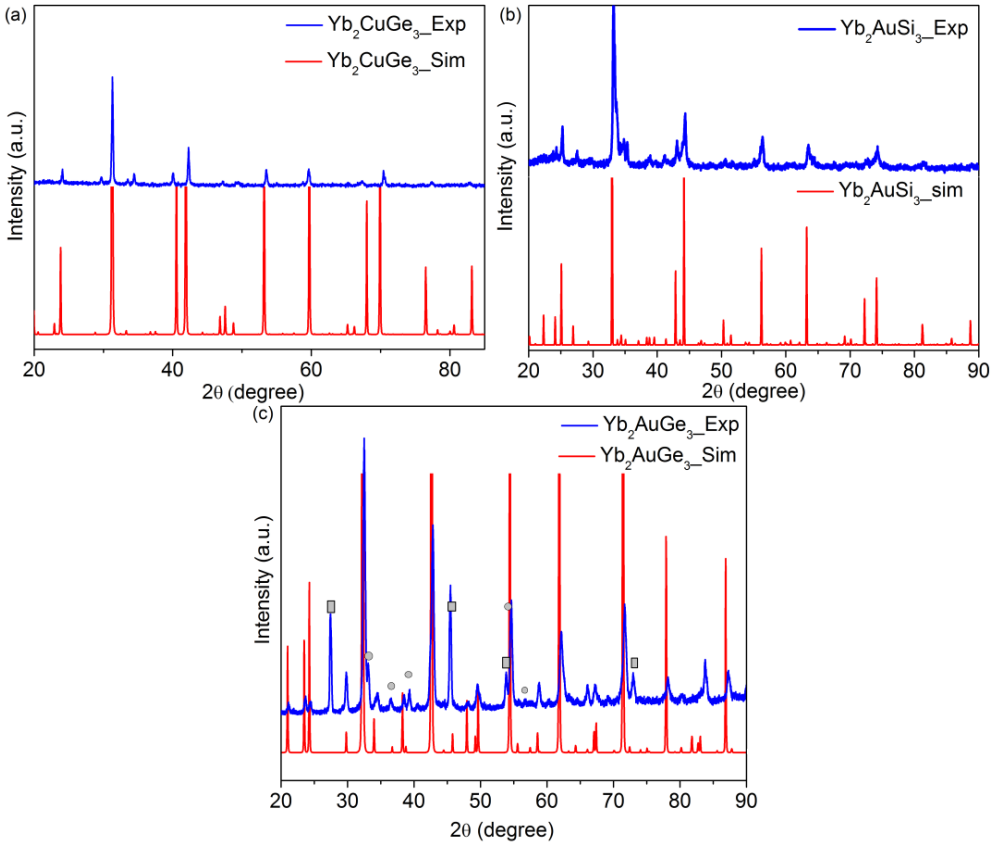

Figure 4.2 Comparison of PXRD pattern of polycrystalline sample of (a) Yb_2CuGe_3, (b) Yb_2AuSi_3 and (c) Yb_2AuGe_3 with that of simulated pattern obtained from the data of XRD on single crystal, the unreacted Ge (cubic, $Fd\bar{3}m$ space group) and In (tetragonal, *I*4/*mmm* space group) peaks are shown by rectangular and circular mark-ups, respectively. The remaining peaks correspond to superstructure diffractions.

4.2.4 Single Crystal XRD

The XRD data of Yb_2AuSi_3 and Yb_2AuGe_3 were collected on a selected single crystal at room temperature using a Bruker Smart Apex II CCD diffractometer equipped with a normal focus, 2.4 kW sealed tube X-ray source with graphite monochromatic Mo$K\alpha$ radiation (λ = 0.71073 Å) operating at 50 kV and 30 mA, with ω scan mode.[31] Semi empirical method was used for the data extraction and integration and to apply absorption corrections. The room temperature data set of Yb_2AuGe_3 was compatible with space group *Fmmm*. The atomic parameters of Ca_2AgSi_3 were then taken as starting values and the structure was refined with SHELXL–97 (full-matrix least-squares on F^2)[32] with anisotropic atomic displacement parameters for all atoms.

4.2.5 Structure Refinement

4.2.5.1 Yb_2AuSi_3

The data for Yb_2AuSi_3 suggested an *F*-centered orthorhombic lattice with lattice parameters a = 8.1886(3) Å, b = 14.1771(5) Å and c = 16.8218(6) Å. The atomic coordinates of the Ba_2LiSi_3 structure type were used as a starting model for the refinement. The preliminary isotropic refinement in least square method with 10 cycles yielded very high residuals ($R1$> 11%) and electron density residuals also very high (> 80 eÅ^3). Anisotropic refinement could not solve the problems of high residuals. In the next step Au and Si positions were mixed as similar to Eu_2AgGe_3 and refined the structure with a reasonable residual parameters.

4.2.5.2 Yb_2AuGe_3

The single crystal data of Yb_2AuGe_3 showed an orthorhombic cell and the systematic extinctions were compatible with the space group *Fmmm*. The Ca_2AgSi_3 structure type,[33] a superstructure of AlB_2 type was already evident from the powder XRD data. The atomic parameters of Ca_2AgSi_3 were taken as starting parameters and the structure was refined using SHELXL-97 (full-matrix least-squares on F^2)[32] with anisotropic atomic displacement parameters for all atoms. As a check for the correct composition, the occupancy parameters were refined in a separate series of least-squares cycles. Initially, there were five crystallographically different positions in the Yb_2AuGe_3 structure - two for each Yb and Ge atoms and one for the Au atom. During isotropic refinement it was observed that the atomic displacement parameters of the gold and germanium atoms were anomalously large. Furthermore, the refinement was largely unsatisfactory giving relatively high residuals (R_1 > 12%), and large electron density residuals (19-20 eÅ^{-3}) around the gold and germanium atoms. Anisotropic refinement did not improve the refinement and also resulted in abnormal cigar-shaped gold and germanium atomic displacement ellipsoids (U_{22} = 0.50 Å^2). The anomalous atomic displacement parameter could not be resolved by subsequent refinement of the occupancy parameters. All these features indicated a crystallographic disorder associated with the Ge and Au atoms. Consequently, gold and germanium atoms were refined by mixing germanium and gold, respectively which makes the compound slightly of different stochiometry. Au/Ge mixing was previously reported on a NaAuGe,[34] EuAuGe[35-36] and a large family of compounds-*RE*AuGe (*RE* = Sc, Y, La-Nd, Sm, Gd-Lu).[37-40] The resulting atomic displacement

parameters of mixed position became well-behaved and the final difference maps showed residuals that were reasonably acceptable. Relatively large displacement parameters of *M*2 and *M*3 positions along the *c*-axis indicates a further symmetry reduction at low temperature similar to our previous report on Eu_2AuGe_3.[20] However, it was not observed in the single crystal data obtained at lowest temperature and no hint from the physical properties (discussed below) as was observed in Eu_2AuGe_3 compounds. Nevertheless, when attempt was made to remove the mirror plane along the *c*-axis and refine the crystal structure in *Fmm*2 space group, large residuals and atomic displacement parameters were obtained. Our attempts to refine the structure in the *F*222 space group also were not successful. With all these it is concluded that Yb_2AuGe_3 gives the best possible refinement within *Fmmm* space group and Ca_2AgSi_3 type structure. The final refinement gives an atomic ratio of $Yb_2Au_{1.029}Ge_{2.971}$. The data collection and refinement parameters for both Yb_2AuSi_3 and Yb_2AuGe_3 are summarized in **Table 4.1**. The atomic coordinates and equivalent atomic displacement parameters, anisotropic atomic displacement parameters and important bond lengths for both the compounds are listed in **Tables 4.2**, **4.3** and **4.4**, respectively.

Table 4.1 Structure refinement data for Yb_2AuSi_3 and Yb_2AuGe_3 at 293(2) K.

Empirical formula	Yb_2AuSi_3	Yb_2AuGe_3
Formula weight	624.15	764.39
Crystal system	Orthorhombic	Orthorhombic
Space group, *Z*	*Fddd*, 16	*Fmmm*, 8
Unit cell dimensions	*a* = 8.2003(16) Å, *b* = 14.187(3) Å, *c* = 16.869(3) Å	*a* = 8.5124(17) Å, *b* = 14.730(3) Å, *c* = 8.4995(17) Å
Volume	1962.5(7) $Å^3$	1065.7(4) $Å^3$
Density (calculated)	8.450 g/cm^3	9.528 g/cm^3
Absorption coeff., *F*(000)	67.628 mm^{-1}, 4157	79.326 mm^{-1}, 2531
Crystal size	0.082 x 0.014 x 0.012 mm^3	0.12 x 0.10 x 0.08 mm^3
θ range for data collection	3.75 to 45.52°	4.79 to 34.26°
Index ranges	-16<=*h*<=16, -28<=*k*<=18, -33<=*l*<=33	-11<=*h*<=13, -23<=*k*<=23, -12<=*l*<=13
Reflections collected	14628	3715
Independent reflections	2092 [R_{int} = 0.0637]	640 [R_{int} = 0.0982]
Completeness to θ = 34.26°	99.8%	98.5%
Refinement method	Full-matrix least-squares on F^2	
Data / restraints / parameters	2092 / 0 / 34	640 / 0 / 26
Goodness-of-fit	1.034	1.188
Final *R* indices [>2σ(I)]	R_{obs} = 0.0433, wR_{obs} = 0.0880	R_{obs} = 0.0544, wR_{obs} = 0.1201
R indices [all data]	R_{all} = 0.0793, wR_{all} = 0.1017	R_{all} = 0.0567, wR_{all} = 0.1212
Extinction coefficient	0.000021(5)	0.00019(4)
Largest diff. peak and hole	9.737 and -6.506 e·$Å^{-3}$	8.003 and -11.322 e·$Å^{-3}$

Table 4.2 Atomic coordinates and equivalent isotropic displacement parameters ($Å^2x10^3$) for Yb_2AuSi_3 and Yb_2AuGe_3 at 293(2) K.

Label	Wy. No.	*x*	*y*	*z*	Occupancy	U_{eq}*
Yb_2AuSi_3						
Yb1	16*g*	0.1250	0.1250	0.0005(1)	1	8(1)
Yb2	16*g*	0.1250	0.1250	0.5003(1)	1	8(1)
*M*1	16*f*	0.1250	0.4582(1)	0.1250	0.77(1)Au+0.23Si	8(1)
*M*2	16*f*	0.1250	0.2904(1)	0.1250	0.08(1)Au+0.92Si	5(1)
*M*3	32*h*	-0.1277(1)	0.5422(1)	0.1249(1)	0.06(1)Au+0.94Si	6(1)
Yb_2AuGe_3						
Yb1	8*i*	0.0000	0.0000	0.2506(1)	1	14(1)
Yb2	8*f*	0.2500	0.2500	0.2500	1	14(1)
*M*1	8*h*	0.0000	0.6667(1)	0.0000	0.71(1)Au+ 0.29(1)Ge	14(1)
*M*2	16o	0.2486(2)	0.0829(1)	0.0000	0.14(1)Au+ 0.86(1)Ge	27(1)
*M*3	8*h*	0.0000	0.1656(2)	0.0000	0.05(1)Au+ 0.96(1)Ge	37(1)

M = [Au+Si/Ge] *U_{eq} is defined as one third of the trace of the orthogonalized U_{ij} tensor.

Table 4.3 Anisotropic displacement parameters ($Å^2x10^3$) for Yb_2AuGe_3 at 293(2) K with estimated standard deviations in parentheses.

Label	U_{11}	U_{22}	U_{33}	U_{12}	U_{13}	U_{23}
Yb_2AuSi_3						
Yb1	8(1)	8(1)	7(1)	1(1)	0	0
Yb2	8(1)	8(1)	7(1)	1(1)	0	0
*M*1	6(1)	6(1)	11(1)	0	1(1)	0
*M*2	3(1)	2(1)	10(1)	0	-2(1)	0
*M*3	4(1)	3(1)	11(1)	-1(1)	2(1)	0
Yb_2AuGe_3						
Yb1	15(1)	12(1)	15(1)	0	0	0
Yb2	15(1)	13(1)	16(1)	0	0	0
*M*1	9(1)	5(1)	29(1)	0	0	0
*M*2	12(1)	9(1)	60(2)	0	0	0
*M*3	13(1)	8(1)	89(2)	0	0	0

Table 4.4 Selected bond lengths [Å] for Yb_2AuGe_3 at 293(2) K with estimated standard deviations in parentheses.

Label	Distances	Label	Distances
Yb_2AuSi_3			
Yb1-*M*3	3.1455(10)	*M*1-*M*3	2.3901(10)
Yb1-*M*2	3.1491(10)	*M*1-Yb1	3.1747(4)
Yb2-*M*1	3.1659(5)	*M*2-*M*3	2.3427(12)
Yb2-*M*3	3.1760(11)	*M*2-Yb2	3.1797(6)
M1-*M*2	2.3816(14)	*M*3-*M*3	2.348(2)
Yb_2AuGe_3			
*M*2-*M*3	2.4411(16)	*M*1-Yb1	3.2443(9)
*M*2-*M*2	2.443(2)	*M*1-Yb2	3.2478(5)
*M*1-*M*3	2.470(2)	*M*2-Yb1	3.2506(11)
*M*1-*M*2	2.4709(13)	*M*2-Yb2	3.2515(10)
*M*3- Yb1	3.2382(17)	*M*3-Yb2	3.2543(9)
*M*2-Yb1	3.2413(11)		

4.2.7 Magnetic Measurements

Magnetic susceptibility measurements on all the samples were carried out with a Quantum Design MPMS SQUID magnetometer. Polycrystalline sample of Yb_2CuGe_3 was used for the measurement whereas in cases of Yb_2AuSi_3 and Yb_2AuGe_3, randomly oriented single crystals were used without grounding into gelatin capsules, mounted on a brass rod. Temperature dependence data were collected in the range of 2 to 300 K, at different applied magnetic fields. Field dependent magnetic measurements were acquired at 5 K. The raw data were corrected for the sample holder contribution.

4.2.8 Electrical Resistivity

The resistivity measurements were performed on selected single crystal Yb_2AuGe_3 over the temperature range of 2–300 K using a four-probe dc technique with contacts made with silver paste. The measurements were conducted using a Quantum Design PPMS magnetometer. The results were reproducible for several crystals. Resistivity measurement on Yb_2CuGe_3 is pending will be done in near future.

4.2.9. Specific Heat

Heat capacity (C_p) measurements were performed on a selected single crystal of Yb_2AuGe_3, by relaxation method using a commercial Quantum Design Physical Property Measurement System (QD-PPMS). The sample was glued to calibrated HC-puck using Apiezon N grease. C_p was measured in the 3-50 K range without applied fields (H).

4.3. Results and Discussions

4.3.1 Crystal Structure

4.3.1.1 Yb_2AuSi_3

The crystal structure of Yb_2AuSi_3 is shown in **Figure 4.3**. Yb_2AuSi_3 crystallizes in the Ba_2LiSi_3 structure type, another ordered superstructure derivative of the hexagonal AlB_2 type with *Fddd* space group and lattice parameters are a = 8.2003(16) Å, b = 14.187(3) Å and c = 16.869(3) Å.

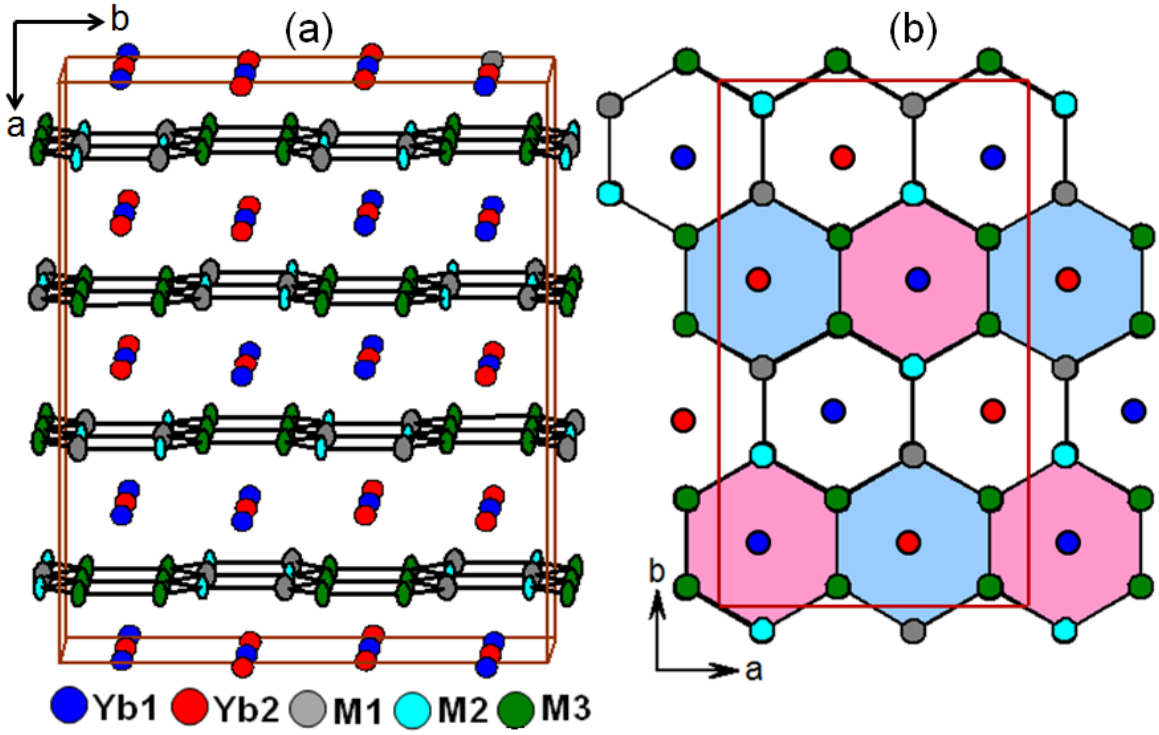

Figure 4.3 Crystal structure of Yb_2AuSi_3 viewed along a- and c-axis. The unit cells are marked with red solid lines. [$M1_2M3_4$] and [$M2_2M3_4$] hexagons are shaded with blue and pink color and [$M1_2M2_2M3_2$] kept open.

Among five different crystallographic positions, there are three crystallographically non-equivalent sites ($M1$, $M2$ and $M3$) with mixed positions of Au and Si atoms building up the infinite hexagonal network of Yb_2AuSi_3. These layers are stacked parallelly along the c-axis with two crystallographically different Yb atoms embedded between two adjacent layers. The interlayer distance between adjacent Yb-Yb ranges from 4.2010-4.2302 Å. Considering the fact that divalent Yb is larger in size (1.86 Å)[39] compared to trivalent Yb (1.66 Å),[41] both Yb atoms in Yb_2AuSi_3 are in the nonmagnetic divalent state, which is later confirmed by the magnetic susceptibility

measurements. The distance between two adjacent hexagonal layers is 4.2150(8)-4.2198(9) Å suggests that the rings are highly planar which is in sharp contrast to the prototype compound Eu_2AgGe_3, where the interlayer distance between the hexagonal rings and adjacent Eu-Eu vary in the wide range of 4.3699 to 4.5396 Å and 4.3086 to 4.3129 Å, respectively, indicating puckered hexagonal rings owing to high anisotropic thermal displacement parameters of Ag and Ge mixed sites along the *c*-axis (U_{33}). Yb1 and Yb2 atoms reside in a hexagonal biprismatic coordination environment (**Figure 4.4**) built up completely by Au and Si mixed positions. The Yb1-*M* and Yb2-*M* distances are in the range of 3.1455(4)-3.1820(4) Å and 3.1659(4)-3.1797(4) Å suggest a strong interaction between them.

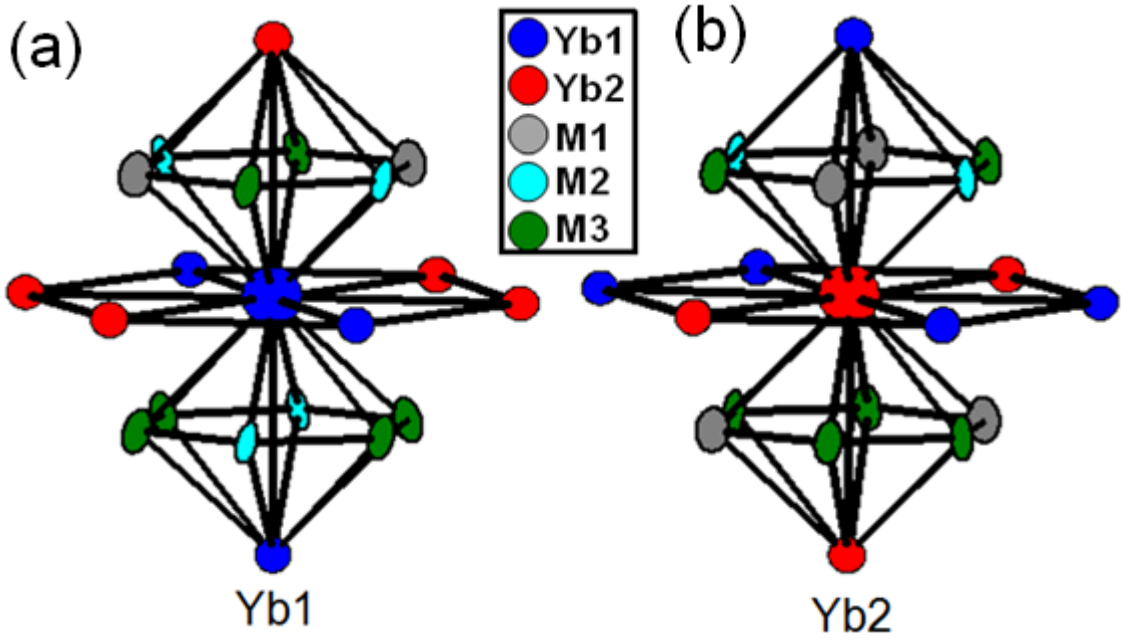

Figure 4.4 Coordination environments of Yb1 (a) and Yb2 (b) in Yb_2AuSi_3.

4.3.1.2 Yb_2AuGe_3

Yb_2AuGe_3 crystallizes in the Ca_2AgSi_3 type structure which is an ordered superstructure of AlB_2 family. This is the first example of Yb based germanide in the RE_2TX_3 family that crystallizes in an ordered superstructure of AlB_2. In Yb_2AuGe_3, *M*1, *M*2 and *M*3 atoms form hexagons that form graphite-like layers (**Figure 4.5**). The shortest distance between the hexagonal layers is 4.2498(8) Å for Yb_2AuGe_3. The Yb atoms are intercalated between the [M_6] layers. The layers are stacked along the *b*-axis in an eclipsed fashion as shown in **Figure 4.5**. Also the shortest distance between the Yb and *M* (3.2382 Å) is slightly larger than the Yb-Ge and Yb-Au distances in other intermetallics, this suggests[42]

a weak interaction between them. The Ge-Ge bond distances (2.4313 – 2.4738 Å) are within the normal range of the Ge-Ge covalent bond length- 2.45Å.[43] The short *M*1-*M*2 distance is a hint of puckering of M_6 layer, but slightly large atomic displacement parameters of *M*3 along the *b*-axis suggests a certain amount of disorder in the stacking registry of the [M_6] layers. It was hypothesized that this disorder could induce a temperature dependent phase transition in Yb_2AuGe_3 similar to the one observed in Eu_2AuGe_3[20] at ~130 K from orthorhombic to a monoclinic system. However, the low temperature single crystal data analysis for Yb_2AuGe_3 down to 4 K did not show any hint of phase transformation and no anomalies were observed in electrical resistivity data in the temperature range 2-300 K (shown in physical property section below).

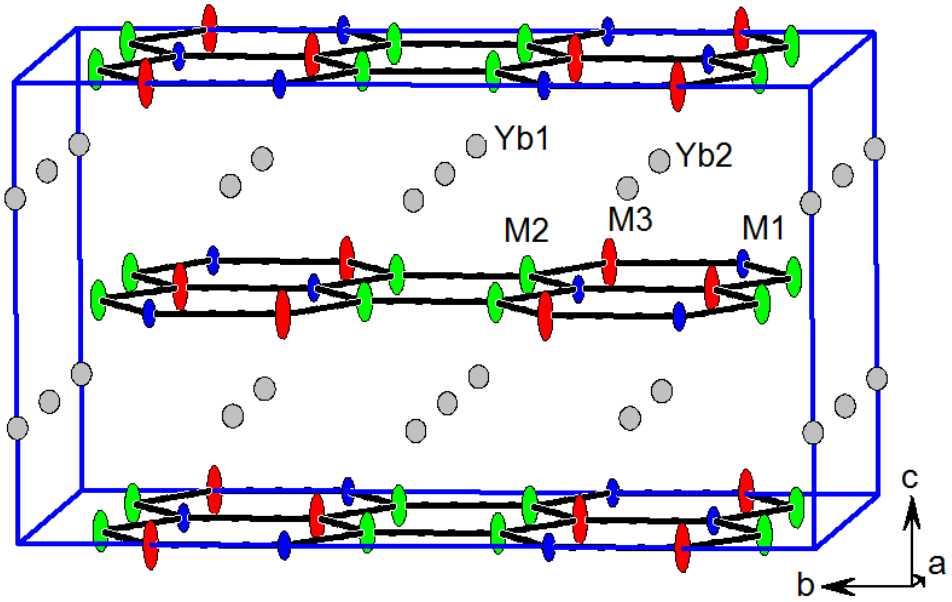

Figure 4.5 View of the Yb_2AuGe_3 structure approximately along the *a*-axis; *M*1 = Au1+Ge1, *M*2 = Au2+Ge2 and *M*3 = Au3+Ge3.

A structural phase transition was found at high temperature as observed in the powder XRD data in the range of 303-1073 K, (**Figure 4.6**). Above 873 K, Bragg peaks corresponding to the superstructure reflections progressively decreased in intensity and peaks which correspond to the substructure (hexagonal) increased. In order to simulate the powder pattern the superstructure reflections were removed from the single crystal XRD data and refined the substructure of Yb_2AuGe_3, in the AlB_2, *P*6/*mmm* space group and lattice constants are $a = b = 4.2476$ (6) Å and $c = 4.2376(8)$ Å. The simulated powder pattern obtained is in agreement with the experimental powder diffraction pattern

obtained at or above 873 K. The comparison of powder XRD patterns at different temperature intervals is shown in **Figure 4.6**. The phase transition occurs over a broad range of temperature starting above 773 K and shows progressively increasing intensity of the hexagonal substructure peaks, which are marked by black arrows. One of the main orthorhombic superstructure peaks (shown by a blue arrow) corresponding to (0 4 2) plane and has been shown in the inset of **Figure 4.6**; the peak intensity decreased with increasing temperature and it was completely vanished at 873 K. This kind of structural phase trnasition from a lower symmetry phase (orthorhombic) to a higher symmetry phase (hexagonal) at high temperature is known as *order-disorder phase transformation*, wherein entropy factor dominates over enthalpy factor giving rise to a *disordered structure in equilibrium*.

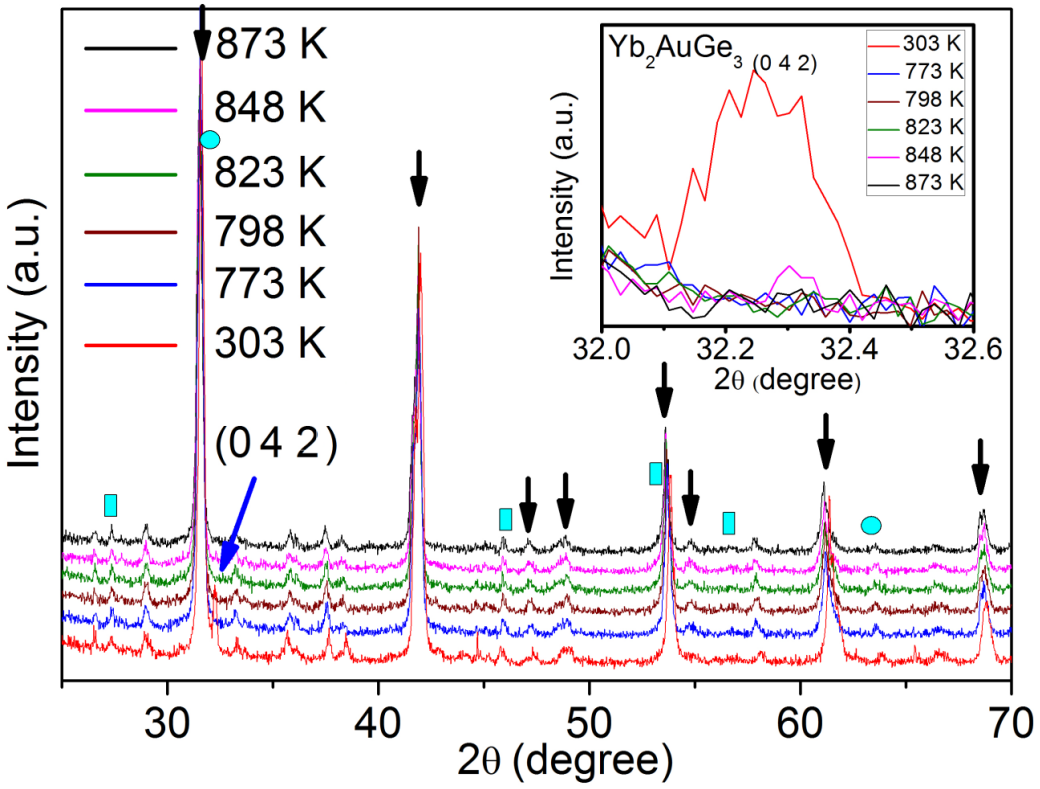

Figure 4.6 PXRD patterns of Yb_2AuGe_3 at different temperature intervals in the vicinity of the phase transition. The superstructure reflection (0 4 2) is marked. The inset shows the intensity of the superstructure peak corresponding to (0 4 2) plane decreasing with increasing temperature. The unreacted Ge (cubic, $Fd\bar{3}m$ space group) and In (tetragonal, *I*4/*mmm* space group) peaks are shown by rectangular and circular mark-ups, respectively. The remaining peaks correspond to superstructure diffractions.

4.3.2 Magnetic Properties

4.3.2.1 Yb_2CuGe_3

The temperature dependent magnetic and inverse susceptibilities data on Yb_2CuGe_3 are shown in **Figure 4.7a**. The susceptibility slowly increases up to 80 K indicating a paramagnetic behavior, below this temperature; it suddenly jumps to higher value hinting towards ferromagnetic ordering which was followed by two successive antiferromagnetic transitions (T_N) at 23.7 and 5.9 K respectively. The inset of **Figure 4.7a** pinpoints the exact ferromagnetic transition at 69 K. The inverse susceptibility curve linearly decreased with temperature up to the same temperature (80 K) below which it deviates significantly from linearity. A Curie-Weiss fit in the temperature range 160-300 K yielded an effective magnetic moment (μ_{eff}) of 4.68 μ_B/Yb and Curie paramagnetic temperature (θ_p) of 2.8 K. The positive sign of θ_p indicates ferromagnetic interaction as a relatively dominant coupling over antiferromagnetic coupling. However, the field dependent magnetization data at 2 K does not show considerable hysteresis, which rules out strong ferromagnetic coupling. The magnetization at high temperature (300 K) increase linearly with applied magnetic field as expected for paramagnetic behavior.

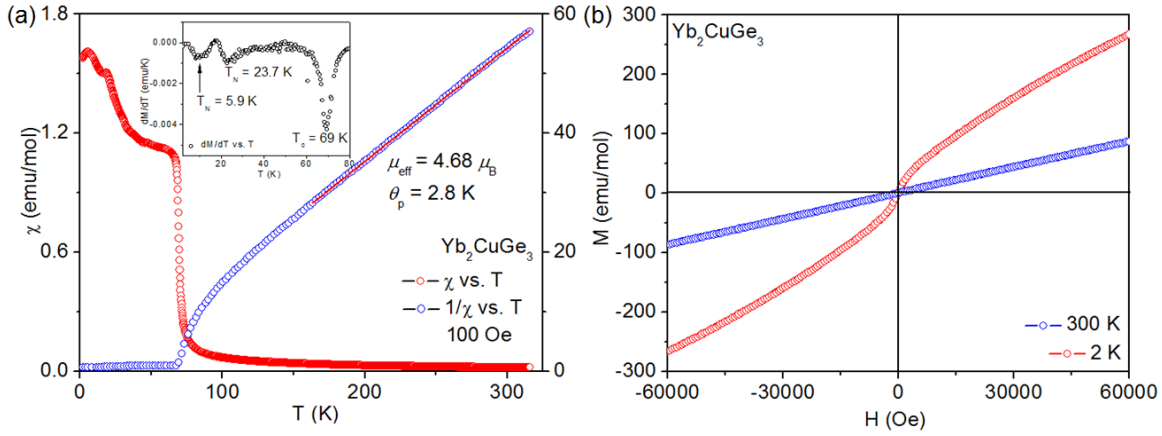

Figure 4.7 (a) Temperature dependent molar magnetic susceptibility and (b) field dependence of magnetic moment of Yb_2CuGe_3.

4.3.2.2 Yb_2AuSi_3

Temperature dependent magnetic susceptibility in both ZFC and FC modes at an applied field of 1000 Oe for the compound Yb_2AuSi_3 are plotted in **Figure 4.8a**. The molar magnetic susceptibility data at room temperature suggests that Yb_2AuSi_3 is a diamagnet wherein the magnetic susceptibility does not vary much with temperature down to 50 K below which it starts increasing exponentially up to 2 K owing to the dominance of field

induced magnetic ordering over thermal agitation, although no sign of magnetic ordering down to the lowest attainable temperature is observed. The field dependence of magnetization is plotted in **Figure 4.8b**. The overall feature of both plots is consistent with that of a diamagnet. At low temperature, the curve decreases logarithmically with increasing field; whereas at higher temperature (300 K), the variation is almost linear similar to a diamagnet. To find out the effect of aerial oxidation on the single crystals of Yb_2AuSi_3, the magnetic measurement were done on the sample of this compound which was kept in aerial conditions for two weeks and found out that the effective magnetic moment (μ_{eff}) of the oxidized sample to be 2.80 μ_B which indicates that around 62% of Yb in the sample is converted into from divalent to trivalent state based on the calculations from χT vs. T plot at 300 K. The Field dependence of magnetization also suggests that the compound behaves like a paramagnet at 300 K, whereas in the case of low temperature (2 K) curve, slope changes continuously with field without any saturation up to the maximum applied field.

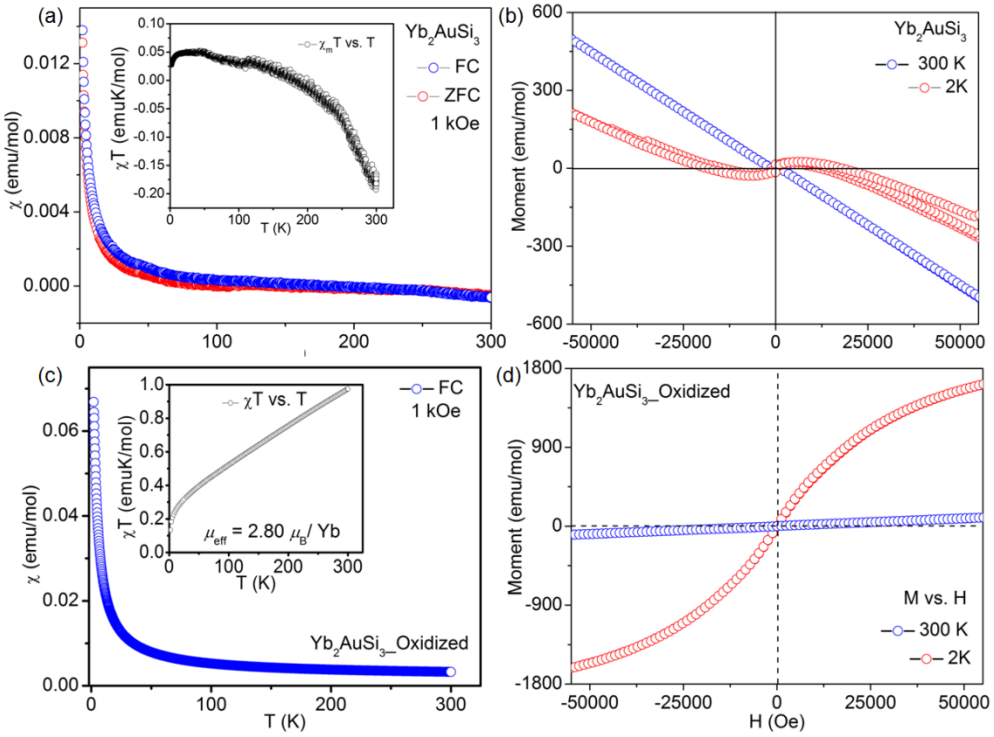

Figure 4.8 (a) Temperature dependent molar magnetic susceptibility and (b) field dependence of magnetic moment of Yb_2AuSi_3. (c) Temperature dependence of molar magnetic susceptibility and (d) Field dependence of magnetic moment of oxidized Yb_2AuSi_3.

This indicates that at low temperature spin-ordering occurs with increasing field but long range ordering does not exist in the partially oxidized sample. The plots of magnetic measurements for oxidized sample are shown in **Figure 4.8c and d**.

4.3.2.3 Yb_2AuGe_3

The temperature dependence of the molar magnetic susceptibility (χ) of a ground sample of Yb_2AuGe_3 measured from 3 to 300 K with applied magnetic field of 1000 Oe are shown in **Figure 4.9a**.

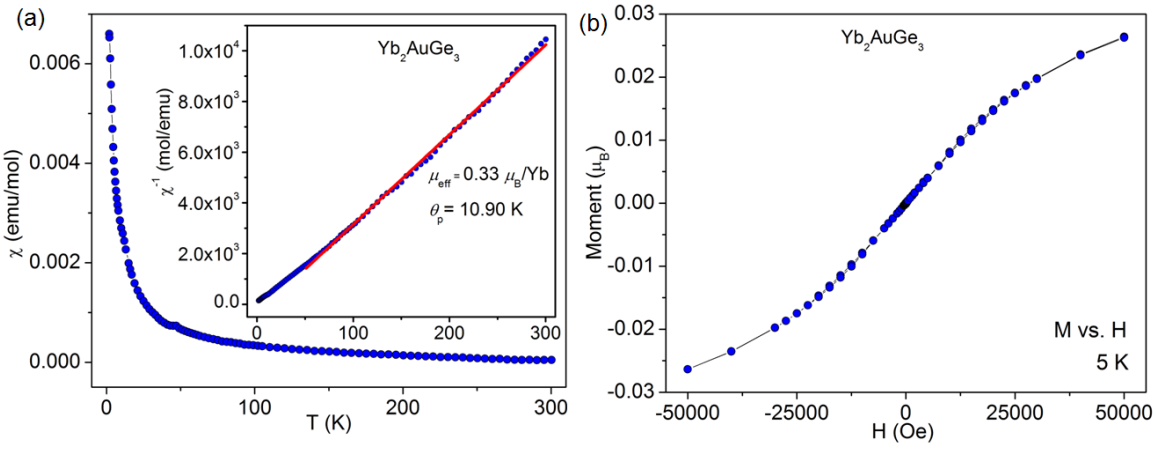

Figure 4.9 (a) Magnetic susceptibility (χ = M/H) as a function of temperature for Yb_2AuGe_3 (polycrystalline) sample measured in a dc field of 1 kOe. The inset highlights the Inverse magnetic susceptibility (χ^{-1} = H/M). (b) Magnetization as a function of applied magnetic field at 5 K for a polycrystalline sample of Yb_2AuGe_3.

No long-range magnetic order could be observed down to 3 K; however there is an upturn in the magnetic susceptibility data around 50 K suggesting paramagnetic behavior.[44] From the linear region of the inverse susceptibility plot (50-300 K), the calculated value for paramagnetic Curie-Weiss temperature (θ_p) is 10.9 (1) K suggest weak ferromagnetic coupling between the Yb moments. The estimated effective moment of 0.33 (2) μ_B, is only ~ 7 % of the value expected for the free-ion Yb^{3+}, 4.54 μ_B. This indicates that the compound contains both Yb^{2+} and Yb^{3+} moieties. The field dependence of the magnetization $M(H)$ for Yb_2AuGe_3 ground sample at 5 K can be found in **Figure 4.9b** exhibit linear behavior up to about 24 kOe at which point the slope changes continuously until about 50 kOe, but no signs of saturation up to highest attainable field of 50 kOe were observed.

4.3.3 Resistivity

The temperature dependent electrical resistivity $\rho(T)$ of Yb_2AuGe_3 in the range 2-300 K is presented in **Figure 4.10**. The resistivity data measured on single crystals along the *c*-axis and at zero applied field reveal metallic conductivity with a room temperature resistivity value ρ(300K) of 1600 $\mu\Omega$ cm. This value of room temperature resistivity, ρ(300) for Yb_2AuGe_3 was comparable with the previously reported Eu_2AuGe_3 (947 $\mu\Omega$ cm).

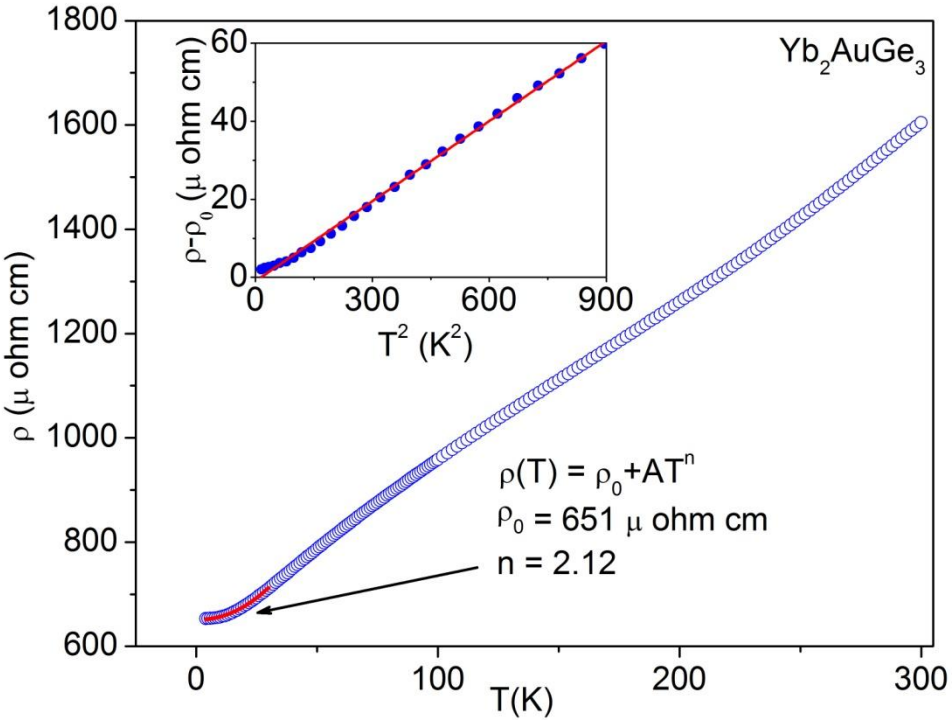

Figure 4.9 Temperature dependence of electrical resistivity $\rho(T)$ plot of a single crystal sample of Yb_2AuGe_3 in the temperature range 2-300 K. The low temperature data has been fitted to the power law, $\rho = \rho 0 + AT^n$. The values obtained from the fit are shown in the figure. A plot of ρ-ρ_0 vs. T^2 showing a linear relationship is shown as an inset.

To further investigate the correlative nature of the conduction electrons in the compound, the $\rho(T)$ vs. T curve was fitted with the power-law function $\rho(T) = \rho_0 + AT^n$ where, $\rho(T)$ is resistivity at any temperature T, ρ_0 is residual resistivity, A and T are fitting parameters in the low temperature range (2-30 K).[45] According to the Fermi-liquid theory, at low temperatures, the resistivity varies as $\rho = \rho_0 + AT^2$.[46] Experimentally it has been observed that when electron-electron scattering dominates over electron-phonon

scattering, $\rho \propto T^2$.[47] The non-linear fitting of the curve in this temperature range gave ρ_0 value of 651 μohm cm and n = 2.12.[21, 48] Thus, in the prescribed temperature range the power law is reduced to $\rho(T) = \rho_0 + AT^2$ which is consistent with the Fermi-liquid behavior. To better illustrate the Fermi-liquid behavior in Yb_2AuGe_3, the resistivity data plotted as $[\rho(T)- \rho_0]$ vs. T^2 as an inset in **Figure 4.10**. The linearity of the data proves that the compound Yb_2AuGe_3 has a strongly correlated Fermi-liquid ground state at low temperature. In this context, it worthwhile to mention that the compound CeRuSi, a moderate heavy fermion with γ value[49] of 180 mJ/molK^2 also shows Fermi-liquid behavior.[50]

4.3.4 Heat Capacity

The temperature dependent specific heat from 1.8-50 K for Yb_2AuGe_3 is shown in **Figure 4.11**. The absence of long-range magnetic ordering in Yb_2AuGe_3 was already observed from the magnetic susceptibility measurements. Further evidence for the same can be found in the plot of specific heat Vs temperature. The C_p decreases as the temperature is lowered. The $C_p(T)$ does not exhibit any anomaly, thus ruling out any type of long range phase transitions. C_p(T) has been shown in different forms as insets in the **Figure 4.11**. The observed specific heat at low temperatures can be described by the equation: $C_p = \gamma T + \beta T^3$, which describes that the total specific heat of the sample comprises of the contributions from the electronic part (coefficient of electronic specific heat, γ) as well as the lattice part (β). Thus, at low temperatures C_p should vary as a function of T^3, which is the plot of C_p/T vs. T^2 should be a straight line.[51] Such a plot is convenient for calculating the values of both γ and β.

A fit from the plot of C_p/T vs. T^2 (T = 7-15 K), resulted the value of γ = 109 mJ/mol K^2 suggesting a moderate heavy-fermion material according to the arbitrary classification of these compounds into “light”, “moderate” and classical heavy-fermions with γ values lying in the range of ~ 50-60, 100-400 and > 400 mJ / mol K^2 respectively.[52] This value of electronic specific heat compares well with the ones found in other mixed valent or intermediate compounds such as $YbNi_2Ge_2$, $YbRh_2Si_2$ and $Yb_2Co_3Ga_9$.[53-54] Debye temperature, Θ_D calculated using the following equation resulted 157 K, normal for Yb based intermetallics. Debye temperature is a measure of phonon contribution toward the overall heat capacity and a low value of Θ_D indicates a large total heat capacity

at low temperatures and hence Yb_2AuGe_3 can be a potential material in refrigeration. It is worth mentioning at this point that $HoCo_2$ which shows good magnetocaloric effect has almost the same value of Debye temperature (160 K) as Yb_2AuGe_3.[55] Field dependent study of heat capacity on this compound is in progress.

$$\theta_D = \left(\frac{1944 \times 10^3 \, n}{\beta} \right)^{1/3}$$

Where, n the number of atoms per formula unit (n = 6), β is in mJ/molK^4 (β = 3 mJ/mol K^4) and Θ_D in Kelvin.

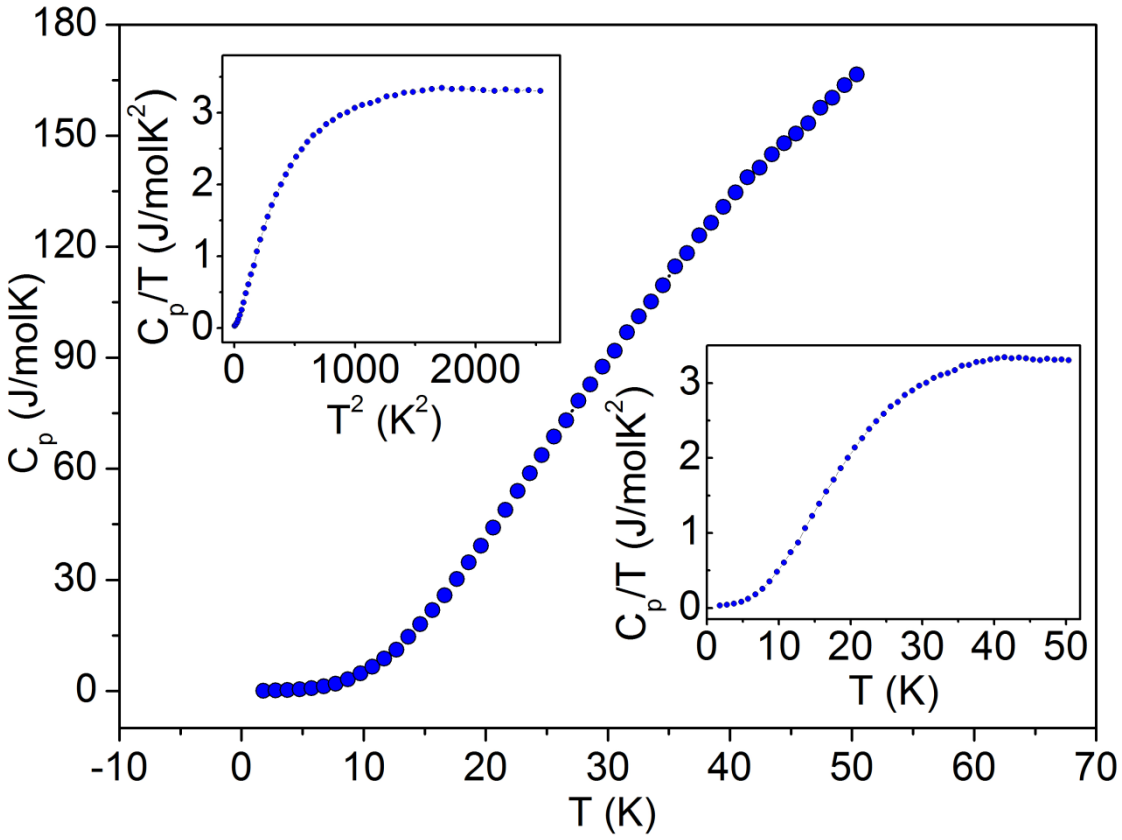

Figure 4.10 Heat capacity (C_p) of Yb_2AuGe_3 measured from 1.8-50 K. The inset figures are C_p/T Vs. T and C_p/T Vs. T^2.

4.4 Concluding Remarks

Three new Yb based intermetallic compounds, namely Yb_2CuGe_3, Yb_2AuSi_3 and Yb_2AuGe_3 crystallizing in the ordered derived superstructure of AlB_2 structure type were discovered. Single crystals of Yb_2AuSi_3 and Yb_2AuGe_3 were obtained from reactions in

molten In used as an inactive metal flux. Similar strategy did not however work in the case of Yb_2CuGe_3 which was later synthesized by *HF*- induction furnace. Temperature dependent powder XRD revealed the phase transformation of Yb_2AuGe_3 above 773 K from orthorhombic to hexagonal symmetry. The magnetization data exhibits absence of long range magnetic interactions and the low temperature resistivity data of Yb_2AuGe_3 are consistent with Fermi-liquid behavior. The specific heat measurements show that the compound exhibits moderate heavy fermion behavior. These findings call for band-structure calculations, XANES measurements and neutron diffraction experiments to further probe the electronic structure and its influence on the phase transformation at higher temperature.

4.5 References

1. Shigetoh, K.; Hirata, D.; Avila, M. A.; Takabatake, T., *J. Alloys Compd.* **2005,** *403*, 15-18.

2. Dilley, N. R.; Freeman, E. J.; Bauer, E. D.; Maple, M. B., *Phys. Rev. B* **1998,** *58* (10), 6287-6290.

3. Nikiforov, V. N.; Pryadun, V. V.; Morozkin, A. V.; Irkhin, V. Y., *Phys. Lett. A* **2014,** *378* (20), 1425-1427.

4. Chondroudi, M.; Peter, S. C.; Malliakas, C. D.; Balasubramanian, M.; Li, Q. A.; Kanatzidis, M. G., *Inorg. Chem.* **2011,** *50*, 1184-1193.

5. Danzenbacher, S.; Kucherenko, Y.; Vyalikh, D. V.; Holder, M.; Laubschat, C.; Yaresko, A. N.; Krellner, C.; Hossain, Z.; Geibel, C.; Zhou, X. J.; Yang, W. L.; Mannella, N.; Hussain, Z.; Shen, Z. X.; Shi, M. P., L.; Molodtsov, S. L., *Phys. Rev. B* **2007,** *75*, 045109.

6. Gaudin, E.; Chevalier, B.; Heying, B.; Rodewald, U. C.; Pöttgen, R., *Chem. Mater.* **2005,** *17*, 2693-2700.

7. Ivanshin, V. A.; Sukhanov, A. A.; Sokolov, D. A.; Aronson, M. C.; Jia, S.; Bud'ko, S. L.; Canfield, P. C., *J. Alloys Compd.* **2009,** *480*, 126-127.

8. Kaczorowski, D.; Leithe-Jasper, A.; Rogl, P.; Flandorfer, H.; Cichorek, T.; Petri, R.; Andraka, B., *Phys. Rev. B* **1999,** *60*, 422-433.

9. Murani, A. P., *Nato Sci. Ser. Ii. Math.* **2003,** *110*, 297-305.

10. Jeong, T.; Pickett, W., *J. Phys.-Condens. Mater.* **2006,** *18*, 6289-6297.

11. Bärnighausen, H., *Commun. Math. Chem.* **1980,** *9* 139–175.

12. Bärnighausen, H.; Müller, U., Universität Karlsruhe and Universität-Gh Kassel: Germany, 1996.

13. Chevalier, B.; Lejay, P.; Etourneau, J. R.; Hagenmuller, P., *Solid State Commun.* **1984,** *49*, 753-760.

14. Gordon, R. A.; Warren, C. J.; Alexander, M. G.; DiSalvo, F. J.; Pöttgen, R., *J. Alloys Compd.* **1997,** *248*, 24-32.

15. Kotsanidis, P. A.; Yakinthos, J. K.; Gamariseale, E., *J. Magn. Magn. Mater.* **1990,** *87*, 199-204.

16. Majumdar, S.; Sampathkumaran, E. V.; Brando, M.; Hemberger, J.; Loidl, A., *J. Magn. Magn. Mater.* **2001,** *236*, 99-106.

17. Szlawska, M.; Kaczorowski, D., *Phys. Rev. B* **2011,** *84*, 094430.

18. Peter, S. C.; Chondroudi, M.; Malliakas, C. D.; Balasubramanian, M.; Kanatzidis, M. G., *J. Am. Chem. Soc.* **2011,** *133*, 13840-13843.

19. Peter, S. C.; Kanatzidis, M. G., *Z. Anorg. Allg. Chem.* **2012,** *638*, 287-293.

20. Peter, S. C.; Malliakas, C. D.; Chondroudi, M.; Schellenberg, I.; Rayaprol, S.; Hoffmann, R. D.; Pöttgen, R.; Kanatzidis, M. G., *Inorg. Chem.* **2010,** *49*, 9574-9580.

21. Peter, S. C.; Malliakas, C. D.; Nakkotte, H.; Kothapilli, K.; Rayaprol, S.; Schultz, A. J.; Kanatzidis, M. G., *J. Solid State Chem.* **2012,** *187*, 200-207.

22. Peter, S. C.; Rayaprol, S.; Francisco, M. C.; Kanatzidis, M. G., *Eur. J. Inorg. Chem.* **2011**, 3963-3968.

23. Peter, S. C.; Sarkar, S.; Kanatzidis, M. G., *Inorg. Chem.* **2012,** *51*, 10793-10799.

24. Salvador, J. R.; Gour, J. R.; Bilc, D.; Mahanti, S. D.; Kanatzidis, M. G., *Inorg. Chem.* **2004,** *43*, 1403-1410.

25. Salvador, J. R.; Malliakas, C.; Gour, J. R.; Kanatzidis, M. G., *Chem. Mater.* **2005,** *17*, 1636-1645.

26. Wu, X. N.; Kanatzidis, M. G., *J. Solid State Chem.* **2005,** *178*, 3233.

27. Zhuravleva, M. A.; Kanatzidis, M. G., *J. Solid State Chem.* **2003,** *173*, 280-292.

28. Zhuravleva, M. A.; Pcionek, R. J.; Wang, X. P.; Schultz, A. J.; Kanatzidis, M. G., *Inorg. Chem.* **2003** *42*, 6412-6424.

29. Zhuravleva, M. A.; Salvador, J.; Bilc, D.; Mahanti, S. D.; Ireland, J.; Kannewurf, C. R.; Kanatzidis, M. G., *Chem. Eur. J.* **2004,** *10*, 3197-3208.

30. Chondroudi, M.; Balasubramanian, M.; Welp, U.; Kwok, W. K.; Kanatzidis, M. G., *Chem. Mater.* **2007,** *19*, 4769-4775.

31. Sheldrick, G. M., *Acta Crystallogr. A* **2008,** *64*, 112-122.

32. Sheldrick, G. M. *SHELXTL: Structure Determination Program*, 5.10; Siemens Analytical X-ray Instruments Inc: Madison, WI, 1998.

33. Gil, R. C.; Carrillo-Cabrera, W.; Schultheiss, M.; K., P.; Schnering, H. G. V., *Z. Anorg. Allg. Chem.* **1999,** *625*, 285-293.

34. Zachwieja, U., *Z. Anorg. Allg. Chem.* **1996,** *622*, 1173-1176.

35. Müllmann, R.; Mosel, B. D.; Eckert, H.; Pöttgen, R.; Kremer, R. K., *Hyperfine Interact.* **1997,** *108*, 389-400.

36. Pottgen, R., *J. Mater. Chem.* **1995,** *5*, 505-508.

37. Pottgen, R.; Borrmann, H.; Felser, C.; Jepsen, O.; Henn, R.; Kremer, R. K.; Simon, A., *J. Alloy Compd.* **1996,** *235*, 170-175.

38. Pottgen, R.; Borrmann, H.; Kremer, R. K., *J. Magn. Magn. Mater.* **1996,** *152*, 196-200.

39. Rossi, D.; Marazza, R.; Ferro, R., *J. Alloy Compd.* **1992,** *187*, 267-270.

40. Schnelle, W.; Pottgen, R.; Kremer, R. K.; Gmelin, E.; Jepsen, O., *J. Phys.-Condens. Mater.* **1997,** *9*, 1435-1450.

41. Allen, F. H.; Kennard, O.; Watson, D. G.; Brammer, L.; Orpen, A. G.; Taylor, R., Table of Bond Lengths Determined by X-Ray and Neutron Diffraction, *J. Am. Chem. Soc.* **1987,** *2*, S1–S19.

42. Merlo, F.; Pani, M.; Canepa, F.; Fornasini, M. L., *J. Alloy Compd.* **1998,** *264*, 82-88.

43. Donohue, J., *The Structures of the Elements*. Wiley: New York, 1974.

44. Buzaneva, E.; Scharff, P., *Frontiers of Multifunctional Nanosystems*. 2002; p 293.

45. Kambe, S.; Suderow, H.; Fukuhara, T.; Flouquet, J.; Takimoto, T., *J. Low Temp. Phys.* **1999,** *117*, 101-112.

46. Coleman, P., *Introduction to Many Body Physics*. Rutgers University Press: Rutgers, 2004.

47. Li, S. Y.; Taillefer, L.; Hawthorn, D. G.; Tanatar, M. A.; Paglione, J.; Sutherland, M.; Hill, R. W.; Wang, C. H.; Chen, X. H., *Phys. Rev. Lett.* **2004,** *93*, 056401.

48. Varma, C. M., *Rev. Mod. Phys.* **1976,** *48*, 219.

49. Sereni, J. G.; Caroca-Canales, N.; Kumar, M.; Oeschler, N.; Berisso, M. G.; Geibel, C., *J. Phys. Confer. Ser.* **2010,** *200*, 012181.

50. Rebelsky, L.; Reilly, K.; Horn, S.; Borges, H.; Thompson, J. D.; Willis, J. O.; Aikin, R.; Caspari, R.; Bredl, C. D., *J. Appl. Phys.* **1988,** *63*, 3405-3407.

51. Gopal, E. S. R., *Specific heat at low temperatures*. Plenum: New York, 1966.

52. Goltsev, A. V.; Golubkov, A. V.; Smirnov, I. A.; Misiorek, H.; Sulkovski, C., *Phys. Solid State* **2006,** *48*, 622-624.

53. Tsujii, N.; Kontani, H.; Yoshimura, K., *Phys. Rev. Lett.* **2005,** *94*, 057201-057204.

54. Tsujii, N.; Kontani, H.; Yoshimura, K., *J. Phys. Soc. Jpn.* **2007,** *76*, 174-177.

55. de Oliveira, N. A.; von Ranke, P. J.; Tovar Costa, M. V.; Troper, A., *Phys. Rev. B* **2002,** *66*, 094402.

Chapter 5

Disordered compounds $RE_2T\text{Ge}_3$ in the α and β polymorphs of ThSi_2 Family

5.1. Introduction

RE based compounds crystallizing in the $ThSi_2$ structure type (both α and β-phases), particularly those with the general formula, RE_2TX_3 (*RE* = Ce, Pr, Nd; *T* = Transition metal, X = Si, In, Ge) is an important class of families owing to their fascinating structural and physical aspects. Here a brief overview on the compounds is given based on Ce, Nd and Pr. The interesting examples are- atom-disorder spin glass behavior was observed in Ce_2CuSi_3, Pr_2CuSi_3, Nd_2CuSi_3, Kondo lattice compound Ce_2NiGe_3 showed spin glass behavior,short range antiferromagnetic ordering was observed in Nd_2NiGe_3, annealed sample of Ce_2NiSi_3 showed antiferromagnetic transition at 4.2 K and additional anomaly at 2.5 K, Ce_2FeSi_3 and Ce_2PdSi_3 exhibit Kondo behavior and ferromagnetic ordering was observed below 16 K in Nd_2PdSi_3,[1-8] Kondo lattice reported in Ce_2IrSi_3 and Ce_2CoSi_3[9-10] weak spin glass behavior was observed in Nd_2PtSi_3.[11] Ce_2RhSi_3 is antiferromagnetic below $T_N < 7$ K, ferromagnetic spiral magnetic ordering was observed at 4.2 K observed in a Nd_2RhSi_3[10, 12] and Ce_2CuGe_3 was reported as to show spin glass behavior.[13] All these compounds crystallize in the AlB_2 type structure (β-$ThSi_2$). Compounds crystallizing in the α-$ThSi_2$-type structure are $CeFe_{0.22}Si_{1.78}$,[14] $CeCu_{0.14}Ge_{1.71}$,[15] $CeTi_{0.23}Ge_{1.77,}$[16] $CeRh_{0.5}Ge_{1.5,}$[17] $PrNi_{0.25}Si_{1.75}$,[18] $PrNi_{0.07}Ge_{1.79}$,[19] $PrAg_{0.24}Ge_{1.76}$,[20] $PrCo_{0.3}Ge_{1.7}$,[21] $NdZn_{0.3}Si_{1.7}$,[22] $NdZn_{0.45}Si_{1.55}$,[23] $NdNi_{0.25}Si_{1.75}$[24] and $NdNi_{0.25}Si_{1.75}$.[18] Among the α-$ThSi_2$-type compounds, the spin glass behavior is reported in $CeRh_{0.5}Ge_{1.5}$.[17] The above mentioned works suggest that there might be other interesting compounds in the α-$ThSi_2$-type structure with interesting physical properties.

In comparison to the compounds with first row transition metals (e.g. Mn, Fe, Co, Ni, Cu), 4*d* and 5*d* block elements (e.g. Ru, Rh, Pd, Ag, Ir, Pt, Au) present an intriguing aspect to the overall physical properties of the compound because of the fact that 4*d* and 5*d* electrons can efficiently hybridize with the localized 4*f* orbitals belonging to lanthanide metals. This type of interaction dictates the conductivity and related properties of the itinerant electrons giving rise to interesting and very often anomalous properties. The other motivation of this work was our continuous search for new superstructures of the AlB_2 type structure similar to our recent studies on ordered compounds Eu_2AuSi_3, Eu_2AgGe_3, Eu_2AuGe_3, Yb_2AuSi_3 and Yb_2AuGe_3, [25-27] even though they were reported in the disordered structures earlier.[18, 28-30] The lack of ordered structure were observed as in $CeAu_xGe_{1-x,}$[31] $CeRh_xGe_{1-x}$[17] and Nd_2NiGe_3,[32] the first two led to the formation of the

mixture of hexagonal and tetragonal crystal systems, but later one crystallize only with the AlB_2 type. Understanding all these analysis, three Ag based compounds RE_2AgGe_3 (*RE* = Ce, Pr, Nd) were synthesized by arc melting method. Our detailed powder and single crystal XRD measurements suggest that they crystallize in the α-$ThSi_2$ structure type. All three compounds found to be pure and further studied for their magnetic and transport properties in detail. Temperature dependent resistivity data reveals that three compounds are metallic in nature. Another compound, Nd_2NiGe_3 was also synthesized by arc melting followed by annealing at 1173 K. The phase purity of the compound was checked by powder XRD. Rietveld refinement on the powder XRD data at 300 K suggests that the compound crystallizes in the AlB_2 structure type, which was confirmed by neutron diffraction (ND). The crystal structure of Nd_2NiGe_3 consists of two dimensional Ni/Ge hexagonal units and the neodymium atoms are sandwiched between the adjacent layers.

5.2. Experimental Section

5.2.1. Synthesis

The following metals were used as purchased without any further purification; *RE* (Ce, Pr and Nd chunks, 99.99%, Alfa-Aesar), Ag (shots, 99.99%, Alfa-Aesar), Ni (wire 99.99%, Alfa Aesar) and Ge (pieces, 99.999%, Alfa-Aesar). In a typical procedure, *RE*, silver and germanium metals were taken in an ideal 2:1:3 atomic ratios (total weight of reactant was ~200 mg) and repeatedly arc melted (flipping 5 times with 30s arc passing) in an argon atmosphere to ensure homogeneity; hard globules were formed. Finally, the samples were crushed and made into powder for further characterization. All the samples are stable under normal atmospheric conditions for several months.

5.2.2. Elemental Analysis

Semi quantitative microanalyses were performed on Ce_2AgGe_3, Pr_2AgGe_3 and Nd_2AgGe_3 single crystals using a Leica 220i electron microscope equipped with Bruker 129 eV energy dispersive X-ray analyzer (**Figure 5.1)**. Data were acquired with an accelerating voltage of 20 kV and 90 s accumulation time. The EDS analysis performed on cleaned surfaces of the single crystals showed the percent atomic composition for Ce_2AgGe_3 is 33(1)% Ce 21(1)% Ag and 46(1)% Ge; for Pr_2AgGe_3 31(1), 19(1)% and 50(1)%; for Nd_2AgGe_3 34(1)% Nd, 13(1)% Ag, 53(1)% Ge.

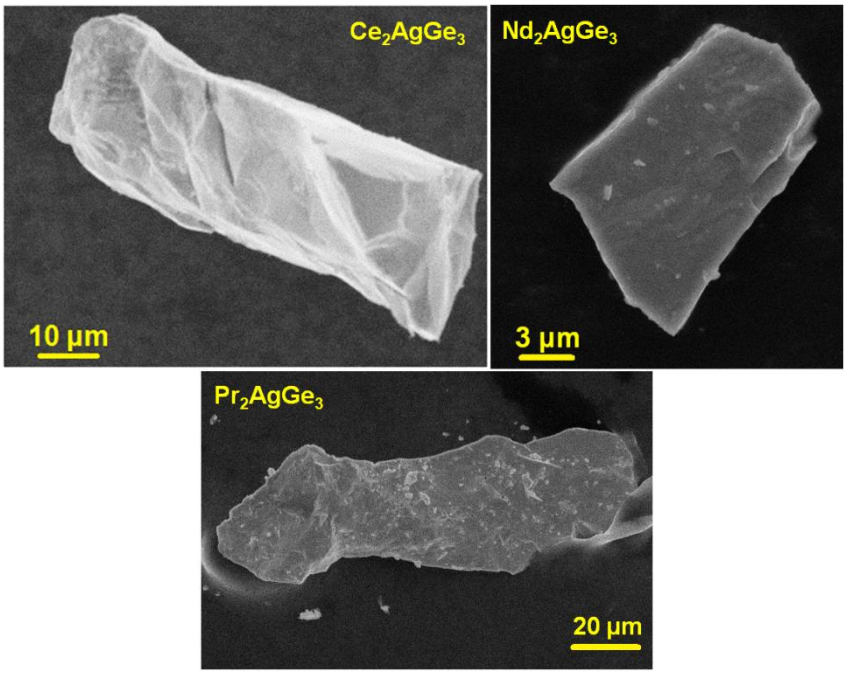

Figure 5.1 FE SEM images of the single crystals of Ce_2AgGe_3, Nd_2AgGe_3 and Pr_2AgGe_3.

The compositions obtained from EDS data are in good agreement with the results derived from the refinement of single crystal X-ray diffraction data. Field emission scanning electron microscopy (FE SEM) images of the representative single crystals are shown in **Figure 5.1**.

5.2.3. Powder XRD

The phase identity and purity of the samples were confirmed by powder XRD measurements carried out with on a Bruker D8 Discover diffractometer using Cu-Kα radiation (λ = 1.5406 Å). All the samples were scanned for 1 hr in the 2θ range of 10˚-90˚ with 0.02˚ step size at room temperature (293 K). Rietveld refinement was performed on all the three samples using the models obtained from the single crystal XRD data as shown in **Figure 5.2a**, **b** and **c,** respectively. The lattice parameters obtained from the Rietveld refinement for all the above compounds were comparable with the values obtained from the SCXRD data (**Table 5.1**).

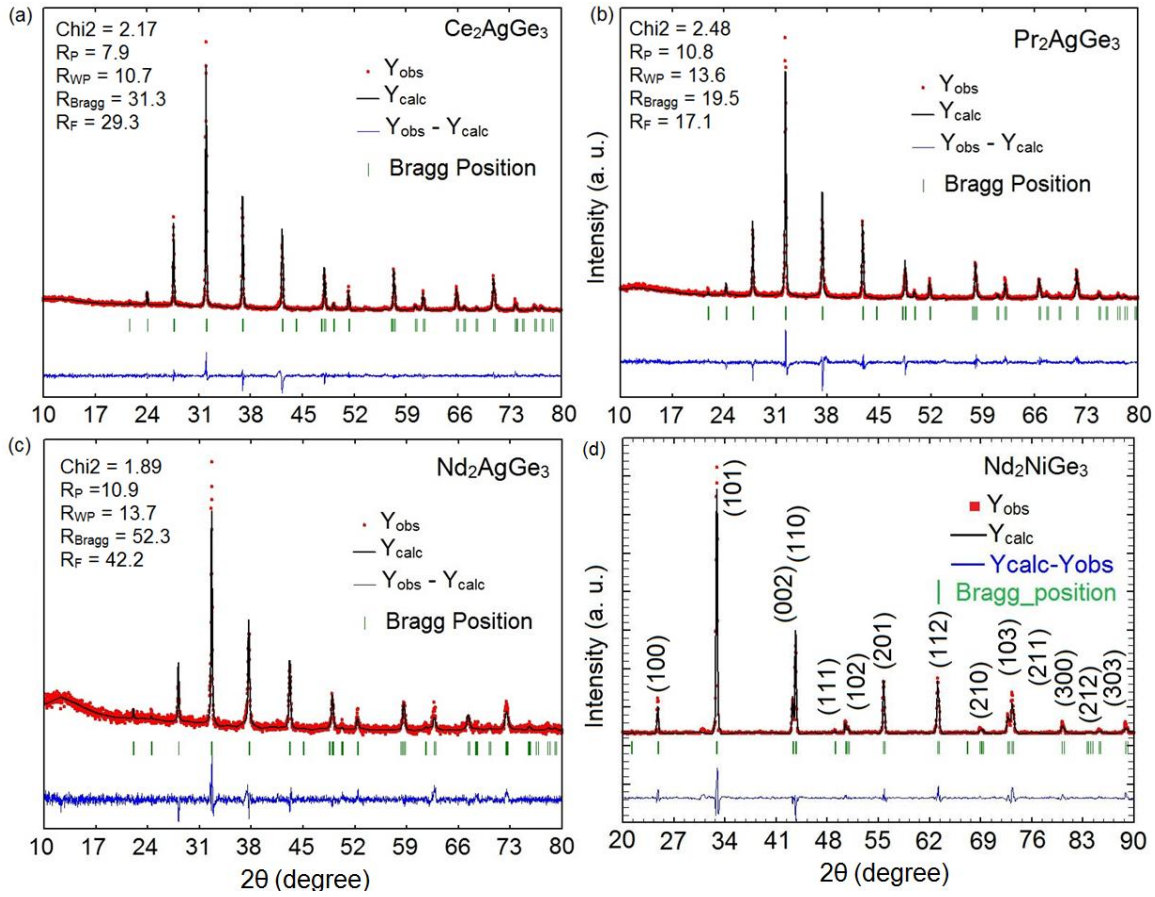

Figure 5.2 Rietveld refinement of experimental powder XRD patterns of a) Ce_2AgGe_3, b) Pr_2AgGe_3 and c) Nd_2AgGe_3 (d) Nd_2NiGe_3 collected at 293 K using models obtained from the single crystal data refinement of each compound.

Table 5.1. Comparison of lattice parameters obtained from single crystal XRD and Reitveld analysis of the powder XRD patterns for Ce_2AgGe_3, Pr_2AgGe_3 and Nd_2AgGe_3

Latt. para.	Ce_2AgGe_3		Pr_2AgGe_3		Nd_2AgGe_3	
	SCXRD	Rietveld	SCXRD	Rietveld	SC XRD	Rietveld
a	4.2754(3)	4.2733(1)	4.2401(6)	4.2270(1)	4.1886(6)	4.1876(3)
c	14.6855(16)	14.7976(1)	14.611(3)	14.6457(1)	14.557(3)	14.5343(2)

5.2.4. Single-Crystal X-ray Diffraction

Selected single crystals of Ce_2AgGe_3, Pr_2AgGe_3 and Nd_2AgGe_3 were mounted on the tip of a glass fiber with glue. The single crystal data sets were collected on Bruker smart Apex-II CCD diffractometer equipped with Mo Kα radiation X-ray tube (λ = 0.71073 Å) and a graphite monochromator with ω scan mode at 293 K. The crystal structures of Ce_2AgGe_3, Pr_2AgGe_3 and Nd_2AgGe_3 were successfully refined in the tetragonal $I4_1/amd$ space group by using SHELXS 97[33] and refined by a full matrix least-squares method using SHELXL[34] with anisotropic atomic displacement parameters (ADP) for all the atoms. The atomic parameters of α-$ThSi_2$ were taken in which Si site is mixed with Ag and Ge atoms. The *RE* and mixed (*M* = Ag+Ge) sites are occupied at Wyckoff positions of 4*a* and 8*e*, respectively. Crystal structures were drawn using Diamond program.[35] Details of crystal data and structure refinement, atomic coordinates, equivalent isotropic displacement parameters and anisotropic displacement parameters for all three compounds are summarized in **Tables 5.2-5.5**.

5.2.5. Neutron diffraction

Neutron diffraction measurements were carried out at various temperatures between 2.8 and 300 K. As can be seen from the magnetization measurements *vide infra*, there are no signatures of long-range magnetic ordering in this compound, similar to another compound of this series, Ce_2NiGe_3.[36] ND data recorded at all temperatures were refined using the *P6/mmm* structure as mentioned earlier and the details of the refinement are summarized in **Table 5.6**. The unit cell volume and cell parameters show decreasing trend from room temperature down to lowest temperature.

5.2.6. Magnetic Measurements

Magnetic measurements were performed on single phase polycrystalline Ce_2AgGe_3, Pr_2AgGe_3, Nd_2AgGe_3 and Nd_2NiGe_3 samples using Quantum design superconducting quantum interference device (QD-SQUID) magnetic property measurement system (MPMS). Magnetic susceptibility of all the compounds were measured in zero field cooled (ZFC) and field cooled (FC) modes under different applied magnetic fields as a function of temperature. Field dependent magnetization measurements were also carried out at selected temperatures as a function of applied magnetic field.

Table 5.2 Crystal data and structure refinement for Ce_2AgGe_3 Pr_2AgGe_3, Nd_2AgGe_3 at 293(2) K. Crystal system – Tetragonal, space group - $I4_1/amd$, $Z = 2$

Empirical formula	$Ce_2Ag_{1.20}Ge_{2.80}$	$Pr_2Ag_{1.15}Ge_{2.85}$	$Nd_2Ag_{1.15}Ge_{2.85}$
Formula weight	612.94	612.75	619.41
Unit cell dimensions	a = 4.2754(3) Å b = 4.2754(3) Å c = 14.6855(16) Å	a = 4.2401(6) Å b = 4.2401(6) Å c = 14.611(3) Å	a = 4.1886(6) Å b = 4.1886(6) Å c = 14.557(3) Å
Volume	268.44(4) $Å^3$	262.68(8) $Å^3$	255.39(7) $Å^3$
Density (calculated)	7.583 g/cm^3	7.747 g/cm^3	8.055 g/cm^3
Absorption coefficient	36.192 mm^{-1}	38.303 mm^{-1}	40.650 mm^{-1}
F(000)	524	527	531
Crystal size (mm^3)	0.1x 0.08x 0.05	0.16 x 0.07 x 0.04	0.12 x 0.09 x 0.08
θ range for data collection	4.97 to 29.15°	5.01 to 27.21°	5.06 to 28.68°
Index ranges	-5<=h<=5, -5<=k<=4, -20<=l<=15	-4<=h<=5, -5<=k<=5, -18<=l<=13	-5<=h<=4, -5<=k<=5, -8<=l<=19
Reflections collected	604	530	983
Independent reflections	113 [R_{int} = 0.0675]	98 [R_{int} = 0.0497]	109 [R_{int} = 0.0186]
Completeness to θ = 27.21°	98.3%	100%	100%
Refinement method	Full-matrix least-squares on F^2		
Data / restraints / parameters	113 / 0 / 9	98 / 0 / 9	109 / 0 / 9
Goodness-of-fit	1.162	1.441	1.256
Final R indices [>2σ(I)]	R_{obs} = 0.0553, wR_{obs} = 0.1332	R_{obs} = 0.0.506, wR_{obs} = 0.1128	R_{obs} = 0.0474, wR_{obs} = 0.1080
R indices [all data]	R_{all} = 0.0594, wR_{all} = 0.1364	R_{all} = 0.0557, wR_{all} = 0.1165	R_{all} = 0.0481, wR_{all} = 0.1086
Extinction coefficient	0.0077(3)	0.00259(18)	0.00642 (19)
Largest diff. peak and hole (e·$Å^{-3}$)	3.538 and -3.375	2.330 and -3.219	2.665 and -3.899

5.2.7. Resistivity

The resistivity measurements were performed on the sintered (500 ˚C for 12hr in a evacuated quartz tube) pellets prepared in a rectangular die of size 8 x 2.5 mm^2 with thicknesses 0.44, 0.41 and 0.42 mm respectively for the samples Ce_2AgGe_3, Pr_2AgGe_3, Nd_2AgGe_3 and Nd_2AgGe_3 over the temperature range of 3–300 K using a four-probe dc technique. Four very thin copper wires with thickness of 50 μm were glued with the help of silver epoxy paste to the pellets. The measurements were conducted using a Quantum Design Physical Property Measurement System (QD-PPMS) at an applying voltage of 95 mV and current of 0.1 mA.

Table 5.3 Atomic coordinates and equivalent isotropic displacement parameters ($Å^2x10^3$) for Ce_2AgGe_3 Pr_2AgGe_3 and Nd_2AgGe_3 at 293(2) K with estimated standard deviations in parentheses.

Compound	Label	Wyckoff site	*x*	*y*	z	Occupancy	U_{eq}*
Ce_2AgGe_3	Ce	4*a*	0	0.7500	0.1250	1	5(1)
	M	8*e*	0	0.2500	0.2918(1)	0.26+0.74	20(1)
Pr_2AgGe_3	Pr	4*a*	0	0.7500	0.1250	1	19(1)
	M	8*e*	0	0.2500	0.2919(1)	0.31+0.69	39(1)
Nd_2AgGe_3	Nd	4*a*	0	0.7500	0.1250	1	11(1)
	M	8*e*	0	0.2500	0.2918(1)	0.27+0.73	31(1)

*U_{eq} is defined as one third of the trace of the orthogonalized U_{ij} tensor. (*M* = Ag+Ge).

Table 5.4 Anisotropic displacement parameters ($Å^2x10^3$) for Ce_2AgGe_3 Pr_2AgGe_3 and Nd_2AgGe_3 at 293(2) K with estimated standard deviations in parentheses.

Compound	Label	U_{11}	U_{22}	U_{33}	U_{12}	U_{13}	U_{23}
Ce_2AgGe_3	Ce	3(1)	3(1)	10(1)	0	0	0
	M	16(1)	23(1)	21(1)	0	0	0
Pr_2AgGe_3	Pr	16(1)	16(1)	26(1)	0	0	0
	M	34(1)	37(1)	45(1)	0	0	0
Nd_2AgGe_3	Nd	11(1)	11(1)	10(1)	0	0	0
	M	28(1)	38(1)	28(1)	0	0	0

The anisotropic displacement factor exponent takes the form: $-2\pi^2[h^2a^{*2}U_{11} + ... + 2hka^*b^*U_{12}]$

Table 5.5 Selected bond lengths for Ce_2AgGe_3, Pr_2AgGe_3 and Nd_2AgGe_3 [Å] at 293(2) K with estimated standard deviations in parentheses.

Compound	Label	Distance	Label	Distance
Ce_2AgGe_3	*M*-*M*	2.4446(14) Å	*M*-*M*	2.4647(7) Å
	Ce-*M*	3.2508(7) Å	Ce-*M*	3.2609(3) Å
Pr_2AgGe_3	*M*-*M*	2.429(2) Å	*M*-*M*	2.4479(12) Å
	Pr-*M*	3.2311(10) Å	Pr-*M*	3.2348(6) Å
Nd_2AgGe_3	*M*-*M*	2.4211(16) Å	*M*-*M*	2.4228(8) Å
	Nd-*M*	3.1996(5) Å	Nd-*M*	3.2069(7) Å

5.3. Results and Discussion

5.3.1. Crystal Structure

***RE_2AgGe_3* (*RE* = Ce, Pr and Nd).** The crystal structures of the compounds Ce_2AgGe_3, Pr_2AgGe_3 and Nd_2AgGe_3 are shown in **Figure 5.3**. They crystallize in the α-$ThSi_2$ structure type having $I4_1/amd$ space group**.**

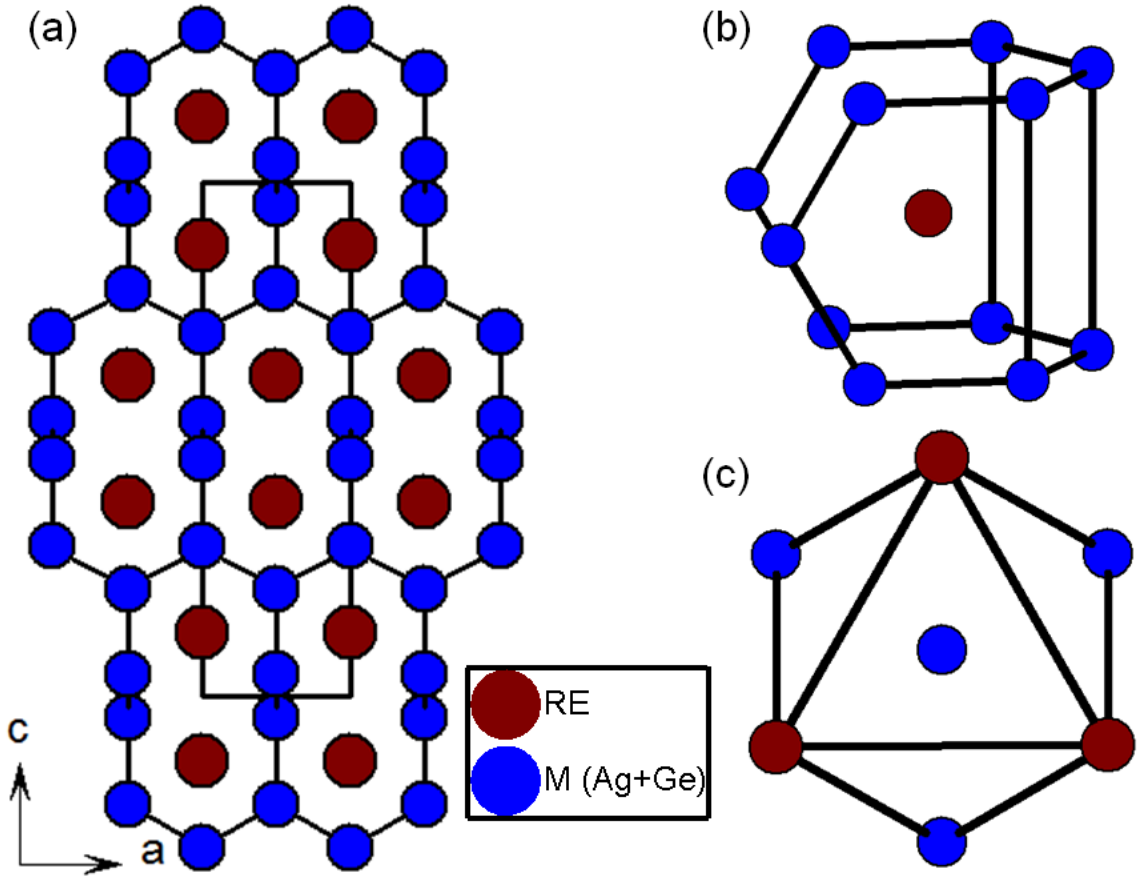

Figure 5.3 (a) Crystal structures of RE_2AgGe_3 (b) Coordination spheres of *RE* and (c) M (Ag+Ge) atoms in the crystal structure of RE_2AgGe_3 are presented.

The detailed crystal structure description can be available elsewhere.[17] The voids and channels of polyanionic network created by three-dimensional perpendicular [$AgGe_3$] layers were occupied by two *RE* atoms. The [$AgGe_3$] layers in the tetragonal crystal system stacked in AABB types and arranged perpendicular to each other. The weak interaction between the *RE* atoms is apparent from the bond distance of Ce–Ce (4.2754(3) Å), Pr-Pr (4.2401(6) Å) and Nd-Nd (4.1886(6) Å) in Ce_2AgGe_3, Pr_2AgGe_3 and Nd_2AgGe_3, respectively, which is much larger than the expected bond distance of Ce–Ce (3.66 Å),[37] Pr-Pr (4.12 Å)[20] and Nd-Nd (4.06 Å).[24] The shortest bond distance of *M*–*M* (*M*

= Ag+Ge) in Ce_2AgGe_3, Pr_2AgGe_3 and Nd_2AgGe_3 are 2.4446(14) Å, 2.429(2) Å and 2.4211(16) Å, respectively, very close to the calculated Ge–Ge bond distances of 2.44 Å,[37] which suggests the germanium contribution at the 2*d* Wyckoff site but it is less than the atomic radii of Ag-Ag (2.88 Å) and Ge–Ag (2.85 Å).[37] The shortest *RE–M* bond distances in Ce_2AgGe_3, Pr_2AgGe_3 and Nd_2AgGe_3 are 3.2508(7) Å, 3.2311(10) Å and 3.1996(5) Å, respectively. Selected bond lengths for Ce_2AgGe_3, Pr_2AgGe_3 and Nd_2AgGe_3 are listed in **Table 5.5**. The coordination environments of *RE* and M sites are shown in **Figure 5.3b** and **5.3c**, respectively. The *RE* atoms are coordinated by 12 *M* atoms forming a pseudo Frank-Kasper cage. The *M* sites, on the other hand, form tricapped trigonal prism comprised of a total 9 metal atoms, 3*M* atoms and six *RE* atoms [M_3RE_6].

Nd_2NiGe_3. Preliminary analysis of powder XRD confirms that the compound is a hexagonal system. Nd_2NiGe_3 was previously reported in the AlB_2 structure type with *P*6/*mmm* space group.[38] In order to understand the detailed structure and properties, ND studies were carried out as well. Structural analyses on XRD and ND data were carried out by Rietveld method using Fullprof suite program.[39-40] A preliminary refinement on the powder XRD data was carried out by adopting a reported structural model and indexed in the *P*6/*mmm* space group and lattice parameters $a = b = 4.1445$ Å and $c = 4.1823$Å. **Figure 5.4** exhibits the Rietveld refined XRD patterns.

The crystal structure of Nd_2NiGe_3 along the *c*-direction is shown in **Figure 5.5a**. The compound crystallizes in the hexagonal AlB_2 structure type, space group *P*6/*mmm*. Nd atoms occupy the Al position while germanium and nickel atoms are statistically distributed in the boron position.[41] The crystal structure is composed of infinite arrays of planar hexagonal [$NiGe_3$] units stacked along the [001] direction and the Nd sites are sandwiched between these parallel hexagonal networks. The local coordination environments of Nd and *M* (*M* = Ni+Ge) atoms in the crystal structure of Nd_2NiGe_3 are presented in **Figure 5.5b** and **5.5c,** respectively. The Nd atom is sandwiched between the hexagonal layers of nickel and germanium atoms forming hexagonal bipyramidal geometry, whereas *M* [Ni+Ge] in Nd_2NiGe_3 is surrounded by 9 atoms (3 *M* atoms and six Nd atoms [M_3Nd_6]) in a tricapped trigonal prismatic geometry.

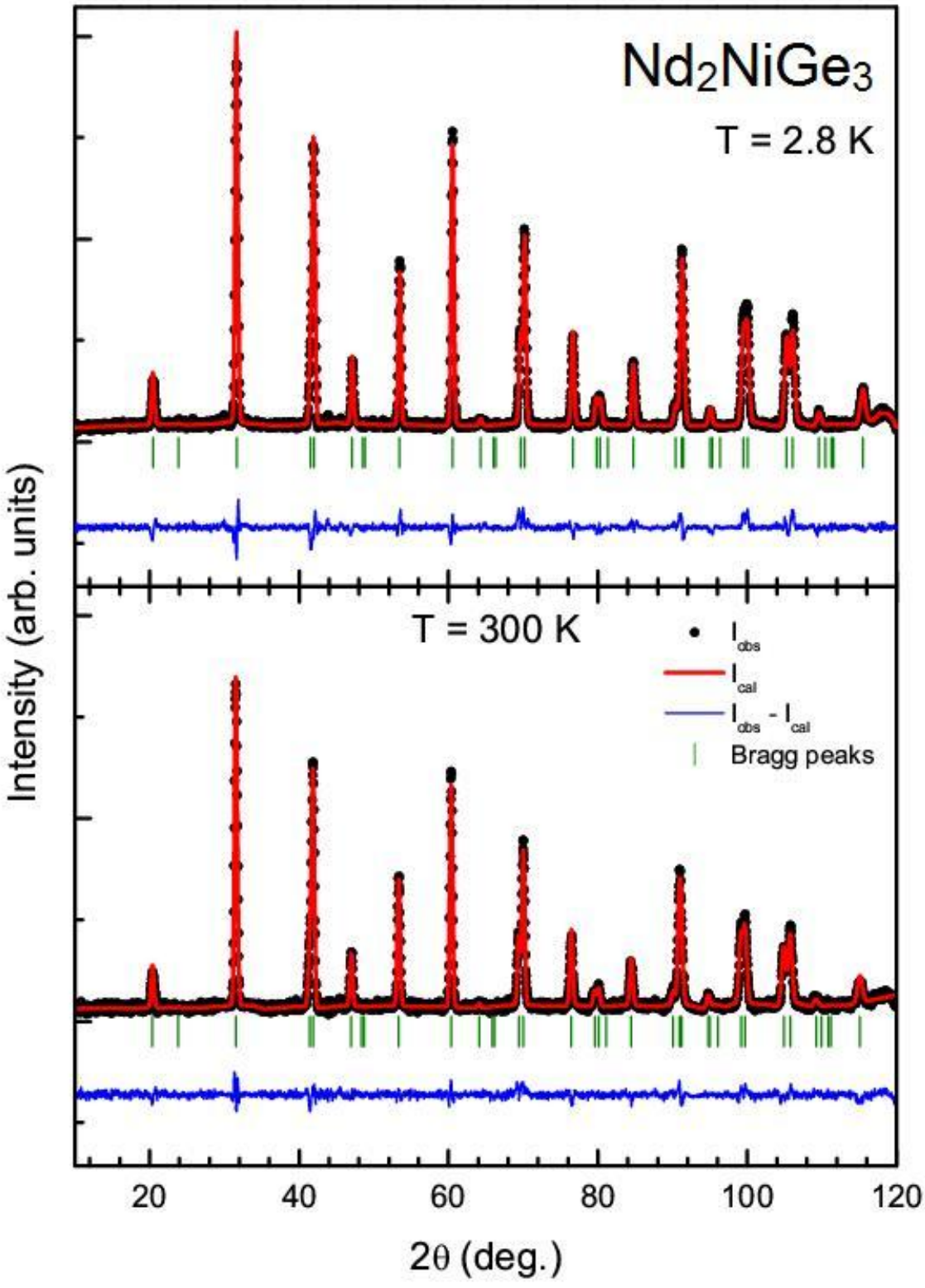

Figure 5.4 Neutron diffraction patterns for the Ni_2NiGe_3 at 2.8 K and 300 K. The solid line through the experimental points is the Rietveld refinement pattern. The difference between the observed and the experimental pattern is shown in blue color and short vertical bars indicate the Bragg peak positions.

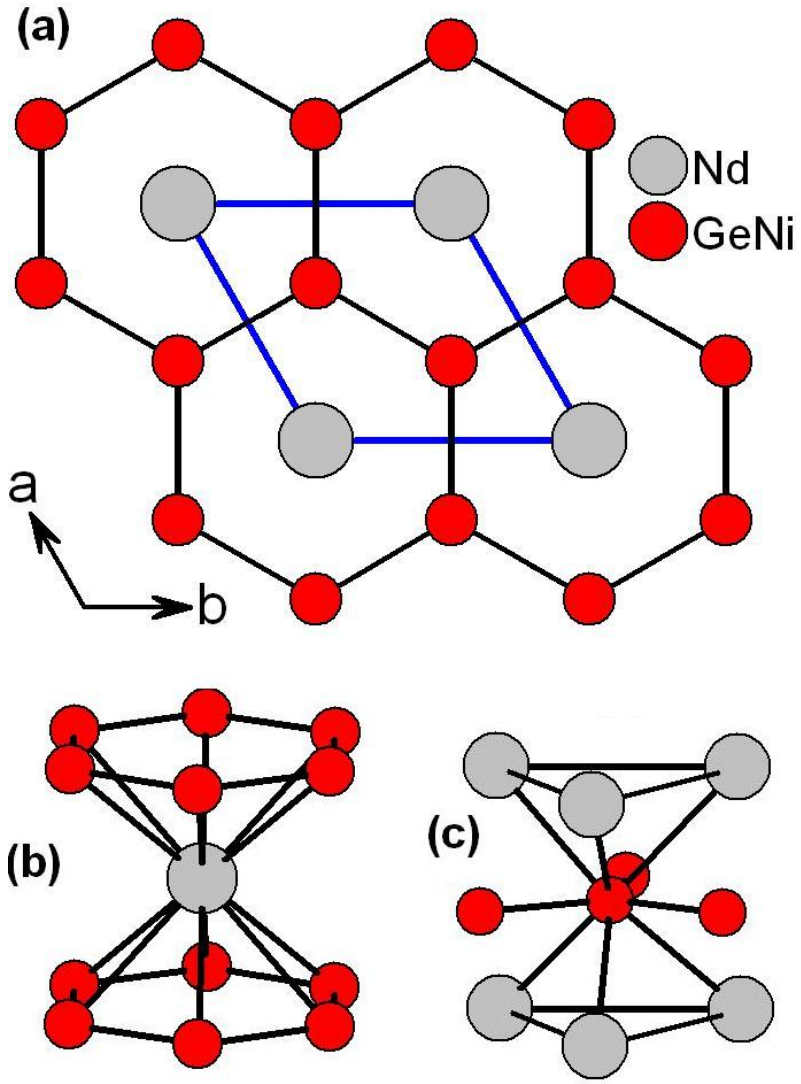

Figure 5.5 (a) Crystal structure of Nd_2NiGe_3 shown along the *c*-direction, (b) Coordination environment of Nd and (c) Coordination environment of Ni/Ge.

3.2.2 Neutron diffraction

ND measurements on Nd_2NiGe_3 were carried out at various temperatures between 2.8 and 300 K. As can be seen from the magnetization measurements *vide infra*, there are no signatures of long-range magnetic ordering in this compound, similar to another compound of this series, Ce_2NiGe_3.[36] ND data recorded at all temperatures were refined using the *P6/mmm* structure as mentioned earlier and the details of the refinement are summarized in **Table 5.6**. The unit cell volume and cell parameters show decreasing trend from room temperature down to lowest temperature (**Figure 5.6**). There is however a very small anomaly observed in cell parameters around 15 K probably due to structural reorientation as expected for the compounds in the AlB_2 type.

In **Figure 5.4**, Rietveld refinement profiles along with raw data are shown for ND patterns recorded at 2.8 and 300 K for direct comparison. As can be clearly seen from the figure, no additional Bragg peaks were observed in the case of 2.8 K profile when compared with the room temperature (300 K) profile. In addition, all the peaks in the pattern could be refined assuming the same structural model. Absence of any additional peak at 2.8 K thus rules out any long range magnetic order in this compound. Similar to Ce counterpart, it is assumed that Nd compound is also a strong candidate for studying the magnetic properties using inelastic neutron scattering experiment.

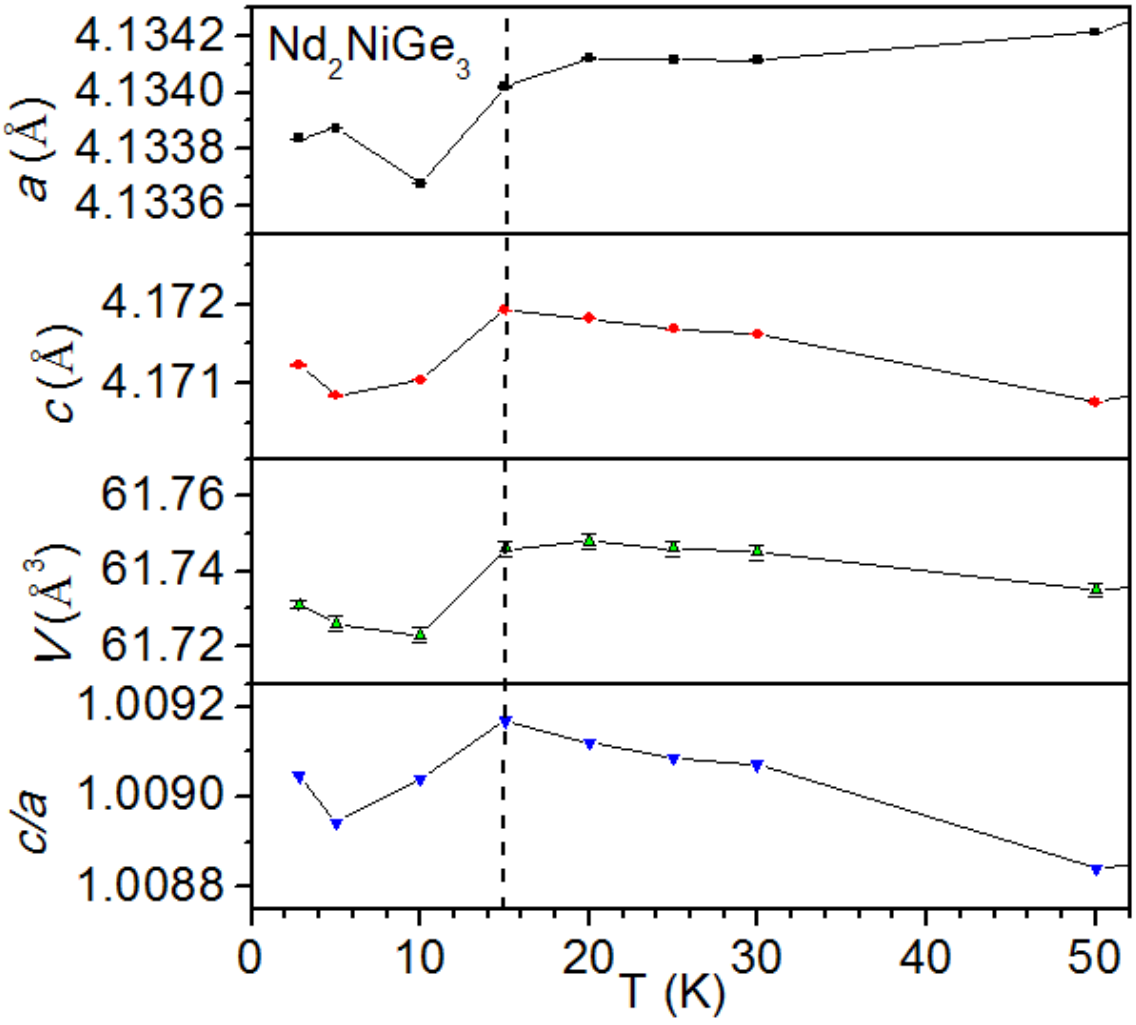

Figure 5.6 Variation of cell parameters as a function of temperature is plotted in different forms. The vertical dashed line is drawn to show the highlight the temperature at which anomaly occurs in the cell parameters.

Table 5.6 Structural parameters obtained from the Rietveld refinement of neutron-diffraction patterns of Nd_2NiGe_3 at temperatures between 2.8 K and 300 K. Space group: *P*6/*mmm* (# 191; general multiplicity = 24). *Nd* is at the atomic position (0 0 0), i.e., 1*a* as per the Wyckoff notation and Ni/Ge are at (1/3, 2/3, 1/2) i.e., at Wyckoff site 2*d*.

Temperature → / **Parameters ↓**	**2.8 K**	**5 K**	**10 K**	**20 K**	**30 K**	**300 K**
a (Å)	4.1338 (5)	4.1338 (5)	4.1336(5)	4.1341(5)	4.1341(5)	4.1425(5)
c (Å)	4.1712 (5)	4.1708 (5)	4.1710(5)	4.1718(5)	4.1716(5)	4.1829(5)
c/a	1.0090	1.0089	1.0090	1.0091	1.0090	1.0097
Volume ($Å^3$)	61.731(3)	61.726(3)	61.723(3)	61.748(3)	61.745(3)	62.173(3)
B_{equ} ($Å^2$)						
Nd@ 1*a*	0.4622	0.4621	0.4621	0.4623	0.4623	0.4645
Ni/Ge @ 2*d*	0.3990	0.4022	0.3722	0.4393	0.5050	0.8384
R-parameters						
R_p	7.57	8.82	8.71	9.57	11.20	9.10
R_{wp}	9.60	11.40	11.40	12.4	14.80	12.10
R_{exp}	3.20	3.24	3.17	3.25	3.53	3.48
χ^2	9.03	12.20	12.80	14.70	17.60	12.20
Bragg-R	5.57	5.66	5.15	5.87	6.14	3.85
Rf-factor	5.18	5.41	5.21	4.46	4.46	3.91
GoF	3.00	3.50	3.60	4.20	4.50	3.40

5.3.2. Magnetic Properties

***RE_2AgGe_3* (*RE* = Ce, Pr and Nd).** The temperature dependent magnetic measurements were carried out in an applied magnetic field of 100 Oe for Ce_2AgGe_3, Pr_2AgGe_3 and Nd_2AgGe_3 as shown in **Figures 5.7a**, **5.7c** and **5.7e,** respectively. At higher temperature, Ce_2AgGe_3 and Pr_2AgGe_3 obeyed Curie-Weiss (CW) law but Nd_2AgGe_3 obeyed modified CW law i.e $\chi(T) = \chi_o + C/(T- \theta_p)$ where, χ_o accounts for the temperature independent part (TIP) of magnetic susceptibility. Upon cooling, the magnetic susceptibility curve of Ce_2AgGe_3 increases sharply below 15 K which could arise due to ferromagnetic interaction. The CW fitting of the inverse magnetic susceptibility data in the range of 160-300 K yielded an effective magnetic moment of (μ_{eff}) 2.53 μ_B/Ce^{3+} and Curie paramagnetic temperature (θ_p) 7.1 (1) K respectively. The magnetic moment value is very close to the spin only value of 2.54 (1) μ_B/Ce^{3+}.[12] A bifurcation of the zero-field

cooled (ZFC) and field cooled (FC) susceptibility curves was observed which could arise due to various reasons like magnetic anisotropy and grain boundary pinning effects, etc (inset of **Figure 5.7a**).[42] The field dependent magnetization study at 2 K shows that Ce_2AgGe_3 exhibits sharp rise in magnetization (M) for small change in field (H). Above few kOe, M varies non-linearly with H, and exhibits hysteresis H → 0 as shown in **Figure 5.7b.**[42-43] Such a behavior may arise due to spin-flop transition. Magnetization of cerium compound at room temperature varies linearly with H, which confirms that the sample is single-phase and there are no undesirable magnetic impurities.

In the case of Pr_2AgGe_3, the temperature dependent magnetic susceptibility curve increases rapidly around 15 K followed by a broad cusp and rapid falling of χ on further decrease in T down to 10 K, followed by a bifurcation in ZFC and FC curves (**Figure 5.7c**) suggesting magnetic anisotropy or weak ferromagnet[44] like behavior. The effective magnetic moment (μ_{eff}) and curie paramagnetic temperature (θ_p) were calculated to be 4.33 (1) μ_B/Pr^{3+} and 4.0(1) K, respectively using the CW fit of the inverse susceptibility curve in the temperature range of 25 to 300 K. The magnetic moment of the compound is slightly higher than the spin only value of Pr (3.58 μ_B/Pr^{3+})[5] probably due to conduction electron polarization as observed in a similar compounds like Tb_2CuIn_3, Tb_2CuGe_3 and $EuAuIn_4$[42 45] although it was not reported in Pr based compounds. The positive θ_p suggests that a ferromagnetic interaction exists among the adjacent spins, but very weak in nature. The field dependent magnetization curve of Pr_2AgGe_3 shows a weak hysteresis at 2K indicating ferromagnetic transition (**Figure 5.7d**). The temperature dependent M vs. H data shows that this weak ferromagnetic coupling is suppressed at higher temperatures (10 and 50 K).

The magnetic susceptibility of Nd_2AgGe_3 shows a large increase below 25 K and has two maxima at T_{N1} = 3.5 K and T_{N2} = 11.8 K (**Figure 5.7e**) which are well supported by the temperature dependent resistivity data. The residual magnetic susceptibility (χ_0), effective magnetic moment (μ_{eff}) and curie paramagnetic temperature (θ_p) for this compound are -0.0013 emu/mol, 3.47(1) μ_B/Nd (theoretical effective paramagnetic moment for Nd^{3+} is 3.62 μ_B)[46] and 12.3(1) K, respectively obtained from the fitting of inverse molar magnetic susceptibility with modified Curie-Weiss law. This kind of multiple magnetic transitions is not uncommon and also observed in Nd_5Ge_3.[47-48]

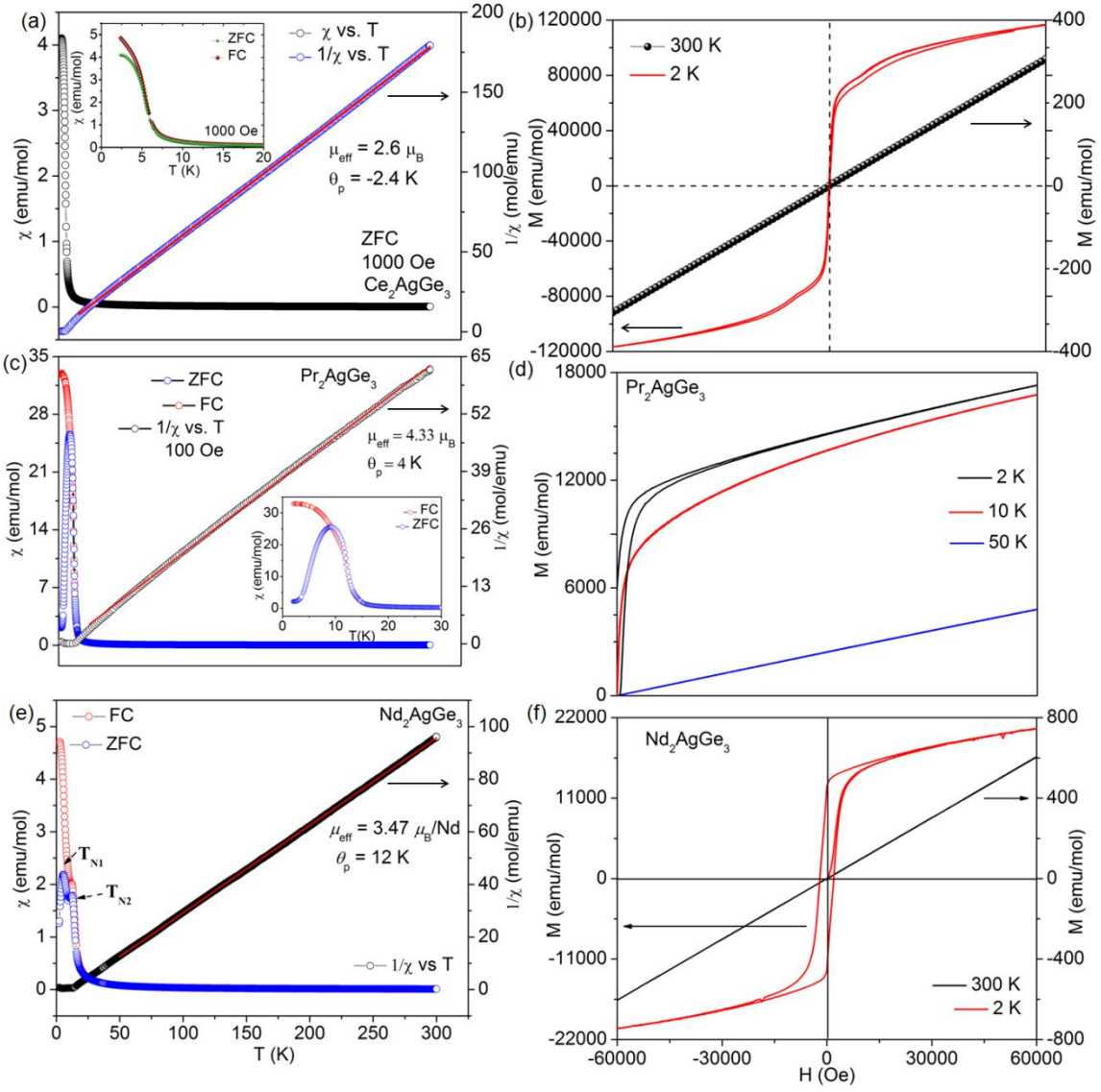

Figure 5.7 (a) Temperature dependence of the molar magnetic susceptibility of Ce_2AgGe_3 at 100 Oe applied magnetic field plotted against the *X* axis on the left-hand side. The inset shows the magnetic susceptibility at FC and ZFC modes. (b) Magnetization measured as a function of magnetic field at T = 2 and 300 K. (c) Magnetic susceptibility as a function of temperature for Pr_2AgGe_3 measured in a dc field of 100 Oe. (d) Magnetization measured as a function of magnetic field at T = 2, 10 and 50 K. (e) Magnetic susceptibility as a function of temperature for Nd_2AgGe_3 measured in a dc field of 100Oe. (f) Magnetization measured as a function of magnetic field at T = 2 and 300 K.

The field dependent magnetization data at 2 and 300 K for Nd_2AgGe_3 have been plotted in **Figure 5.7f**. M varies linearly with H in the measurement done at 300 K. At low temperature (2 K), a strong hysteresis is observed, which indicates ferrimagnetic like-coupling is the dominant magnetic interactions among the magnetic spins. It is not clear

at this moment that what should be the reason for a ferrimagnetic like behavior, since there is only one Nd site per formula unit in this structure. However, owing to the fact that there are two antiferromagnetic transitions, it is possible that at low temperatures, both the antiferromagnetic states coexist, giving rise to such a hysteretic magnetization behavior. Ferrimagnetic like state, two magnetic transitions and strong magnetic anisotropy makes this system an interesting candidate for detailed study using different probes and techniques.

Nd_2NiGe_3. The temperature dependent molar magnetic susceptibility and inverse susceptibility of Nd_2NiGe_3 is shown in **Figure 5.8a**. The measurement was carried out in a field of 1 kOe after cooling the sample in presence and absence of applied magnetic field. Fitting the curve with Curie-Weiss law in the temperature range 20-300 K gives an effective magnetic moment (μ_{eff}) of 5.42 μ_B/f. u., which turns out to be about 3.83 μ_B/Nd. The value of μ_{eff} per Nd atom is slightly higher than theoretical value (3.62 μ_B) of the trivalent free Nd ion (considering S = 3/2, L = 6 and J = 9/2).[38] The calculated paramagnetic Curie temperature (θ_P) is -2.1 K, which indicates antiferromagnetic interactions although its low magnitude hints that this interaction is very weak in nature. With decreasing temperature, the magnetic susceptibility increases gradually and does not exhibit any sharp transition which could be considered as a magnetic ordering and hence this compound can be classified as a weak paramagnet or a Pauli paramagnet at this field.[38] However, a sharp upturn can be observed at very low magnetic field (10 Oe) as shown in the inset of **Figure 5.8a**. This clearly indicates that the adjacent Nd spins order antiferromagnetically at lower applied field but this coupling being very weak in nature collapses under higher applied field. At this point, the role of the Ni sublattice is not clear and is perhaps quenched by stronger paramagnetic interaction of the *RE* atoms. The effective magnetic moment does not seem to be much affected by Ni sublattice.

The field dependence of magnetic moment at 300 and 2 K is shown in **Figure 5.8b**. The high temperature curve increases linearly with magnetic field passing through the origin hinting a paramagnetic behavior. At low temperature (2 K), the moment, however, increases sharply up to 30 kOe followed by a curvature. The moment however does not saturate up to the highest applied field and is calculated to be 2.2 μ_B which is around 61% of the expected value indicating the presence of crystalline field effect in this compound resulting in the reduction of the expected saturation magnetization value.

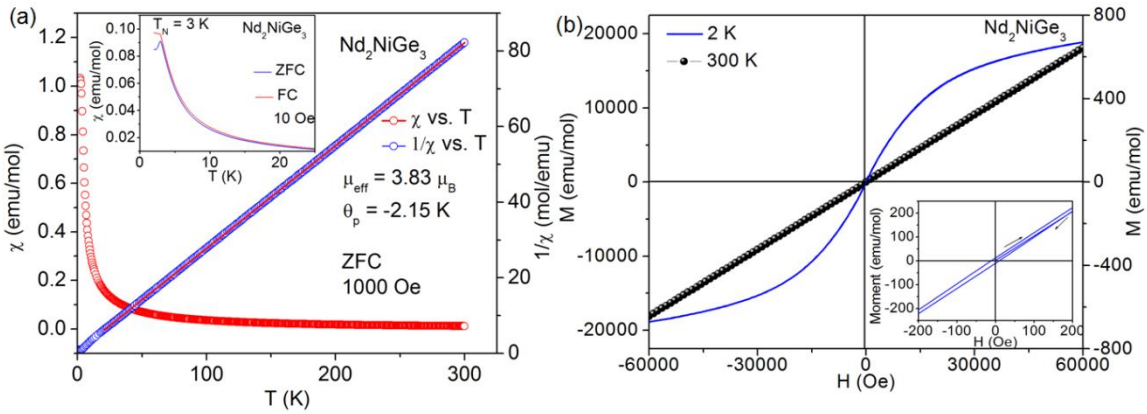

Figure 5.8 (a) Temperature dependence of magnetic susceptibility and inverse magnetic susceptibility at 1000 Oe applied magnetic field, the inset shows Temperature dependence of magnetic susceptibility in zero field cooled (ZFC) and field cooled (FC) modes at 10 Oe. (b) Field dependence of magnetic moment at 2 and 300 K. The inset shows the expanded view of the weak hysteresis.

5.3.4. Resistivity

The electrical resistivity of Ce_2AgGe_3, Pr_2AgGe_3 and Nd_2AgGe_3 are shown in **Figure 5.9a, b**, and **c,** respectively. In the high temperature range, resistivity increases with increase in temperature for all the samples which is a typical and common behavior of metallic systems. The resistivity of Ce_2AgGe_3 measured is equal to 10.86 $\mu\Omega$ cm at 200 K, decreases with temperature down to about 22 K[49] beyond which it increases up to 15 K. This behavior is reminiscent of Kondo scattering which has been observed in many other Ce based compounds like Ce_2RhSi_3.[12] At low temperature region, ρ vs T shows a maxima at 6.4 K and finally drops down to a value of 10.2 $\mu\Omega$ cm at 3 K indicating a magnetic phase transition in corroboration with the magnetic susceptibility data. The resistivity of Pr_2AgGe_3 decreases linearly with decreasing temperature from 200 K down to 15 K followed by a peak at 11 K indicating the magnetic ordering observed in magnetic susceptibility measurement. A similar behavior was also observed in case of Pr_2CuSi_3.[2]

Nd_2AgGe_3 also follows the same trend at higher temperature range wherein the resistivity decreases almost linearly down to 25 K. Below this temperature, a dip is observed around 20 K which is followed by a rise in resistivity with decrease in temperature. The occurrence of a dip in the low temperature resistivity plot in a Nd based intermetallic compound is unusual since this phenomenon cannot be attributed to Kondo

effect arising from Nd *f*-electrons. The situation is similar to that observed in cases of previously reported $GdPd_2Si$[50] and $GdNi_2Si_2$[51] where the authors have proposed spin-fluctuations at the transition metal lattices as the possible origin of increase in resistivity at low temperature. The actual reason for this phenomenon, however, still remains questionable and urges for further investigations.

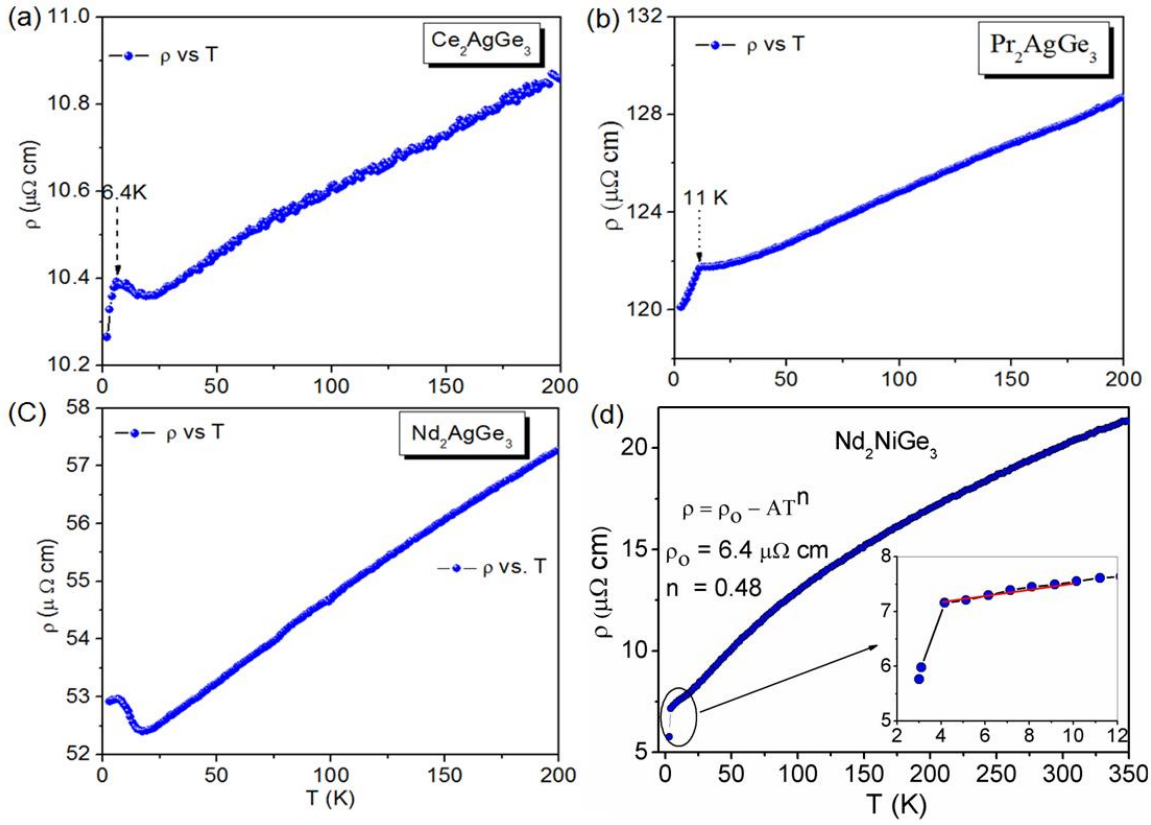

Figure 5.9 Electrical resistivity (ρ) of (a) Ce_2AgGe_3, (b) Pr_2AgGe_3 and (c) Nd_2AgGe_3 and (d) Nd_2NiGe_3 measured as a function of temperature.

Nd_2NiGe_3. The temperature dependent electrical resistivity of the Nd_2NiGe_3 sample in the temperature range 3-300 K is shown in **Figure 5.9d**. In the low temperature range, there is a sudden drop in resistivity near 3 K and it sharply decreases with further decrease in temperature. This could arise due to onset of ferromagnetic ordering as also observed in another AlB_2 type compound, Eu_2CuSi_3.[52 53] At temperatures below 10 K, the ρ(T) data can be fitted to the power law function, $\rho = \rho_0 + AT^n$, where ρ_0 is the residual resistivity expressed in units of $\mu\Omega$ cm and A and n are the fitting parameters.[54] The residual resistivity (ρ_0) was 6.4 μΩ cm and power factor was 0.48. The low value of n hints that the conduction electrons are not strongly correlated to the localized 4*f* orbitals and the system shows non-Fermi liquid behavior (NFL)[55] i.e. it does not behave like a

Fermi liquid in its ground state, in that case the power value would have been closer to two.[56] The residual resistivity ratio (RRR), ρ_{300}/ρ_0 for this compound is 3.2, considerably higher than 1, indicates that the sample purity is quite high and defect free.[57]

5.4. Concluding Remarks

A series of disordered compounds have been synthesized in both the α and β polymorphs in the α-$ThSi_2$ family. The first series consists of already known Pr_2AgGe_3 and two new compounds namely, Ce_2AgGe_3 and Nd_2AgGe_3, which crystallize in the tetragonal α-$ThSi_2$ type structure. All the compounds reported here show interesting magnetic properties which provide a robust platform for further detailed study of the magnetic structure of these compounds using neutron diffraction technique. In the second Existence of these compounds in the RE_2AgGe_3 series further motivated us to look for new compounds with other rare earth elements. Preliminary attempts to synthesize the Sm and Gd analogues by arc melting technique were unsuccessful; however, different methods and various reaction conditions are being explored currently.

5.5. References

1. Huo, D. X.; Sakurai, J.; Kuwai, T.; Isikawa, Y.; Lu, Q. F., *Phys. Rev.B* **2001,** *64*, 224405.

2. Tien, C.; Luo, L.; Hwang, J. S., *Phys. Rev. B.* **1997** *56*, 11710.

3. Hwang, J. S.; Lin, K. J.; Tien, C., *Solid State Commun.* **1996,** *100*, 169.

4. Li, D. X.; Zhao, X.; Nimori, S., *J. Phys.: Condens. Mat.* **2009** *21*, 026006.

5. Chen, J. W.; Guan, S. Y.; Wang, C. H., *The 2nd International Symposium on Advanced Magnetic Materials and Applications, July 12–16,2010 Sendai, Japan* **2011,** *266*, 012006.

6. Rojas, D. P.; Rodríguez Fernández, J.; Espeso, J. I.; Gómez Sal, J. C.; da Silva, L. M.; Gandra, F. G.; dos Santos, A. O.; Medina, A. N., *J. Magn. Magn. Mater.* **2010,** *322* 3192.

7. Gordon, R. A.; Warren, C. J.; Alexander, M. G.; Disalvo, F. J.; Pöttgen, R., *J. Alloys Compd.* **1997,** *24*, 248.

8. Szytuła, A.; Hofmann, M.; Penc, B.; Slaski, M.; Majumdar, S.; Sampathkumaran, E. V.; Zygmunte, A., *J. Magn. Magn. Mater.* **1999** *202*, 365.

9. Szlawska, M.; Kaczorowski, D., *Phys. Rev. B.* **2011,** *84*, 094430.

10. Yubuta, K.; Yamamura, T.; Shiokawa, Y., *J. Phys.: Condens. Mat.* **2006,** *18* 6109.

11. Li, D. X.; Nimori, S.; Shiokawa, Y.; Haga, Y.; Yamamoto, E.; Onuki, Y., *Solid State Commun.* **2001,** *120* 227.

12. Kase, N.; Muranaka, T.; Akimitsu, J., *J. Magn. Magn. Mater.* **2009** *321*, 3380.

13. Cheng, T.; Chung, H. F.; Ching, S. W.; Jenq, J. L., *Phys. Rev. B* **2000,** *61*, 12151-12158.

14. Raghavan, V., *J. Phase Equilib. Diff.* **2008,** *29* (5), 436-437.

15. Salamakha, P. S.; Konyk, M. B.; Dzyanyi, R. B.; Sologub, O. L.; Bodak, O. I., *Pol. J. Chem.* **1996** *70* 270-274.

16. Morozkin, A. V., *J. Alloys Compd.* **2004,** *370* (1-2), L1-L3.

17. Kalsi, D.; Udumula, S.; Rayaprol, S.; Peter, S. C., *J. Solid State Chem.* **2014,** *212*, 73-80.

18. Mayer, I.; Felner, I., *J. Solid State Chem.* **1973,** *8* (4), 355-356.

19. Fedyna, M. F.; Pecharskii, V. K.; Bodak, O. I., *Dopov. Akad. Nauk Ukr. RSR (Ser. B).* **1987**, 2-50.

20. Dzioba, M. M.; Savysyuk, I. A.; Shcherban, O. O.; Gladyshevskii, E. I., *Visn. L'viv. Derzh. Univ. (Ser. Khim.)* **1996**, 36-59.

21. Fedyna, M. F.; Bodak, O. I.; Pecharskii, V. K., *Inorg. Mater.* **1991,** *27*, 918-920.

22. Demchenko, P. Y.; Bodak, O. I., *J. Alloys Compd.* **2000,** *307*, 215-217.

23. Salamakha, P. S.; Demchenko, P. Y.; Sologub, O. L.; Bodak, O. I., *J. Alloys Compd.* **1998,** *278*, 227-230.

24. Bodak, O. I.; Salamakha, P. S.; Sologub, O. L., *J. Alloys Compd.* **1997,** *256*, L8-L9.

25. Sebastian, C. P.; Malliakas, C. D.; Chondroudi, M.; Schellenberg, I.; Rayaprol, S.; Höffmann, R. D.; Pöttgen, R.; Kanatzidis, M. G., *Inorg. Chem.* **2010,** *49* (20), 9574-9580.

26. Sarkar, S.; Gutmann, M. J.; Peter, S. C., *CrystEngComm.* **2013,** *15*, 8006–8013.

27. Sarkar, S.; Peter, S. C., *J. Chem. Sci.* **2012,** *124* (6), 1385-1390.

28. Merlo, F.; Pani, M.; Canepa, F.; Fornasini, M. L., *J. Alloy Compd.* **1998,** *264* (1-2), 82-88.

29. Pani, M.; Merlo, F.; Fornasini, M. L., *Z. Kristallogr.* **1999,** *214* (2), 108-110.

30. Pöttgen, R.; Gibson, B.; Kremer, R. K., *Z. Kristallogr.* **1997,** *212* (1), 58-58.

31. Sebastian, C. P.; Kanatzidis, M. G., *J. Solid State Chem.* **2010,** *183* (4), 878-882.

32. Sarkar, S.; Kalsi, D.; Rayaprol, S.; Peter, S. C., *J. Alloys Compd.* **2015,** *632* (0), 172-177.

33. Sheldrick, G. M., *SHELXTL 5.10; Bruker Analytical X-ray Systems, Inc.: Madison,WI,* **1998**.

34. Sheldrick, G. M., *SHELXTL, Structure Determination Program,version 5; Siemens Analytical X-ray Instruments, Inc.: Madison, WI,* **1995**.

35. Putz, H.; Brandenburg Gb R, K. i. G. B., (Ed.).

36. Kalsi, D.; Rayaprol, S.; Siruguri, V.; Peter, S. C., *J. Solid State Chem.* **2014,** *217*, 113-119.

37. Pauling, L., *Third ed.,Cornel University Press, Ithaca, NY.* **1960**.

38. Chen, J. W.; Guan, S. Y.; Wang, C. H., *J. Phys. Conf. Ser.* **2011,** *266*, 012006.

39. Rietveld, H. M., *J. Appl. Crystallogr.* **1969,** *2*, 65.

40. Rodriguez-Carvajal, J., *Physica B* **1993,** *192*, 55.

41. Chevalier, B.; Pottgen, R.; Darriet, B.; Gravereau, P.; Etourneau, J., *J. Alloy Compd.* **1996,** *233* (1-2), 150-160.

42. Majumdar, S.; Sampathkumaran, E. V., *Solid State Commun.* **2001,** *117* (11), 645-648.

43. Sarkar, S.; Subbarao, U.; Joseph, B.; Peter, S. C., *J. Solid State Chem.* **2015,** *225* (0), 181-186.

44. Lacerda, A.; Canfield, P. C.; Beyermann, W. P.; Hundley, M. F.; Thompson, J. D.; Sparn, G.; Fisk, Z.; Burns, C.; Barnhart, D.; Lawson, A. D.; Kwei, G. H.; Goldstone, J., *J. Alloys Compd.* **1992,** *181*, 191.

45. Sarkar, S.; Gutmann, M. J.; Peter, S. C., *Dalton Trans.* **2014,** *43* (42), 15879-15886.

46. Kozak, R.; Kaczorowski, D.; Gladyshevskii, R., *Chem. Met. Alloys* **2012,** *5*, 16-22.

47. Roy, S. B.; Chattopadhyay, J. K.; Chaddah, P.; Moore, J. D.; Perkins, G. K.; Cohen, L. F.; Gschneidner Jr, K. A.; Pecharsky, V. K., *Phys. Rev. B* **2006,** *74*, 012403.

48. Tsutaoka, T.; Tanaka, A.; Narumi, Y.; Iwaki, M.; Kindo, K., *Physica B.* **2010,** *405*, 180-185.

49. Dremov, R. V.; Koblyuk, N.; Mudryk, Y.; Romaka, L.; Sechovsky, V., *J. Alloys Compd.* **2001,** *317*, 293−296.

50. Rawat, R.; Das, I., *J. Phys. Condens. Matter.* **2001,** *13* (3), L57.

51. Das, I.; Sampathkumaran, E. V., *Phys. Rev. B* **1994,** *49* (6), 3972-3974.

52. Cao, C. D.; Klingeler, R.; Vinzelberg, H.; Leps, N.; Löser, W.; Behr, G.; Muranyi, F.; Kataev, V.; Büchner, B., *Phys. Rev. B* **2010,** *82* (13), 134446.

53. Majumdar, S.; Mallik, R.; Sampathkumaran, E. V.; Rupprecht, K.; Wortmann, G., *Phys. Rev. B* **1999,** *60* (9), 6770-6774.

54. Kambe, S.; Suderow, H.; Fukuhara, T.; Flouquet, J.; Takimoto, T., *J. Low Temp. Phys.* **1999,** *117*, 101-112.

55. Stewart, G., *Rev. Mod. Phys.* **2001,** *73*, 797-855.

56. Coleman, P., *Introduction to Many Body Physics*. In Rutgers University Press: USA, 2004.

57. Sarkar, S.; Gutmann, M. J.; Peter, S. C., *Cryst. Growth Des.* **2013,** *13* (10), 4285-4294.

Chapter 6

Crystal Structure and Magnetic Properties of Indium Flux Grown $EuTIn_4$ and $EuAu_2In_4$

6.1. Introduction

Indides containing *RE* atoms as one of the active constituents are widely studied for their interesting and versatile physical properties e.g. the compounds EuAuIn and EuPdIn show metamagnetic behavior,[1] EuInGe shows multiple magnetic transitions,[2] EuRhIn is a ferromagnet at 22 K,[3] YCu_4In and $LuCu_4In$ are semimetallic in nature,[4] Dy_2CuIn_3 shows spin glass behavior below 9 K,[5] Ce_2Pt_2In and YbPtIn show Kondo effect[6-7] and $CeAg_xIn_{1-x}$ shows structural transition.[8] Indides containing Ce, Eu and Yb may further show anomalous behaviors owing to the valence fluctuation as these elements have two energetically closely spaced valence states namely $Ce^{3+/4+}$, $Eu^{2+/3+}$ and $Yb^{2+/3+}$, respectively. Important examples of mixed and intermediate valency in intermetallics include CeRhIn,[9] CeNiIn,[10] Ce_2T_2In (T = Ni and Pd)[11] and $YbCu_4In$[12]. Apart from the physical properties mentioned above, these indides are also important owing to their wide range of structural versatility.

Compounds containing In-In polymeric units are in general known as polyindides. A common structural feature in most of the *RE* based ternary polyindides containing transition metals (generally represented as $RE_xT_yIn_z$, (where, *RE* = alkaline and rare earth metals, *T* = transition metals) is the occurrence of two- or three-dimensional $[T_xIn_y]$ polyanionic network. The *RE* atoms reside in the cage-like channels created by the transition metals and indium atoms. Many indium rich compounds are well studied because of their interesting physical properties. For example, heavy fermion behavior in $Ce_5Ni_6In_{11}$[13] and Ce_2AgIn_3,[14] heavy fermion superconductivity in Ce_2Tin_8 (*T* = Pd, Pt) and $CeTIn_5$ (*T* = Co, Rh, Ir)[15] and mixed valence behavior in $YbCu_6In_6$.[16,17]

$EuIrIn_4$ is the first member in the Eu-Ir-In family, however, there are many compounds which were explored within the Eu-Au-In family by researchers, the equiatomic EuAuIn[1] crystallizes in the simple TiNiSi structure type but the structural complexity increases with increasing indium content in $EuAuIn_2$,[18] $EuAu_3In_3$[19] and $Eu_2Au_3In_4$.[20] Compounds with general formula RE_2Au_2In are quite interesting owing to their selective adoption of the U_3Si_2 structure type when *RE* = La-Gd, whereas compounds with *RE* = Tm-Lu adopt the Zr_3Al_2 type structure. Two new indium rich compounds have been synthesized in this family, $EuAu_2In_4$ and $EuAuIn_4$ for the first time using In as active metal flux. The structural aspects of polyindides with general formula $RETIn_4$ have been widely studied in the past. $CaTIn_4$ (*T* = Rh, Pd, Ir), $EuPdIn_4$, $YbPdIn_4$,

$YbRhIn_4$, *RE*$NiIn_4$ (*RE* = Ca, Ce, Eu, Yb), $EuCuIn_4$ are a few representative indides in this family. These compounds mainly crystallize in the $YNiAl_4$ or $LaCoAl_4$ structure types and also consist of three dimensional polyanionic units of [*T*In_4] resulting in the cage-like channels in which the *RE* atoms are embedded. Salvador and Peter *et al* reported[21-22] a few *RE*Au_2In_4 compounds with *RE* = La, Ce, Pr, Nd and Yb. Except Yb analog, members in this family crystallize in an orthorhombic structure with *Pnma* space group. These compounds can be regarded as polar intermetallics consisting of a complex $[Au_2In_4]^{2-}$ polyanionic network in which the *RE* ions are embedded. The $[Au_2In_4]^{2-}$ network features In tetramer units, which defines the compounds as polyindides. The motivation of this chapter is the continued development of the intermetallic chemistry of Eu and the deeper understanding of its ability to adopt different structures and mixed oxidation states.[2, 23-24] Recent discoveries on new compounds using indium as metal flux are also inspiring to exploratory synthetic chemists.[25-32]

In this chapter two classes of compounds will be discussed; the first belongs to Eu*T*In_4 (*T* = Ir and Au) and the second compound is $EuAu_2In_4$ which is a new member in the previously mentioned *RE*Au_2In_4 family. Both of these families belong to a homologous series of $EuAu_nIn_4$ (n = 1, 2) having rod and plate like shapes respectively, and were synthesized using indium as an active metal flux. A deep insight into the crystal structure of these compounds as will be discussed in details in the subsequent sections reveals that though these structures may apparently look different, they, in effect, are evolved from the same AlB_2 prototype by infusing transition metals and indium atoms in the ordered vacancies of $EuIn_2$ structure (which is basically a vacancy ordered superstructure derived from AlB_2 structure). This kind of stuffing however causes a many structural distortions e.g. modulation of the unit into a supercell, puckering/flattening of the layers, etc. which have further implications in their physical properties as well. All the compounds discussed in this chapter crystallize in orthorhombic system and can be classified as polyindide systems due to the presence of [In_4] tetrameric units. Both $EuIrIn_4$ and $EuAuIn_4$ adopts the $YNiAl_4$ structure type with *Cmcm* space group and lattice parameters *a* = 4.5206(9) Å, *b* = 16.937(3) Å, *c* = 7.2661(15) Å and *a* = 4.6080 (3) Å, *b* = 17.0454 (8) Å and *c* = 7.5462 (4) respectively. $EuAu_2In_4$ crystallizes in the $NdRh_2Sn_4$ structure type with *Pnma* space group and lattice parameters *a* = 18.5987 (7) Å, *b* = 4.6616 (2) Å and *c* = 7.4669 (3) Å. $EuAuIn_4$ and $EuIrIn_4$ consist of three dimensional [*T*In_4] units and the europium atoms reside in the distorted hexagonal channels, whereas

in $EuAu_2In_4$, the europium atoms are enclosed by three dimensional cages of $[Au_2In_4]$ polyanionic units. Magnetic susceptibility measurements on $EuIrIn_4$ showed two successive antiferromagnetic transitions at 5.4 and 10.8 K respectively and the modified Curie-Weiss fitting on the inverse magnetic susceptibility data within the temperature region 15-300 K gave the effective magnetic moment of 8.45 μ_B/Eu. $EuIrIn_4$ also showed pronounced magnetic anisotropy perpendicular to the direction of applied magnetic field The effective magnetic moment (μ_{eff}) for $EuAuIn_4$ and $EuAu_2In_4$ were 5.88 μ_B and 7.76 μ_B/Eu atom, respectively.

6.2 Experimental Section

6.2.1 Synthesis

Europium (ingots, 99.99%, ESPI metals), iridium (powder, 99.99%, Alfa Aesar), gold (ingots, 99.99%, Alfa-Aesar) and indium (tear drops, 99.99%, Alfa Aesar) were used as purchased without any further purification.

6.2.1.1 Metal flux method

One mmol of europium, 1 mmol of gold/iridium and 10 mmol of indium for $Eu\mathit{T}In_4$ (T = Ir and Au) and 1 mmol of europium, 2 mmol of gold and 16 mmol of indium for $EuAu_2In_4$ were combined in an alumina crucible under an inert (argon) atmosphere inside a glove box. Here the excess indium acts as an active metal flux. The crucible was placed in a 13 mm quartz tube and was flame-sealed under vacuum of 10^{-6} torr, to prevent oxidation during heating. The tube was then placed in a vertical tube furnace and was heated to 1273 K in 10 h, kept at that temperature for 6 h. The temperature was then lowered down to 1123 K in 2 h and annealed at this temperature for 72 h. On the other hand for the synthesis of $EuAu_2In_4$, the tube was heated to 1273 K over the period of 10 h, annealed at that temperature for 72 h. Finally, the system was allowed to cool slowly to room temperature in 48 h. The reaction products were isolated from the excess indium flux by heating at 623 K and subsequent centrifugation through a coarse frit. The remaining flux was removed by immersion and sonication in glacial acetic acid for 24 h. The final crystalline product was rinsed with water and dried with acetone in a vacuum oven at 350 K overnight. $EuIrIn_4$ were formed as rod shaped shiny single crystals (**Figure 6.1a**). During the synthetic optimization of $EuIrIn_4$ with different reaction conditions, another new phase $Eu_3Ir_2In_{15}$, was discovered which crystallizes in tetragonal *P*4/*mbm*.

This compound was studied separately and is not included in this thesis as does not belong to AlB_2 family. The $EuAuIn_4$ compound was grown as shiny plate like crystals with an average length of 4-5 mm and 1-2 mm in breadth (**Figure 6.1b**), whereas, $EuAu_2In_4$ grew as metallic silver rods (**Figure 6.1c**) with average size of 3-4 mm. All three compounds were stable in air and moisture with no decomposition observed even after several months. Eu*T*In_4 was obtained in 80% yield with $EuIn_2$ and $AuIn_2$ as the main impurity phases whereas $EuAu_2In_4$ was produced in relatively high yield of around 97%. Single crystals were carefully selected for elemental analysis, structure characterization and magnetic measurements.

6.2.1.2 High frequency induction heating

Europium, gold/iridium and indium metals were taken in the ideal 1:1:4 and 1:2:4 atomic ratios for Eu*T*In_4 and $EuAu_2In_4$, respectively, and sealed in tantalum ampoules in an arc-melting apparatus (Edmund Bìühler Gmbh, compact arc melter MAM-1) under argon atmosphere. The sealed tantalum ampoules were then placed in a water-cooled sample chamber of an induction furnace (EasyHeat induction heating system, Model 7590), first rapidly heated to ca. 1273 K and kept at that temperature for 30 min. Then the induction furnace was switched off and the sample was cooled down to room temperature naturally. The brittle product with metallic lustre could easily be separated from the tantalum tube. No reaction with the container was observed. The compounds are stable in air for at least several months. The products were obtained in high yield and no other impurity phases were found up to the detection limit of XRD.

6.2.2 Elemental Analysis

Quantitative microanalysis on $EuIrIn_4$, $EuAu_2In_4$ and $EuAuIn_4$ were performed with a FEI NOVA NANOSEM 600 instrument equipped with an EDAX® instrument. Data were acquired with an accelerating voltage of 20 kV and a 100 s accumulation time. Typical metallic rod and plate shaped single crystals of $EuAu_2In_4$ and $EuAuIn_4$ obtained from the flux method are shown in **Figure 6.1a**, **6.1b** and **6.1c**, respectively. The EDAX analysis was performed using P/B-ZAF standardless method (where, Z = atomic no. correction factor, A = absorption correction factor, F = fluorescence factor, P/B = peak to background model) on visibly clean surfaces of the crystals. The microanalysis on different spots on the crystal gave an average atomic wt % composition16(2)% Eu, 16(3)% Ir and 65(2)% In for $EuIrIn_4$; 16(1)% Eu, 18(2)% Au and 65(4)% In for $EuAuIn_4$;

13(2)% Eu, 32(3)% Au and 55(3)% In for $EuAu_2In_4$ which match well with the composition obtained from XRD on single crystals.

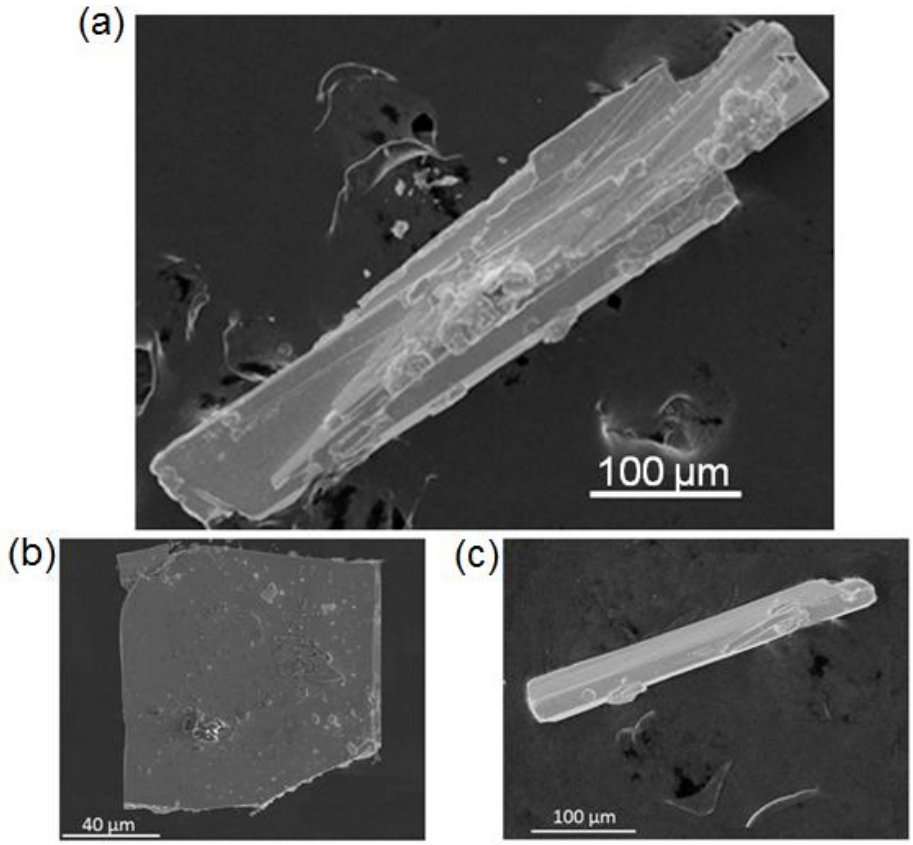

Figure 6.1 FE SEM images of representative single crystals of (a) $EuIrIn_4$, (b) $EuAuIn_4$ and (c) $EuAu_2In_4$.

6.2.3 Powder XRD

To determine the phase identity and purity, powder XRD pattern of $EuIrIn_4$, $EuAuIn_4$ and $EuAu_2In_4$ were collected at room temperature on a Bruker D8 Discover X-ray diffractometer with Cu-K_α X-ray source (λ = 1.5406 Å), equipped with a position sensitive detector in the angular range $20^o \leq 2\theta \leq 90^o$ with the step size 0.02^o and scan rate of 0.5 s/step calibrated against corundum standards. The experimental patterns were compared to the pattern calculated from the single crystal structure refinement. The comparison of the powder patterns with the simulated pattern obtained from the single crystal data are shown in **Figure 6.2a**, **b** and **c**, respectively.

6.2.4 Single Crystal XRD

Manually selected single crystals of the corresponding samples ($EuIrIn_4$, $EuAuIn_4$ and $EuAu_2In_4$) were mounted on a thin glass fiber. X-ray single crystal structural data were

collected at room temperature on a Bruker Smart CCD diffractometer equipped with a normal focus, 2.4 kW sealed tube X-ray source with graphite monochromatic Mo-Kα radiation (λ = 0.71073 Å) operating at 50 kV and 30 mA. A crystal of suitable size was cut from a rod-shaped crystal and mounted on a thin glass (~0.1 mm) fiber with commercially available super glue. The program SAINT[33] was used for integration of diffraction profiles along with the SADABS package suite[34] to apply numerical absorption corrections.

6.2.5 Structure Refinement

Preliminary data analysis suggested that both $EuIrIn_4$ and $EuAuIn_4$ possess *c*-centered orthorhombic crystal system and *mmm* Laue class. The lattice parameters obtained were *a* = 4.5206(9) Å, *b* = 16.937(3) Å and *c* = 7.2661(15) Å and *a* = 4.6080 (3) Å, *b* = 17.0454 (8) Å, *c* = 7.5462 (4) Å, respectively for $EuIrIn_4$ and $EuAuIn_4$ were compatible with the $YNiAl_4$ structure type. EDAX data also hinted a rough composition (atomic weight %) of 1:1:4 for Eu, Ir/Au and In, respectively. Therefore, the atomic coordinates of $YNiAl_4$ were taken as a model and the structures were refined using SHELXL-97 (full-matrix least-squares on F^2)[35] with anisotropic atomic displacement parameters for all atoms. The occupancy parameters were refined in a separate series of least-squares cycles in order to check the correct composition. The data collected at high exposure time (40s/frame) owing to the high X-ray absorption cross-section of Ir. Due to the unusual displacement parameter for In1 for the data at room temperature, the data had to be collected at low temperature (100 K) for $EuIrIn_4$, whereas in case of the Au analogue the data was collected at room temperature with an exposure time of 30s/frame. In the case of $EuAu_2In_4$ showed a primitive orthorhombic cell and the systematic extinctions were compatible with the space group *Pnma* with lattice parameters *a* = 18.5987 (7) Å, *b* = 4.6616 (2) Å and *c* =7.4669 (3) Å. Finally, the resulting atomic displacement parameters of all positions became well-behaved and the final difference maps showed residuals that were reasonably acceptable. The final compositions obtained from single crystal XRD data corroborate well with EDAX data.

The data collection and refinement parameters for all compounds are summarized in **Table 6.1**. The atomic coordinates and equivalent atomic displacement parameters, anisotropic atomic displacement parameters and important bond lengths are listed in **Tables 6.2**, **6.3** and **6.4**, respectively.

Table 6.1 Crystal data and structure refinement for $EuIrIn_4$, $EuAuIn_4$ and $EuAu_2In_4$

Empirical formula	$EuIrIn_4$	$EuAuIn_4$	$EuAu_2In_4$
Formula weight	803.44	808.21	1005.17
Temperature	100.00(10) K	293(2) K	293(2) K
Wavelength		0.71073 Å	
Crystal system		Orthorhombic	
Space group	*Cmcm*	*Cmcm*	*Pnma*
Unit cell dimensions	a = 4.5206(9) Å, b = 16.937(3) Å, c = 7.2661(15) Å	a = 4.6080 (3) Å, b = 17.0454 (8) Å, c = 7.5462 (4) Å	a = 18.5987 (7) Å, b = 4.6616 (2)Å, c = 7.4669 (3) Å
Volume	556.32(19) $Å^3$	592.72 (1) $Å^3$	647.38 (5) $Å^3$
Z	4	4	4
Density	9.593 g/cm^3	9.06 g/cm^3	10.31 g/cm^3
Absorption coefficient	51.064 mm^{-1}	50.223 mm^{-1}	68.535 mm^{-1}
F(000)	1344	1352	1668
Crystal size (mm^3)	0.2 x 0.1 x 0.07	0.36 x 0.2 x 0.1	0.15 x 0.04 x 0.03
θ range for data collection	3.7 to 45.6°	2.4 to 40.8°	2.9 to 29.4°
Index ranges	-8<=h<=9, -33<=k<=34, -14<=l<=12	-8<=h<=8, -31<=k<=31, -13<=l<=13	-25<=h<=23, -6<=k<=6, -10<=l<=10
Reflections collected	7237	9016	4755
Independent reflections	1338 [R_{int} = 0.0777]	1103 [R_{int} = 0.0982]	928 [R_{int} = 0.0829]
Completeness to θ = 34.26°	99.4%	99.6%	99.64%
Refinement method	Full-matrix least-squares on F^2		
Data / restraints / parameters	1338 / 0 / 24	1103/ 0 / 23	928 / 0 / 44
Goodness-of-fit	1.055	0.776	1.017
Final R indices [>2σ(I)]	R_{obs} = 0.0367, wR_{obs} = 0.0689	R_{obs} = 0.025, wR_{obs} = 0.073	R_{obs} = 0.0367, wR_{obs} = 0.103
R indices [all data]	R_{all} = 0.051, wR_{all} = 0.077	R_{all} = 0.029, wR_{all} = 0.094	R_{all} = 0.041, wR_{all} = 0.101
Extinction coefficient	0.00154(8)	0.0052(4)	0.00061(10)
Largest diff. peak and hole (e·$Å^{-3}$)	6.207 and -7.003	4.199 and -1.992	2.797 and -4.614

Table 6.2 Atomic coordinates ($x10^4$) and equivalent isotropic displacement parameters ($Å^2x10^3$) for $EuIrIn_4$, $EuAuIn_4$ and $EuAu_2In_4$ with estimated standard deviations in parentheses

Label	Wyckoff site	*x*	*y*	*z*	Occupancy	U_{eq}*
$EuIrIn_4$						
Eu	4*c*	0	3748(1)	2500	1	5(1)
Ir	4*c*	0	7190(1)	2500	1	5(1)
In1	8*f*	0	1858(1)	448(1)	1	5(1)
In2	4*c*	0	5650(1)	2500	1	6(1)
In3	4*a*	0	0	0	1	7(1)
$EuAuIn_4$						
Eu	4*c*	0	3743(1)	2500	1	16(1)
Au	4*c*	0	7252(1)	2500	1	15(1)
In1	8*f*	0	1795(1)	492(1)	1	15(1)
In2	4*c*	0	5635(1)	2500	1	21(1)
In3	4*a*	0	0	0	1	23(1)
$EuAu_2In_4$						
Eu	4*c*	3581(1)	-2500	5265(1)	1	14(1)
Au1	4*c*	2187(1)	2500	5333(1)	1	14(1)
Au2	4*c*	4603(1)	-7500	7458(1)	1	19(1)
In1	4*c*	689(1)	2500	4912(2)	1	21(1)
In2	4*c*	4648(1)	-7500	3526(2)	1	18(1)
In3	4*c*	3112(1)	2500	2334(2)	1	12(1)
In4	4*c*	3136(1)	2500	8285(2)	1	13(1)

*U_{eq} is defined as one third of the trace of the orthogonalized U_{ij} tensor.

Table 6.3 Anisotropic displacement parameters ($Å^2x10^3$) for $EuIrIn_4$, $EuAuIn_4$ and $EuAu_2In_4$ with estimated standard deviations in parentheses.

Label	U_{11}	U_{22}	U_{33}	U_{12}	U_{13}	U_{23}
$EuIrIn_4$						
Eu	4(1)	5(1)	6(1)	0	0	0
Ir	5(1)	6(1)	5(1)	0	0	0
In1	3(1)	7(1)	4(1)	0	0	0(1)
In2	6(1)	5(1)	8(1)	0	0	0
In3	6(1)	5(1)	10(1)	0	0	-1(1)
$EuAuIn_4$						
Eu	15(1)	12(1)	20(1)	0	0	0
Au	15(1)	14(1)	16(1)	0	0	0
In1	16(1)	15(1)	13(1)	0	0	0(1)
In2	23(1)	12(1)	27(1)	0	0	0
In3	24(1)	14(1)	30(1)	0	0	0(1)
$EuAu_2In_4$						
Eu	14(1)	11(1)	16(1)	0	-2(1)	0
Au1	15(1)	11(1)	14(1)	0	0(1)	0
Au2	18(1)	18(1)	21(1)	0	-1(1)	0
In1	15(1)	26(1)	22(1)	0	1(1)	0
In2	13(1)	17(1)	23(1)	0	1(1)	0
In3	15(1)	13(1)	9(1)	0	-1(1)	0
In4	15(1)	12(1)	11(1)	0	1(1)	0

The anisotropic displacement factor exponent takes the form: $-2\pi^2[h^2a^{*2}U_{11} + ... + 2hka^*b^*U_{12}]$.

Table 6.4 Grouped bond lengths [Å] for $EuIrIn_4$, $EuAuIn_4$ and $EuAu_2In_4$ with estimated standard deviations in parentheses.

Label	Distance	Label	Distance
$EuIrIn_4$			
Eu1-In2	3.2201(12)	Ir1-In2	2.6109(11)
Eu1-In1#1	3.2791(6)	In1-In1#7	2.9813(12)
Eu1-Ir1#5	3.4733(7)	In1-In3#4	3.1628(8)
Eu1-In3#2	3.5918(5)	In2-In3#9	3.1016(5)
Ir-In1#10	2.6804(7)		
$EuAuIn_4$			
Eu-In1 x 4	3.3535(3)	Au-In2	2.7559(7)
Eu-In2	3.2252(8)	In1-In1	3.0304(7)
Eu-In3 x 3	3.6687(3)	In1-In3	3.0816(4)
Eu-Au x 2	3.4305(4)	In2-In3 x 4	3.1684(2)
In1-Au	2.7820(4)		
$EuAu_2In_4$			
Eu-In3 x 2	3.3138(9)	Au1-In4	2.8228(12)
Eu-In2 x 2	3.3251(9)	Au2-In1	2.8172(13)
Eu-In4 x 2	3.3472(9)	Au2-In2	2.9376(13)
Eu-Au2 x 2	3.4249(7)	Au2-In4	2.7984(12)
Eu-Au1 x 2	3.4860(7)	In1-In2	3.2163(16)
Au1-In1	2.8035(14)	In2-In3	2.9907(15)
Au1-In3 x 3	2.8240(12)	In3-In4	3.0237(15)

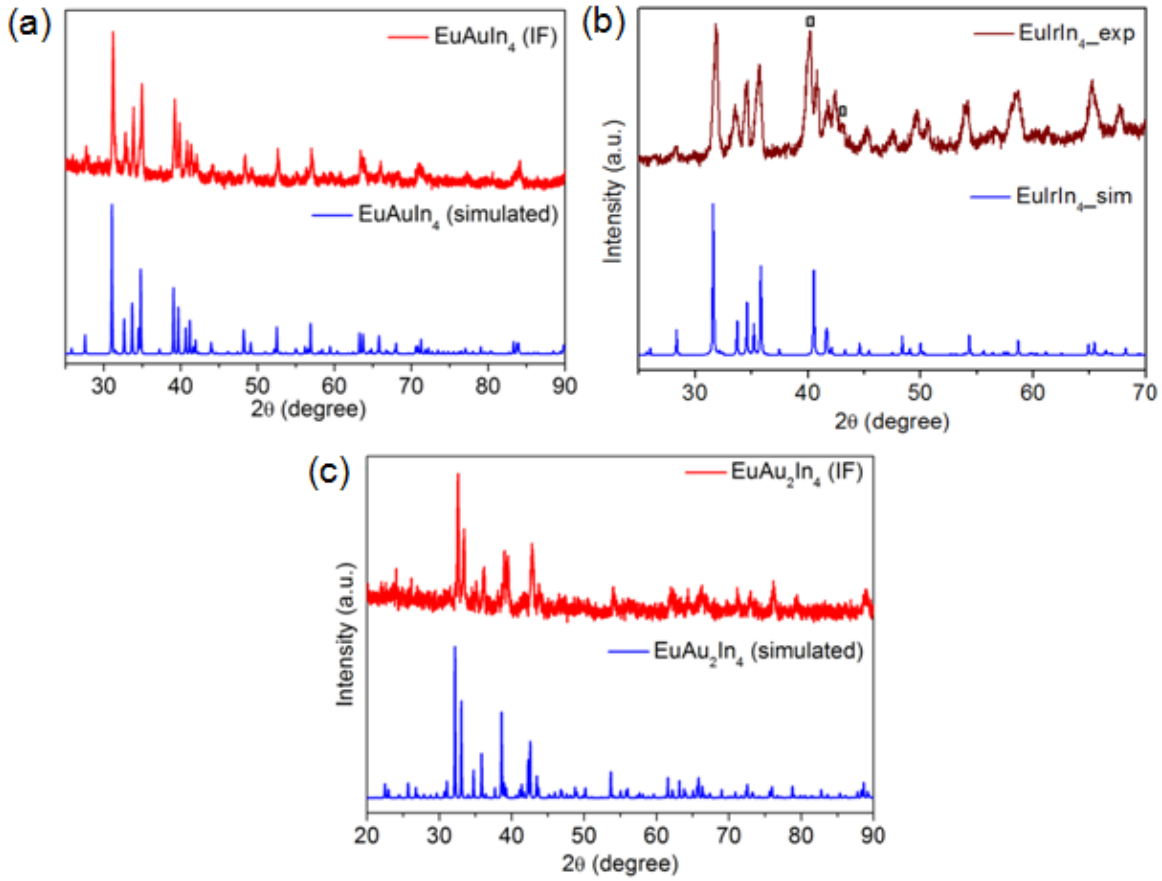

Figure 6.2 Comparison of PXRD patterns of EuAuIn$_4$ and EuAu$_2$In$_4$ with their respective simulated PXRD patterns from SCXRD data.

6.2.6 Magnetic Measurements

Magnetic measurements were done on the randomly oriented single crystals of EuIrIn$_4$, EuAuIn$_4$ and EuAu$_2$In$_4$ with a Quantum Design Magnetic Property Measurement System-Superconducting Quantum Interference Device (MPMS-SQUID) dc magnetometer. Temperature dependent magnetization data were collected in the field cooled mode (FC) in the temperature range 2 to 300 K at an applied magnetic field of 1000 Oe. Field dependent magnetization data were collected at 20 and 5 K for EuAuIn$_4$ and EuAu$_2$In$_4$ respectively with field sweeping from −60 kOe to 60 kOe.

6.2.7 Electrical Resistivity

The resistivity measurements were performed on a single crystal of EuIrIn$_4$ and pellets of EuAuIn$_4$ and EuAu$_2$In$_4$ over the temperature range of 3–300 K using a four-probe dc technique. Four very thin copper wires were glued to the crystal/pellets using a strongly conducting silver epoxy paste. The measurements were conducted using a Quantum

Design Physical Property Measurement System (QD-PPMS). The measurements were initially done applying a voltage of 95 mV with an applied current of 5 mA, but the resistivity plots for both the samples were highly noisy with very low value of resistivity. This clearly established the highly conducting nature of both the samples. Hence, a low voltage (0. 1 mV) was applied keeping the current constant.

6.3 Results and Discussion

6.3.1 Crystal Structure

6.3.1.1 Eu*T*In_4 (*T* = Ir, Au)

$EuIrIn_4$ is the first intermetallic compound reported in Eu-Ir-In series. Unlike the other group 9 transition metal containing compounds having general formula $RETX_4$, which generally crystallize in the $LaCoAl_4$ type (a = 7.701 Å, b = 4.082 Å and c = 7.023 Å) with *Pmma* space group, $EuIrIn_4$ crystallizes in the orthorhombic $YNiAl_4$ structure type (a = 4.5206(9) Å, b = 16.937(3) Å and c = 7.2661(15) Å) with *Cmcm* space group. $EuAuIn_4$ also crystallizes in the same crystal structure with lattice parameters a = 4.6080 (3) Å, b = 17.0454 (8) Å and c = 7.5462 (4) Å. It has been described in the previous literature that $RETX_4$, with T = Au, Ir, Pt compounds have low valence electron count (VEC)[36] due to electron deficient transition metals with high relativistic effects[37-38] causing shrinkage in cell volume and shorter homoatomic as well as heteroatomic (*X*-*X* and *T*-*X*) bond distances. This argument, however, does not hold in case of Eu*T*In_4 series of compounds as all of these crystallize in *Cmcm* space group with a cell volume approximately double of the primitive counterpart belonging to *Pmma* space group. The crystal structure of Eu*T*In_4 is shown in **Figure 6.3**.

The structure can be described as Eu atoms are embedded in the pentagonal [$IrIn_4$] networks separated by two different kinds of tetrameric networks; one of these is a puckered zig-zag [Ir_2In_2] layer (**Figure 6.3b**) and another puckered $[In]_4$ tetrameric network (**Figure 6.3c**). In view of the previously studied compounds, e.g. $CaPdIn_4$,[39] $LaNiIn_4$,[40] etc. which crystallize in *Cmcm* space group, the present compounds can also be described in terms of Zintl concept with a formula $Eu^{2+}[IrIn_4]^{2-}$. The divalent nature of Eu was evident from both crystallographic as well as magnetic data as discussed in the next section. At this point, it will be worthwhile to compare the structures of $EuIrIn_4$ and $SrIrIn_4$[41] geometrically, the later crystallizes in the $LaCoAl_4$ structure type. The representative structures of these two compounds are shown in **Figure 6.4**.

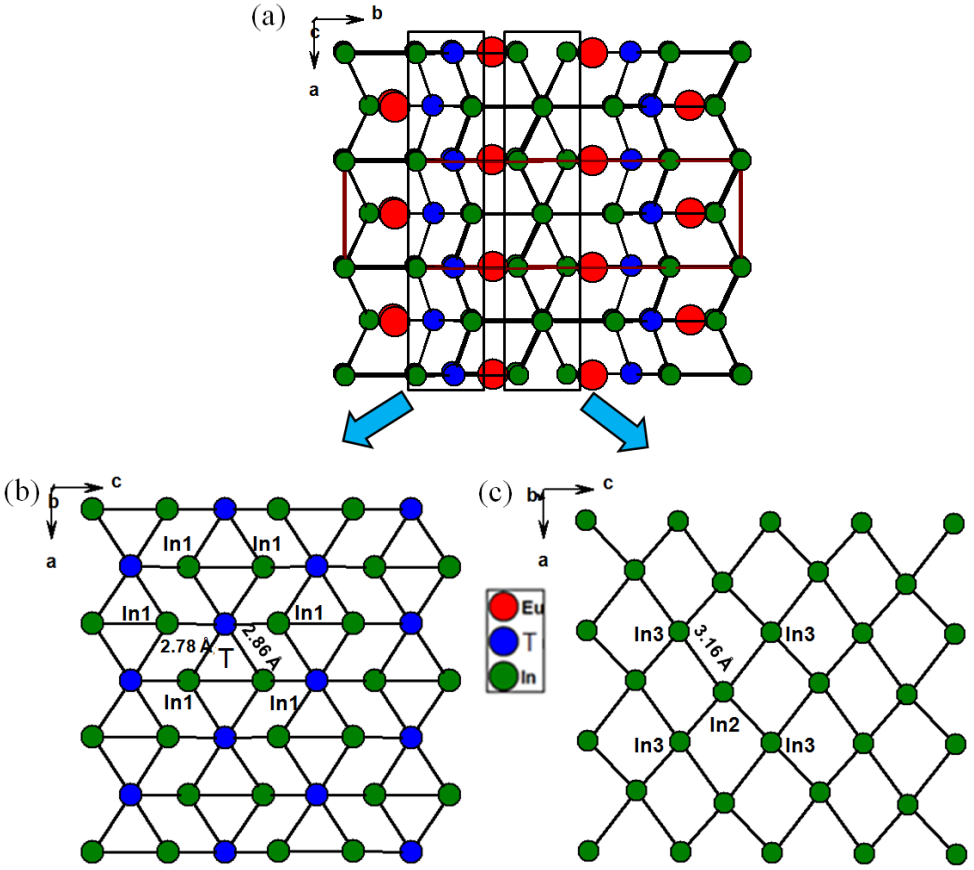

Figure 6.3 (a) The crystal structure of Eu*T*In$_4$ (*T* = Ir, Au) viewed along *c*–axis; (b) quasi-three dimensional [T_2In$_4$] network is shown along *b*–axis; (c) distorted tetragonal [In$_4$] units shown along *b*-axis.

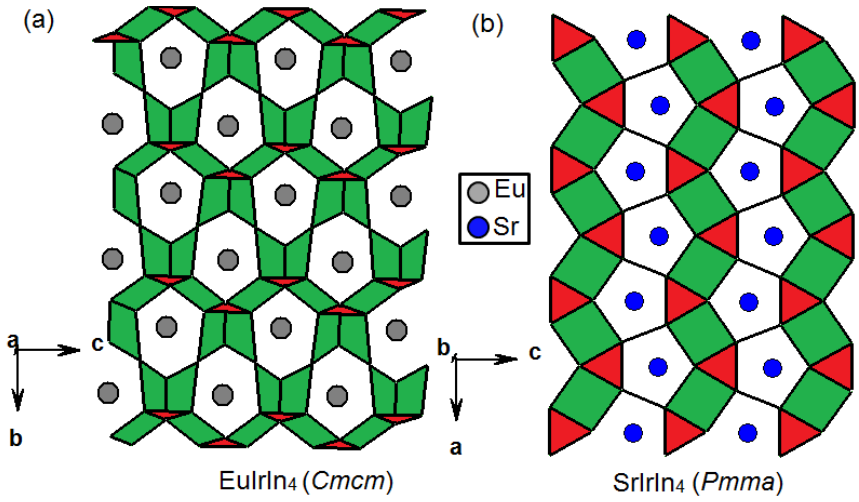

Figure 6.4 Comparison between the crystal structures of (a) EuIrIn$_4$ and (b) SrIrIn$_4$ viewed along *a* and *b* -axis respectively.

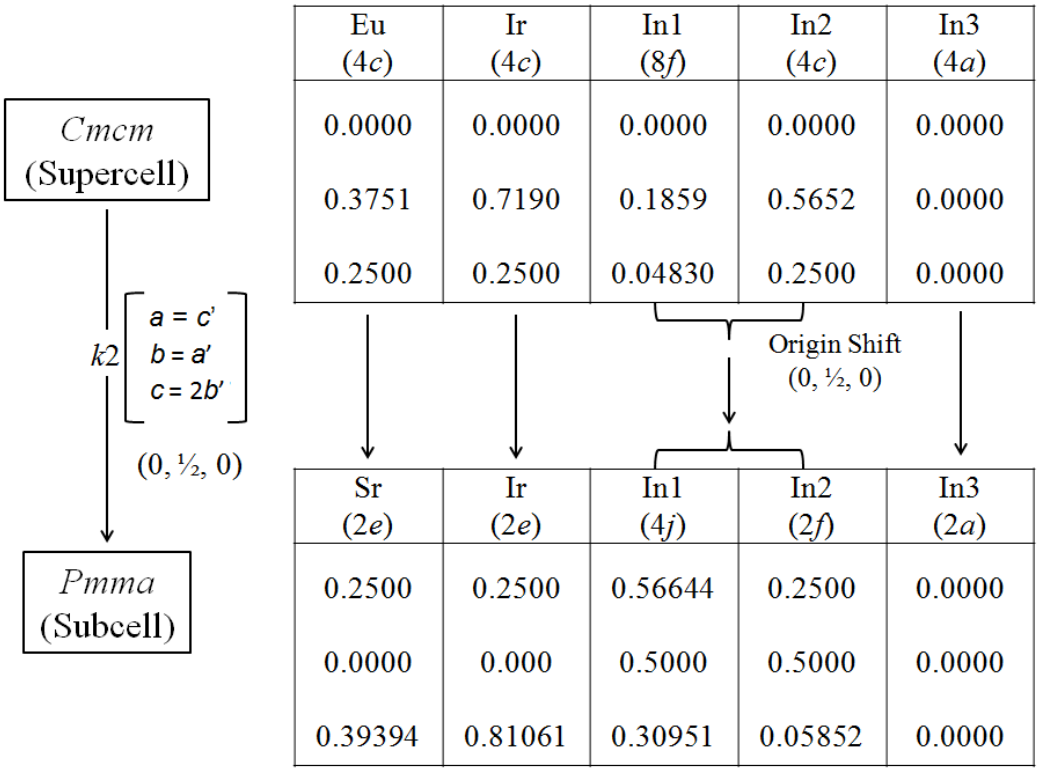

Eu (4*c*)	Ir (4*c*)	In1 (8*f*)	In2 (4*c*)	In3 (4*a*)
0.0000	0.0000	0.0000	0.0000	0.0000
0.3751	0.7190	0.1859	0.5652	0.0000
0.2500	0.2500	0.04830	0.2500	0.0000

Sr (2*e*)	Ir (2*e*)	In1 (4*j*)	In2 (2*f*)	In3 (2*a*)
0.2500	0.2500	0.56644	0.2500	0.0000
0.0000	0.000	0.5000	0.5000	0.0000
0.39394	0.81061	0.30951	0.05852	0.0000

Figure 6.5 Group−subgroup scheme of subcell and the superstructure of $EuIrIn_4$. The indices for the klassengleiche (*k*) transition of degree 2 and the unit cell transformations are given. The evolution of the atomic parameters is shown at the right.

As a matter of fact, both the structures are built up by zig-zag ribbons of tetrameric and trimeric units of $[IrIn_4]$, but the main difference is in the way they are arranged. In case of the *C*-centered structure i.e. for $EuIrIn_4$, there are two kinds of arrangements; one is propagated along the *c*- axis and another is arranged along the two diagonals of the *bc* plane and these two diagonal ribbons are tangled or interconnected at every triangular unit. The primitive structure, $SrIrIn_4$ is however simpler where the ribbons are propagated along *a*–axis parallelly separated by $[Ir_2In_3]$ pentagonal structures and never crosses each other. These two structures can also be compared crystallographically by symmetric reduction shown in **Figure 6.5**.

The non-centrosymmetric space group, *Pmma* can be deduced from centrosymmetric *Cmcm* space group by a simple klassengleichen (*k*) operation of index 2 followed by a shift of origin to (0, 1/2, 0). This removes the center of symmetry rendering the unit cell to primitive orthorhombic. The coordination environments of each atom in both structures have been compared side by side in **Figure 6.6**. The two compounds differs only in terms of the coordination environment of the central atom i.e. Eu and Sr,

respectively, for $EuIrIn_4$ and $SrIrIn_4$. Eu resides in a distorted pseudo Frank-Kasper type cage ($Eu_2In_{13}Ir_2$) which is equivalent to a hexagonal bipyramidal structure, Sr on the other hand, resides in open type 15- membered Frank-Kasper cage ($IrIn_{12}Sr_2$). All the In atoms, namely In1, In2 and In3 in both compounds have cubooctahedron type coordination polyhedral (CP) with a coordination number of 12. The transition metal, i.e. Ir has tricapped trigonal prismatic CP in both compounds. This observation clearly establishes that low valence electron count and the size effect of the transition metal is not sufficient criteria for dense crystal packing giving rise to *Pmma* space group. The reason for this anomalous behavior is unknown to us and urges further theoretical as well as experimental studies. It is also worthwhile to discuss the bonding characteristics in the crystal structure of $EuIrIn_4$. Ir-In bond distance range from 2.6109(11) to 2.6804(7) Å, which is slightly shorter than the covalent bond length of Ir-In (2.83 Å)[42] hinting towards strong bonding interactions between Ir and In. The In-In distance varies in a wide range 2.9813(12) - 3.1628(8) Å suggests considerable distortion in the In cubes which are the basic structural unit in $EuIrIn_4$. The Eu-Eu bond distance 4.5206(9) is comparable to the Eu-Eu bond distances in compounds with divalent Eu moiety in other intermetallic compounds like $EuCu_2Si_2$ and $EuGe_2$,[43-45] which corroborate with the magnetic measurements as well.

6.3.1.2 $EuAu_2In_4$

$EuAu_2In_4$ crystallizes in the orthorhombic $NdRh_2Sn_4$ type structure with *Pnma* space group and lattice parameters are a = 18.5987 (7) Å, b = 4.6616 (2) Å, c = 7.4669 (3) Å (**Figure 6.7**). Like other members of the $REAu_2In_4$ (*RE* = La, Ce, Pr, Nd) family, $EuAu_2In_4$ is also composed of a complex $[Au_2In_4]^{2-}$ polyanion network in which the RE ions are embedded.

In order to demonstrate the crystallographic evolutions of $EuTIn_4$ and EuT_2In_4 from the binaries $EuIn_2$ and $EuIn_4$ a hierarchy has been shown in **Figure 6.8** taking the Au analogues as analogue. There are two paths, which can be assumed for the structural evolution of $EuAuIn_4$ and $EuAu_2In_4$ compounds from their parent binary compounds $EuIn_2$ and $EuIn_4$. The first one (path a) starts with $EuIn_2$ which gives $EuAuIn_2$ with an addition of one Au atom. This is followed by the addition of two In and one more Au in two consecutive steps giving rise to $EuAuIn_4$ and $EuAu_2In_4$, respectively. $EuIn_2$ belongs

to the AlB_2 family of compounds with the $CaIn_2$ structure type having $P6_3/mmc$ space group.[46]

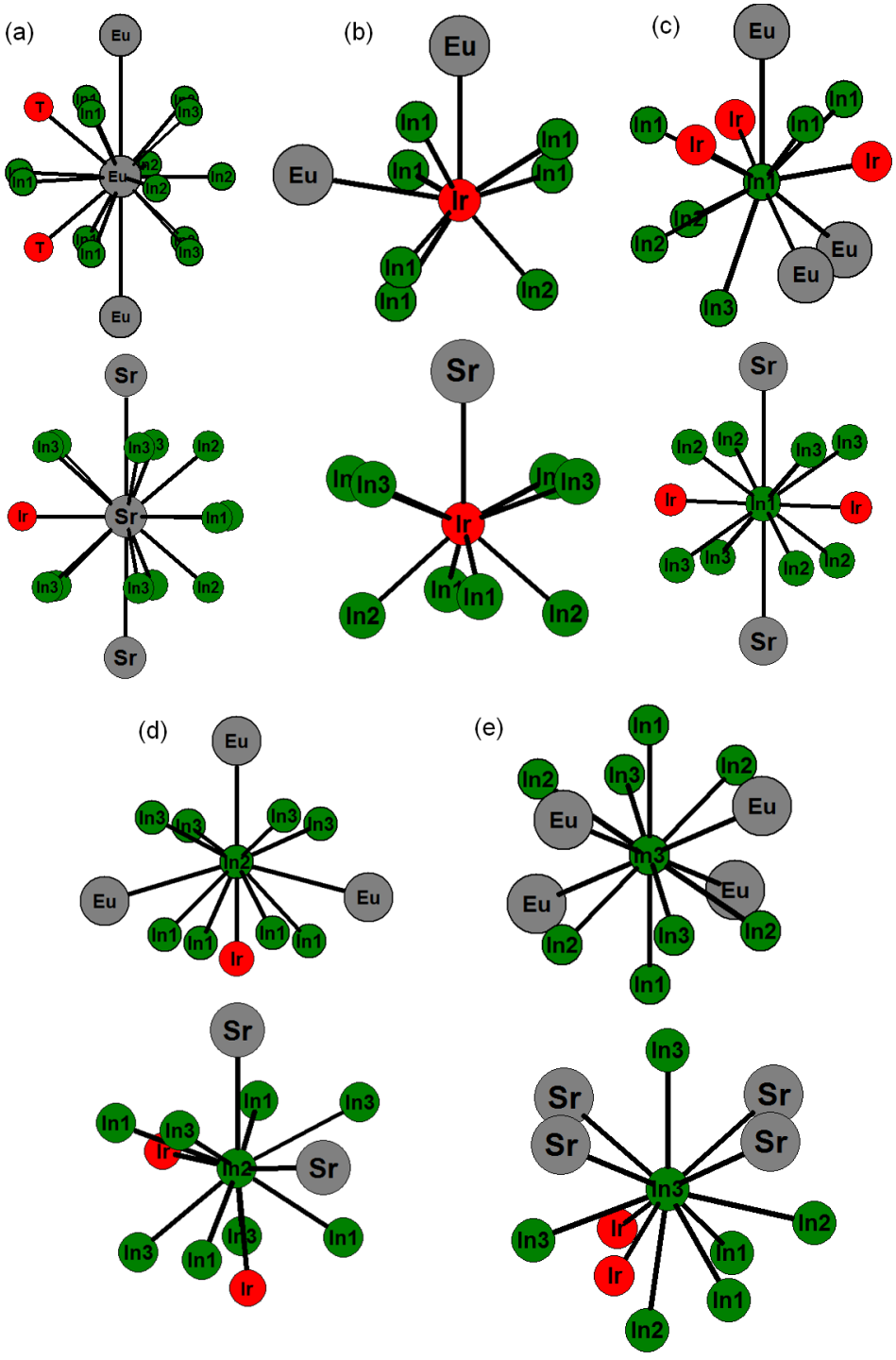

Figure 6.6 Coordination environment of different atoms in $EuIrIn_4$ and $SrIrIn_4$: (a) Pseudo Frank-Kasper type coordination for Eu and Sr (b) tricapped trigonal prism type coordination for Ir; (c, d, e) Cuboctahedron type coordination for In1, In2 and In3, respectively.

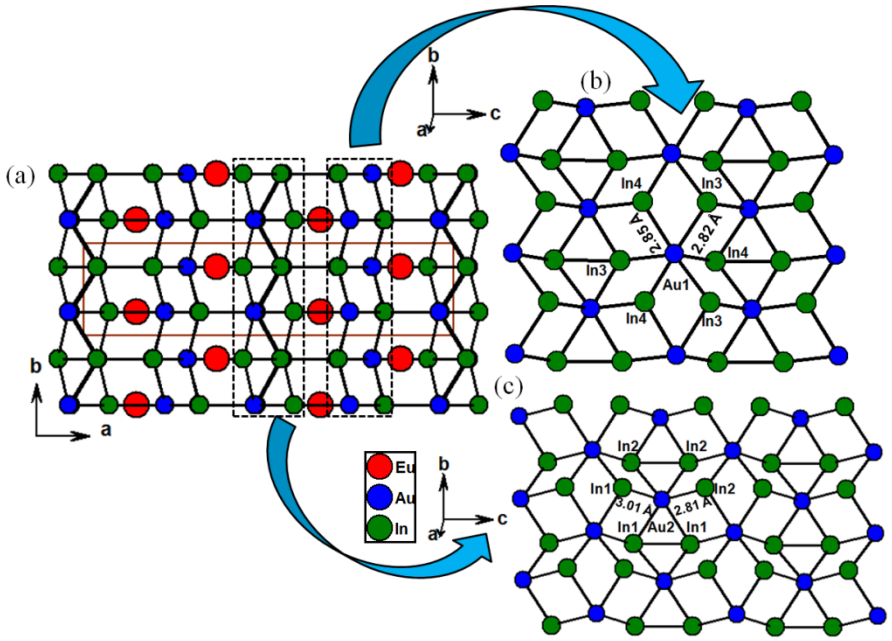

Figure 6.7 (a) Crystal structure of EuAu$_2$In$_4$ viewed along *c*-axis; (b) and (c) The two different types of [Au$_2$In$_4$] networks.

This compound has highly puckered chair shaped hexagonal network of In atoms and the Eu atoms are embedded between two adjacent layers.[47] The In atoms from two interlayers are alternatively connected. The intermediate EuAuIn$_2$ crystallizes in the MgCuAl$_2$ structure type (space group, *Cmcm*) and is a gold filled variation of EuIn$_2$.[48]

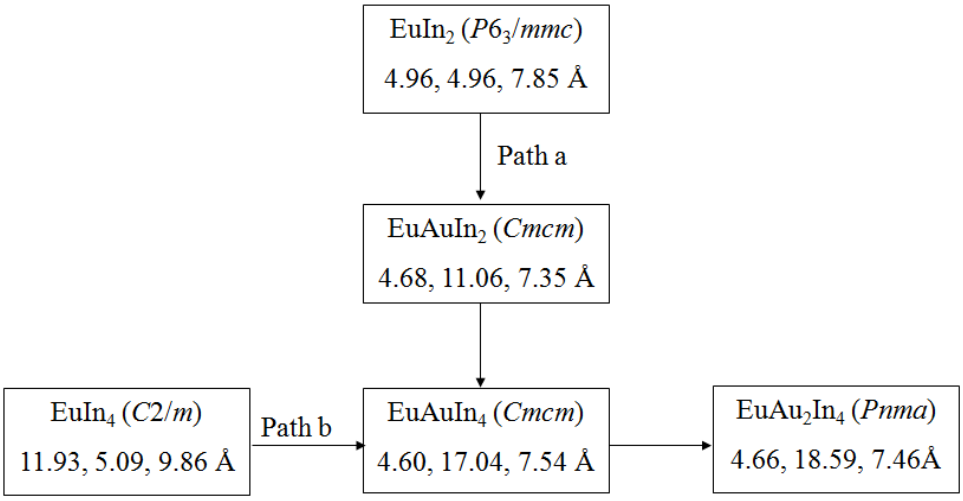

Figure 6.8 Two different paths for the crystallographic evolution of EuAu$_2$In$_4$ from the binaries EuIn$_2$ and EuIn$_4$. The space groups are given in brackets and the numbers indicate the lattice parameters.

The Eu-Eu distance (4.96 Å) in $EuIn_2$ corresponds to the unit cell length along *a* and *b*- axis (hexagonal system) whereas in $EuAuIn_2$, the *a* and *c* lattice parameters remains almost the same but the *b*-axis increases to 11.05 Å.

The inclusion of an Au site results in loss of six-fold screw-inversion symmetry and introduction of centering into the unit cell. Insertion of two more In into $EuAuIn_2$ gives rise to $EuAuIn_4$.

A general structural comparison between the two families i.e. Eu*T*In_4 (*T* = Ir, Au) and EuT_2In_4 (*T* = Au in this chapter), the binaries and the intermediate is shown in **Figure 6.9**. $EuAuIn_2$ (**Figure 6.9b**) can be considered as an orthorhombically distorted gold filled variant of $EuIn_2$ (**Figure 6.9a**)[48] and Eu*T*In_4 (**Figure 6.9d**) can be considered to be an indium-filled variant of Eu*T*In_2.[49] The structure of the Eu*T*In_2 compound can be considered as a fusion of two [$Eu_2T_2In_4$] units without leaving any gap (**Figure 6.9b**), which is similar in $EuIn_2$ and $EuIn_4$ (**Figure 6.9a** and **c**). In Eu*T*In_4, these two units are separated by a zig-zag chain of indium atoms (**Figure 6.3**) and hence the *b*-lattice parameter in $EuAuIn_4$ increases in comparison to Eu*T*In_2.

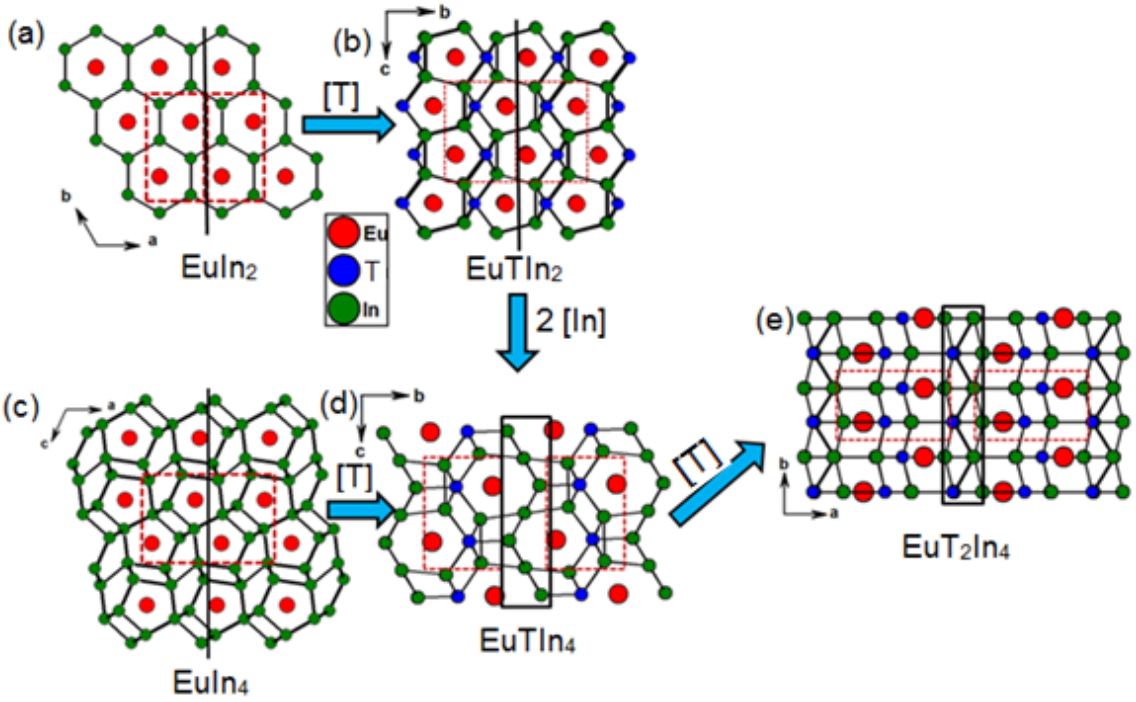

Figure 6.9 Structural relationships among the $EuIn_2$, Eu*T*In_2, $EuIn_4$, Eu*T*In_4 and EuT_2In_4 compounds are shown. The building units are marked by brown squares. The solid line in figures (a), (b) and (c) shows no separation between the building blocks. In (d) and (e), the building blocks (black rectangle) are separated by zig-zag In and [$AuIn_3$] layers.

This separation between the $[Eu_2T_2In_4]$ units further increases in EuT_2In_4 due to intrusion of a zig-zag $[T_2In_4]$ units (**Figure 6.7c**).

It should be noted that crystal growth in $EuAu_2In_4$ occurs along the *b*-axis, as a result the *b* and *a* lattice parameters of this compound are interchanged in comparison to $EuAuIn_4$ (**Figure 6.7**). It is interesting to note that upon addition of one atomic unit of T, the expansion along the crystal growth direction (*a*-axis) is almost closer to the atomic radius of T atom (1.46 Å). The crystal structure of $EuAu_2In_4$ has been explained by Salvador *et al*[22] and is shown in **Figure 6.7**.

Each Eu site resides in a trigonal biprismatic cages built by two-dimensional zig-zag layers of $[Au_2In_4]$ units. This kind of zig-zag chains formed by Au atoms in $REAu_2In_4$ can also be seen in $REAu_3In_3$ (*RE* = Sr, Eu).[13] The adjacent cages share their pentagonal faces along the *b*-axis to form a two dimensional hollow channel which is occupied by the europium atoms. These channels further share their tetragonal faces along the *bc*-plane to construct the overall three dimensional network. When compared with other homologous compounds in $REAu_2In_4$ (*RE* = La, Ce, Pr, Nd) series, both *a* and *b* lattice parameters as well as the unit cell volume increase from La to Nd (**Figure 6.10**) which is in accordance with the lanthanide contraction but both these parameters increase anomalously for the Eu compound. This can only be explained if Eu is present in divalent state unlike its remaining analogous compounds in this series which occur in trivalent state, which is later confirmed by our magnetic susceptibility measurements (discussed below). The ionic radius of Eu^{2+} is higher than Eu^{3+} and thus the cell volume will also be higher.

The second path starts with $EuIn_4$ which does not crystallize in the usual $BaAl_4$-type tetragonal structure,[50] probably due to the large covalent radii of Eu (1.98 Å) compared to Ba (1.49 Å); it rather adopts monoclinic structure type with a distorted fragment of $BaAl_4$.[51] $EuIn_4$ contains interconnected zig-zag In chains with In_4 tetrameric units growing along the *ac*-plane to build up three dimensional cages which in turn stack along the pentagonal faces leading to a channel in which the Eu atoms are encapsulated along the *b*-axis. These features are inherited by the gold containing higher gold containing homologues of $EuIn_4$ i.e. $EuAuIn_4$ and $EuAu_2In_4$, respectively. The coordination environment of Eu in $EuAuIn_4$ and $EuAu_2In_4$ and related parent binary and the intermediate ternary compounds are shown in **Figure 6.11**.

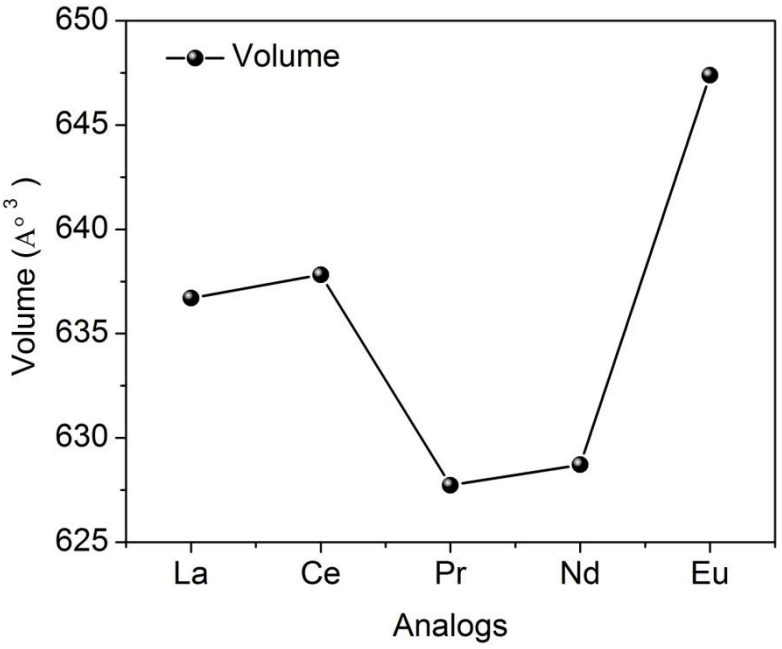

Figure 6.10 Variation of cell volume for *RE*Au_2In_4 (*RE* = La, Ce, Pr, Nd and Eu).

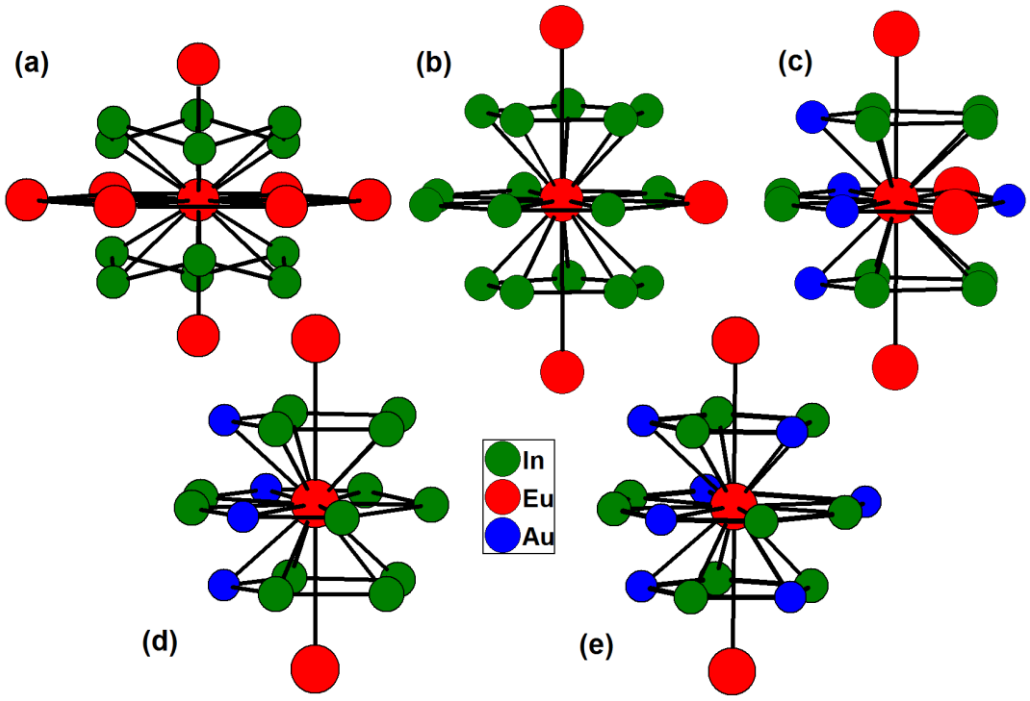

Figure 6.11 Coordination environment of Eu in (a) $EuIn_2$ and (b) $EuIn_4$ (c) $EuAuIn_2$ (d) $EuAuIn_4$ and (e) $EuAu_2In_4$.

Eu in both $EuAuIn_4$ and $EuAu_2In_4$ resides in a three dimensional distorted pseudo Frank-Kasper type cage comprised of Au and In atoms. In the former compound each Eu atom is surrounded by 2 adjacent Eu, 4 Au and 13 In atoms. The number of Au atoms

increases to 7 in the latter along with 10 In atoms. The bonding in *RE* based ternary indides has been summarized by Kalychak *et al*.[48] In Eu-Au-In family of compounds, the *RE* metal is the most electropositive and Au is the most electronegative. Indium forms polyanionic networks by taking electrons from Eu atoms leaving two positive charges on Eu. Au also attracts electrons from the In network and as a result In-In bond length becomes longer. Hence, along path a of scheme 1, the average In-In bond distance increases from 2.9495 Å in $EuIn_2$ to 3.1166 Å in $EuAuIn_2$. With the incorporation of Au and In atoms, the Eu-Eu bond distance increases from 3.9250 Å in $EuIn_2$ to 4.1246 Å in $EuAuIn_2$. Similar trend is also observed along path b, the average In-In bond distance (considering the first coordination sphere) increases from 2.9395 Å in $EuIn_4$ to 3.0994(5) Å in $EuAuIn_4$ to 3.1033(1) Å in $EuAu_2In_4$ with increase in Au content. The unit cell volume is increased due to the incorporation of Au atom which in turn enhances the adjacent Eu-Eu distance from 4.3361(1) Å in $EuIn_4$, 4.6080(3) Å in $EuAuIn_4$ to 4.6616(2) Å in $EuAu_2In_4$.

6.3.2 Magnetism

6.3.2.1 $EuIrIn_4$

The molar magnetic susceptibility of randomly oriented single crystals of $EuIrIn_4$ was measured in an applied field of 1 kOe (**Figure 6.12a**). The plot exhibits a sharp peak around 5.4 K (T_{N1}) indicating antiferromagnetic phase transition followed by another broad hump at around 10.8 K (T_{N2}) which corresponds to another antiferromagnetic transition. Above T_{N2}, the χ (T) falls rather sharply and decreases with increasing temperature. The plot of inverse susceptibility (χ^{-1}) as a function of temperature deviates substantially from linearity and hence was fitted with the modified Curie-Weiss in the temperature range 15-300 K. The curve became linear above T_{N2} after subtracting the residual magnetic susceptibility (χo = -0.011 emumol^{-1}). The fitting gives the value of paramagnetic Curie temperature (θp) of -18.7 K and an effective magnetic moment (μ_{eff}) of 8.45 μ_B/Eu. The value of μ_{eff} is abnormally higher than the expected free ion moment of divalent Eu (7.94 μ_B), and can be attributed to factors such as conduction electron polarization.[52] This kind of high magnetic moment over spin only moment was also observed in case of Tb_2CuGe_3.[52] **Figure 6.12b** shows the magnetization of the sample while varying the magnetic field on the same sample. Above the ordering temperature (300 K), the magnetic moment varies almost linearly with applied field hinting toward the

fact that at this temperature the Eu moments hardly order with applied magnetic field and do not saturate even up to the highest attainable field. Below the ordering temperature (2 K) the compound shows weak metamagnetic transition above a critical field (20 kOe). This could be because of sudden spin flopping towards the applied magnetic field. This kind of transition is often encountered in many Eu containing intermetallic compounds which order antiferromagnetically below a critical temperature (T_N).[53-54] The magnetic susceptibility, χ, on the single crystal of $EuIrIn_4$ has been measured in two orientations, one being parallel to the applied magnetic field (marked as H || *a*-axis) and other being perpendicular to the field (marked as H ⊥ *a*-axis) (**Figure 6.13**).

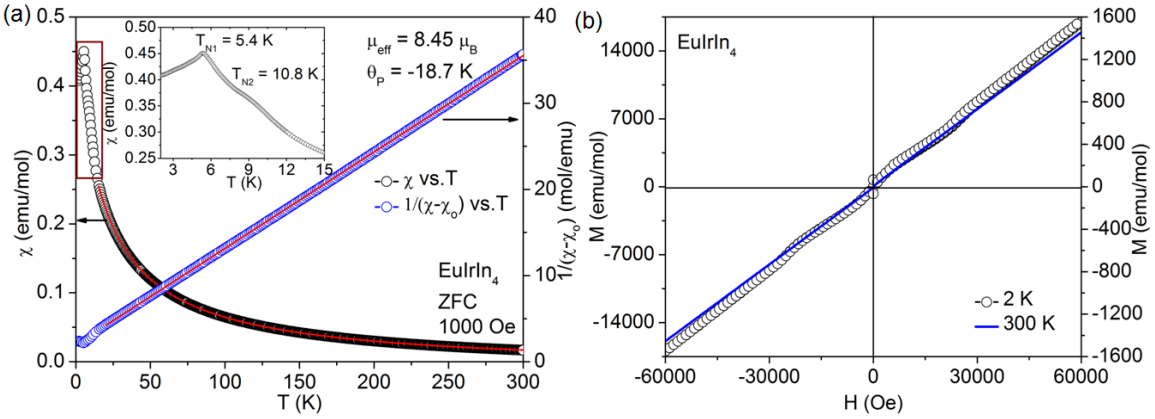

Figure 6.12 (a) Temperature dependence of magnetic susceptibility and inverse magnetic susceptibility (the inset shows a closer look into the ordering temperature) and (b) field dependence of molar magnetization of $EuIrIn_4$.

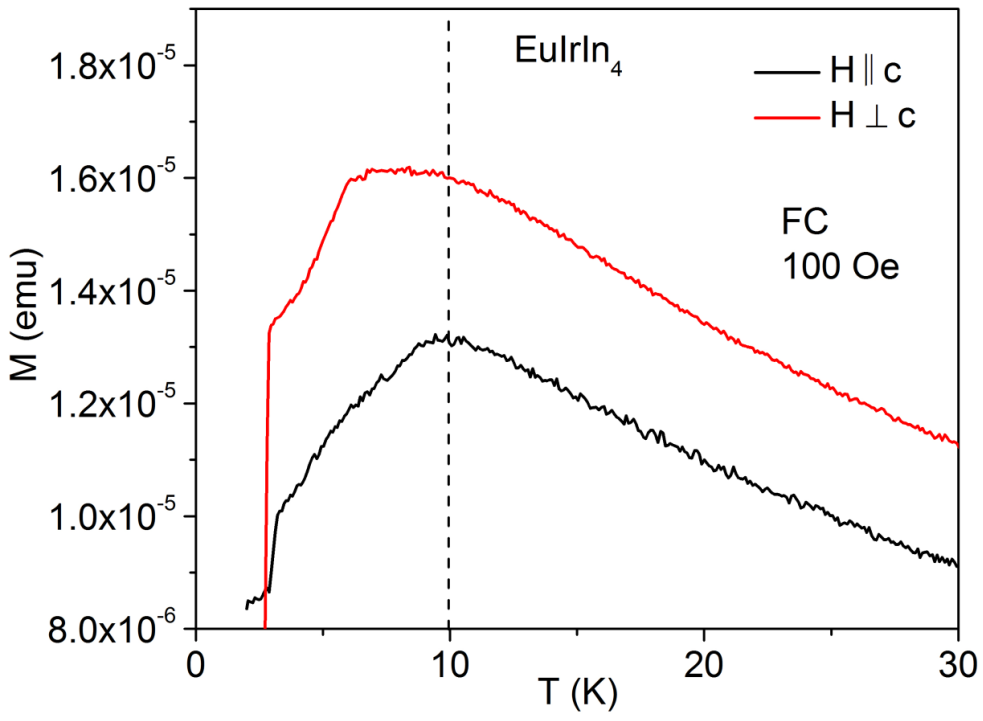

Figure 6.13 Anisotropic magnetic studies on a $EuIrIn_4$ single crystal; Magnetic field applied parallel and perpendicular to *a*-axis. The blue box shows the demagnetization perpendicular to *a*-axis. The Dashed line and arrow shows a subtle shift in ordering temperatures.

Qualitatively, the data of the single crystal with field perpendicular to the *c*-axis is similar to data measured on a polycrystalline sample. In both measurements, χ increases gradually with increasing temperature and undergoes magnetic ordering (T_N) around 11 K. The χ falls rapidly above 11 K with increasing temperature up to 200 K and then decreases marginally. The anisotropy between the perpendicular and the parallel directions of the single crystal is clearly evident from **Figure 6.13**. Below 11 K, it is seen that the behavior of χ(T) for both directions is slightly different in terms of the value of χ at the lowest temperature. For H $\perp$ *a*-axis, χ tends to saturate whereas for H || *a* χ tends to increase.

6.3.2.2 $EuAuIn_4$

The temperature dependent magnetic susceptibility data for $EuAuIn_4$ at an applied magnetic field of 1 kOe are shown in **Figure 6.14a**. No magnetic ordering is observed down to the lowest temperature measured (2 K). The hump around 69 K may be attributed to the presence of EuO on the surface of the sample although, which was not detected by XRD. The temperature dependent inverse susceptibility is linear down to 80 K. A Curie-Weiss fitting in the temperature range 80-300 K yields an effective magnetic moment (μ_{eff}) of 5.88 μ_B and the value of the Curie paramagnetic temperature (θ_p) was -36 K. The effective magnetic moment is well below the spin only magnetic moment of Eu^{2+} (7.94 μ_B). The low magnetic moment can occur either due to mixed valent behavior of Eu or crystal field effect present in the system.

The low magnetic moment for a divalent system was already noticed in Eu_2AuGe_3 compound, and was further confirmed by ^{151}Eu Mössbauer spectroscopy.[23] Similarly, a spectroscopic technique such as XANES is also required or ^{151}Eu Mossbauer spectroscopy to confirm the actual valence state of Eu in this compound. The negative θ_p value hints towards antiferromagnetic interaction between adjacent Eu moments. The field dependent magnetization for $EuAuIn_4$ is shown in **Figure 6.14b**. The curve at 20 K is almost a straight line with no hysteresis revealing paramagnetic nature dominates with

no strong ordering at this temperature. The curve does not saturate even at highest attainable field (60 kOe).

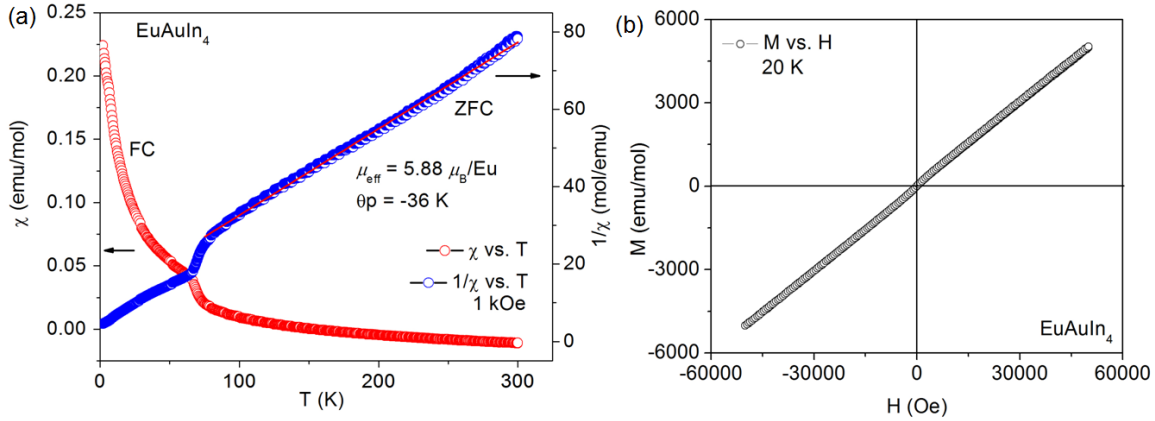

Figure 6.14 (a) Temperature dependent plot of magnetic susceptibility and inverse magnetic susceptibity; (b) Field dependence of magnetization at 20 K of $EuAuIn_4$.

6.3.2.3 $EuAu_2In_4$

The magnetic susceptibility of $EuAu_2In_4$ decreases rapidly below 8.5 K hinting towards an antiferromagnetic ordering at this particular temperature (**Figure 6.15a)**. The inverse magnetic susceptibility has been plotted in the same graph. The curve is linear down to 10 K but deviates from linearity below this temperature. The fitting with a Curie-Weiss law in the temperature range 10 to 300 K yielded an effective magnetic moment (μ_{eff}) of 7.76 μ_B/ Eu atom and the Curie-Weiss paramagnetic temperature, (θ_P) -4.4 K. The effective magnetic moment value is very close to the theoretical moment of divalent europium (7.94 μ_B) suggest Eu^{2+} is predominantly contributing to the overall magnetic behavior of this compound. This is supported by the fact that the Eu-Eu bond distance in this compound is close to other already reported intermetallic compounds consisting of purely divalent Eu, such as, Eu_2AuGe_3,[23] $EuCu_2Si_2$,[44-45] $EuGe_2$[43] etc. whereas the Eu-Eu distance in $EuPd_3$[55] with purely trivalent Eu is 4.10 Å which is comparatively smaller than the values observed in divalent Eu containing intermetallics. The small negative θ_P value indicates that the adjacent Eu atoms interact antiferromagnetically with each other, though these interactions are very weak in nature. The field dependent magnetization data at 5 K for $EuAu_2In_4$ has been plotted **Figure 6.15b**. The magnetization varies almost linearly with applied field hinting toward the fact that at this temperature (5 K) the Eu moments hardly order with applied magnetic field and do not saturate even up to the highest attainable field. Interestingly, none of the analogous compounds in $REAu_2In_4$ (*RE* = La,

Ce, Pr, Nd) shows magnetic ordering down to 2 K, which has been explained based on very long *RE-RE* bond distance (4.61-4.68 Å) resulting in weak coupling between the adjacent spins. The Yb analog is different from the rest of the members as this compound undergoes a broad valence transition from Yb^{2+} to an intermediate valence state in between 2^+ to 3^+.

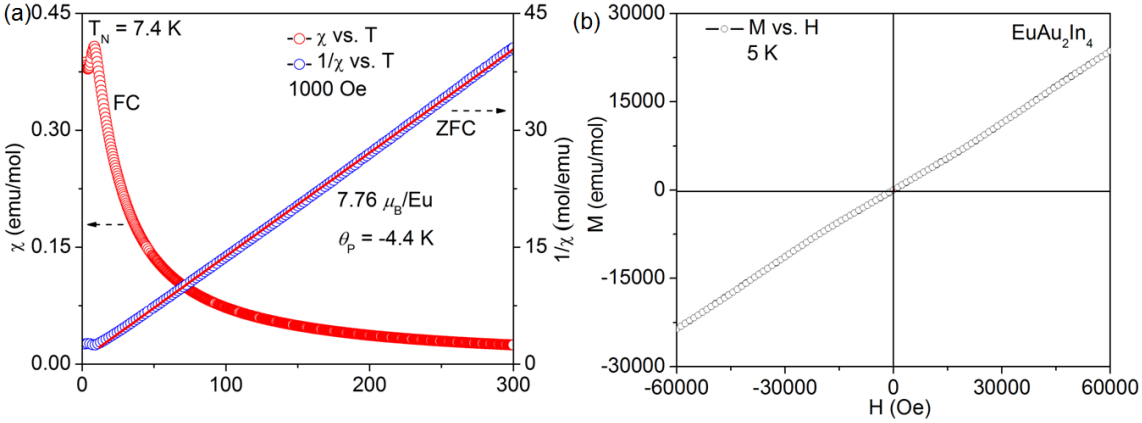

Figure 6.15 (a) Temperature dependent plots of magnetic susceptibility and inverse magnetic susceptibity; (b) Field dependence of magnetization at 5 K of $EuAu_2In_4$.

6.3.3 Electrical Resistivity

The temperature dependent electrical resistivity for $EuIrIn_4$, $EuAuIn_4$ and $EuAu_2In_4$ are shown in **Figure 6.16a**, **6.16b** and **6.16c** respectively. In case of all the compounds, resistivity increases almost linearly with temperature indicating metallic nature. A slow increase followed by a sudden decrease in the resistivity plot for $EuIrIn_4$ at low temperature could be due to the presence of minute quantity of indium (T_c = 3.3 K) respectively. The low temperature data (3-15 K) was fitted with power law equation, $\rho = \rho_0 + AT^n$ (ρ_0 is the residual resistivity and A and n are the fitting parameters),[55] which yielded a residual resistivity of 6 $\mu\Omega$ cm and *n* value of 2.08. Thus for this compound at very low temperature ρ varies with T^2 which establishes the fact that this compound shows Fermi-liquid behavior at low temperature.[23, 56-57] The low residual resistivity and high residual resistivity ratio (RRR, ρ_{300}/ρ_0), 7.3 for this compound proves the high purity of the sample.[58] For the latter compound, i.e. $EuAu_2In_4$ the resistivity decreases with decreasing temperature indicating metallic nature of the compound. Here it is important to mention that the slight curvature of the pattern could possibly arise due to weak scattering of conduction electrons by localized *d*-band near the Fermi level.[59] The residual resistivity (ρ_0) was calculated to be 42 $\mu\Omega$ cm and the power (*n*) was close to 1 (1.12)

which indicates a probable non Fermi-liquid (NFL)[60] ground state for this compound. The high purity of the sample is evident from the high value of residual resistivity ratio, RRR (ρ_{300}/ρ_0) of 2.85.

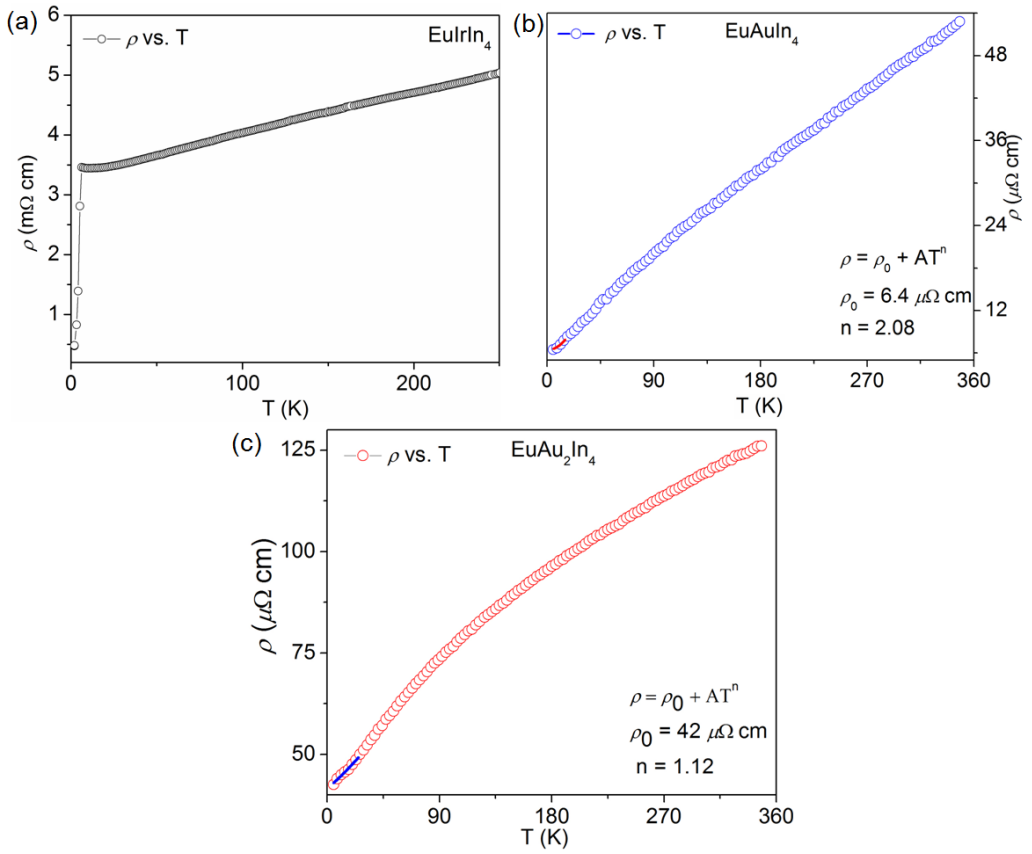

Figure 6.16 The temperature dependence of electrical resistivity for (a) $EuIrIn_4$ and (b) $EuAuIn_4$ and (c) $EuAu_2In_4$.

6.4 Concluding Remarks

In this chapter, structure and properties of a group of polyindide compounds, $EuTIn_4$ and $EuAu_2In_4$ have been discussed in detail along with their evolution from the AlB_2 prototype. Indium has successfully been used as an inactive metal flux for the crystal growth of these compounds. It is anticipated that the next higher homologues i.e. Eu_2AuIn_8 in the Eu-Au-In family may also exists and currently working on its synthesis. *RET*In_4 (*RE* = alkaline/rare earth, *T* = transition metals) family of compounds may offer good scope of future research as many of them are either completely unexplored or not studied for their physical properties such as magnetism and conductivity.

6.5 References

1. Pöttgen, R., *J. Mater. Chem.* **1996,** *6*, 63-67.

2. Subbarao, U.; Sebastian, A.; Rayaprol, S.; Yadav, C. S.; Svane, A.; Vaitheeswaran, G.; Peter, S. C., *Cryst. Growth Des.* **2013,** *13*, 352-359.

3. Pöttgen, R.; Höffmann, R.-D.; Moller, M. H.; Kotzyba, G.; Kunnen, B.; Rosenhahn, C.; Mosel, B. D., *J. Solid State Chem.* **1999,** *145*, 174-181.

4. Nakamura, H.; Ito, K.; Shiga, M., *J. Phys.: Condens. Mat.* **1994,** *6*, 9201-10.

5. Siouris, I. M.; Kremer, R. K.; Hoelzel, M., *J. Magn. Magn. Mater.* **2011,** *323*, 2903-2911.

6. Kaczorowski, D.; Leithe-Jasper, A.; Rogl, P.; Flandorfer, H.; Cichorek, T.; Petri, R.; Andraka, B., *Phys. Rev. B* **1999,** *60*, 422-433.

7. Trovarelli, O.; Geibel, C.; Cardoso, R.; Mederle, S.; Borth, R.; Buschinger, B.; Grosche, F. M.; Grin, Y.; Sparn, G.; Steglich, F., *Phys. Rev. B: Condens. Matter Mater. Phys.* **2000,** *61*, 9467-9474.

8. Ihrig, H.; Lohmann, W., *J. Phys. F* **1977,** *7*, 1957-63.

9. Adroja, D. T.; Malik, S. K.; Padalia, B. D.; Vijayaraghavan, R., *Phys. Rev. B: Condens. Mat.* **1989,** *39*, 4831-3.

10. Chevalier, B.; Kahn, M. L.; Bobet, J. L.; Pasturel, M.; Etourneau, J., *J. Phys.: Condens. Mat.* **2002,** *14*, L365-L368.

11. Hauser, R.; Michor, H.; Bauer, E.; Hilscher, G.; Kaczorowski, D., *Physica B (Amsterdam)* **1997,** *230-232*, 211-213.

12. Nowik, I.; Felner, I.; Voiron, J.; Beille, J.; Najib, A.; De Lacheisserie, E. d. T.; Gratz, G., *Phys. Rev. B: Condens. Mat.* **1988,** *37*, 5633-8.

13. Tang, J.; Gschneidner, K. A., Jr.; White, S. J.; Roser, M. R.; Goodwin, T. J.; Corruccini, L. R., *Phys. Rev. B: Condens. Matt.* **1995,** *52*, 7328-33.

14. Nishioka, T.; Tabata, Y.; Taniguchi, T.; Miyako, Y., *J. Phys. Soc. Jpn.* **2000,** *69*, 1012-1015.

15. Macaluso, R. T.; Sarrao, J. L.; Moreno, N. O.; Pagliuso, P. G.; Thompson, J. D.; Fronczek, F. R.; Hundley, M. F.; Malinowski, A.; Chan, J. Y., *Chem. Mater.* **2003,** *15*, 1394-1398.

16. Subbarao, U.; Peter, S. C., *Inorg. Chem.* **2012,** *51*, 6326-6332.

17. Lei, X.-W.; Yue, C.-Y., *Chin. J. Struct. Chem.* **2012,** *31*, 389-395.

18. Höffmann, R. D.; Pöttgen, R.; Zaremba, V. I.; Kalychak, Y. M., *Z. Naturforsch. B* **2000,** *55b*, 834-840.

19. Muts, I. R.; Schappacher, F. M.; Hermes, W.; Zaremba, V. I.; Pöttgen, R., *J. Solid State Chem.* **2007,** *180*, 2202-2208.

20. Höffmann, R.-D.; Pöttgen, R.; Rosenhahn, C.; Mosel, B. D.; Kunnen, B.; Kotzyba, G., *J. Solid State Chem.* **1999,** *145*, 283-290.

21. Peter, S. C.; Salvador, J.; Martin, J. B.; Kanatzidis, M. G., *Inorg. Chem.* **2010,** *49*, 10468-10474.

22. Salvador, J. R.; Hoang, K.; Mahanti, S. D.; Kanatzidis, M. G., *Inorg. Chem.* **2007,** *46*, 6933-6941.

23. Peter, S. C.; Malliakas, C. D.; Chondroudi, M.; Schellenberg, I.; Rayaprol, S.; Höffmann, R.-D.; Pöttgen, R.; Kanatzidis, M. G., *Inorg. Chem.* **2010,** *49*, 9574-9580.

24. Sarkar, S.; Peter, S. C., *Inorg. Chem.* **2013,** *52* (17), 9741-9748.

25. Chondroudi, M.; Peter, S. C.; Malliakas, C. D.; Balasubramanian, M.; Li, Q. A.; Kanatzidis, M. G., *Inorg. Chem.* **2011,** *50*, 1184-1193.

26. Kanatzidis, M. G.; Pöttgen, R.; Jeitschko, W., *Angew. Chem., Int. Ed.* **2005,** *44*, 6996-7023.

27. Peter, S. C.; Chondroudi, M.; Malliakas, C. D.; Balasubramanian, M.; Kanatzidis, M. G., *J. Am. Chem. Soc.* **2011,** *133*, 13840-13843.

28. Peter, S. C.; Kanatzidis, M. G., *J. Solid State Chem.* **2010,** *183*, 2077-2081.

29. Peter, S. C.; Kanatzidis, M. G., *Z. Anorg. Allg. Chem.* **2012,** *638*, 287-293.

30. Peter, S. C.; Rayaprol, S.; Francisco, M. C.; Kanatzidis, M. G., *Eur. J. Inorg. Chem.* **2011,** *2011*, 3963-3968.

31. Peter, S. C.; Sarkar, S.; Kanatzidis, M. G., *Inorg. Chem.* **2012,** *51*, 10793-10799.

32. Sarkar, S.; Peter, S., *J. Chem. Sci.* **2012,** *124* (6), 1385-1390.

33. *SAINT*, 6.02; Bruker AXS: Madison, WI, 1999.

34. Sheldrick, G. M. *SHELXTL, Structure Determination Program*, 5; Siemens Analytical X-ray Instruments Inc.: Madison, WI, 1995.

35. Sheldrick, G. M. 5.10; University of Göttingen: Göttingen, Germany, 1997.

36. Palasyuk, A. M.; Corbett, J. D., *Inorg. Chem.* **2008,** *47* (20), 9344-9350.

37. Pyykkö, P., *Chem. Rev.* **1998,** *88*, 563-594.

38. Pyykkö, P., *Angew. Chem. Int. Ed.* **2002,** *41*, 3573-3578.

39. Höffmann, R. D.; Pöttgen, R., *Chem. Eur. J.* **2000,** *6* (4), 600-607.

40. Kalychak, Y. M.; Zaremba, V. I.; Galadzhun, Y. V.; Miliyanchuk, K. Y.; Hoffmann, R. D.; Pöttgen, R., *Chem. Eur. J.* **2001,** *7* (24), 5343-5349.

41. Muts, I. R.; Zaremba, V. I.; Pöttgen, R., *Z. Anorg. Allg. Chem.* **2007,** *633*, 2234-2237.

42. Emsley, J., Clarendon Press: Oxford, 1989.

43. Takigawa, Y.; Noguchi, S.; Okuda, K., *J. Magn. Magn. Mater.* **1988,** *76–77*, 345–346.

44. Pagliuso, P. G.; Sarrao, J. L.; Thompson, J. D.; Hundley, M. F., *Phys. Rev. B* **2001** *63*, 092406.

45. Bobev, S.; Bauer, E. D.; Thompson, J. D.; Sarrao, J. L.; Miller, G. J.; Eck, B.; Dronskowski, R., *J. Solid State Chem.* **2004,** *177*, 3545–3552.

46. Höffmann, R. D.; Pöttgen, R., *Z. Kristallogr.* **2001,** *216*, 127-145.

47. Iandelli, A., *Z. Anorg. Allg. Chem.* **1964,** *330*, 221-32.

48. Kalychak, Y. M.; Zaremba, V. I.; Pöttgen, R.; Lukachuk, M.; Höffmann , R.-D., *Handbook on the Physics and Chemistry of Rare Earths*. Elsevier, B. V.: 2005; Vol. 34.

49. Perlitz, H.; Westgren, A., *Ark. Kemi, Miner. Geol.* **1943,** *16B*, 1.

50. Andress, K. R.; Alberti, E., *Z. Metallkd.* **1935,** *27*, 126-8.

51. Fornasini, M. L.; Cirafici, S., *Z. Kristallogr.* **1990,** *190*, 295-304.

52. Majumdar, S.; Sampathkumaran, E. V., *Solid State Commun.* **2001,** *117* (11), 645-648.

53. Hiranaka, Y.; Nakamura, A.; Hedo, M.; Takeuchi, T.; Mori, A.; Hirose, Y.; Mitamura, K.; Sugiyama, K.; Hagiwara, M.; Nakama, T.; Onuki, Y., *J. Phys. Soc. Jpn.* **2013,** *82* (8), 083708.

54. Hossain, Z.; Trovarelli, O.; Geibel, C.; Steglich, F., *J. Alloy Compd.* **2001,** *323*, 396-399.

55. Kambe, S.; Suderow, H.; Fukuhara, T.; Flouquet, J.; Takimoto, T., *J. Low Temp. Phys.* **1999,** *117*, 101-112.

56. Li, S. Y.; Taillefer, L.; Hawthorn, D. G.; Tanatar, M. A.; Paglione, J.; Sutherland, M.; Hill, R. W.; Wang, C. H.; Chen, X. H., *Phys. Rev. Lett.* **2004,** *93*, 056401.

57. Varma, C. M., *Rev. Mod. Phys.* **1976,** *48*, 219-38.

58. Sasakawa, T.; Suemitsu, T.; Kitagawa, J.; Sologub, O.; Salamakha, P.; Takabatake, T., *J. Phys.: Condens. Mat.* **2002,** *14*, L267-L272.

59. Kowalczyk, A.; Falkowski, M.; Toliński, T., *J. Appl. Phys.* **2010,** *107*, 123917.

60. Seaman, C. L.; Maple, M. B.; Lee, B. W.; Ghamaty, S.; Torikachvili, M. S.; Kang, J. S.; Liu, L. Z.; Allen, J. W.; Cox, D. L., *Phys. Rev. Lett.* **1991,** *67*, 2882-5.

Chapter 7

Ordered Pd_2Ge Intermetallic Nanoparticles for Enhanced Activity and Stability towards Ethanol Electro-Oxidation

7.1 Introduction

It is experimentally proven that palladium is a better electrocatalyst than platinum for ethanol oxidation reaction (EOR) in alkaline media.[1] Still more effort is needed to further improve the electrocatalytic performance of Pd-based catalysts. Ethanol is relatively less studied than methanol, the reason could be because the C-C bond cleavage in ethanol requires very high dissociating energy (~350 KJ/mol).[2] However, the use of ethanol is advantageous over methanol because it is less toxic, highly abundant, low cost and results in 12 electrons per molecules when it is completely oxidized to CO_2 and H_2O. Some of the catalysts which have been used for electrochemical oxidation of ethanol are SnO_2/Pt-Sn alloys,[3] Ni supported/Pt-Ru alloys[4] and Pt/C on other oxides like CeO_2 and NiO.[5] In alkaline medium, it has been shown that the reaction catalyzed by Pt is sluggish as compared to Pd. Hence, Pd on various support materials along with its alloys have been highly studied during last two decades. A few examples of this class are Pd on TiO_2/C,[6] Al_2O_3/C, VOx/C,[7] CeO_2/C,[8] Co_3O_4/C,[9] MnO_2/C,[10] NiO/C, In_2O_3/C,[11] CNts (both SWCNT and MWCNT),[9,12] and the alloys PdNi,[13] PdPt,[14] PdAu,[15] and PdRu.[16]

Apart from the above mentioned systems, several catalysts have been reported in the recent past for the electrochemical oxidation of ethanol applying different strategies to improve both the activity and the durability of the catalyst. The examples are Pt-Sn[17] and Pd-Sn[18] based alloy nanoparticles are considered as superior catalyst in ethanol electrochemical oxidation because of their high activity and durability in acidic and alkaline medium, respectively. However, these compounds do not form ordered intermetallic phases under normal reaction conditions. In the same manner $TaPt_3$ ordered intermetallic nanoparticles[19] were reported to show far better activity than Pt_3Sn nanoparticles. However, the ordered phase of $TaPt_3$ was obtained only after the post synthetic heating at a very high temperature (1000 ^oC). PtRh alloy nanocubes supported on graphene[20] were shown to have high activity towards ethanol electrochemical oxidation, however, both the constituents are costly. PdAu nanowires[21] were synthesized in presence of Br- and PVP as shape directing and stabilizing agent. Presence of an additive on the catalyst surface is detrimental to its catalytic activity as these polymer molecules significantly reduce the effective coverage of ethanol molecules.

Motivated by the incredible catalytic activity of Pd-Sn based alloy nanoparticles, the ordered intermetallic compound Pd_2Ge was synthesized in nano dimension by

modified polyol method at 220 ^oC without using any sort of additives or post synthetic heating. The compound Pd_2Ge crystallizes in the Fe_2P type crystal structure with two each independent crystallographic position for Pd and Ge atoms.[22]

The electrochemical oxidation of ethanol was studied in alkaline medium using Pd_2Ge as a catalyst synthesized over a reaction time 24 hrs (Pd_2Ge_24) and 36 hrs (Pd_2Ge_36) of synthesis. Our compounds showed superior activity compared to the commercially available Pd/C, which is in the order of activity towards electrochemical oxidation of ethanol is: Pd_2Ge_36> Pd_2Ge_24> Pd/C. The presence of Ge deficiency in the Pd_2Ge_24 sample showed immense effect on the catalytic activity of the compound owing to the localized defects developed as deficiency. Interestingly, the increase in the catalytic activity for the Pd_2Ge_36 sample was due to the dealloying effect with the evolution of small amount of Pd, which outweighed the presence of localized defects in the Pd_2Ge_24 sample.

7.2 Experimental Section

7.2.1 Chemicals

Potassium tetrachloropalladate (K_2PdCl_4), tetraethylene glycol (TEG), and super-hydride ($Li(Et_3BH)$) were purchased from Sigma-Aldrich. Germanium (IV) chloride ($GeCl_4$) and ethylene glycol were purchased from Alfa Aesar. All materials were used as purchased and all air-sensitive samples were handled inside an Ar filled glove box (H_2O, O_2 <0.1 ppm).

7.2.2 Synthesis

Pd_2Ge nanoparticles were synthesized by solvothermal method. In a typical solvothermal reaction, 0.2 mmol K_2PdCl_4 and 0.1 mmol $GeCl_4$ were mixed in 18 ml TEG with vigorous stirring and loaded in a 23 ml teflon lined autoclave. The autoclave was kept at 220 ^oC for 24 and 36 hrs. The product was repeatedly washed several times with ethanol. The first row transition metal (Mn, Co, Ni and Cu) substituted compounds were synthesized under similar conditions up to 24 h. Co formed disordered cubic phase and hence was not studied.

7.2.3 PXRD

PXRD measurements were done at room temperature on a Rigaku Miniflex X-ray diffractometer with Cu-K_α X-ray source (λ = 1.5406 Å), equipped with a position

sensitive detector in the angular range $30^o \leq 2\theta \leq 80^o$ with the step size 0.02^o and scan rate of 0.5 s/step calibrated against corundum standards. The experimental patterns were compared to the pattern calculated from the single crystal structure refinement.

7.2.4 Elemental analysis

Quantitative microanalysis on all the samples were performed with a FEI NOVA NANOSEM 600 instrument equipped with an EDAX® instrument. Data were acquired with an accelerating voltage of 20 kV and a 100 s accumulation time. The EDAX analysis was performed using P/B-ZAF standardless method (where, Z = atomic no. correction factor, A = absorption correction factor, F = fluorescence factor, P/B = peak to background model) on selected spots and points.

7.2.5 TEM and SAED Analysis

TEM images and SAED patterns were collected using a JEOL 200 TEM instrument. Samples for these measurements were prepared by sonicating the nanocrystalline powders in ethanol and dropping a small volume onto a carbon-coated copper grid.

7.2.6 XPS Studies

XPS measurement was performed on an Omicron Nanotechnology spectrometer using Mg-Kα (1253.6 eV) X-ray source with a relative composition detection better than 0.1%.

7.2.7 Electrochemical Studies

All the electrochemical measurements were performed on a CHI 660A electrochemical workstation at 25 $^{\circ}$C. Three electrode set-up was used with a glassy carbon electrode (having diameter 3 mm) as working electrode, platinum wire as counter and Hg/HgO (MMO) as reference electrode. All the solutions were purged with nitrogen gas for 20 minutes prior to the measurement. The catalyst ink was prepared by dispersing 5 mg of catalyst in 1 mL of mixed solvent solution (IPA:H_2O=1:1 v/v) and 10 μL of 1 wt.% Nafion binder. The Nafion binder (Signa Aldrich, 5 wt%) was diluted to 1 wt% with isopropyl alcohol (IPA). 20 µL of the catalyst ink was dropcasted on to glassy carbon [4] electrode and dried overnight at room temperature. Before depositing the catalyst, the GC was polished with 0.05 µm alumina slurry, washed several times with distilled water (16.2 mΩ) and IPA. Commercial Pd/C (10wt. %, Sigma Aldrich) was used for comparison of the activity with the Pd_2Ge catalyst. The blank cyclic voltammetry (CV) measurement was carried out with 1M KOH aqueous solution at a scan rate 50 mV/sec.

CV and chronoamperometry (CA) measurements were performed in 1M KOH/1M EtOH electrolyte solution at a scan rate 50 mV/sec. Linear sweep voltammetry (LSV) was recorded with a sweep rate of 1 mV/sec at 1000 rpm in 1M KOH/1M EtOH electrolyte solution. Tafel plots (TP) were derived from LSV measurement.

7.2.7 Computational Details

The first principal calculations have been done by in collaboration with Prof. Umesh Waghmare and his group. The first principles calculations were performed on the density functional theory as implemented in quantum espresso package.[23] The exchange-correlation energy of electrons was treated with local density approximation with Perdew-Zunger parametrized form.[24] A periodic boundary conditions was employed with 4X4 and 3X3 supercell of Pd and Pd_2Ge surfaces, respectively, and include a vacuum of about 14 Å to keep interaction between periodic images low. A kinetic energy cut off of 35 Ry was used to truncate the plane wave basis.A uniform mesh of 3X3X1 and 3X3X2 k-points was used for Pd and Pd_2Ge surfaces, respectively, in sampling integration over the brillouin zone. Different orientation of OH and CH_3CO were employed on surface and relax the system until the Hellmann-Feynman forces on each atom are less than 0.03 eV/Å. Pd_2Ge_24has been considered as a Ge-deficient surface and Pd_2Ge_36 as a pristine Pd_2Ge phase throughout our calculation.

7.3 Results and Discussions

7.3.1 Phase Analysis

From the PXRD analysis, it was found out that Pd_2Ge crystallizes in the hexagonal Fe_2P structure type ($P\bar{6}2c$ space group) which is a vacancy ordered variant superstructure of the AlB_2 prototype. Among the four crystallographically different sites, two are occupied by the Pd atoms (Wyck. no. 3*f* and 3*g*) and the other two are occupied by the Ge atoms (Wyck. no. 2*a* and 1*b*). The Fe_2P structure can be derived from the AlB_2 structure type using Bärnighausen formalism (**Figure 1.8**) through a series of symmetry reduction method. The formula of this compound can be written as $(Fe2)_3[(Fe1)_3\Delta(P2)_2]P1$. Here the Fe2 atoms substitute the aluminum positions whereas the Fe1 and P2 atoms substitute boron positions, Δ corresponds to the vacancies. The Fe_2P structure bears a lot of resemblance to Th_3Pd_5 type structure (**Figure 7.1**), which can be considered as a defect variant of the AlB_2 structure with every sixth boron position remains unoccupied in the resulting structure. The defects originated by the vacancies shifts the Pd positions, which

in turn, gives rise to tripling of the unit cell along the *c*-axis for Th_3Pd_5. In case of Fe_2P structure, these vacancies remain unfilled whereas only those are filled which shift by half the ***c*** lattice vector.

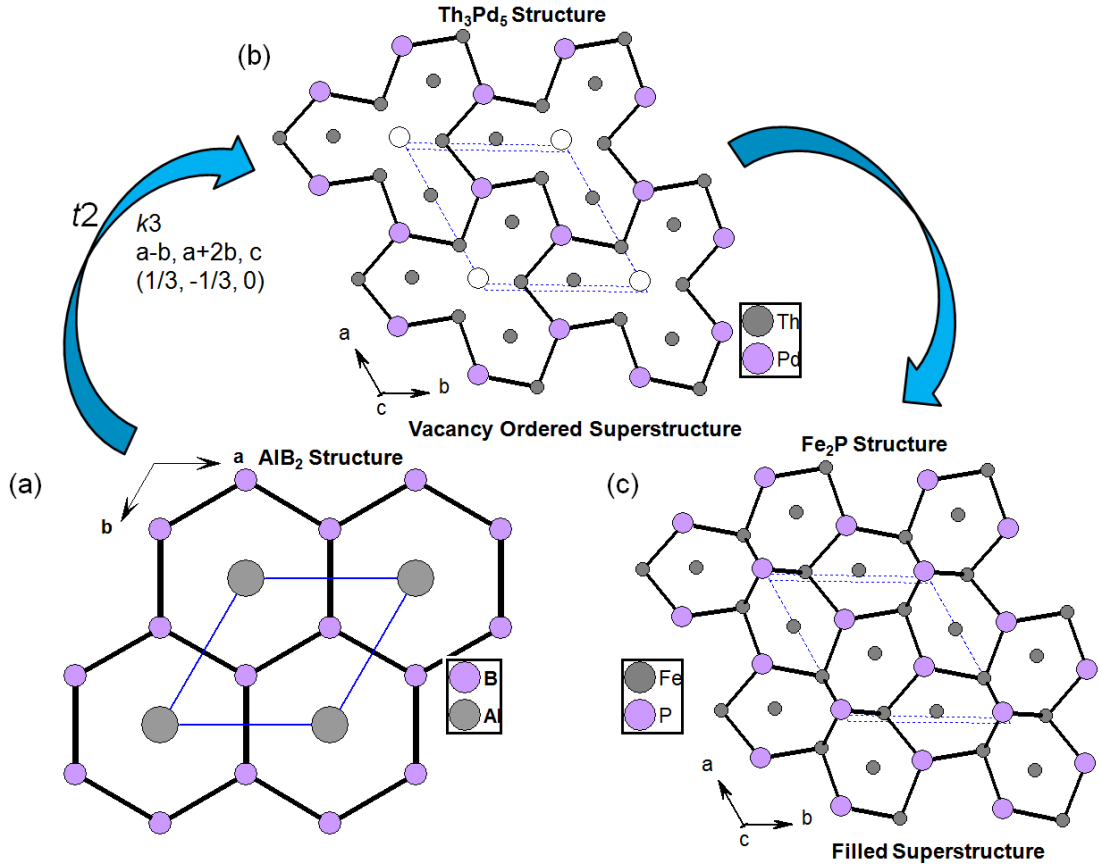

Figure 7.1 Crystal structure of (a) AlB_2, (a) Th_3Pd_5 and (a) Fe_2P and their structural relationship.

Figure 7.2a shows the PXRD patterns of Pd_2Ge nanoparticles synthesized at 220 ^oC varying the reaction time. Comparison of the experimental PXRD patterns with the simulated pattern of the bulk compound[16] confirmed that Pd_2Ge crystallizes in the ordered phase without any impurities. In the case of Pd_2Ge_24, the relative shift of the PXRD pattern with respect to the bulk compound to the lower angle indicates the increase in lattice constant i.e. deficiency in Ge content (**Figure 7.2b**). However, there was no shift in the XRD pattern of Pd_2Ge_36 in comparison to the simulated pattern suggests the absence of Ge deficiency (**Figure 7.2b**), which can be explained as either the vacancy of Ge filled slowly or the chemical etching of Pd due to the strain present in Pd_2Ge_24 sample. Although it is expected that the slow reduction of Ge compared to Pd, the filling of Ge vacancy can be ruled out due to the negligible difference in the atomic composition

of Pd and Ge obtained from the EDAX measurements which shows the Pd and Ge contents in Pd_2Ge_24 and Pd_2Ge_36 samples are 72-76% and 28-24%, respectively (**Figure 7.3**). In addition, powder XRD of Pd_2Ge_36 sample contains sizable intense (111) peak at $2\theta = 40.1^{o}$ represents metallic Pd confirmed that Pd slowly etched out of the system and exist in the composition $Pd_x/Pd_{1-x}Ge_y$. This dealloying process, interestingly enhances the catalytic activity of Pd_2Ge_36 compared to Pd_2Ge_24. The crystallite sizes calculated using the Scherer formula for the compounds Pd_2Ge_24 and Pd_2Ge_36 are 15 and 18 nm, respectively.

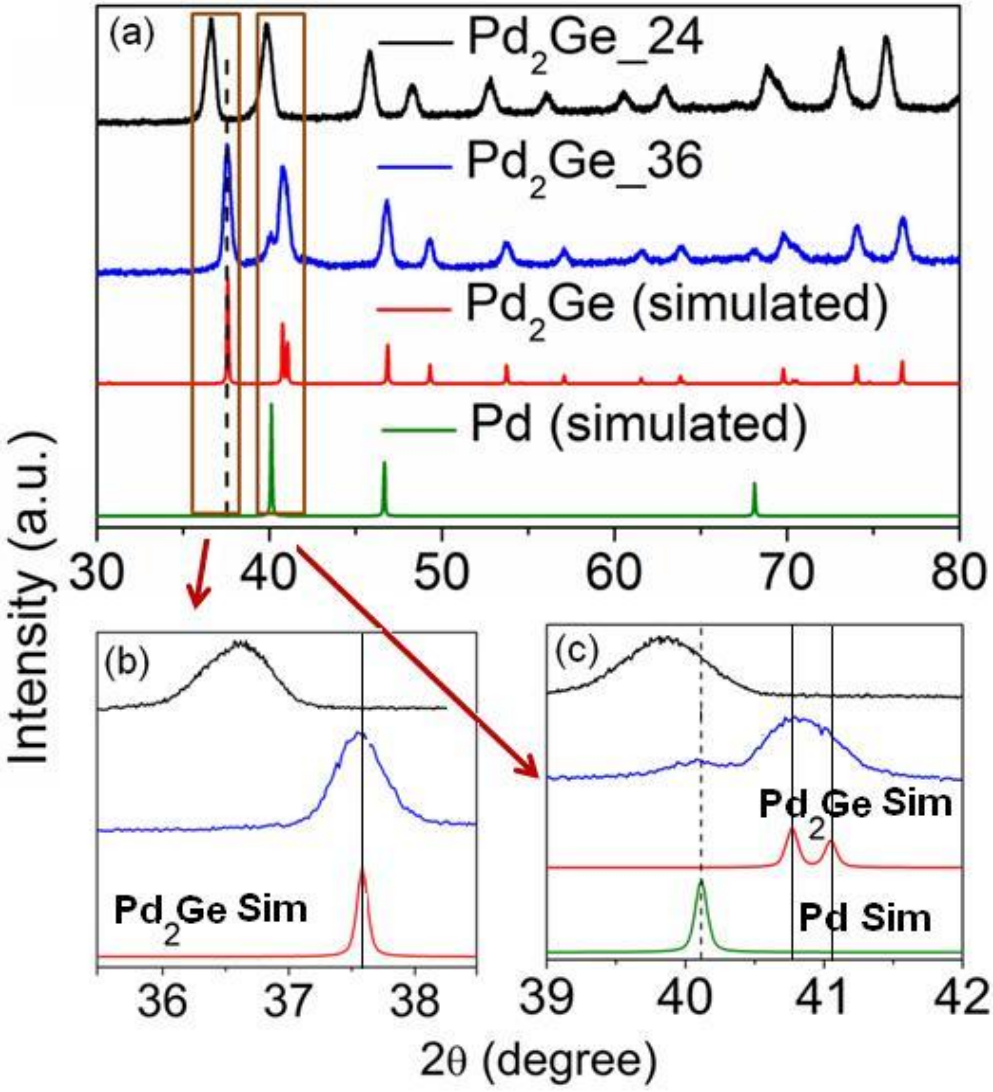

Figure 7.2 (a) Comparison of PXRD patterns of Pd_2Ge nanoparticles synthesized by solvothermal technique at 220 ^{o}C after 24 h and 36 h with simulated powder pattern from bulk Pd_2Ge intermetallic compound and Pd. (b) Enlarged plot showing the relative shift of Pd_2Ge_24 compared to the bulk compound. (c) Enlarged plot represent the presence of Pd in Pd_2Ge_36 sample.

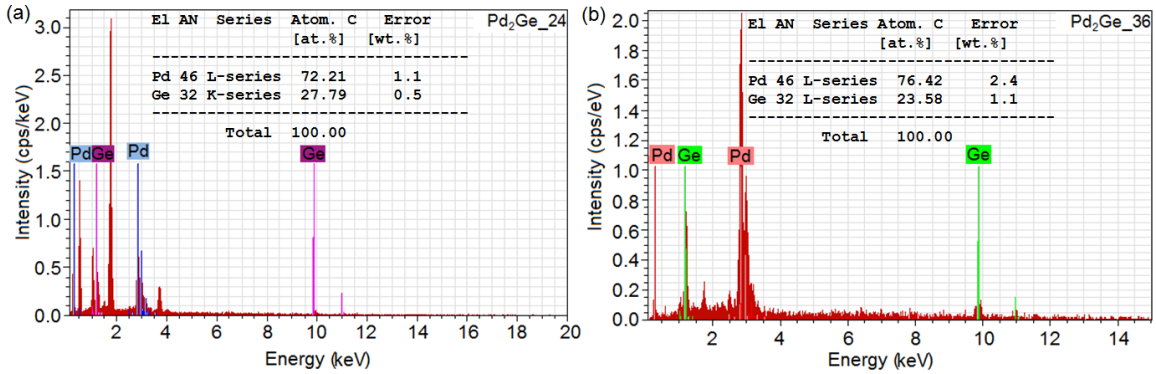

Figure 7.3 EDAX data of Pd_2Ge NPs synthesized after (a) 24 h and (b) 36 h of reaction time.

However no traces of extraneous Pd could be concluded from the elemental mapping experiment (**Figure 7.4**) on the corresponding sample.

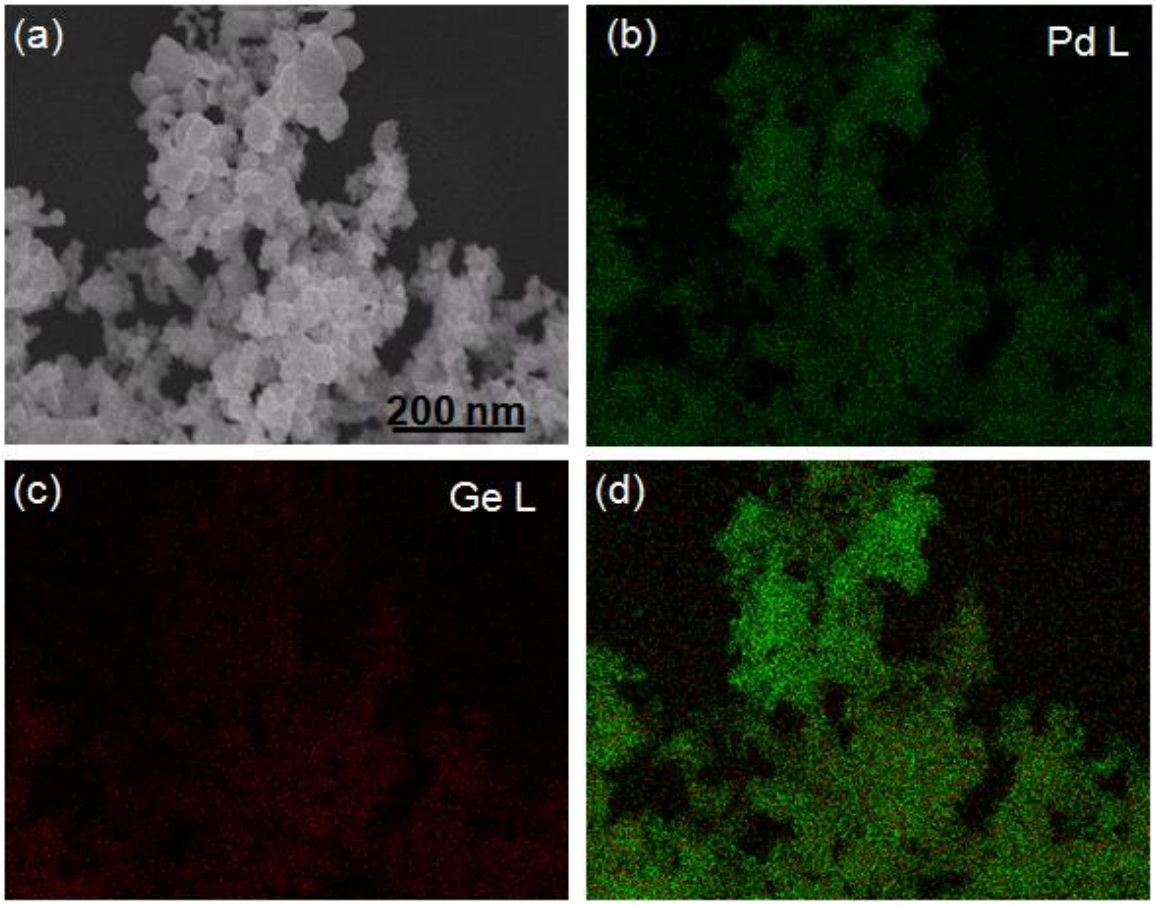

Figure 7.4 Elemental mapping on Pd_2Ge_36; (a) the spot on which measurement was done, (b) spectrum of Pd-*L* edge (green), (c) spectrum of Ge-*L* edge (red) and (c) merged spectra of the compound.

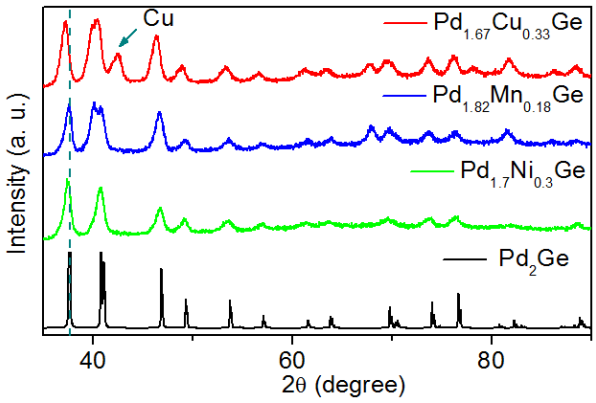

Figure 7.5 Comparison of PXRD patterns of $Pd_{1.7}Cu_{0.3}Ge$, $Pd_{1.7}Mn_{0.3}Ge$, $Pd_{1.7}Ni_{0.3}Ge$ and Pd_2Ge nanoparticles synthesized by solvothermal technique at 220 ^oC after 24 h.

7.3.2 Morphological Analysis

Figure 7.6 shows the TEM images for Pd_2Ge_24. The sample mostly contains worm like one dimensional interconnected structures can also be called as nanowire of Pd_2Ge similar to PdAu.[25] From the TEM images it is clear that Pd^{2+} and Ge^{4+} are first co-reduced to form Pd_2Ge intermetallic nanoparticles and gradually grow with time. There are spherical particles in a few parts of the grid as well (**Figure 7.6a and 7.6b**).

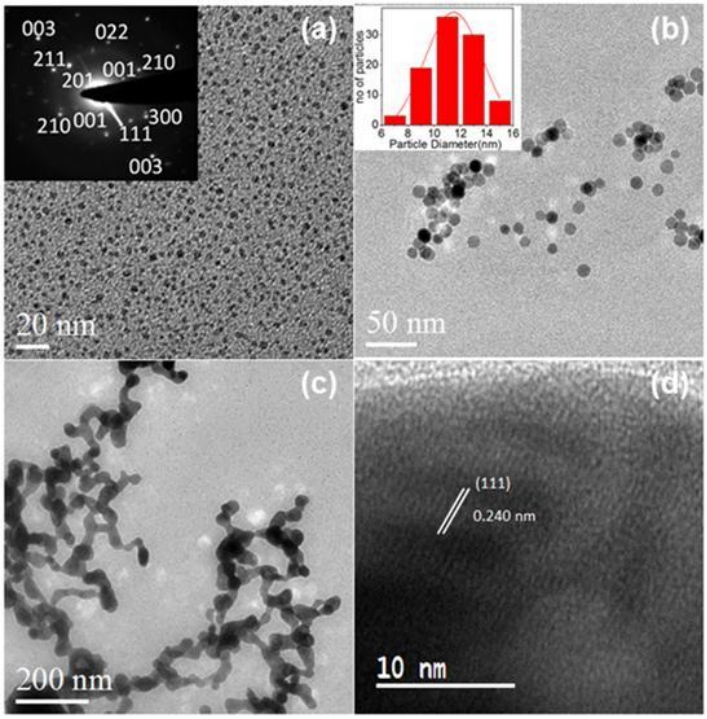

Figure 7.6 (a) TEM images of Pd_2Ge nanoparticles showing the growth from ultrasmall nanopartilcles (< 5 nm), (b) spherical shaped 5-10 nm particles and inset shows the electron diffraction pattern on this region, (c) worm like network and (d) HRTEM image from the tape like network.

From HRTEM image, d-spacing (between two lattice fringes) was calculated to be 0.240 nm clearly indicates the presence of (111) plane of ordered Pd_2Ge intermetallic nanoparticles. Formation of intermetallic Pd_2Ge nanoparticle was further proved by SAED pattern (**Figure 7.6a** inset). The diffraction pattern contains (001), (111), (210), (003) planes confirm the formation of ordered intermetallic Pd_2Ge nanoparticle.

The bigger particles become ellipsoidal and smaller branches join up (**Figure 7.7a and 7.7b**) to form large connected network (**Figure 7.7c**). It is well known that conversion of spherical nanoparticles into nanowires occurs via an oriented attachment mechanism.[26] The network consists of several kinks and grains, which were also reported in case of AuCu nanowires grown by the same mechanism.[26] This is further supported by the observation of worm like network observed in Pd_2Ge_36 (**Figure 7.7c**).

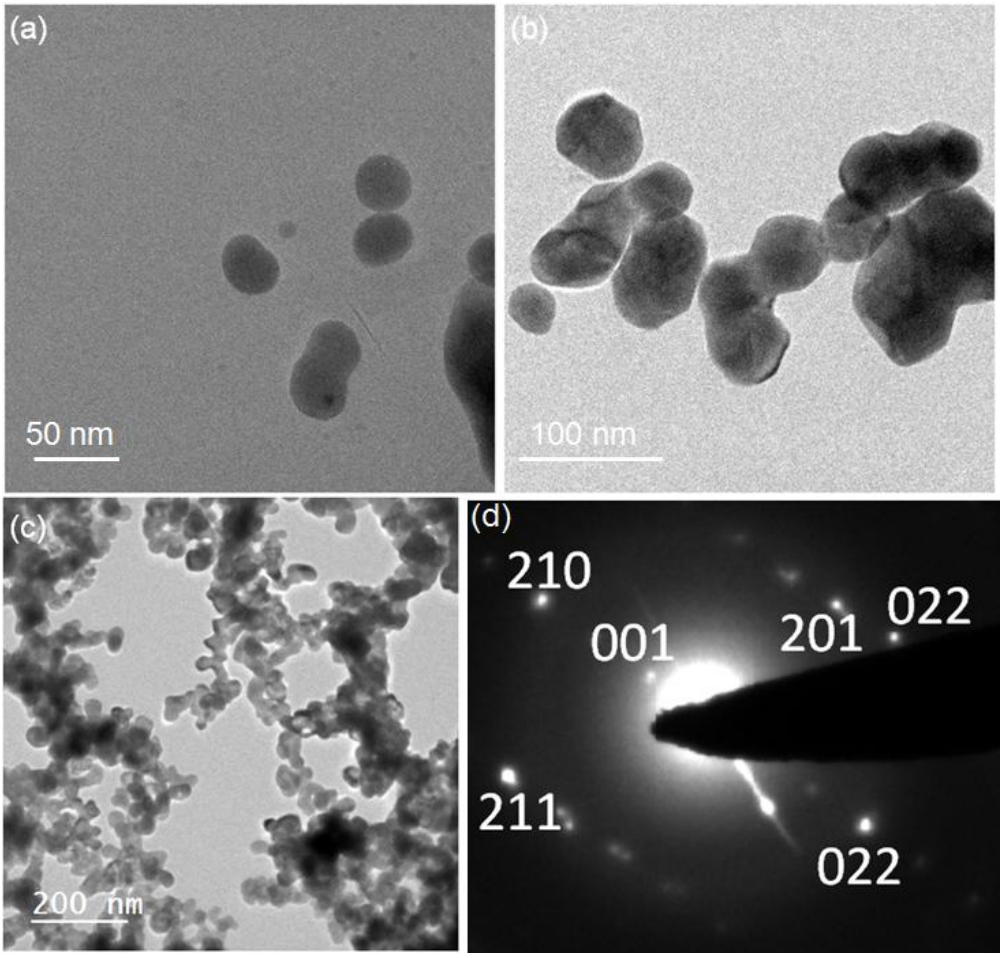

Figure 7.7 TEM images of Pd_2Ge_24 nanoparticles (a) growth of ellipsoidal particles from small nanopartilcles (<15 nm) (b) to smaller joined structures (c) highly connected network of Pd_2Ge_36 nanoparticles (d) shows SAED pattern from the Pd_2Ge_36 network.

7.2.3 Ordered intermetallic structure

In order to have an insight into the nature and bonding of the compounds, X-ray photoemission spectroscopic studies were performed for both Pd_2Ge_24 and Pd_2Ge_36 samples (**Figure 7.8**).[27] In case of Pd_2Ge_24, Pd $3d_{5/2}$ peak appears at 335.3 eV with the other spin-orbit coupling component at 341 eV corresponding to $3d_{5/2}$ state.[28] Another broad peak appeared at 337.1 eV arising from PdO.[28] In case of Pd_2Ge_36, two $3d_{5/2}$ components appeared at 335 and 336.3 eV which correspond to Pd metal and PdO_{ads}.[28] Interestingly, the former peak is downshifted by 0.3 eV in comparison to the same peak in Pd_2Ge_24. Ge $3d_{3/2}$ peak appears at 32.4 eV.[29] Ge $3d_{5/2}$ peaks appear at 28.6 and 30.5, which correspond to Ge metal and GeO with divalent germanium.[29] The germanium peak downshifts by 0.7 compared to elemental Ge, which hints towards strong covalent bond formation between palladium and germanium. A satellite peak of $3d_{5/2}$ was observed at 32.5 eV which could be assigned to GeO_2 formed on the surface of the nanoparticles.[29] Elemental mapping on Pd_2Ge_36 (Figure 7.4) further shows uniform distribution of palladium and germanium and hence ordered intermetallic structure of the compound. No localized palladium could be trace on the surface of the Pd_2Ge_36 nanoparticles as was detected by PXRD analysis probably because of its minute quantity.

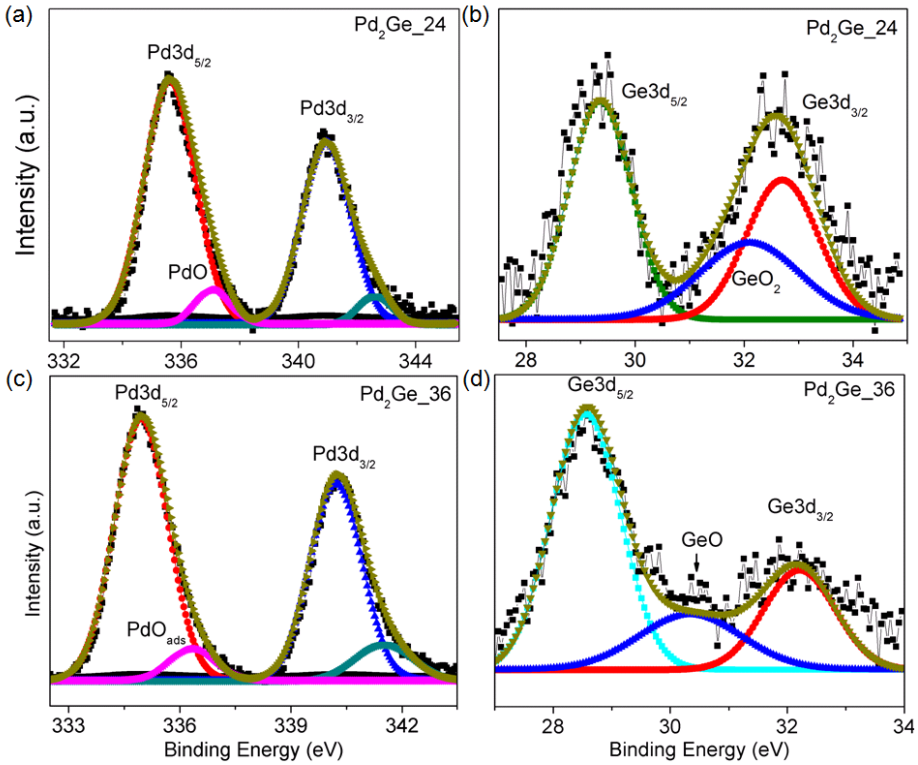

Figure 7.8 XPS data on Pd_2Ge_24 and Pd_2Ge_36 for (a, c) Pd 3*d* and (b, d) Ge 3*d* orbitals, respectively.

7.3.4 Electrochemical Studies

7.3.4.1 Detailed Study on Pd_2Ge Nanoparticles

The parameters obtained from the electrochemical measurements are given in **Table 7.1**. The stability of the catalysts was studied by running cyclic voltametric sweeps in the range -0.8 to 0.25 V in 1M aqueous KOH solution as shown in **Figure 7.9**. In the anodic sweep, the peaks correspond to the desorption of hydrogen (-0.8 to -0.6 V) and oxidation of Pd (0.0 to 0.25) are quite prominent. In the cathode sweep part, the reduction of PdO (-0.05 to -0.3 V) and adsorption of hydrogen are also apparent. The processes desorption of hydrogen, oxidation of Pd, reduction of PdO and adsorption of hydrogen are marked as a, b, c and d in **Figure 7.9a**. Since the Pd_2Ge_36 sample proved to be a better catalyst compared to the Pd_2Ge_24 sample in terms of current, the stability of this catalyst was studied in alkaline medium up to 10 cycles (**Figure 7.9b**). The current value increases with increasing cycle numbers, which could be accounted by the dealloying process of Pd atoms from the bulk to the surface and hence there is an increment in the current value. This was supported by the powder XRD data with a shift of peaks towards higher 2θ (**Figure 7.2b**). Since PdO reduction peak current is proportional to the exposure of Pd catalytic surface to OH^- adsorption, the electrochemically active surface area (ECSA) was calculated by the integration of charges from PdO reduction region considering the value of 405 $\mu C/cm^2$ for PdO monolayer reduction.[24]

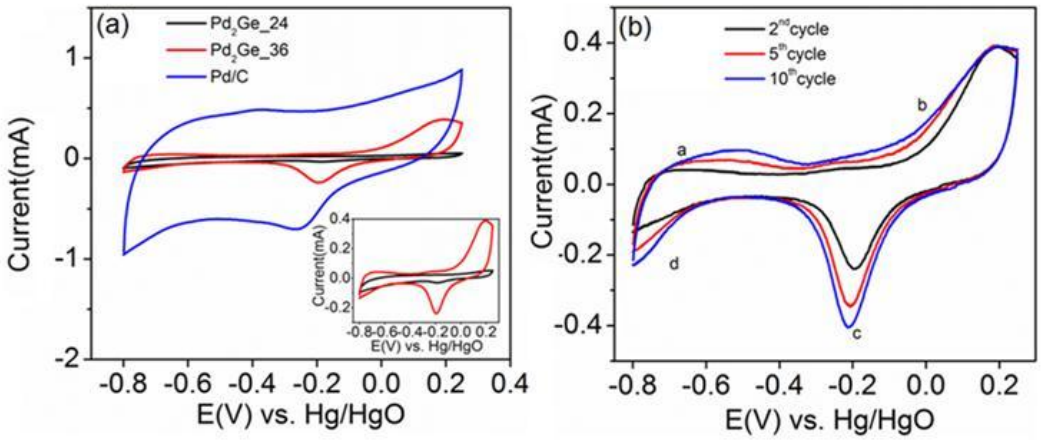

Figure 7.9 (a) CV measurements obtained for Pd_2Ge_24, Pd_2Ge_36 and Pd/C in alkaline (1M KOH) solution at a scan rate of 50 mV/sec. The inset shows the comparison plot of CV for Pd_2Ge_24 and Pd_2Ge_36. **(b)** CV profile of Pd_2Ge_36 with respect to cycles (up to 10^{th} cycle) at a scan rate of 50 mV/sec to check the stability of the catalyst in alkaline (1M KOH) medium.

Table 7.1 Summary of important parameters obtained from the ethanol oxidation.

Catalyst	ECSA (cm^2)	2nd Cycle (Forward Sweep)		250th Cycle (Forward Sweep)		j at -0.1V at 900s (mA/cm^2)
		J ($mAcm^{-2}$)	E (V)	J ($mAcm^{-2}$)	E (V)	
Pd/C	3.10	1.91	-0.081	0.73	-0.12	0.069
Pd_2Ge_24	0.096	2.19	-0.087	3.11	-0.11	0.138
Pd_2Ge_36	1.41	4.1	-0.074	4.64	-0.051	1.57

Typical cyclic voltammograms for EOR on Pd_2Ge_24h, Pd_2Ge_36h and Pd/C are shown in **Figure 7.10**. A significant increase in surface area normalized current density 4.1 $mAcm^{-2}$ (2.2 times) is observed for the sample Pd_2Ge_36 in comparison with commercial Pd/C (1.94 $mAcm^{-2}$) for the same loading clearly indicating that Ge plays a very important role in enhancing the EOR activity. A plausible reason for this could be efficient interaction of Ge with OH^- synergetic with adsorption and desorption of ethanol on Pd, which is also seen observed case of Pd-Sn catalysts.[18] Pd_2Ge_24 shows marginal increase in current density 2.12 $mAcm^{-2}$ as compared to Pd/C 1.94 $mAcm^{-2}$ for forward oxidation process in the second cycle.

The ethanol oxidation efficiency of Pd_2Ge_36 was better than its counterpart, Pd_2Ge_24 and Pd/C as observed in the cycling study (**Figure 7.10a and 7.10b**). It was seen that the catalyst is highly active till 250th cycle with current density of 4.6 $mAcm^{-2}$, whereas 4.1 $mAcm^{-2}$ for the 2nd cycle. The high stability of the catalyst in terms of current density up to such large cycle life infers that the catalyst is greatly resistant to surface poisoning. Still the shift of forward peak potential with 100th and 250th (-0.07V to -0.04V) shows the catalyst is prone to catalytic poisoning at higher cycles. In **Figure 7.10a**, it was noticed that the difference in current density between Pd_2Ge_24 and Pd/C was marginal but the same comparison plot for 250th cycle for ethanol oxidation (**Figure 7.10c**), the current density of Pd_2Ge_24 has increased by 4.3 times more than that of commercial Pd/C with negligible change in peak potential strongly suggesting that the ordering in the structure plays significant role in the stability of Pd_2Ge towards EOR activity. Interestingly, the current density of Pd/C has dropped by 2.7 times at the 250th cycle as compared to the 2nd cycle. In addition, as expected, the efficient catalyst Pd_2Ge_36 showed highest current density, which is 6.4 times more than that of Pd/C.

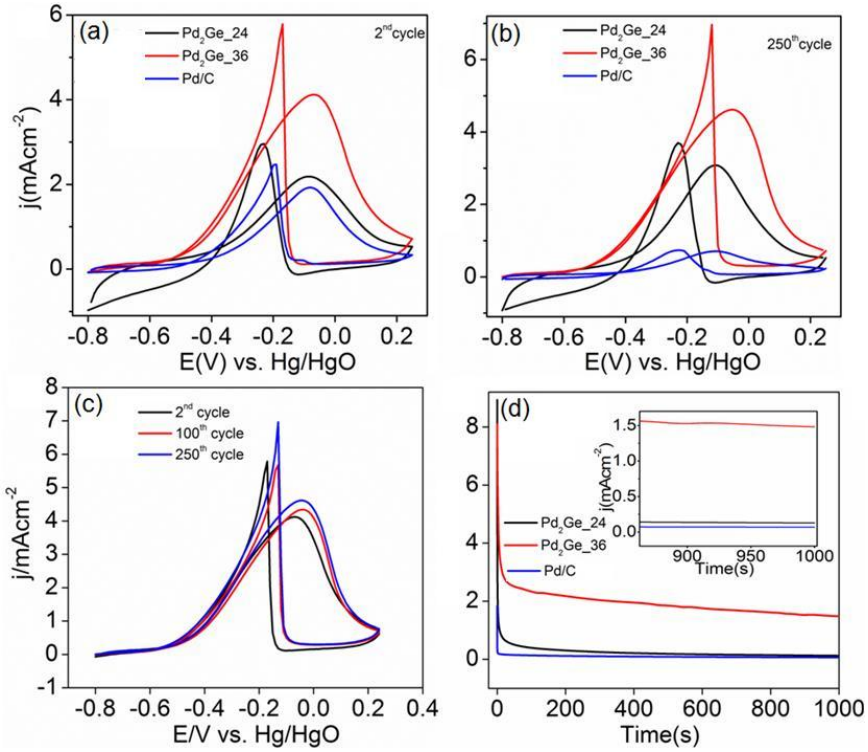

Figure 7.10 (a) CV curves measured for the 2nd cycle for the catalysts Pd_2Ge_24, Pd_2Ge_36 and Pd/C, (b) CV curves measured for the catalyst Pd_2Ge_36 with respect to cycle and (c) CV curves measured for the 250th cycle for the catalysts Pd_2Ge_24, Pd_2Ge_36, Pd/C. In all above cases 1 M KOH containing 1 M ethanol solution at a scan rate of 50 mV/sec were used. (d) Chronoamperometric measurements (CA) of Pd_2Ge_24, Pd_2Ge_36, Pd/C in 1 M KOH + 1M ethanol solution for 1000 sec at electrode potential of -0.1V vs Hg/HgO.

Figure 7.10d shows the chronoamperometric (CA) measurement for Pd_2Ge_36, Pd_2Ge_24 and Pd/C at -0.1V vs. Hg/HgO for the catalytic ethanol oxidation of 1M ethanol in 1M KOH for 1000s was carried out to follow the electrochemical stability of the catalyst. The stability of Pd_2Ge_36 is better than the other two catalysts. The order of decay observed was in the order of Pd_2Ge_36< Pd_2Ge_24< Pd/C, with Pd/C showing 21.7 times decay profile than Pd_2Ge_36 between 900-1000s. **Table 7.1** summarises the comparable data for ethanol oxidation over Pd_2Ge_24, Pd_2Ge_36 and Pd/C. The presence of Ge in Pd_2Ge crystal lattice increases the stability of the catalysts for the elelctrocatalytic oxidation of ethanol in alkaline medium. This clearly suggests that more ordering or in other words less deficiency in Pd_2Ge favours better catalytic activity and more stability towards EOR. Stability was further verified by performing HRTEM and SAED studies on both the catalysts after 250 cycles of CV run. It was found out that there

was almost no change in either the morphology or in the *d*-spacing (**Figure 7.11**) of the electrode material examined which clearly reveals the morphological as well as structural robustness of this material.

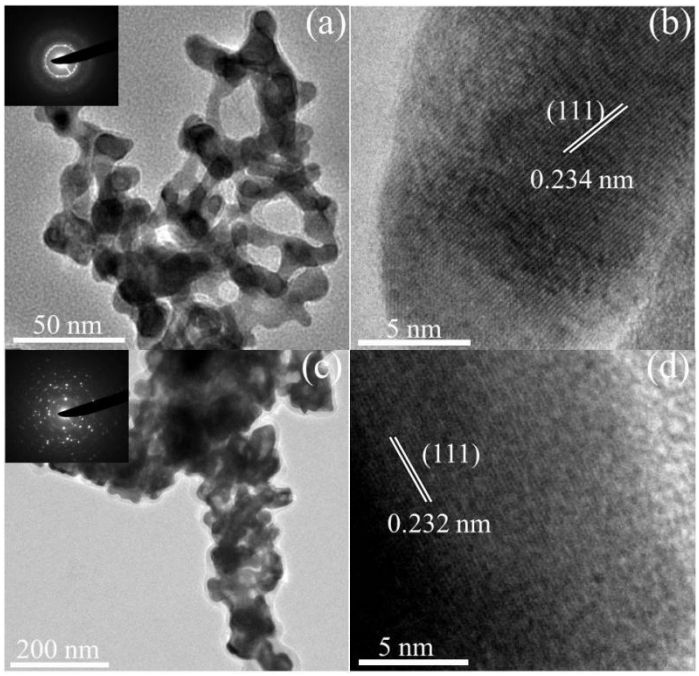

Figure 7.11 TEM characterization of Pd_2Ge catalysts after 250 cycles. TEM and HRTEM images of (a, b) Pd_2Ge_24, and (c, d) Pd_2Ge_36 respectively. Inset shows corresponding SAED patterns.

Figure 7.12 shows preliminary cyclic voltametric study of the transition metal substituted Pd_2Ge synthesized after 24 h under similar reaction conditions. In this case the catalyst loading was reduced to 5 μL taken from a solution of 1 mg/mL of catalyst slurry (1:1 water/isopropanol + 20 μL Nafion solution). Same was repeated for Pd_2Ge_24 again. It was observed that the activity of the materials is in the order of $Pd_{1.82}Mn_{0.18}Ge$ > $Pd_{1.7}Ni_{0.3}Ge$> $Pd_{1.7}Cu_{0.3}Ge$ > Pd_2Ge even with very low loading. More detailed study is underway to get a deep insight into the reason of this reactivity order.

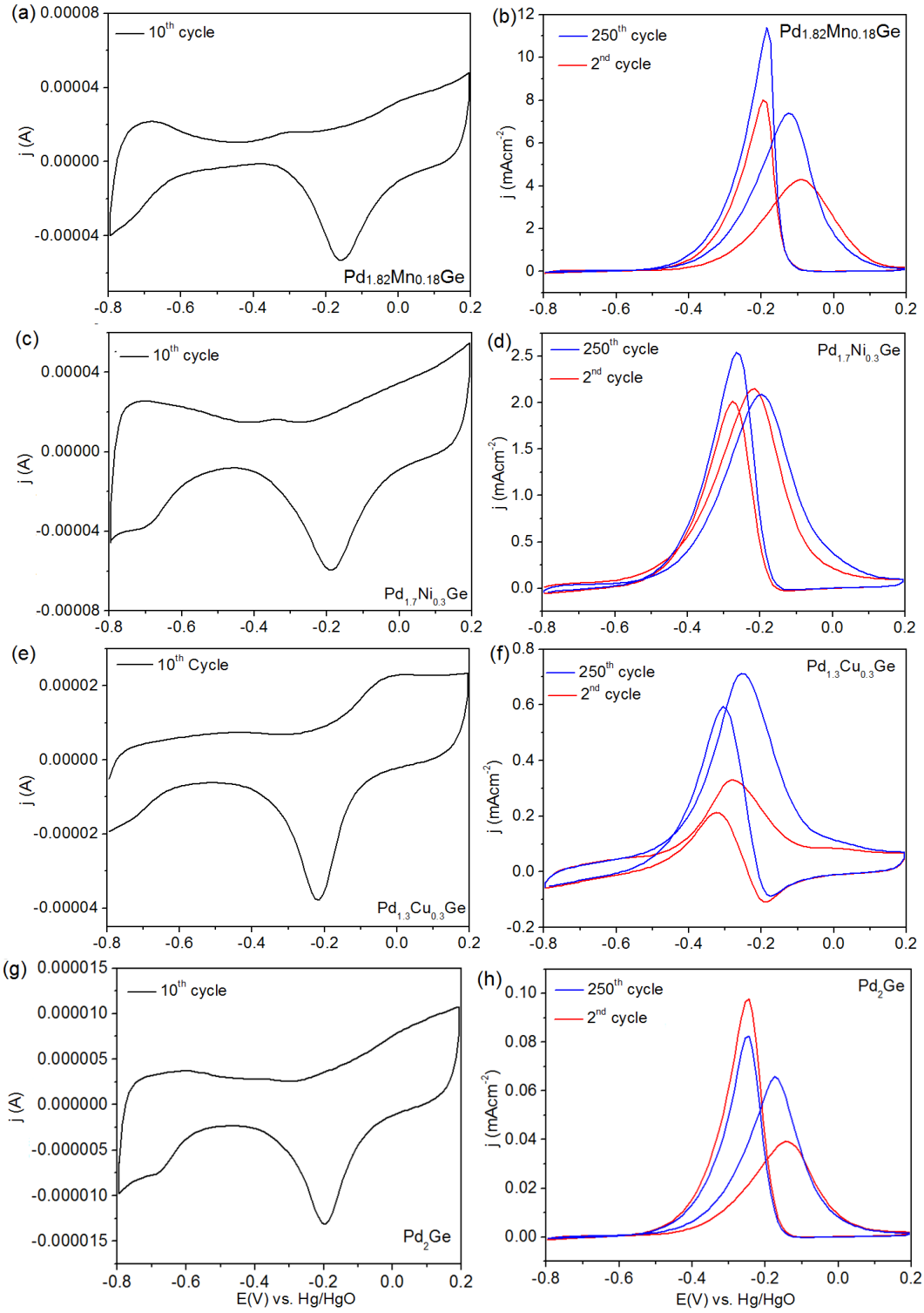

Figure 7.12 (a, b) CV curves measured for the 2nd cycle for the catalysts $Pd_{1.82}Mn_{018}Ge$ and in presence of EtOH, (c, d) CV curves measured for the 2nd cycle for the catalysts $Pd_{1.3}Ni_{0.3}Ge$ and in presence of EtOH, (e, f) CV curves measured for the 2nd cycle for the catalysts $Pd_{1.7}Cu_{0.3}Ge$ and in presence of EtOH, (g, h) CV curves measured for the 2nd cycle for the catalysts Pd_2Ge and in presence of EtOH.

Figure 7.13 shows the charge transfer kinetic behaviour for Pd_2Ge_36 and Pd/C for EOR on based on Tafel plots obtained from the LSV measurements. Since Pd_2Ge_36 showed better activity than Pd_2Ge_24, it was chosen for the investigation of quasi steady state Tafel polarization in comparison with Pd/C. The onset potential obtained are -0.52 and -0.49 for Pd_2Ge_36 and Pd/C, respectively (**Table 7.2**) used in the calculation Tafel slope, which is a measure of charge transfer kinetic activity. Inset in **Figure 7.13** shows the linear Tafel plot obtained from the plot of log current density vs. potential, where the potential range is -0.5V to -0.2V. The expression relating current density and potential is

$$\eta = 2.303RT \log (j/j_o)/\alpha \, n \, F \; ... \; \textbf{eq. 7.1}$$

Where η is the overpotential (η = E-E_{theory}), α is the anodic transfer coefficient, n is the number of electrons transferred in the reaction and j_o is the exchange current density, j is the current density obtained experimentally at a particular potential.

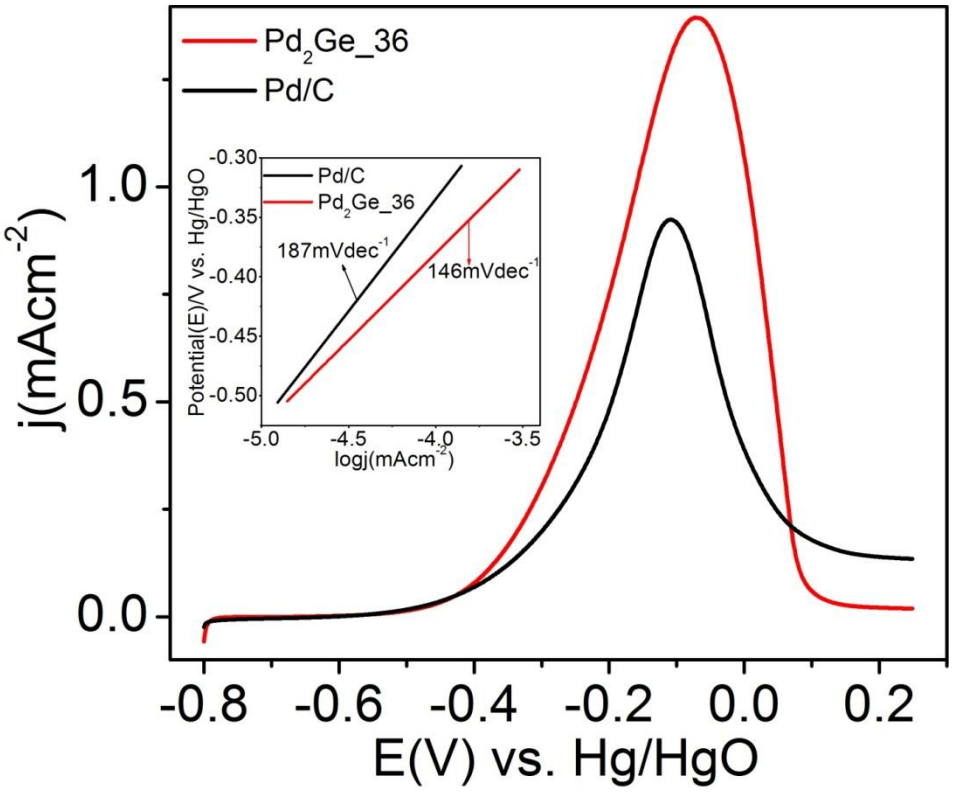

Figure 7.13 Quasi-steady state linear scan voltammograms of Pd/C and Pd_2Ge_36 catalysts in 1 M KOH + 1M ethanol solution, at 1.0mV/sec (Inset is the Tafel plot of Pd/C andPd_2Ge_36 in 1 M KOH + 1M ethanol solution).

The starting potential observed as 230 mV and is higher than the theoretical potential (E_{theory}) -0.87 mV.[17] Tafel slope obtained for Pd_2Ge_36 (146 $mVdec^{-1}$) is lower

than Pd/C (187 $mVdec^{-1}$) indicating that Pd_2Ge_36 possess higher charge transfer kinetic activity for the EOR on the electrode surface. As a result, it can be stated that the catalyst Pd_2Ge_36 has higher efficiency for the adsorption of OH^-, which in turn affects the kinetics of EOR.[17,24] This leads to the oxidation of intermediates adsorbed on the electrode surface.

Exchange current density was calculated by extrapolating the Tafel line, where the over potential is zero. The surface activity normalized exchange current density (j_O/$mAcm^{-2}$) for Pd_2Ge_36 (38.9 $mAcm^{-2}$) is 6.6 times higher than Pd/C (5.8 $mAcm^{-2}$), as shown in **Table 7.2**. Based on the Tafel slope and j_O it can be concluded that Pd_2Ge_36 is kinetically more active than the commercial Pd/C for the EOR on the catalyst surface.

Table 7.2 Parameters obtained from the Tafel plot based on LSV studies.

Catalyst	Onset Potential (V vs Hg/HgO)	Tafel Slope (mV/dec)	Exchange current density (mA/cm^2)
Pd/C	-0.49	187	5.8
Pd_2Ge_36	-0.52	146	38.9

7.3.5 Theoretical analysis

Most catalytic reactions are governed by Sabatier principle, which states that catalytic activity will be optimum when binding of reactive intermediates with catalytic surface has *intermediate free energies of adsorption* (*binding energies*).[30] This principle was used as a basis to rationalize the catalytic activity of Pd_2Ge. The ethanol electro-oxidation reaction in alkaline medium on the metal surface involves many steps and intermediates among which the formation of CH_3COOH (shown below) is the rate determining step.[31]

$$M - (CH_3CO)_{ads} + M - (OH)_{ads} \longrightarrow M - CH_3COOH + M \quad \textbf{eq. 7.2}$$

The main intermediate species during ethanol electro-oxidation are CH_3CO[31] and OH,[31] the latter helps in cleaning the surface of the catalyst through oxidizing the carbonecious species. Various initial configurations of CH_3CO and OH were used on Pd_2Ge and Pd (111) surfaces.

The most favorable binding configurations of CH_3CO and OH adsorbed on Pd_2Ge are determined through minimization of energy (**Figures 7.14a and 7.14b**, respectively). OH adsorbs at a minimum distance of 1.2 Å, 1.1 Å and 1.2 Å from the surface atoms on

Pd (111), Pd_2Ge _24 and Pd_2Ge _36 surfaces respectively, whereas, CH_3CO adsorbs at a minimum distance of 1.79 Å, 1.49 Å and 1.79Å from the surface atoms on Pd (111), Pd_2Ge_24 and Pd_2Ge_36 surfaces, respectively. Corresponding adsorption energies are summarized in **Table 7.3**. On the basis of adsorption energy it can clearly be seen that OH binds quite strongly with Pd_2Ge surfaces compared to Pd (111) surface. After OH adsorption, Pd_2Ge surface undergoes strong relaxation of about 0.2 Å compared to ~0.1 Å in case of Pd surface. This strong relaxation of Pd_2Ge surfaces shows the strong interaction between the surface and the adsorbate and hence stronger binding of OH compared to Pd (111) surface. This is also evident in density of states as shown in **Figure 7.15**. In case of Pd_2Ge _24and Pd_2Ge _36, OH binds strongly to the former. Also, Pd_2Ge binds strongly to CH_3CO followed by Pd (111) and Pd_2Ge_36.

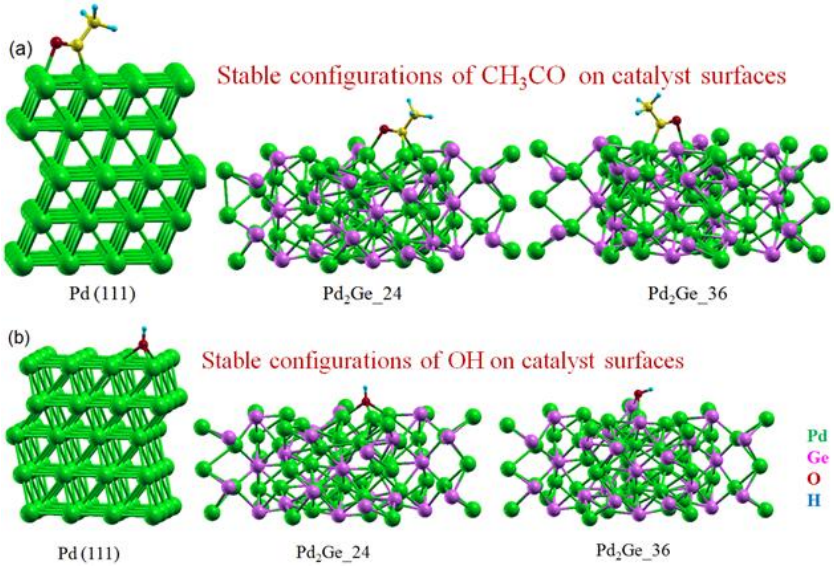

Figure 7.14 The binding configuration of the adsorption of a) CH_3CO and b) OH on Pd(111), Pd_2Ge_24 and Pd_2Ge_36 samples.

To get a better insight into it, *d*-band model was applied as proposed by Hammer and Nørskov.[32] According to this model, higher the *d*-band centre greater is the binding and hence, the catalytic activity. The *d*-band center (ε_d) is given by the following relation in this model:

$$\varepsilon_d = \frac{\int_{-\infty}^{E_F} E\rho_d(E)dE}{\int_{-\infty}^{E_F} \rho_d(E)dE} \quad \text{... eq. 7.3}$$

where, ρ_d is the projected density of *d*-states of surface atoms, E is the energy and E_F is the Fermi level.

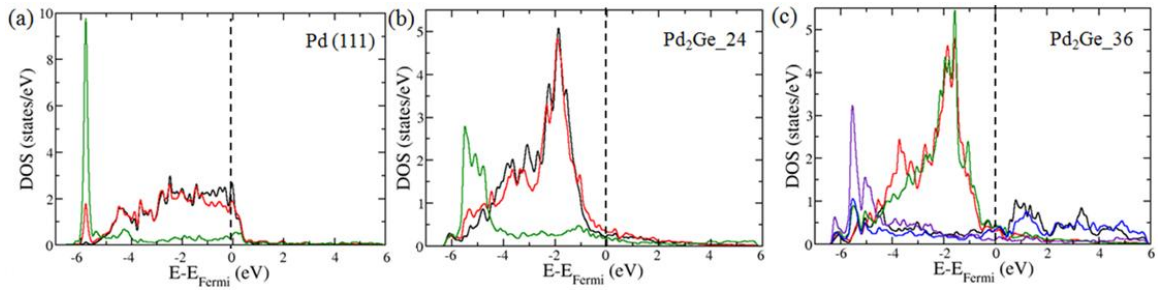

Figure 7.15 Projected density of states of Pd-4*d*, Ge-4*p*, and O-2*p* orbitals of surfaces. (a, b) The states arising from surface Pd atoms, Pd atom to which O is attached and O atoms have been represented by black, red and green curves respectively. (c) States arising from surface Ge, surface Pd, Ge and Pd to which O is attached and O atoms are represented by black, red, green, blue and indigo curves respectively.

The average *d*-band center for CH_3CO and OH adsorbed on the surface atoms was obtained (**Table 7.3**). The *d*-band model fails for Pd(111) and Pd_2Ge_24 surfaces but value of *d*-band center of Pd_2Ge_36 correlates well with its binding energy. Pd_2Ge _36 has fairly high value of d-band center and hence can bind strongly with OH. In case of CH_3CO adsorption *d*-band center lie below the Fermi level and hence binds weakly with the Pd_2Ge_36 surface. Pd_2Ge_24 is Ge-deficient and hence possesses vacant Ge sites on its surface, which have two important consequences on the binding ability with the adsorbate: first, these vacant sites themselves act as an active adsorption sites[33] and secondly, Ge vacancies will expose Pd sites to both CH_3CO and OH radicals (which also act as a catalyst poison at higher adsorption energy) to a greater extent leading to decreased coordination number,[34] and high adsorption energy (**Table 7.3**). Thus, the too much strong binding of adsorbate will poison the catalyst surface by decreasing the effective coverage of incoming CH_3CH_2OH molecules. Also, a good catalyst for ethanol oxidation should bind strongly with OH and weakly with CH_3CO, these two criteria are well satisfied by Pd_2Ge_36 and Pd_2Ge_24 shows the intermediate catalytic activity between Pd (111) and Pd_2Ge_36.

The potential required for ethanol oxidation for different catalysts has been shown in **Table 7.1**. Using the relation, E(NHE) = E(Hg/HgO) + 0.108 V[35] the potentials were converted to NHE scale. On NHE scale, the minimum potential required for ethanol oxidation is around 4.5 eV. The work function (ϕ_s) (**Table 7.3**) was calculated using the following relation:

$$\phi_s = V_{vacuum} - V_{Ferni}$$

Here, V_{vacuum} and V_{Fermi} are the potentials in the vacuum and at Fermi level. ϕ_s value clearly shows that the Pd (111) lies below on the potential scale of ethanol oxidation compared to Pd_2Ge surfaces. This also confirms the strong catalytic activity of Pd_2Ge surfaces in comparison to Pd (111) surface.

Table 7.3 Adsorption energies (kJ/mol) for CH_3CO and OH radicals on different catalyst surfaces. Average value of *d*-band centers[19] of CH_3CO and OH adsorbed surface atoms has been shown in the brackets. The work functions for different catalyst surfaces also listed.

Catalyst	CH_3CO	OH	ϕ_s [19]
Pd (111)	-335.0 (-2.50)	388.10 (-2.24)	5.7
Pd_2Ge_24	-368.78 (-2.73)	489.53 (-2.40)	5.0
Pd_2Ge_36	-288.0 (-2.90)	436.42 (-2.33)	4.9

7.4 Conclusion

Pd_2Ge nanoparticles were synthesized for the first time using the solution based chemistry. The ordered intermetallic nature of this compound was confirmed by X-ray and electron diffraction techniques. The material was tested for its electrochemical activity towards ethanol oxidation and was found to be highly active and durable up to 250 cycles compared to the commercially available catalyst (Pd/C). Our work establishes the fact that *p*-block elements can also be used like the first row transition metals as an active constituent along with the noble metals in the form of bimetallic/alloys and/or intermetallic compound and paves the way to the detailed study of other unexplored compounds of this class. Moreover, ordered Pd_2Ge nanoparticles can also be regarded as a model system where a perfect balance between the adsorption energies of CH_3CO and OH on the catalyst surface dictates its electrocatalytic activity and the presence of vacancies in the inactive sites undoubtedly affects the course of reactivity.

7.5 References

1. Shao, M., *Electrocatalysis in Fuel Cells: A Non- and Low- Platinum Approach*. Springer Science & Business Media: 2013.

2. Mcmurry, J. E.; Fay, R. C., Pearsons publications: New Delhi, 2008.

3. Meenakshi, S.; Sridhar, P.; Pitchumani, S., *RSC Adv.* **2014,** *4* (84), 44386-44393.

4. Bagchi, J.; Bhattacharya, S. K., *J. Power Sources* **2007,** *163* (2), 661-670.

5. Xu, C.; Shen, P. k.; Liu, Y., *J. Power Sources* **2007,** *164* (2), 527-531.

6. Wang, M.; Guo, D. J.; Li, H. L., *J. Solid State Chem.* **2005,** *178* (6), 1996-2000.

7. Zhang, K. F.; Guo, D. J.; Liu, X.; Li, J.; Li, H. L.; Su, Z. X., *J. Power Sources* **2006,** *162* (2), 1077-1081.

8. Xu, C. W.; Shen, P. K.; Liu, Y. L., *J. Power Sources* **2007,** *164* (2), 527-531.

9. Zheng, H. T.; Li, Y. L.; Chen, S. X.; Shen, P. K., *J. Power Sources* **2006,** *163* (1), 371-375.

10. Xu, C. W.; Tian, Z. Q.; Shen, P. K.; Jiang, S. P., *Electrochim. Acta.* **2008,** *53* (5), 2610-2618.

11. Chu, D. B.; Wang, J.; Wang, S. X.; Zha, L. W.; He, J. G.; Hou, Y. Y.; Yan, Y. X.; Lin, H. S.; Tian, Z. W., *Catal. Commun.* **2009,** *10* (6), 955-958.

12. Sun, Z. P.; Zhang, X. G.; Liu, R. L.; Liang, Y. Y.; Li, H. L., *J. Power Sources* **2008,** *185* (2), 801-806.

13. Zhang, Z. Y.; Xin, L.; Sun, K.; Li, W. Z., *Int. J. Hydrogen Energ.* **2011,** *36* (20), 12686-12697.

14. Lin, S. C.; Chen, J. Y.; Hsieh, Y. F.; Wu, P. W., *Mat. Lett.* **2011,** *65*.

15. Shi, L. H.; Wang, A. Q.; Huang, Y. Q.; Chen, X. W.; Delgado, J. J.; Zhang, T., *Eur. J. Inorg. Chem.* **2012,** (16), 2700-2706.

16. Yi, Q. F.; Niu, F. J.; Song, L. H.; Liu, X. P.; Nie, H. D., *Electroanal.* **2011,** *23* (9), 2232-2240.

17. Herranz, T.; Ibáñez, M.; Gómez de la Fuente, J. L.; Pérez-Alonso, F. J.; Peña, M. A.; Cabot, A.; Rojas, S., *ChemElectroChem.* **2014,** *1* (5), 885-895.

18. Subbarao, U.; Peter, S. C., *Inorg. Chem.* **2012,** *51*, 6326-6332.

19. Kodiyath, R.; Ramesh, G. V.; Koudelkova, E.; Tanabe, T.; Ito, M.; Manikandan, M.; Ueda, S.; Fujita, T.; Umezawa, N.; Noguchi, H.; Ariga, K.; Abe, H., *Energ. Environ. Sci.* **2015**.

20. Rao, L.; Jiang, Y.-X.; Zhang, B.-W.; Cai, Y.-R.; Sun, S.-G., *Phys. Chem. Chem. Phys.* **2014,** *16* (27), 13662-13671.

21. Hong, W.; Wang, J.; Wang, E., *ACS App. Mater. Inter.* **2014,** *6* (12), 9481-9487.

22. Wopersnow, W. S., K. , *J. Less-Common Met.* **1977,** *52*.

23. Paolo, G.; Stefano, B.; Nicola, B.; Matteo, C.; Roberto, C.; Carlo, C.; Davide, C.; Guido, L. C.; Matteo, C.; Ismaila, D.; Andrea Dal, C.; Stefano de, G.; Stefano, F.; Guido, F.; Ralph, G.; Uwe, G.; Christos, G.; Anton, K.; Michele, L.; Layla, M.-S.; Nicola, M.; Francesco, M.; Riccardo, M.; Stefano, P.; Alfredo, P.; Lorenzo, P.; Carlo, S.; Sandro, S.; Gabriele, S.; Ari, P. S.; Alexander, S.; Paolo, U.; Renata, M. W., *J. Phys.: Condens. Matter.* **2009,** *21* (39), 395502.

24. Perdew, J. P.; Zunger, A., *Phys. Rev. B* **1981,** *23* (10), 5048-5079.

25. Hong, W.; Wang, J.; Wang, E., *ACS Appl. Mater. Inter.* **2014,** *6* (12), 9481-9487.

26. Shi, L. H.; Wang, A. Q.; Huang, Y. Q.; Chen, X. W.; Delgado, J. J.; Zhang, T., *Eur. J. Inorg. Chem.* **2012,** (16), 2700-2706.

27. Corcoran, C. J.; Tavassol, H.; Rigsby, M. A.; Bagus, P. S.; Wieckowski, A., *J. Power Sources* **2010,** *195* (24), 7856-7879.

28. Casella, I. G.; Contursi, M., *J. Electroanal. Chem.* **2006,** *588* (1), 147-154.

29. Prabhakaran, K.; Ogino, T., *Surf. Sci.* **1995,** *325* (3), 263-271.

30. Sabatier, P., *Ber. Deutschen Chem. Gesellschaft* **1911,** *44*, 1984-2001.

31. Liang, Z. X.; Zhao, T. S.; Xu, J. B.; Zhu, L. D., *Electrochim. Acta* **2009,** *54* 2203–2208.

32. Hammer, B.; Nørskov, J. K., *Surf. Sci.* **1995,** *343* (3), 211-220.

33. Gonzalez, E.; Jasen, P.; Gonzalez, G.; Moro, L.; Juan, A., *Phys. Status Solidi* **2009,** *B246*, 1275–1285.

34. Calle-Vallejo, F.; Martinez, J. I.; Garcia- Lastra, J. M.; Sautet, P.; Loffreda, D., *Angew. Chem. Int. Ed.* **2014,** *53*, 8316 –8319.

35. Nickell, R. A.; Zhu, W. H.; Payne, R. U.; Cahela, D. R.; Tatarchuk, B. J., *J. Power Sources* **2006,** *161* (2), 1217-1224.

Summary

Summary

In this thesis, an exploratory synthetic approach involving mainly metal flux method was adopted in order to synthesize many new bulk intermetallic compounds in the RE_2TX_3 series as well as other related superstructures derived from the AlB_2 prototype and it is shown that this method is very effective in order to obtain not only new phases but also for high quality single crystal growth which is an essential requirement for both precise determination of crystal structure (known as complete structure determination) and anisotropic properties measurement which is not possible in case of polycrystalline sample. In addition, single crystals are more desirable than pellets made up of compressed polycrystalline sample, which, in most of the times, is limited by grain boundaries and micro cracks that hinder proper transport property measurements. In many cases, however, this method failed to produce the desired product, which constitutes a major drawback of metal flux technique. In those cases, conventional high temperature methods like direct heating in a furnace, arc-melting, *HF*- induction heating have been utilized for the synthesis of the compounds with stoichiometric ratio. Special focus has been given to Ce, Eu and Yb based compounds, owing to their ability to form mixed/intermediate valence compounds, which in turn, gives way to a variety of physical properties. At this point, it is worthwhile to mention the driving factors that give rise to different superstructure derivatives in the AlB_2 family. First, the size of the atoms substituting at the Al and/or B positions is perhaps the most crucial facor. Larger atoms give rise o higher strain in the hexagonal ring leading to puckering which in turn may lead to reduction in symmetry; second, mixing of atomic sites, mostly among transition and *p*-block metals in the hexagonal ring is another factor which brings in disorder in the system and may cause superstructure formation; third, presence of *RE* atoms which can show multiple valency (e.g. Ce, Eu and Yb) may also impart superstructure formation due to difference in radii of the two mixed valence species (3+/4+ for Ce and 2+/3+ for Eu, Yb). Two Ce based compounds, namely, Ce_2PdGe_3 and Ce_2PtGe_3 were synthesized by arc-melting method. The former shows three different crystal structures with slight variation in Pd to Ge ratio. Among the polymorphs, β-Ce_2PdGe_3 crystallizes in tetragonal structure whereas γ-Ce_2PdGe_3 crystallizes in a new hexagonal superstructure of the AlB_2 type. Detailed magnetic measurements suggest spin glass behavior in the former compounds and magnetic exchange bias phenomenon in the latter. Ce_2PtGe_3 adopts a new orthorhombic superstructure type with *Cmca* space group. Advanced single crystal XRD

suggest that this compound is a modulated structure, which is considered as the first one in this family. This compound undergoes spin-glass transition at low temperature, which was verified by Isothermal Remnant Magnetization and AC susceptibility measurements. In the Eu based series, three compounds, Eu_2CuGe_3, Eu_2AuSi_3 and Eu_2AgGe_3 were synthesized. Temperature dependent reentrant structural phase transitions which was explained based on a lattice displacive mechanism was observed in the latter compound. The compound also underwent multiple magnetic transitions at low temperature. Field dependent resistivity measurements on Eu_2AgGe_3 suggest the compound is Kondo behavior at lower temperature or pseudo-gap at higher temperature. Three Yb based compounds: Yb_2CuGe_3, Yb_2AuSi_3 and Yb_2AuGe_3 were studied for their structure and physical properties. Yb_2AuGe_3 showed temperature dependent structural phase transition which was explained based on a general order-disorder phase transition mechanism and Yb was found out to be in mixed valence state. All these compounds are completely ordered superstructure variants, however, four other compounds, RE_2AgGe_3 (*RE* = Ce, Pr, Nd) and Nd_2NiGe_3 were also studied. The first three compounds crystallize in the α-$ThSi_2$ structure type, whereas Nd_2NiGe_3 in disordered AlB_2 type. The structural relationship between AlB_2 and α-$ThSi_2$ prototypes was also discussed. Eu*T*In_4 (*T* = Ir, Au) and $EuAu_2In_4$ series of compounds are examples of polyindides, which were synthesized by using indium as an active metal flux. The structural evolution of these two families from AlB_2 prototype were shown both geometrically and crystallographically. The concept of ordered intermetallic phase in AlB_2 family was further extended to the nanoscale where the synthesis, characterization and study of electrocatalytic activity of Pd_2Ge nanoparticles and its variants substituted with first row transition metals. All these compounds crystallize in Fe_2P crystal structure, which is a vacancy ordered superstructure of AlB_2 structure type. The catalytic activity of all these compounds has been studied by the electrochemical oxidation of ethanol. Transition metal substituted Pd_2Ge materials improved the properties further. The reaction mechanism was studied by electronic structure calculations. The stability of the materials was checked by chronoamperometric measurements, which confirmed that the materials under study are more stable than commercial Pd/C.

List of Publications

1. *On the modulated superstructure and pseudogap formation in Ce_2PtGe_3,* Sarkar, S.; Kalsi, D.; Rawat, S.; Peter, S. C. **2016** (Manuscript in preparation).

2. *Synthetically Tuned Structural Variations in Ce_2PdGe_3 Towards Exchange Bias and other Physical Properties,* Sarkar, S.; Halappa, P.; Kalsi, D.; Banerjee, S.; Pati, S. K.; Ghara, S.; Sundaresan, A.; Silva, I. D.; Rawat, R.; Rayaprol, S.; Joseph, B.; Peter, S. C., **2016** (Manuscript in preparation).

3. F*acile Aqueous Phase Synthesis of $PtAu/Bi_2O_3$ Hybrid Catalyst for Efficient Electro-Oxidation of Ethanol,* Sarkar, S.; Jana, R.; Vadlamani, H.; Ramani, S.; Mumbaraddi, D.; Peter, S. C. **2016** (Submitted).

4. *$Eu_3Ir_2In_{15}$: A Mixed-Valent and Vacancy-Filled Variant of the $Sc_5Co_4Si_{10}$ Structure Type with Anomalous Magnetic Properties,* Sarkar, S.; Banerjee, S.; Jana, R.; Siva, R.; Pati, S. K.; Balasubramanian, M.; Peter, S. C., *Inorg. Chem.* **2015**, 54, 10855-10864.

5. *Ordered Pd_2Ge Intermetallic Nanoparticles as Highly Efficient and Robust Catalyst for Ethanol Oxidation*, Sarkar, S.; Jana, R.; Suchitra; Waghmare, U. V.; Kuppan, B.; Sampath, S.; Peter, S. C., *Chem. Mater.* **2015**, *27*, 7459-7467.

6. *A Review on the Synthesis, Crystal Growth, Structure and Physical Properties of Rare Earth based Quaternary Intermetallic Compounds*, Mumbaraddi, D.; Sarkar, S.; Peter, S. C., *J. Solid State Chem.* Doi:10.1016/j.jssc.2015.10.032, **2016**.

7. *Magnetic and X-ray absorption studies on the $RE_5X_2Sb_6$ (RE = Eu, Yb; X = Al, Ga, In) compounds,* Subbarao, U.; Sarkar, S.; Joseph, B.; Peter, S. C., *J. Alloys Comp.* **2016**, *658*, 395-401.

8. *Heterostructure Composites of rGO/GeO_2/PANI with Enhanced Performance for Li Ion Battery Anode Material,* , Sarkar, S.; Borah, R.; Santhosha, A. L.; Dhanya , R.; Narayana, C.; Bhattacharyya, A. J.; Peter, S. C. *J. Power Sources*, **2016**, 306, 791-800.

9. *Structure and physical properties of RE_2AgGe_3 (RE = Ce, Pr, Nd) compounds*, Sarkar, S.; Mumbaraddi, D.; Halappa, P.; Kalsi, D.; Rayaprol, S.; Peter, S. C., *J. Solid State Chem*. **2015**, *229*, 287-295.

10. *Crystal structure and properties of tetragonal $EuAg_4In_8$ grown by metal flux technique*, Subbarao, U.; Sarkar, S.; Peter, S. C. *J. Solid State Chem.* **2015**, *226*, 126-132.

11. *Studies on the structure and magnetic properties of Nd_2NiGe_3 using neutron diffraction as a complementary technique to X-ray diffraction and magnetic susceptibility*, Sarkar, S.; Kalsi, D.; Rayaprol, S.; Peter, S. C., *J. Alloys Compd.* **2015**, *632*, 172-177.

12. *Mixed valence and metamagnetism in a metal flux grown compound $Eu_2Pt_3Si_5$*, Sarkar, S.; Subbarao, U.; Joseph, B.; Peter, S. C. *J. Solid State Chem.* **2015**, *225*, 181-186.

13. *Crystal growth, structure and magnetic properties of $Sm_3Ni_5Al_{19}$: A compound in the $Sm_{2n+m}Ni_{4n+m}Al_{15n+4m}$ homologous series*, Subbarao, U.; Ghosh, A.; Sarkar, S.; Peter, S. C. *J. Chem. Sci.* **2014**, *126*, 1605-1613.

14. *Crystal structure and magnetic properties of a Zintl phase EuIrIn4: the first member in the Eu-Ir-In family*, Sarkar, S.; Guttmann, M. J.; Peter, S. C. Dalton Trans. **2014**, *43*,15879-15886.

15. *Effect of ordered and disordered phases of Ag_3In on the catalytic reduction of p-nitrophenol*, Sarkar, S.; Balisetty, L.; Shanbogh, P.; Peter, S. C. *J. Catal.* **2014,** *380***,** 143-150.

16. *Crystal structure of Yb_2CuGe_6 and $Yb_3Cu_4Ge_4$ and the valency of ytterbium*, Peter, S. C.; Subbarao, U.; Sarkar, S.; Vaitheeswaran, G.; Svane, A.; Kanatzidis, M. G. *J. alloys Compd.* **2014**, *589*, 405-411.

17. *Ligand mediated valence fluctuation of copper in new hybrid materials constructed from decavanadate and Cu(1,10-phenanthroline) complex*, Iyer, A. K.; Roy, S.; Haridasan, R.; Sarkar, S.; Peter, S. C. *Dalton Trans.* **2014**,*43, 2153-2160*.

18. *$Yb_5Ga_2Sb_6$: A mixed valent and narrow-band gap material in the $RE_5M_2X_6$ family*, Subbarao, U.; Sarkar, S.; Gudelli,V.; Kanchana, V.; Vaitheeswaran, G.; Peter, S. C. *Inorg. Chem.* **2013**, *52*, 13631–13638.

19. *Crystal Structure and Magnetic Properties of Indium Flux Grown $EuAuIn_4$ and $EuAu_2In_4$*, Sarkar, S.; Gutmann, M. J.; Peter, S. C. *Cryst. Growth Des.* **2013**, *13*, 4285–4294.

20. *Structural Phase Transitions in a New Compound Eu_2AgGe_3*, Sarkar, S.; Peter, S. C. *Inorg. Chem.*, **2013**, *52*, 9741–9748.

21. *Crystal Structure and physical Properties of Indium Flux Grown RE_2AuSi_3 (RE=Eu, Yb)*, Sarkar, S.; Gutmann, M. J.; Peter, S. C. *CrystEngComm*, **2013**, *15*, 8006-8013.

22. *Effect of Li and Mg Substitution on the Crystal Structure and Magnetism of the $REGa_2$ (RE=Ce and Eu) and $EuGa_4$ Compounds*, Iyer, A. K.; Balisetty, L.; Sarkar, S.; Peter, S. C. *J. Alloys Compd.* **2014**, *582*, 305-312.

23. *Metallic Yb_2AuGe_3: An ordered Superstructure in the AlB_2 type Family with Mixed Valent Yb and a High Temperature Phase Transition*, Peter, S. C.; Sarkar, S.; Kanatzidis, M. G. *Inorg. Chem.* **2012**, *51*,10793.

24. *Single Crystal Growth of Europium and Ytterbium Based Intermetallic Compounds Using Metal Flux Technique*, Sarkar, S.; Peter, S. C. *J. Chem. Sci.* **2012**, *124*, 385-390.